Improving Charge Transport via Self-assembly in Semiconducting Donor/Acceptor Supramolecular Polymers

Thesis Submitted to AcSIR For the Award of the Degree of
DOCTOR OF PHILOSOPHY
In Chemical Science

By
Saibal Bhaumik
Registration Number: 10CC11J26035

Under the guidance of
Dr. S. K. Asha

CSIR-National Chemical Laboratory

Dedicated to My Family
for their limitless love & encouragement……

DECLARATION

I hereby declare that the research work embodied in the thesis entitled **"Improving Charge Transport via Self-assembly in Semiconducting Donor/Acceptor Supramolecular Polymers"** has been carried out by me at Polymer Science and Engineering Division of CSIR-National Chemical Laboratory, Pune under the supervision of Dr. S. K. Asha I also affirm that this work is original and has not been submitted in part or full, for any other degree or diploma to this or any other University or Institution.

Saibal Bhaumik **September 2016**
Polymer Science and Engineering Division
CSIR-National Chemical Laboratory,
Pune-411 008, India.

राष्ट्रीय रासायनिक प्रयोगशाला
(वैज्ञानिक तथा औद्योगिक अनुसंधान परिषद)
डॉ. होमी भाभा रोड, पुणे - 411 008. भारत
NATIONAL CHEMICAL LABORATORY
(Council of Scientific & Industrial Research)
Dr. Homi Bhabha Road, Pune - 411008. India

Certificate

This is to certify that the work incorporated in this Ph.D. thesis entitled **"Improving Charge Transport via Self-assembly in Semiconducting Donor/Acceptor Supramolecular Polymers"** submitted by **Mr. Saibal Bhaumik** to **Academy of Scientific and Innovative Research (AcSIR)** in fulfillment of the requirements for the award of the Degree of Doctor of Philosophy, embodies original research work under my supervision. I further certify that this work has not been submitted to any other University or Institution in part or full for the award of any degree or diploma. Research material obtained from other sources has been duly acknowledged in the thesis. Any text, illustration, table etc., used in the thesis from other sources, have been duly cited and acknowledged.

Saibal Bhaumik
(Student)

Dr. S. K. Asha
(Supervisor)

Communications Channels ☎ +91 20 25902000 +91 20 25893300 +91 20 25893400 Fax +91 20 25902601 (Director) +91 20 25902660 (Admin.) +91 20 25902639 (Business Development) URL : www.ncl-india.org

ACKNOWLEDGEMENTS

One looks back with appreciation to the brilliant teachers, but with gratitude to those who touched our human feelings. The curriculum is so much necessary raw material, but warmth is the vital element for the growing plant and for the soul of the child.

— Carl Jung

After an intensive period of five years, today is the day: writing this note of thanks is the finishing touch to my thesis. It has been a period of intense learning for me, not only in the scientific arena, but also on a personal level. Writing this thesis has had a big impact on me. I would like to reflect on the people who have supported and helped me so much throughout this period.

Firstly, I would like to express my sincere gratitude and thanks to my research supervisor Dr. S. K. Asha for the continuous support that she provided to my Ph.D. study and related research, for her patience, motivation, and immense knowledge. Her guidance helped me throughout the period of research and writing of this thesis. I could not have imagined having a better advisor and mentor for my Ph.D. study.

I owe my most sincere gratitude to Dr. M. Jayakannan (Department of Chemistry IISER, Pune) for his valuable suggestions that have been very helpful for this study.

I am highly thankful to Prof. K. S. Narayan (JNCASR- Bangalore) and Dr. K. Krishnamoorthy for their active collaboration which helped me to understand the semiconducting properties of my system in better way and gave fruitful results.

I would also like to thank Dr. R. Nandini Devi for her valuable scientific discussion during my Ph.D. work.

Besides my advisor, I would like to thank the rest of my DAC committee: Dr. Subashchandrabose C, Dr. K. Krishnamoorthy, Dr. J. Nithyanandhan, for their insightful comments and encouragement, but also for the hard question which incented me to widen my research from various perspectives.

My sincere thanks also goes to Dr. S. Sourav Pal (former director CSIR – NCL) and Prof. Ashwini Kumar Nangia (director CSIR – NCL) for providing me such a fantastic infrastructure to do better research.

I gratefully acknowledge Dr. Prakash Wadagoankar, Dr. Ashish Lele (Head of Polymer Science and Engineering Division), Dr. Rahul Banerjee, Dr. Sayam Sen Gupta, Dr. Ramesh C., Dr. K. Guruswamy, Dr. P. A. Joy, Dr. Avdhani, Dr. Ashutosh Ambade, Prof Ramakrishnan (IISc Banglore) for their valuable suggestions and untried help at various phases of my research, whenever I approached them.

I gratefully acknowledge the financial assistance in form of research fellow under meritorious student fellowship program, University Grants Commission (UGC), Govt. of India, New Delhi.

I extend my thanks to Mr. Shamal K. Menon for helping me in GPC measurements. I would also like to thank Mrs. B. Santhakumari, Mr. Pankaj Sankapalli, Mr. Venkatesh Thogiti and Mr. Pankaj Raj for helping me lot in various characterization of my samples. I extend my thanks to Mrs. Deepa Dhoble, Mrs. Anuya Nisal, Mr. Saroj Kumar Jha and Mrs. Poorvi Purohit for their kind help in giving training for the divisional instrumental facility.

I would like to address special thanks to the unknown reviewers of my thesis, for accepting to read and review this thesis. I wish to thank the authors, developers and maintainers of the open source used in this work. I would like to appreciate all the researchers whose works I have used, initially in understanding my field of research and later for updates. I would like to thank the many people who have taught me starting with my school teachers, my undergraduate teachers, and my graduate teachers especially Mr. Subhas Sir, Dr. Sumon Das and Mr. Pradip Nandi.

I sincerely admire the contribution of all my lab seniors Dr. Nagesh B. Kolhe, Dr. Kaushlendra kumar, Dr. Chinmay G. Nardele, Dr. Rekha Narayan, Dr. T. Senthil kumar, along with my seniors and colleagues Dr. Balamurugan, and Dr. Anadraj, Dr. Basab Dhar, Dr. Joyashish Debgupta, Dr. Arijit Mallick, Dr. Shyamsundar Das, Dr. Krishanu Show, Dr. Saikat Haldar, Dr. Kanak Roy, Dr. Munmun Ghosh, Dr. Arpan Manna, Dr. Tamash Panda, Dr. Subhodeep Das, Dr. Prabat Mondal, Dr. Subhodeep Saha, Dr. Debasis Pati, Dr. Debasis Dey, Dr. Sujit Pal for extending their unstinted support, timely motivation, sympathetic attitude and unfailing help during the entire course of study.

I owe my special thanks to all my labmates and friends from CSIR-NCL and IISER Pune, Shekhar, Prajitha, Sandeep, Swapnil, Shrikant, Sarabjoth, Moumita Roy, Dr. Nisha, Ghanashyam, Bavitha, Indra, Jeena, Vinay, Charu, Alok, Vikash, Akshata, Harish, Vidhya, Priyanka, Devendra, Shreya, Durga, Smita, Dr. Mahima, Dr. Pramod, Dr. Bapu, Moumita Gupta, Bhagyashree, Narsimha, Rajendra, Nilesh, Sonashree, Maitri,

Nitesh,Yogita and Mehak for their unstinted support, timely motivation and maintaining cheerful environment in lab.

I would like to address my special thanks to all my beloved friends Soumen Das, Jagadish Khamari, Soumen Dey, Gautom Manna, Bikash Gharai, Shiva Kumar Burugu, Bhaskara Rao, Shantanu, Bittu, Dr. Chakadola Panda, Vinita, Bhawana, Sandeepan Jana, Basudeb, Korra Praveen, Anagh, Dr. Sushma Kumari, Sumon, Sharath K, Manik Sil, Meena Ghosh, Mitra Ghosh, Shantanu Baitalik, Leena chechi, Tanaya Bose, Jhumur Seth, Chayanika, Mrinmoy Chini, Ramkrishna Laha, Animesh Negel, Akash, Pradip, Ravi, Anil, Soumyajyoty, Sudhakar, Manoj K. Sharma, Hridesh, Rajesh, S. Chithiravel, Manik Bhosle, Satej, Rajshree, Arul, Soumya, Nagendra, Nagnath, Mohan Raj, Yogesh Marathe, Arun Torris.

Words cannot express the feelings I have for my parents for their constant unconditional support - both emotionally and financially. I feel a deep sense of gratitude to my late grandmother Smt Nandabala Bhaumik who inspired me to take this subject (Chemistry). I have learnt a lot from my parents, specially my father Mr. Samarendra Nath Bhaumik, One of the most important teacher in my life. My father has contributed a lot towards increasing my curiosity and the spirit to seek a deep understanding of the world around me. Words prove a meagre media to write down my feelings for my mother Smt Anupama Bhaumik, brother Saikat Bhaumik, sister Subhra Bhaumik and all my relatives for providing me constant encouragement, divine presence and supporting me spiritually throughout. Along with my parents, I would also like to sincerely thank all my aunts and uncles for having showered so much love on me since my childhood.

Above all, praises and thanks to the God, the Almighty, for His showers of blessings throughout my research task to complete the research successfully.

Saibal Bhaumik

TABLE OF CONTENTS

List of Abbreviations

Abbreviations	Expansion
CH_3CN	Acetonitrile
Al	Aluminum
Å	Angstrom
ATR	Attenuated total reflectance
AFM	Atomic force microscopy
cm	Centimeter
$CHCl_3$	Chloroform
T_c	Crystallization temperature
Jsc	Current density
dL	Deciliter
T_D	Decomposition temperature
DFT	Density functional theory
$CDCl_3$	Deuterated chloroform
DMSO-d_6	Deuterated dimethyl sulfoxide
ODCB	1,2 –Dichlorobenzene
DCM	Dichloromethane
DSC	Differential scanning calorimetry
DMAc	N,N-Dimethylacetamide
DMF	N,N-Dimethylformamide
Eg (ele)	Electronic band gap
eV	Electron volt
EtOAc	Ethyl acetate
F.F.	Fill factor
FL	Fluorescence
FT-IR	Fourier transform infrared
GPC	Gel permeation chromatography
T_g	Glass transition temperature
Au	Gold
gm	Gram
HMDS	Hexamethylenedisilazane
HOMO	Highest occupied molecular orbital
HCl	Hydrochloric acid
ITO	Indium tin oxide
η_{inh}	Inherent viscosity
KJ	Kilojoule
LC	Liquid crystal
LCPs	Liquid crystalline polymers
LUMO	Lowest occupied molecular orbital
MALDI-TOF	Matrix-assisted laser desorption ionization-time of flight
MHz	Megahertz
T_m	Melting temperature
µL	Micro liter
mg	Milligram
mL	Milliliter
mol	Mole
nm	Nanometer

N_2	Nitrogen
NMR	Nuclear magnetic resonance
Voc	Open circuit voltage
Eg (opt)	Optical band gap
OD	Optical density
OFET	Organic field effect transistor
OLED	Organic light emitting diode
ppm	Part per million
PLM	Polarized light microscope
K_2CO_3	Potassium carbonate
KI	Potassium iodide
PCE	Power conversion efficiency
RCA	Radio corporation of America
η_{red}	Reduced Viscosity
RI	Refractive index
SEM	Scanning electron microscope
s	Second
SiO_2	Silicon dioxide
Ag	Silver
SEC	Size exclusion chromatography
SAXS	Small angle X-ray scattering
SCLC	Space charge limited current
H_2SO_4	Sulfuric acid
n-Bu_4PF_6	Tetrabutyl ammonium hexafluorophospahte
TGA	Thermo gravimetric Analysis
TEM	Transmission electron microscopy
TFA	Trifluoroacetic acid
UV	Ultraviolet
V	Volt
λ	Wavelength
Mw	Weight average molecular weight
WXRD	Wide angle X-ray diffraction
ZnO	Zinc oxide

PREFACE

The bottom-up self-assembly of donor-acceptor semiconducting materials into well-defined nanoscale assemblies is crucial for several optoelectronic applications. In this regard the templated self-assembly approach using polymeric supports like the poly(4-vinyl pyridine) (P4VP) to develop supramolecular comb assemblies of small molecules with the polymer is very promising. Pioneering work has been reported from the group of Ikkala and ten Brinke *et. al* who studied hierarchical architecture formation between small surfactant molecules and P4VP or its block copolymer with polystyrene–PS-b-P4VP. Initial reports of extending the benefits of this supramolecular comb polymer assembly to assemblies incorporating semiconducting materials were promising.

Although self-assembly of small donor and acceptor molecules using strong complementary hydrogen bonding interactions were pursued as a means of arriving at the desired 'ideal' active layer morphology in the early stages of development of materials for photovoltaic assemblies, it was quickly realized that such strong interactions were counterproductive in improving the mobility or solar cell efficiency of devices made using them as active layer. However weakly interacting moieties incorporated into donor and acceptor molecules could be expected to result in the desired ideal organization if there were multiple sites of interaction. Thus, the pyridine unit on the polymer P4VP scaffold results in supramolecular comb polymer complexes with hydroxyl or carboxyl functionalized small molecules, even though the pyridine-hydroxyl interaction is weak in nature. Assemblies of the 'n' type rylene bisimides with P4VP or mixed donor-acceptor assemblies with P4VP were explored for their improvement in charge transport upon complex formation. It was observed in all the P4VP complexes that the non-covalent interaction resulted in altered molecular packing compared to pristine small molecule as observed using wide angle X-ray diffraction studies. Furthermore, the concept of polymer as a templating scaffold could be extended to complexes of only donor and acceptor small molecules, where the donor was designed with polymerizable units, which could be polymerized after it formed a complex with the acceptor molecules. The mobility values as measured using space charge limited current (SCLC) studies indicated improvement as a result of the supramolecular assembly.

In this thesis work, the polymer and small molecular complexes were made in suitable solvent under ambient conditions. Structural characterization was carried out using FT-IR and ^{1}H NMR analysis; micro structure analysis was done by wide angle X-ray diffraction (WXRD) and small angle X-ray scattering (SAXS) studies. Transmission electron microscope (TEM) was recorded to understand the morphology of the

supramolecular complexes. Charge carrier mobility [Electron (μ_e) and hole (μ_h)] was measured via SCLC and OFET method.

Chapter 1 gives a brief introduction about organic electronics. This section includes organic electronics and their use, charge transport mechanism, challenges and opportunities, effect of self-assembly in device performances, types of organic semiconductor devices, optoelectronic devices (organic light emitting diode, organic field effect transistor, organic photovoltaic devices), techniques to measure the mobility in organic semiconductors are discussed. Synthetic approaches, optical, electrochemical and semiconducting properties of some specific (n-type and p-type) semiconducting materials, naphthalenediimide (n-type), perylenediimide (n-type) and oligo (*p*-phenylene vinylene) (p-type) are discussed in detail with latest literature examples including small molecules and polymers.

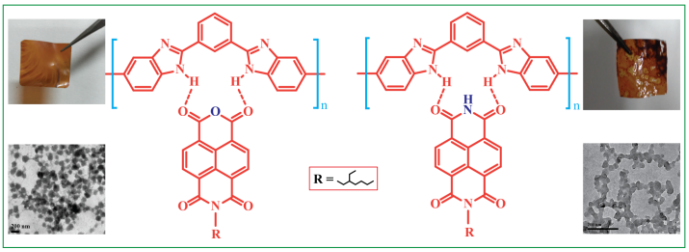

Chapter 2 explains the composites formation of unsymmetrically substituted n-type naphthalenemonoimide (NMI) and naphthalenediimide (NDI) small molecule with polybenzimidazole (PBI) with the help of noncovalent hydrogen bonded interaction. The resultant composites formed stable nanostructures with capability to form good transparent free standing film over a large area with reasonable semiconducting characteristics. PBI-NMI composite showed space charge limited current (SCLC) mobility in the order of 10^{-7} cm^2/Vs, which was similar to that of the pristine naphthalenemonoimide (NMI) alone.

Chapter 3 describes the supramolecular crosslinked polymer network formation between Poly(4-vinyl pyridine) (P4VP) and symmetric Perylene bisimide or naphthalene bisimide molecules with free –OH group at both the termini. Complex formation was confirmed by FT-IR and ^{1}H NMR spectroscopy. Micro structure of the complex was analyzed with the help of wide angle X-ray diffraction (WXRD). Transmission electron microscopy (TEM) was used to study the thin film morphology of supramolecular polymer network. Effect of self-organization on bulk

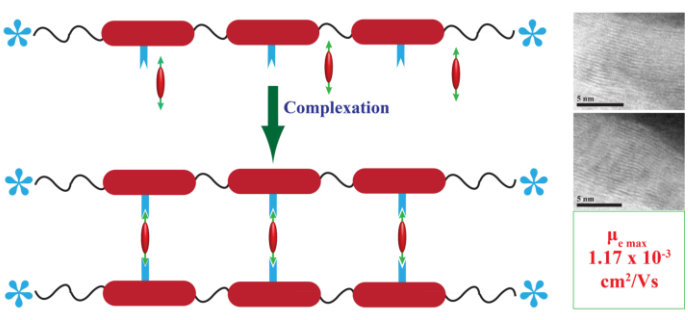

mobility was measured via SCLC which showed electron mobility in the order of 10^{-3} and 10^{-4} cm^2/Vs, which were 2-3 orders higher in magnitude compared to the pristine rylene bisimide molecules.

In **chapter 4**, an acceptor molecule based on perylene bisimide was developed with free –OH group at the termini (UPBI-PDP). A donor molecule based on oligo(p-phenylene vinylene was also developed with hydroxyl (-OH) group at one of the termini (OPVCN-OH). Supra-molecular nano organization of UPBI-PDP and OPVCN-OH with the polymer matrix of Poly(4-vinyl pyridine) (P4VP) was achieved with the help of noncovalent interaction like H-bonding and π-π stacking. FT-IR and ^1H NMR spectroscopy were used for confirmation of complex formation.

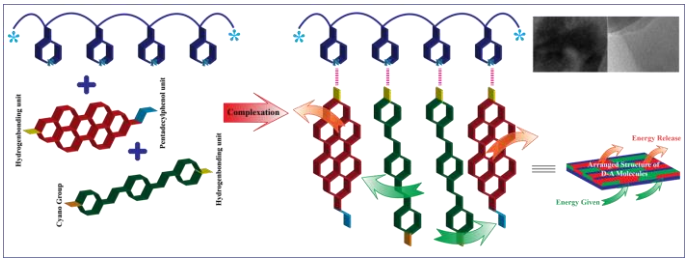

Small angle X-ray scattering (SAXS) and wide angle X-ray diffraction (WXRD) were used to understand the solid state supramolecular structure. Thin film morphology of the donor-acceptor complexes with P4VP showed nice lamellar arrangement in the range of < 10 nm. Effect of self-organization of donor acceptor assembly on bulk mobility was measured via SCLC method and highest hole mobility (μ_h) was obtained in the order of 10^{-2} cm^2/Vs.

In **chapter 5**, a nanostructured supramolecular donor-acceptor assemblies were formed when an oligo(*p*-phenylenevinylene) (OPVM-OH) complementarily functionalized with hydroxyl unit and polymerizable methacrylamide unit at the other termini was complexed with

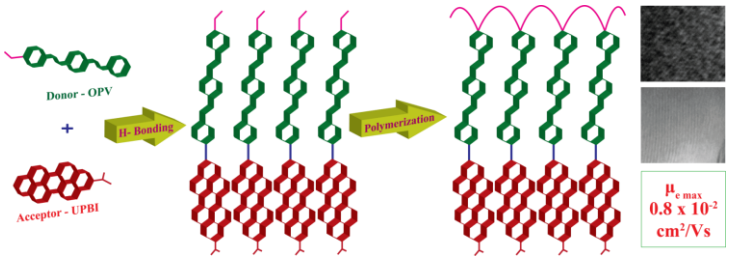

unsymmetrical N-substituted pyridine functionalized perylenebisimide (UPBI-Py). The resulting supramolecular complex $[UPBI\text{-}Py\ (OPVM\text{-}OH)]_{1.0}$ upon photoinduced polymerization formed well-defined supramolecular polymeric nanostructures. Wide angle X-ray diffraction analysis indicated changes in cell parameters of OPVM-OH upon complex formation. Thin film morphology showed the uniform lamellar organization in the domain range < 10 nm for 1:1 molecular complex as well as the supramolecular polymer complex. The donor-acceptor supramolecular complex $[UPBI\text{-}Py\ (OPVM\text{-}OH)]_{1.0}$ exhibited space charge limited current (SCLC) with a bulk mobility estimate which was two orders of magnitude higher accompanied by a higher photoconductivity yield compared to the pristine UPBI-Py. Thus, a versatile method to obtain spatially defined organization of n and p-type semiconductor materials was developed

based on suitably functionalized donor and acceptor molecules resulting in improved photocurrent response using self-assembly.

Chapter 1

Introduction

1.1 Introduction to Organic Electronics

1.1.1 History and Discovery

A remarkable technological maturity has been achieved with the help of organic semiconductors in the field of high-tech electronics. The main driving force for todays' fast growing world mainly depends on microelectronics, which was introduced for the first time in the 20th century. The field effect transistor is the basic building block for many electronic devices. This great discovery was made by Julius Lilienfeld in 1926. Thereafter, the silicon industry has been trying to downsize the device retaining high performance. However, single crystalline silicon is very difficult to fabricate in a large area with high degree of flexibility at low cost. The challenges in the single crystalline silicon research propelled the search for alternate choices like organic materials that could exhibit reasonably good electronic behaviour. This gave birth to a new area of electronics and in the 20th century, C. H. Lewis introduced the term "Molecular electronics" for the first time at a conference organized by the US air force.[1] IBM introduced the concept of molecular electronics in 1974. However, organic electronics was unable to make high impact in the market. In this direction, the greatest discovery of semiconducting polymer was done by the polymer chemist Hideki Shirakawa, an inorganic chemist Alan MacDiarmid and a physicist Alan Heeger in 1977.[2] They showed that polyacetelene could conduct electricity in its oxidized state (using iodine as an oxidant). After this discovery, the semiconducting polymers have made a significant impact in the history of molecular electronics. In 2000, Hideki Shirakawa, Alan MacDiarmid and Alan Heeger were awarded the Nobel Prize for their greatest discovery in the field of molecular electronics. The organic electronics field started mainly in the late 1970s with the introduction of various devices such as organic light emitting diodes (OLEDs),[3-6] organic field effect transistor (OFETs),[7-13] organic photovoltaics (OPVs).[14-20] After this revolution in the field of conducting polymers, many kinds of conjugated polymers were developed which have advanced their technological applications. In this direction, the first discovery of polymer light emitting diode from poly (phenylevinylene) was made by Burroughes *et al.*[21] A few years later, Saraciftci *et al.* proved the photoinduced electron transfer from conducting polymer to C_{60}.[22-25] Charge separated state of donor polymer and C_{60} was also confirmed from the subsequent quenching of photoluminescence after interaction of donor polymer with C_{60}. The conjugated polymers were classified broadly in three categories (i) first generation, (ii) second generation and (iii) third generation by Heeger.[26] The first generation includes polyacetylene, the second generation is focused on the processability

and solubility of the polymers and copolymers like poly (alkylthiophene) and poly (phenylenevinylene). The structures of some important first, second and third generation semiconducting polymers are shown in Chart 1.1. The third generation appeared with more complex molecular structures. Along with that, many optoelectronic devices were developed like solution and solid state laser,[27-35] organic photovoltaic devices (OPVs),[14-20] organic light emitting diode (OLED),[3-6] organic field effect transistor (OFET),[7-13] sensors,

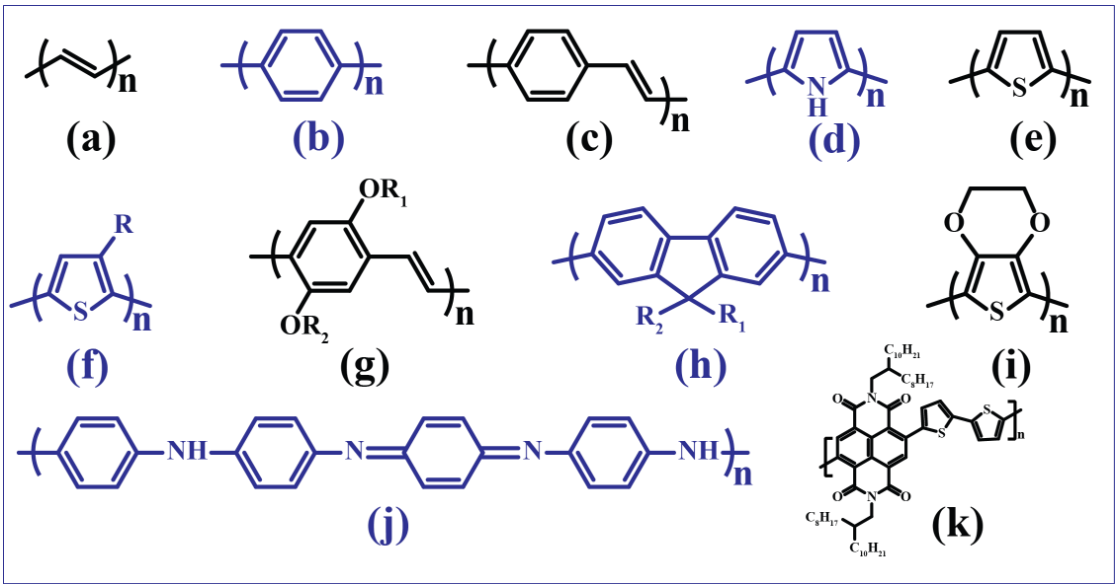

Chart 1.1 Some of the important first, second and third Generation semiconducting polymers with molecular structures (a) Polyacetelene (PA); (b) Polyparaphenylene (PPP); (c) Polyparaphenylene vinylene (PPV); (d) Polypyrrole (PPy); (e) Polythiophene (PT); (f) Poly (3-alkyl) thiophene (P3AT) (R= Me, Bu etc.); (g) Poly (2, 5 dioxy)paraphenylene vinylene (e.g. MEH-PPV); (h) Polyfluorene (PFO); (i) Polyethylene dioxythiophene (PEDOT) (j) Polyaniline (PANI) (k) NDI based polymer P(NDI2OD-T2)

[36-42] photo detectors (PD)[43-46] etc. Among all these electronic devices, OLEDs have been used heavily in modern electronics, such as mobile phones, thin display and light industry. The drastic improvements in the design and development of the organic electronics since the time of their discovery has helped to improve the performance of organic semiconductor based devices like plastic solar cell, radio frequency identification tags (RFID), light weight ultrathin television display etc.

1.1.2 Organic Electronics: Usefulness

Due to their unique properties like processability, good physical properties etc., organic electronics has created a huge impact in industry and the electronic market. Organic semiconductors have some unique difference with respect to conventional inorganic semiconductors, which is tabulated in table 1.1. These differences make the organic electronic field more useful in modern electronic industry and they have some notable features such as:

Table1.1: Differences between conventional electronics and organic electronics.

Conventional Inorganic Electronics	Organic Electronics
High Cost	Reduced cost
Complex technique of processing	Simple processing
Small area fabrication	Large area fabrication
No Mechanical flexibility	Mechanical flexibility
Heavy weight	Light weight
Good performance	Average performance

a) Synthetic tuneability: desired organic semiconducting molecule or polymers can be prepared by a variety of methods and can be tuned very easily by easy synthetic strategy.

b) Processability: Organic semiconductor can be processed into large area electronics with the help of very simple and easy techniques like solution drop casting,[47, 48] spin coating,[10, 49] screen printing, ink-jet printing and vacuum deposition.

c) Self-assembly: Self-assembly is a mandatory criteria to get good device performance which can be controlled very easily in organic semiconductor materials at very low length scale. A variety of self-assembled structures can be achieved by simple variations in small molecule as well as polymers.[50-54]

Figure 1.1 depicts the chart for the broad range of applications of organic semi conducting materials. Some of the most fruitful and potential applications of organic electronics include organic light emitting diodes (OLEDs), sensors, organic field effect transistors (OFETs), plastic solar cell devices (PSCDs), and radio-frequency identificat-

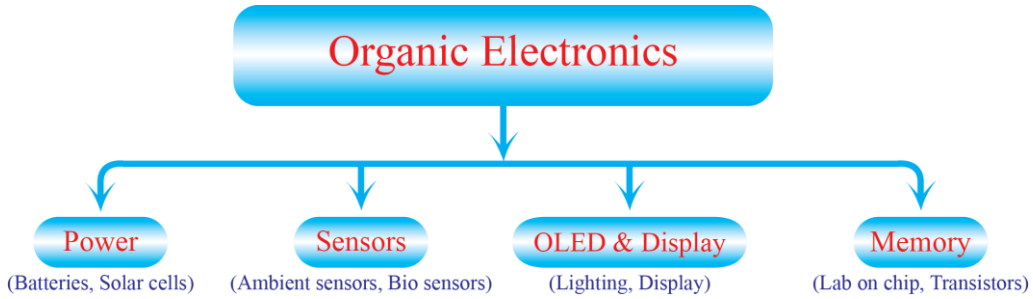

Figure 1.1: Organic electronics and its broad range of applications.

ion (RF-ID) tags.[55] Because of their low cost fabrication and good performance, it is very promising to develop an electronic device like OLEDs, OFETs etc. However, several technological challenges have to be overcome to improve their performances for commercialization. Specially, organic thin film transistor (OTFT) is not good enough to commercialize due to its low charge carrier mobility, high contact resistance, problem in the fabrication process and device stability. It is very true that device performances of organic semiconductors are poor compared to silicon. Therefore, organic semiconductors are not expected to overcome the performance of silicon based semiconductors because silicon industry is aimed for high performance and high–end smart products, whereas organic semiconductor industry is aimed for cost-effective, low-end disposable products.

1.1.3 Charge Transport in Organic Semiconductor

Organic semiconductors can be classified broadly into two categories, (a) small molecules or oligomers, generally processed in vacuum and (b) polymers, generally processed by wet chemical technique. Carrier mobility is the key characteristics of charge transport in organic semiconductors. Charge transport can be defined as the movement of charges in a material by applying an external electric field. Different mechanistic pathways are available for transporting of charges. Semiconducting polymers can be described in terms of energy band which is shown schematically in figure 1.2. Typically these bands are generated due to overlap of π-orbitals in conjugated polymer. According to band theory, solids are mainly divided into three sections (a) conductor, (b) semiconductor and (c) insulator depending upon the abundance of electron present in valence band and the conduction band. All the available electrons present in materials fill the conduction band at 0 Kelvin. In metals the forbidden gap or band gap (Eg), which simply explains the overlap of the valence band and the conduction band (Eg) = 0 eV. Hence the electron can readily conduct electricity from the partially filled conduction band. This band gap

between valence band and conduction band is very high (> 4 eV) for insulator. The energy gap is too high for an electron to jump from valence band to conduction band in

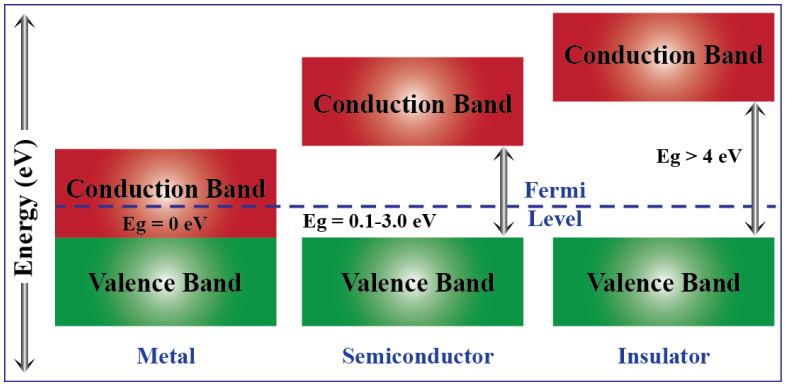

Figure 1.2: Energy band diagram of metals, insulators and semiconductors.

the insulator. As a result, insulators are very poor for electrical conductance at ambient temperatures. In case of semiconductors conduction bands are completely empty and valence bands are rich in electrons. HOMO and LUMO energy levels can be defined as the highest occupied molecular orbital of the valence band and the lowest unoccupied molecular orbital of conduction band respectively. By applying some external voltage it is possible to transfer electrons from valence band to conduction band (Eg = < 3 eV) for semiconductors. A band like charge transport mechanism is observed in the highly crystalline inorganic materials like silicon (Si), Germanium (Ge) etc., due to their very strong covalent bond with energy as high as 76 kcal/mol. The resultant mobility is very high in the order of 10^3 cm^2/Vs for these materials. On the other hand, organic polymers are amorphous in nature and charge transport follow mainly the hopping mechanism at higher temperature which limits the mobility in the order of 1-10 cm^2/Vs.[56] Conjugated polymers contain alternate double and single bonds in its backbone and charge transport occurs after suitable doping. Overlapping of the sp^2 hybridized orbital of alternating σ and un-hybridized π orbitals makes a continuous path for the movement of free electrons. Orbital overlapping of two adjacent P_z orbitals of two carbon atoms generates one low lying π-bonding (HOMO) and high energy π*-anti-bonding orbital (LUMO), which leads to the delocalization of the electrons in the polymer backbone. The high HOMO–LUMO energy gap makes conventional polymers act as insulators. The conducting class of polymers shows conducting behaviour due to the delocalization of π electrons into their backbone which reasonably reduces the HOMO–LUMO energy gap. Due to lack of intrinsic charge carriers, conjugated polymers need doping for charge conduction. Doping

can be done by partial oxidation at HOMO or partial reduction at LUMO to create charges into the active material which will be able to transport charge. Various chemical and electrochemical methods are available for doping of conjugated polymers.[57] Generally, iodine or alkali vapour is used for chemical doping. Electrochemical doping is achieved by applying an electric potential between polymer coated electrode and reference electrode immersed in an electrolytic solution. Photo doping is also possible, wherein photo excitation of electrons from HOMO to LUMO of the active polymer generates a charge bound state called exciton. For example, Polyaniline (PANI) shows very high conductivity among conjugated polymers in the moderately oxidized emeraldine base form.[58] This form of PANI consists of equal ratios of imine (=N–) and amine (–NH–) sites. Bipolaron (dication salt) can be formed after protonic acid doping at imine site. Finally, rearrangement of bipolaron results in polaron lattice (polysemiquinone radical-cation salt) as shown in figure 1.3. This resultant emeraldine structure shows very good conductivity in the order of 10^2 S/cm and it is reasonably good with respect to com-

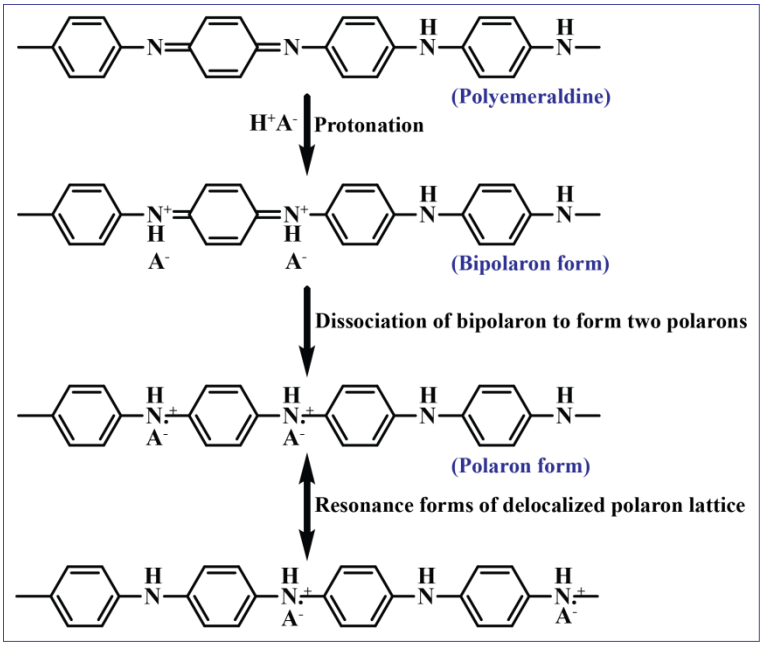

Figure 1.3: Neutral and charged state structure of polyaniline (PANI) after doping.

mon polymers (< 10^{-9} S/cm). Now it is almost accepted that charge carriers move through the localized defect state known as polarons,[59] whereas crystalline organic semiconductor materials follow the band like charge transport mechanism. The charge transport mechanism is not so well understood for the disordered organic semiconducting

polymers and it is considered that charge transport happens via hopping mechanism at high temperature state.

1.2 Types of Organic Semiconductor Devices

Organic semiconductors are mainly divided into three categories: (a) organic light emitting diodes (OLEDs), (b) organic field effect transistor (OFETs) and (c) organic photovoltaics (OPVs).

1.2.1 Organic Light Emitting Diodes

Tungsten filament bulbs are one of the important sources of lighting system which consume more power. Present lighting system uses around 33% of the total electricity produced. Organic light emitting diode (OLED) which is eco-friendly, self-illuminating can solve the problem of more power consumption in contrast to tungsten or fluorescent lamp to some extent. OLEDs are extremely thin with good emission even in solid state. OLEDs are one of the most studied devices for solid state lighting which basically originates from organic small molecules or semiconducting polymers. Interest in developing the polymer based OLEDs are growing fast due to low cost fabrication like inject printing, spin coating over the traditional vapor deposition. OLEDs are the most successful among the organic semiconductor devices and has been already commercialized. It has been used in many commercial applications like LED light, mobile phone display, portable digital media player, digital cameras, television (TV) screen etc. Flexible display can be made from OLEDs. Structurally OLEDs can be divided in four categories (a) single-layer, (b) double-layer, (c) triple-layer and (d) multi-layer OLEDs. Active layer should have very high quantum efficiency with good electron or hole transport properties to get better device performance. In two layer OLEDs, n-type materials transport electrons and p-type materials transport holes. Recombination of electron-hole pair occurs at the interface of two layers which produces the energy in the form of light. Different colour band can be produced by varying the HOMO-LUMO energy gap of the active layer.[60, 61] Three-layer and multi-layer OLEDs are somewhat complex in their configuration. Polymer based OLED configuration is shown schematically in figure 1.4. The substrate is generally a transparent conducting ITO coated glass with high work function $\varphi_w \approx 4.7 - 4.9$ eV. Anode is also transparent and injects holes into the organic layer. Ca and Al are generally used as cathode materials which actually helps to minimize the energy gap between the LUMO of organic materials

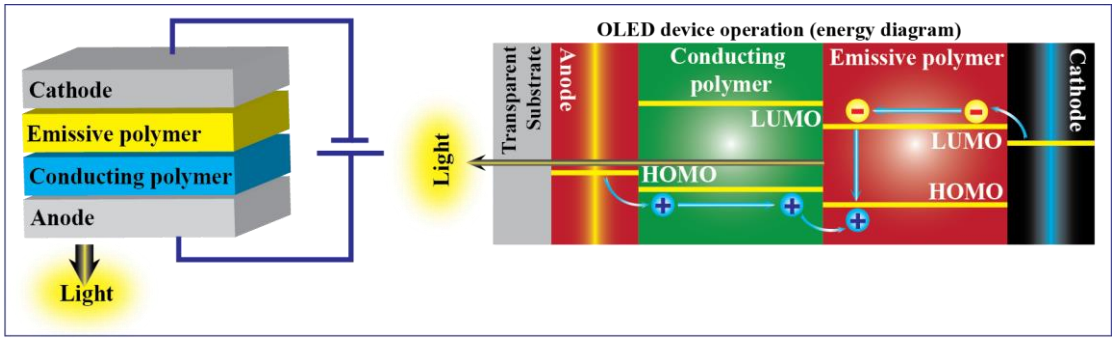

Figure 1.4: OLED device configuration and operation principle.

and Fermi-level of metal resulting in better electron injection. In 1960, Pope *et al.* from New York University observed electroluminescence in single crystals of anthracene under vacuum.[62] Later on in 1965, double injection recombination electroluminescence of anthracene single crystal was developed by Helfrich *et al.*[63] In 1987, the first double layer OLED was made by Ching W. Tang and Steven Van Slyke at Eastman Kodak.[64, 65] Afterwards, polymeric OLEDs made a significant contribution to fundamental science as well as in industry.

1.2.2 Organic Field Effect Transistor

Transistors are the basic building blocks for modern integrated circuit. It is used as signal amplifiers or molecular switches. Apart from this, OFET is a very popular and important device architecture to extract the mobility of semiconducting materials. Field effect is a phenomenon where conductivity of a semiconducting material changes with varying electric field. OFETs are made up of three terminals namely source, drain and gate with a semiconductor layer and insulating layer situated in between semiconductor and gate. OFETs can be fabricated in four possible ways, namely, (a) bottom gate top contact, (b) top gate bottom contact, (c) bottom gate bottom contact and (d) top gate top contact as depicted in figure 1.5. The source and drain electrode are separated by semiconducting layer called channel length. The potential difference between source and drain is called source-drain voltage (V_{DS}) and the developed potential between source and gate is called source-gate voltage (V_{GS}). A certain amount of voltage is applied to gate to control the current flow between source and drain. p-types are the most common among the variety of OFETs due to their high hole mobility. A negative voltage (greater in magnitude than the threshold voltage) is applied to gate which generates positive charges in the conducting channel and holes are transported across source and drain electrode. In case of n-type OFETs, positive gate voltage creates negative charges in the conducting channel. In most of the cases, the initial gate voltage is not sufficient to allow the electron or holes

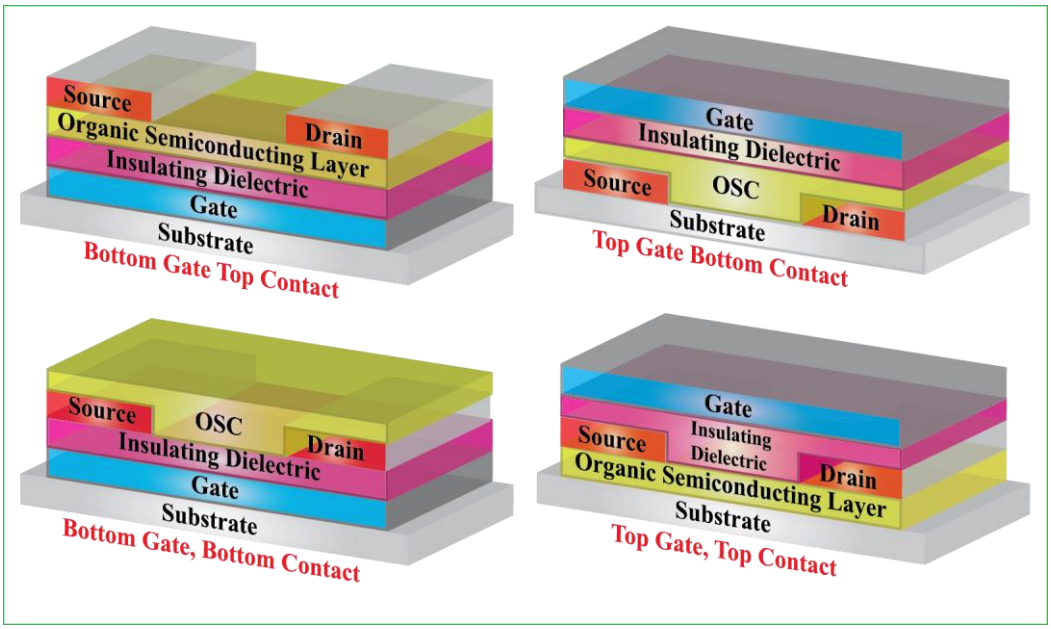

Figure 1.5: Schematic representation of device configuration fabricated for OFET (bottom gate top contact, top gate bottom contact, bottom gate bottom contact and top gate top contact).

to flow from source to drain. The minimum voltage required for the electrons or holes to flow between source and drain at gate electrode is called threshold voltage. Upon application of voltage between source and drain (V_{DS} << V_G-V_T), current increases linearly between source and drain. This linear region is known as "ohmic region" (shown in figure 1.6a). With further increase of drain voltage (V_{DS} = V_G-V_T) a point appears called "pinch-off" point (figure 1.6b) where the drain current reaches its maximum value. With further increase in drain voltage (V_{DS} >> V_G-V_T) no increase in current occurs which is known as saturation regime (figure 1.6c) in typical OFETs. The output curves represent the drain-source current (I_{DS}) versus drain voltage (V_{DS}) as a function of gate

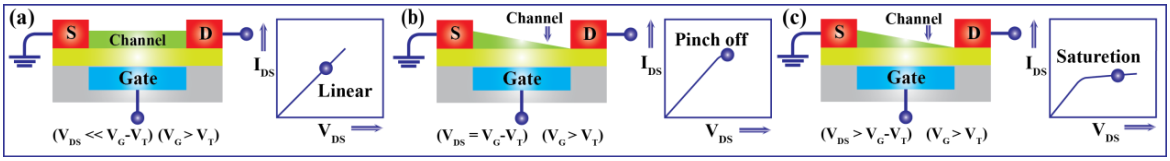

Figure 1.6: Linear, pinch off and saturation region of a transistor operation at different source to drain voltage (V_{DS}).

voltage (V_G) (figure 1.6). It contains two regions called linear region and saturation region.[66] The charge carrier mobility can be extracted from both regions as follows:

$$I_{DS} = \frac{W}{L} \mu C_S [(V_G - V_T) - \frac{V_{DS}}{2}]V_{DS} \quad \text{(linear region)} - (1)$$

Where, W is the width and L is the length of the semiconductor channel; μ is the charge carrier mobility; C_S represents the capacitance per unit area of insulating layer; V_T is the threshold voltage. Charge carrier mobility can also be calculated from the slope of this transfer curve as

$$\frac{\partial I_{DS}}{\partial V_{GS}} = \frac{W}{L} \mu C_S V_{DS} \quad (2)$$

The above equations (1) and (2) are applicable only for linear region ($V_{DS} << V_G$-V_T). Saturation region ($V_{DS} << V_G$-V_T) output curve can be defined as

$$I_{DS} = \frac{W}{2L} \mu C_S (V_G - V_T)^2 \quad (3)$$

Equation (3) can be used to extract the charge carrier mobility from saturation region of transfer curve. Similarly, from the slope ($I_{DS}^{1/2}$ *vs* V_G) of saturation region one can extract the charge carrier mobility. Interface between the materials fabricated in OFET plays an important role to give better output curves. Dielectric layer also has a significant role for the performance of the OFET. Especially for the n-type materials, hydroxyl groups present in dielectric can act as traps for electron. Charge carrier mobility (μ), threshold voltage (V_T) and I_{on}/I_{off} ratio are the governing factors to characterize the performance of the OFET. Charge carrier mobility in the order of 0.1–1.0 cm^2/Vs are considered as good for device application. Good switching behaviour of the OFET depends on high I_{on}/I_{off} ratio and ideally this should be in the order of 10^6.[67] Practically most of the organic semiconducting materials are very poor in performance. Many factors are responsible for the poor device performance out of which some are inherent poor charge carrier mobility of semiconductors, morphology of the active materials, contact resistance between the semiconductor and electrode interface, etc. Materials with higher degree of crystallinity or long range lamellar ordering are highly desirable for the better performance in OFET device.

1.2.3 Organic Photovoltaics

Organic photo voltaic solar cells represent a transformative technology that aims to serve as an earth-abundant and low-energy-production photovoltaic solution. This technology has the potential to provide flexible, low cost solid state power generator than first- and second-generation solar technologies. The working principle of organic photovoltaics is

exactly opposite to OLEDs where, light energy transforms directly into electrical energy. A solar cell device is the device which converts sunlight directly to electrical energy by the photovoltaic effect. This was first discovered by Becquerel in 1839 on silver chloride electrode in an electrolyte solution.[68] The first solar cell device was made by Fritts. Organic solar cell can be broadly divided into three categories: (i) Flat-Heterojunction solar cell[69, 70] (ii) Bulk-Heterojunction (BHJ) solar cell[71-73] and (iii) Dye-sensitized solar cells.[74-79] Materials used in organic photovoltaic cells are small molecule,[80-82] polymers,[83-87] organic-inorganic hybrid materials, etc. Polymer solar cells generally consists of four layers: Glass, ITO, active layer, calcium or aluminium (figure 1.7).[88] The glass substrate serves as a supporting layer in the solar cell device and it should not possess any absorption in the visible region, since the solar cell device uses this light to generate power. Transparent polymers, can also be used as more flexible supporting layers in photovoltaic devices. Aluminium and ITO (indium tin oxide) serves as electrodes in the photovoltaic cell. The built-in electric field generally generated by the difference in the

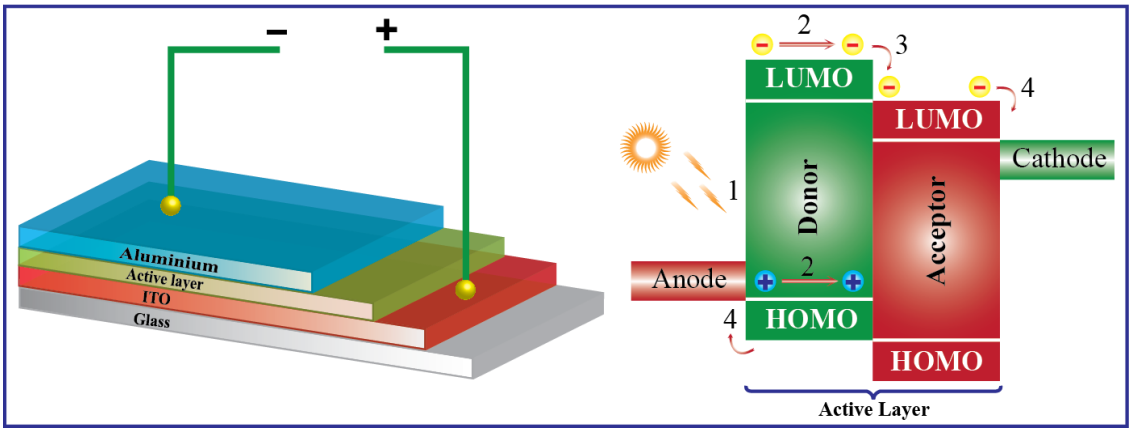

Figure 1.7: Schematic representation of organic solar cell device and the working principle.

metals' work functions used in solar cell. This generated electric field is used to dissociate the excitons. Excitons are generated after the absorption of light by active layer. The ITO layer is transparent in the visible origin like glass. Its built-in electric field and the device performance can be further increased by introducing calcium and PEDOT:PSS (poly[3,4-(ethylenedioxy)-thiophene]:poly(styrene sulfonate)) into solar cell device. The active layer in this polymer solar cell consists of a donor-acceptor system. Different types of systems like P3HT, MEH-PPV, CN-PPV, OPV, FT8BT are used as donors and PCBM, perylenediimide, naphthalenediimide, diketo pyrrole are used as

acceptors.[89-103] A polymer solar cell is a type of flexible solar cell made up of polymer that produces electricity from sunlight by the photovoltaic effect. Currently, high grade silicon crystals, similar to the materials (wafer silicon) used in the production of computer chips and integrated circuits, are also used to make the commercial solar cell devices. But due to their high cost and production complexicity; some alternate photovoltaic technologies are needed. Polymer solar cells (PSC)[104, 105] is one of the possible replacements. Inorganic solar cells are not easily processable and are very expensive, therefore it becomes challenging for scientists to develop organic solar cells of high efficiency like the inorganic silicon solar cell as well as make it cost effective. The major breakthrough in the field of organic photovoltaics was done by Tang *et al*. by introducing the first heterojunction organic solar cell with power conversion efficiency (PCE) of 1%.[106] In this direction, in 2010 power conversion efficiency was achieved up to 8.3 % from the group of Konarka which they further increased to 10.7 %.[107] In the current state OPVs, power conversion efficiency (PCE) has reached up to ~11 % and ~20 % for a single cell or even higher for tandem cell by proper tuning of the material properties like band gap, charge mobility, morphology etc. Fabrication of the organic solar cell is another challenge to get better efficiency. ~ 50 % efficiency is lost during the fabrication of a solar cell from a champion device to large area device. This loss is mainly due to improper metrology during large volume fabrication process. Translation efficiency is very poor in flexible solar cell device because of very high resistance of ITO coated plastic. In addition, due to the brittle nature of the ITO it is not a suitable electrode for flexible solar cell. Development of new transparent and robust flexible electrode material is required to produce viable product in organic photovoltaics. Diffusion of exciton is one of the most important steps for better charge separation in active layer of a solar cell. This step typically depends on the nanoscopic arrangement of the donor-acceptor in the length scale of <10 nm where the exciton lifetime is essentially high. Therefore, active layer morphology is crucial to provide better power conversion efficiency.[108] For example, bilayer solar cell (figure 1.8a) made up of individual donor (D) and acceptor (A) layer creates a large interface barrier for which the effective dissociation of excitons generated at the D-A interface fails. BHJ device architecture (figure 1.8b) somehow solved this problem by reducing the D-A interface barrier or more specifically grain boundaries. Particularly, in this case D-A were intimately mixed together to form a composite, which was then used as active layer.[109] Therefore, several interfaces were created between donor and acceptor at desired length scale. This way, efficiency was improved significantly in

organic solar cell device and highest efficiency achieved was 9.48 %.[110] However BHJ device architecture faces the problem of phase separation between D-A over a long period. This problem can be solved by introducing the ideal BHJ device (figure 1.8c), where donor and acceptor are expected to form a well-organized micro phase separated structure at the length scale of 10-20 nm, comparable to exciton diffusion length. Improvement in efficiency was observed from normal BHJ to ideal BHJ for same D-A blend. This clearly tells the impact of active layer morphology in the efficiency of an organic solar cell which is one of the important aspect of ongoing research to improve power conversion efficiency.

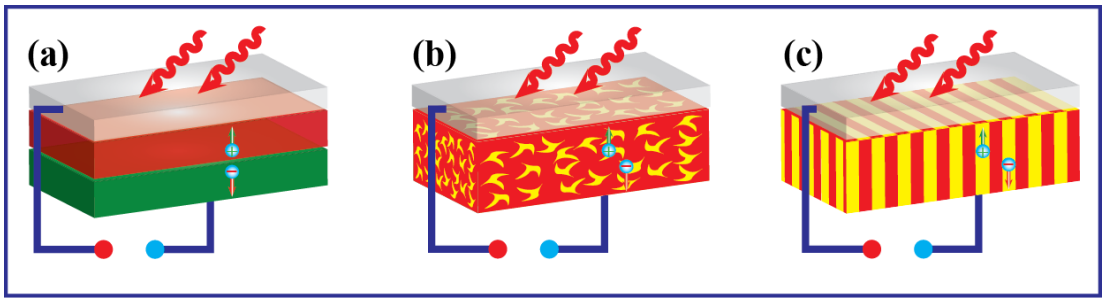

Figure 1.8: Device architecture of (a) bilayer, (b) bulk-heterojunction (BHJ) and (c) ideal BHJ solar cell.

Figure 1.9 represents the typical current vs voltage (J vs V) curve for organic solar cell in dark and under illumination. Under dark basically there is no current flow and the curve crosses the origin. Upon illumination, the J-V curve is shifted to the fourth quadrant of the J-V plot as shown in figure 1.9. Much valuable information can be extracted like the open circuit voltage (V_{OC}), short circuit current (J_{SC}) and power conversion efficiency (PCE). Largest power output can be calculated by multiplying voltage and current at maximum power point (MPP) as shown in figure 1.9. Power conversion efficiency can be calculated by the following equation:

$$PCE = \frac{FF \cdot J_{SC} \cdot V_{OC}}{P_{IN}} \qquad (4)$$

Where FF is the fill factor (*FF = J_{MPP}. V_{MPP}/P_{IN} and J_{MPP} and V_{MPP} = current and voltage at maximum power point*) and P_{IN} = input power.

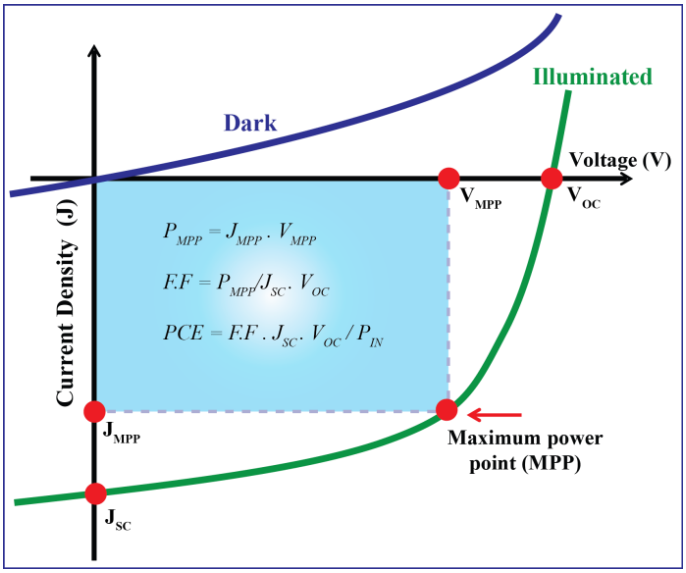

Figure 1.9: Current vs voltage (J-V) characteristics of organic solar cell under dark and illumination.

1.3 Different Techniques to Measure the Mobility in Organic Semiconductors

Charge carrier mobility is a key parameter that contributes to the performance of organic optoelectronic and electronic devices fabricated from variety of organic small molecules and polymers. Charge carrier mobility is therefore very much essential to improve performance in OLEDs, OPVs and OFETs. Characterization of carrier mobility in organic semiconductors is essential from the context of academia as well as industry. Carrier mobility (μ) can be defined as movement of charged particle through a medium under the applied electric field. Charge carrier mobility can be expressed as:

$$\mu = \frac{\nu}{E} \qquad (5)$$

Where, ν is the drift velocity of the charge carrier and E represents applied electric field. Alternative techniques are applied to extract the carrier mobility of organic semiconductors, such as, space charge limited current (SCLC), organic field effect transistor (OFET), double injection (DoI), carrier extraction by linearly increasing voltage (CELIV), photogenerated charges in CELIV (photo CELIV), time of flight (TOF), impedance spectroscopy (IS) and pulse-radiolysis time-resolved microwave conductivity. Among all, we have used SCLC and OFET for the measurement of our compounds.

SCLC technique consists of one charge injection contact and one injection blocking contact. Active organic semiconducting material with thickness around 200 nm to 2 μm is sandwiched between two electrodes similar to diode configuration as shown in figure 1.10a. It has been found from theoretical calculation as well as experiment, that the

injection barrier for a SCLC device should not exceed the value 0.3 e.[111] Figure 1.10b represents the J-V diagram of different regions of a typical SCLC measurement. In the Ohmic regime, the generated current is proportional to the applied electric field ($J \propto V$).

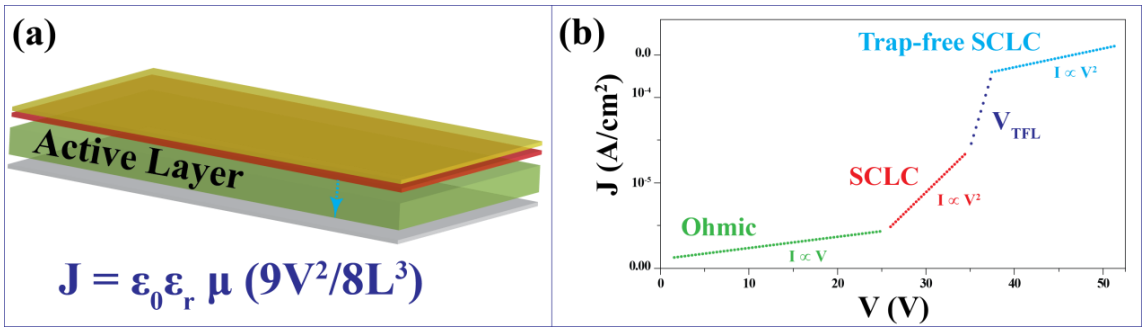

Figure 1.10: (a) SCLC diode configuration and (b) typical J-V characteristics of SCLC measurement.

The space-charge-limited-current regime (SCLC) generates when the equilibrium charge concentration (before charge injection) is negligible compared to the injected charge concentration. After applying the voltage in the injecting electrode, a space charge cloud is generated which dies out very rapidly away from the electrode. In this portion, the current increases linearly with square of the electric field ($J \propto V^2$). By increasing the voltage, trap levels present in the active layer is filled. With further increment in applied voltage called trap-free voltage limit (V_{TFL}), all traps are filled and the device generates the trap-free SCLC. The above figure 1.10b summarizes the process. Charge carrier mobility can be extracted from Mott-Gurney equation as follows:

$$J_{SCLC} = \varepsilon_0 \varepsilon_r \mu \frac{9V^2}{8L^3} \quad (6)$$

Where J_{SCLC} is the current density, ε_0 and ε_r are the permittivity of free space and relative dielectric constant respectively, μ is the charge carrier mobility (electron or hole), V is the applied voltage and L is the thickness of the device.

OFET measurement can be used to extract the charge carrier mobility for organic semiconducting materials which was discussed already in section **1.2.2**.

1.4 Charge Carrier Mobility and Molecular Packing

The performance of organic semiconducting materials largely depends on charge carrier mobility of that material. All electronic devices like OLEDs, OFETs, OPVs etc, demand

high charge carrier mobility for better performance in actual devices. Mobility of organic semiconductor majorly depends on two factors (i) transfer integral and (ii) reorganization energy. The first one involves the splitting of HOMO and LUMO and reorganization energy is the energy loss when a charge carrier passes through semiconductor material. Reorganization energy largely depends on conjugation length and packing of the material. It has been seen that, larger the transfer integral and smaller the reorganization energy higher the mobility. So, transfer integral and reorganization energy are largely dependent on molecular packing of organic semiconducting materials. Therefore, molecular packing is an important factor to improve charge carrier mobility. Millions of organic semiconductors can be made with the help of modern technology, addressing the structure property relationship which is one of the logical way to select the better candidate for device applications. The interactions among the neighboring molecules develop through noncovalent interaction like π-π interaction, H-bonding interaction, van der waal forces, etc. Different interactions develop different packing which influence carrier mobilities. It is of great interest to investigate the molecular packing for the ultimate design of organic semiconductors with higher mobility. More research is required to understand the effect of microscopic structure on macroscopic mobility. Four kinds of packing motifs are observed for organic semiconducting materials as shown in figure 1.11 (a) herringbone packing (without π-π overlap); (b) herringbone stackpacking with π-π overlap (slipped π

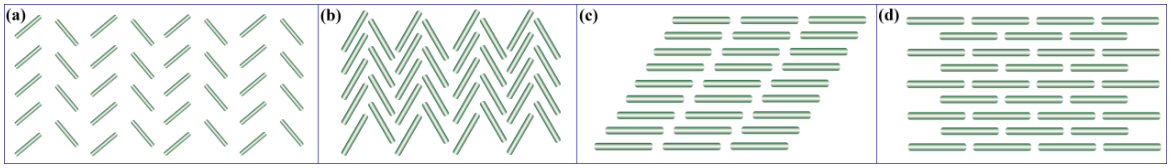

Figure 1.11: Different kinds of packing motif in crystal (a) herringbone packing (without π-π overlap); (b) herringbone packing with π-π overlap (slipped π stack); (c) Lamellar organization with 1-D π stack and (d) Lamellar packing with 2-D

stack); (c) Lamellar organization with 1-D π stack and (d) Lamellar packing with 2-D stack. It is believed that lamellar packing with 2-D π stacks is the most efficient organization to produce better charge carrier mobility.[112] Particularly in this case, the transfer integral reaches maxima and charge carrier travels to the respected electrodes via the shortest route (straight line). Both molecular arrangement and morphology of the

active material plays very important role in the performance of organic electronic devices. Direct measurement of charge carrier mobility as a function of intermolecular proximity and molecular orientation is only allowed for single crystalline structure. In OFET measurement to get efficient charge transport, organic semiconductors should pack along the direction of current (preferred orientation is edge-on). Figure 1.12 represents a possible mechanism for the efficient charge transport by taking a polymer as an example. Single crystalline structure with perfect molecular packing, minimum amount of trap

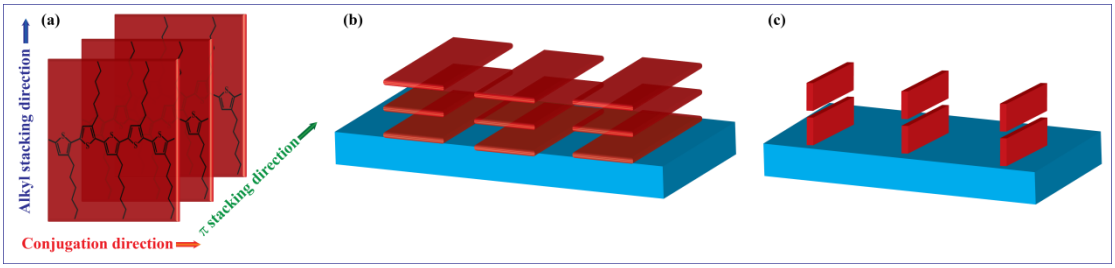

Figure 1.12: (a) Possible charge transport mechanisms in crystalline polymer films (using P3HT for illustration); (b) Face-on packing and (c) edge-on packing of the polymer with respect to substrates.[113]

state and no grain boundaries surely facilitates the carrier mobility rather than a thin film. For example, oligo thiophene crystal structure shows higher mobility at high temperature with respect to low temperature phase structure.[114] Different solid state packing of rubrene are also known to result in higher mobilities.[115]

1.5 Organic Semiconductors and Their Types

Organic semiconductors are the class of compounds having ability to conduct electrons. These molecules show conductivity in a very broad window 10^{-9} to 10^{3} Ω^{-1} cm^{-1} which lies in between that of metal and insulators. Organic semiconductors are interesting to study as their fabrication and processing are much easier than inorganic semiconductors. The building block of organic semiconductors is π bonded molecules, made up mainly by carbon and hydrogen. Organic semiconductors are mainly classified into two categories (i) small molecule based semiconductors and (ii) polymer based semiconductors. Small molecule based semiconductors are always attractive due to minimum steps in synthesis with very high degree of purity. They show definite molecular weight even after changing from one batch to another. Packing motifs are very precise in a small molecular semiconductor system. Furthermore, one can easily control the structural engineering of a

small molecular semiconductor with the help of simple organic transformations. They possess a definite melting and therefore can be fabricated easily by vacuum deposition technique. Morphology of thin film can be easily controlled by varying the evaporation rate of the semiconductors. Lower evaporation rate is beneficial to make a uniform film with less grain boundaries. Highly crystalline semiconductors facilitate charge conduction by making a compact and definite channel for the movement of charges. Ordered band like charge transport results in high charge carrier mobility in device. Small molecule based semiconductors can be classified further into three categories, (i) linear fused ring compounds; (ii) two dimensional fused ring compounds and (iii) heterocyclic oligomers. The linear fused ring compound, pentacene exhibited very high thin film mobility of 2 cm^2/Vs. Rylenebisimides (mainly perylene and naphthalene) are n-type two dimensional fused ring compounds that have shown reasonable electron mobility in different device configuration.[116] Heterocyclic oligomers, for example hexamer of 2,5-linked thiophene exhibited p-type semiconductor properties and further attachment of long alkyl chain (n-hexyl) at the termini of the oligo thiophene improved the mobility in OFET device.[117] Polymer based semiconductors have numerous degrees of advantages over small molecules based semiconductors. They are easily solution processable from many organic solvents. They simplify the process of fabrication with the help of cost effective techniques like spin coating, screen printing, inject printing, etc. Viscosity of a polymeric material is always higher than small molecule which really helps to fabricate large area device. Dendrimers are also used as organic semiconductors. A comparison between small molecular semiconductor and polymeric semiconductor is depicted in figure 1.13. It shows that vapor deposited small molecules (n-type) resulted in high charge carrier mobility ($\sim$1 cm^2/Vs) compared to polymers.[118] Organic semiconductors can be divided further into three categories on the basis of their electronic properties and charge carrier mobility namely (i) electron deficient or n-type; (ii) electron rich or p-type and (iii) amipolar (able to transport both hole and electron).

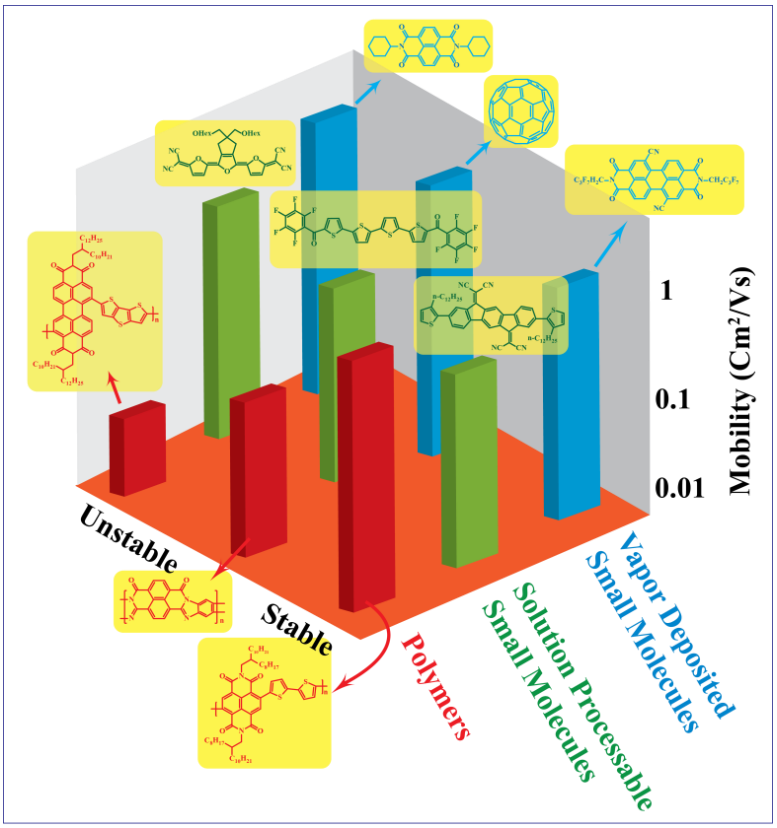

Figure 1.13: Chart of mobility values of n-type small molecules and polymeric semiconductors.

1.5.1 n-Type Semiconductor

Organic n-type semiconductors are known to transport electrons. They always prefer to accept electron as they are electron deficient in nature. N-type semiconductors are equally important as p-type semiconductors in any p-n junction device. From the beginning of organic semiconductor research, p-type semiconductors were studied extensively compared to n-type semiconductors. Recently, many developments were done on n-type semiconductors to improve their performance, stability, etc. Most of the n-type organic semiconductors are not air stable due to diffusion of negative charge generated by water and oxygen present in the air. However, this problem was solved partly by giving more effort into the design principal of n-type semiconducting materials.[66, 118] Nevertheless, there are certain desirable aspects that apply across the spectrum of n-type semiconductors which include air stability, easy synthesis, high carrier mobility, phase stability etc. All these factors are not the inherent properties of semiconductors alone but also are the properties of the device physics. Therefore, it is important to understand the device configuration and processing with manipulation of molecular structure to obtain

good device output. Some of the concepts related to the improvements of n-type semiconducting device performance are as follows: **(a) Concept 1:** n-type organic semiconductor should be electron deficient. This character does not have that much importance on the carrier mobility of an electron transporter. Charge injection in the electrode necessarily depends on the electron deficiency of a n-type material since electron deficient materials with low lying LUMO can be reduced more easily than electron rich material. Furthermore, after reduction of the electron deficient materials they are hard to reduce further (thermodynamically less reactive) and will be stable in oxygen and water. Literature shows that materials with reduction potential lower than that of oxygen or water are stable in air.[119, 120] The mobility of organic semiconductors is majorly measured at ambient temperature where charges move via thermally activated hopping mechanism. In this process electron transfer mainly depends on the electronic coupling and reorganization energy of the molecules which can be explained properly by Marcus theory.[56] **(b) Concept 2:** Strong electronic coupling between molecules with highly delocalised π electrons (π-π stacking) is a necessary criterion to improve electron mobility. However, in some cases it was observed that effective overlap was present without extensive π-π interaction whereas strong π overlap lacked effective overlap in wave function. Brédas pointed out this phenomenon that one must not only consider the orbital overlap through space, but also consider the phase relation of the corresponding orbital for each molecule.[56, 121] Therefore it is not necessary that extensive π stacking is required to produce high mobility. This discussion suggested that examination of a semiconducting material designed for high mobility applications should look in depth for precise nature of π stacking rather than simple π stacking interaction. **(c) Concept 3:** More electron deficient n-type semiconductors facilitate the electron injection. More precisely, electron deficiency means the position of the energy level, namely HOMO-LUMO of the material. Linear extension of the π conjugated system results in the rise in HOMO and lowering of LUMO level, which make the material easily oxidisable as well as reducable. Ambipolar materials can be implemented easily by this strategy where the molecule is able to transport both hole and electron. LUMO energy level can be reduced effectively by introducing π acceptors (eg. carbonyls, cyano etc.) with smaller impact on HOMO level. This causes effective mixing of the π* of acceptor and LUMO of conjugated π system results in stabilised LUMO of the π acceptor molecule. Many other methods are there to modify the HOMO-LUMO energy level of electron deficient material to make it more electron deficient for better charge injection.[66, 122] Figure 1.14

represents some typical n-type semiconductors used in OFET applications. n-type organic semiconductor based on Fullerene (C_{60}) (N1) and its derivative have shown electron mobility of 5 cm^2/Vs. This important class of C_{60} derivatives exhibited very high on-off (I_{on}/I_{off}) ratio of 10^6-10^8 in OFET device.[123] Rylenediimides mainly perylene and naphthalenediimide are the next promising n-type semiconducting material. Many PDI and NDI based small molecule semiconductors have been developed and studied by the research group of Dodabalapur in detail.[124] The highest electron mobility was found to be 0.57 cm^2/Vs for compound N2 under ambient conditions.[125] In 1996, Katz, Dodabalapur and co-workers reported the N3 and N4 with OFET mobility in the order of 10^{-3} cm^2/Vs deposited at a substrate temperature of 55 ^oC under vacuum.[126] Later on tremendous development was carried out to increase the mobility of NDI based semiconductors. In 2008, Shukla *et al.* reported an NDI based semiconductor (N5) with mobility up to 6.2 cm^2/Vs (OFET mobility) under a continuous flow of argon (Ar) with relative humidity of 22 %.[127] It showed on/off ratio in the order of 10^8. Furthermore, Zhu *et al.* reported core-expanded NDI small molecule semiconductors (N6 and N7) which exhibited electron mobility from 0.12 cm^2/Vs to 0.51 cm^2/Vs under different ambient conditions in solution processed OTFTs. N8 with fluorophenylethyl substitution at imide position showed mobility up to 0.23 cm^2/Vs - 0.57 cm^2/Vs.[128] Recently, Marder and co-workers reported bis(NDI) derivatives with conjugated bridging groups based on fused heterocycle ring systems (N9) with solution processed OFET mobility of 1.5 cm^2/Vs.[129] NDI derivatives based on unsymmetrical substitution at imide positions (N10) also exhibited promising n-type mobility of 0.10 cm^2/Vs.[130] Naphthalene (NDI-8CN2) (N11) and perylenediimides (PDI-CN2) (N12) substituted with cyano group also exhibited reasonable electron mobility up to 0.15 cm^2/Vs.[131-133] OFET measured for single crystal of N13 showed electron mobility of 6 and 3 cm^2/Vs in vacuum and air respectively.[134] Horowitz et al reported n-type semiconductor based on PDI with electron mobility in the order of 10^{-5} cm^2/Vs. In 2004, Daniel Frisbie *et al.* synthesised three PDI derivatives with variations in alkyl chain length at imide position as shown in.[135] Devices were fabricated as bottom gate top contact configuration. All the PDI derivatives, namely N14, N15 and N16, exhibited very high electron mobility up to 0.1, 0.6 and 0.2 cm^2/Vs respectively in linear regime. No p-channel conduction was observed for any of the PDI derivatives. Air stable N,N'-dioctyl-3,4,9,10-perylene tetracarboxylic diimide (PTCDI C8H)exhibited electron mobility up to 0.6 cm^2/Vs with on/off ratio $>10^5$ in a bottom contact configuration.[136] The same PDI derivatives showed increased mobility up to 1.7 cm^2/Vs in nitrogen

atmosphere.[135] Michael R. Wasielewski and co-workers synthesized bay substituted PDI derivatives with –CN (N17 and N18) as shown in. Both N17 and N18 (air stable) showed reasonably high mobility of 0.1 cm^2/Vs and 0.64 cm^2/Vs respectively.[132]

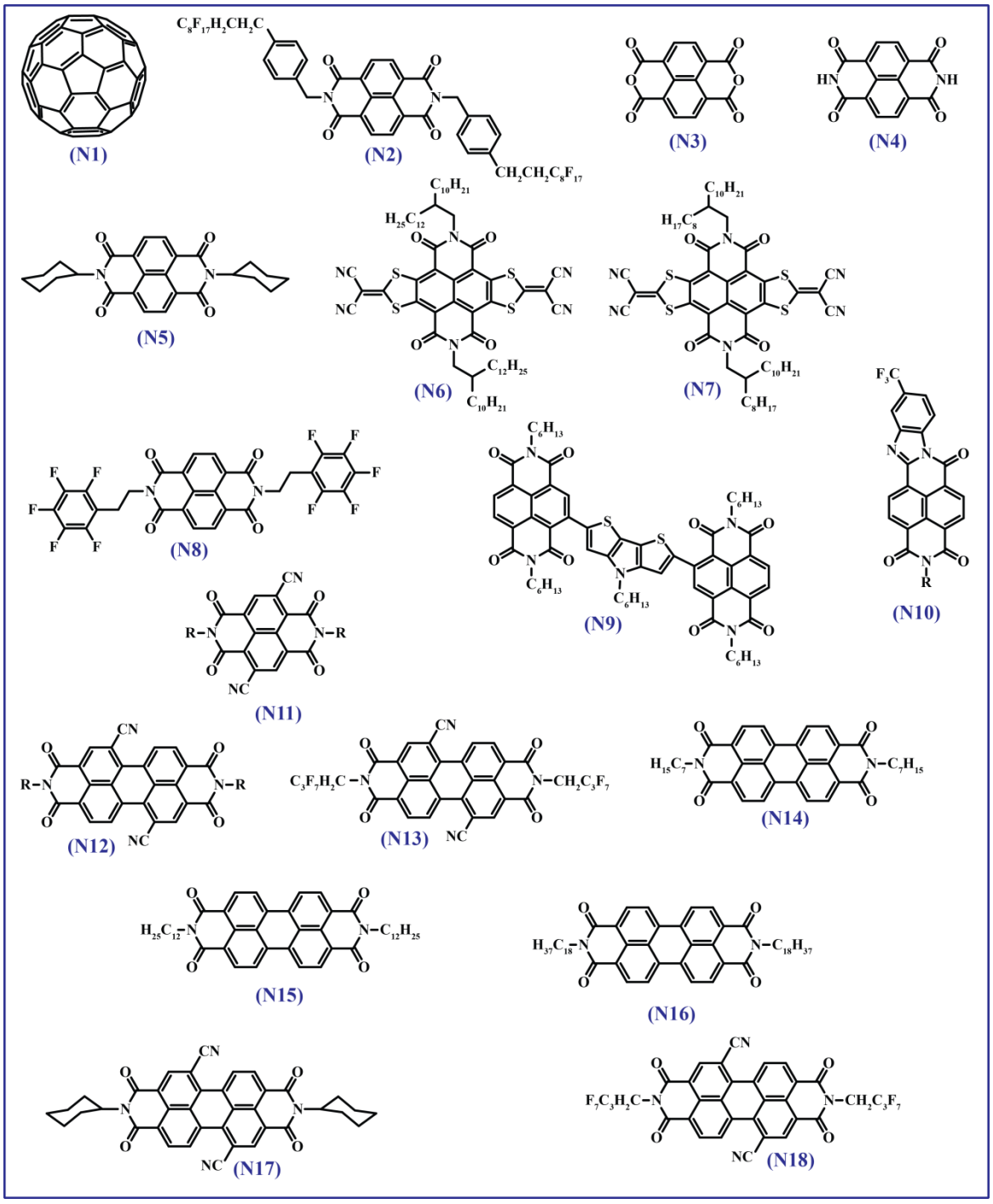

Figure 1.14: Examples of n-type semiconductors based on small molecules with structure.

High charge carrier mobility was observed for small molecule semiconductors based on NDI and PDI. Mainly OFET mobility was obtained from NDI, PDI based small molecule semiconductors for vacuum deposited thin films. This technique is somewhat expensive and needs several optimization to get uniform morphology of thin film. On the other hand, solution process techniques like inject printing, spin coating, flexographic printing etc., are less expensive and easy. This method is more successful for polymers as their solution viscosity is higher than that of small molecules.[137, 138] In addition large area roll to roll production is also possible for polymeric semiconductors. Recently, PDI and NDI based polymers exhibited high mobility comparable to small molecules. Further development is required to improve the performance of polymeric n-type semiconductors. In 2003, n-channel TFT-active ladder poly(benzobisimidazo-benzophenanthroline) BBL (pN-1) (figure 1.15) was introduced for the first time by Jenekhe *et al*. This acceptor polymer showed electron mobility in the order of 0.1 cm^2/Vs in thin film state.[139] However, limited solubility of this polymer (soluble only in strong acidic solutions like methane sulfonic acid: MSA) restricted their use in electronic device. Marder *et al*. first introduced PDI based polymer (pN-2) with electron mobility as high as 1.3×10^{-2} cm^2/Vs with on/off current ratio > 10^4. For the investigation of solar cell characteristics, they used pN-2 as acceptor and bi(thienylenevinylene)-substituted polythiophene as donor.[140] Bulk heterojunction (BHJ) device exhibited a fill factor (FF) of 0.39, V_{OC} of 0.63 V and J_{SC} of 4.2 mA/cm^2. This solar cell device showed average power conversion efficiency of more than 1 %. Alternating copolymer of PDI bearing *tert*–butyloxy side chain at core position (pN-3) was reported from the Mikroyannidis research group with SCLC mobility of 8.5 x 10^{-3} cm^2/Vs. BHJ solar cell was fabricated using this copolymer pN-3 which exhibited PCE of 2.23 %.[141] More than 2 % solar cell efficiency was achieved with PDI based copolymer pN-4 used as electron transporting material in BHJ solar cell.[100, 142] Facchetti *et al*. independently developed a NDI-based polymer P(NDI2OD-T2) (pN-5) which exhibited OFET mobility of 0.85 cm^2/Vs in top-gate/bottom-contact device configuration.[143] Bulk mobility was also measured for this copolymer via SCLC method which exhibited electron mobility up to 5 x 10^{-3} cm^2/Vs. Further, this copolymer was commercialized as PolyeraActivInk (N2200) for printed OFETs. In this direction, Luscombe reported a series of polymers by varying the thiophene units in pN-5 polymer backbone. Among the series of NDI-oligothiophene based copolymers, PNDI-3Ph (pN-6) showed the OFET mobility as high as 0.076 cm^2/Vs in bottom-gate/top-contact device architecture.[144] Very recently, Jenekhe *et al*. reported a NDI-selenophene based

copolymer (PNDIS-HD) (pN-7) which showed a record efficiency of 3.3 % in all polymer solar cells where they used thiazolothiazole copolymer (PSEHTT) as the donor material.

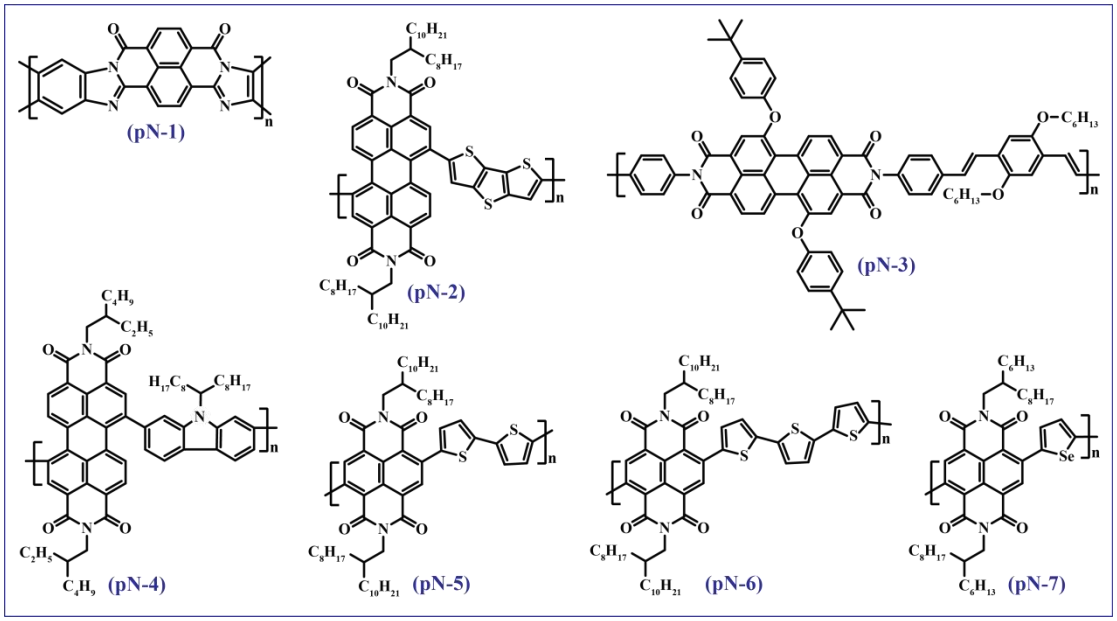

Figure 1.15: Example of NDI and PDI based main chain semiconducting polymers.

Most of the n-type polymers reported based on PDI and NDI are either main-chain polymer or bay substituted copolymer. Some literature is available where PDI was used as a pendant group in side-chain polymer. Thelakkat *et al.* introduced PDI as pendant group in side-chain polymer. They synthesised the homopolymer of perylene acrylate (PPerAcr) and its diblock copolymer with polystyrene (PS-*b*-PPerAcr) via stable free-radical polymerization (SFRP) technique (Nitroxide mediated radical polymerization) (figure 1.16). These side-chain polymers exhibited highest electron mobility up to 1.2×10^{-3} cm^2/Vs at 210 ^oC under inert atmosphere.[145]

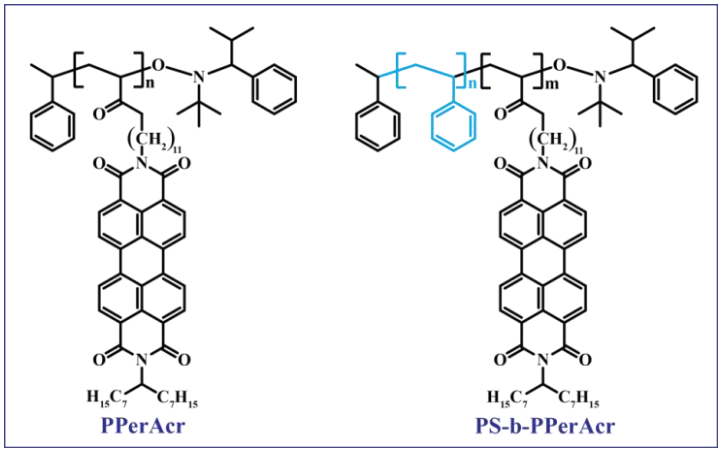

Figure-1.16: Molecular structures of side-chain polymer PPerAcr and PS-*b*-PPerAcr.

1.5.2 p-Type Semiconductor

P-type organic semiconductors or hole transporting materials are electron rich in nature and always like to donate electrons to other materials to generate holes. So, low ionization potential along with low electron affinity makes a material superior for hole transport. Parameters like electron affinity (EA), energy gap (Eg) and ionization potential (IP) are important factors to understand and control the optical and electrical properties of conducting polymers. Eg is important to understand the optical transition and intrinsic electrical properties and IP value can help to determine whether a p-type dopant is capable of ionizing the polymer chain. One can obtain EA by subtracting the IP from Eg, which is also important to understand the doping process.[146] For example poly(3-hexylthiophene) exhibited p-type character with low ionization potential of 5.2 eV.[147] Materials with homo energy level of 4.8 to 5.2 eV favours hole injection. In the past few decades, many research groups have carried out extensive research for the development of p-type or hole transporting semiconductors. Figure 1.17 shows some chemical structures of p-type semiconductors used in OFETs. Pentacene derivatives (shown in figure 1.17 P1) showed very high hole mobility upto 5 cm^2/Vs with on/off (I_{on}/I_{off}) ratio of 108.[148] Thieono [3,2-*b*] thieno- [2',3':4,5] thieno [2,3-*d*] thiophene derivatives (P2) exhibited the best OFET mobility of 0.14 cm^2/Vs.[148] Fong *et al.* synthesised a dialkylated tetrathienoacene (P3) based copolymer which showed hole mobility up to 0.3 cm^2/Vs.[149] H. Sirringhaus *et al.* reported the effect of orientation on hole mobility of polymeric semiconductor hexyl substituted poly(thiophene) (P4). They observed the increment of hole mobility from 0.05 cm^2/Vs to 0.1 cm^2/Vs with changing orientation of the semiconductor coated on respective substrate.[150] Iosip *et al.* reported a p-type semiconductor based on dithieno[3,2-b:20,30-d]thiophene and thiophene units (P5) with high mobility of 2×10^{-2} cm^2/Vs.[151] Poly (2,5 bis(3-alkylthiophen-2yl)thieno [3,2-b] thiophene) PBTTT (P6) was synthesised and crystallized from its liquid crystalline phase which exhibited hole mobility up to 0.6 cm^2/Vs.[152] Very less number of reports based on OPV molecules are there for the application of semiconducors. However, the polymeric analogue namely poly (*p*-phenylene vinylene) (PPV) has been used as an active semiconductor in solar cell devices. The first BHJ solar cell was made by random mixing of MEH-PPV (p-type) and C_{60} (n-type).[153] Later on MDMO-PPV was developed as an active p-type material in solar cell devices. Meijer *et al.*, developed donor-acceptor self-assembled system with hydrogen bonding units. They reported a donor-acceptor system based on OPV (BOPVUP) (P7) and methanofullerene phenyl-[6,6]-C_{61}-butyric acid

methyl ester (PCBM) (P7). They prepared spin coated film by mixing these two materials with 1:2.8 weight ratio in chlorobenzene for the photovoltaic measurement.[154] Polyethylene-dioxythiophene polystyrenesulfonate (PEDOT:PSS, 90 nm) was used as a conducting layer for the above device mesurement. ITO/PEDOT:PSS/BOPVUP:PCBM/Al device configuration showed a diode behaviour with high rectification ratio of 1×10^3 at ± 2 V. PCE was very poor for this system with I_{SC} and V_{OC} of 0.32 mA/cm^2 and 0.82 V respectively. René A. J. Janssen *et al*. reported a OPV-C_{60} system (OPV4-C_{60}) (P8) with very low power conversion efficiency with I_{SC} and V_{OC} of 235 μA/cm^2 and 650 mV respectively.[155] In photovoltaic cell, device efficiency generally depends on charge-carrier generation and mobility. These two factors can be improved by ordering of the π-conjugated materials in the molecular level. So ordering of the active π-conjugated chromophore along the side chain of the polymer can increase the charge carrier mobility to improve device efficiency in solar cell.[87, 156] Apart from these p-type materials many other derivatives like BODIPY, diketopyrrolopyroles (DPP), squarene, methalphthalocynine,[150] tripenylene derivavtive etc., were successfully synthesised and used as hole transporting semiconductors.

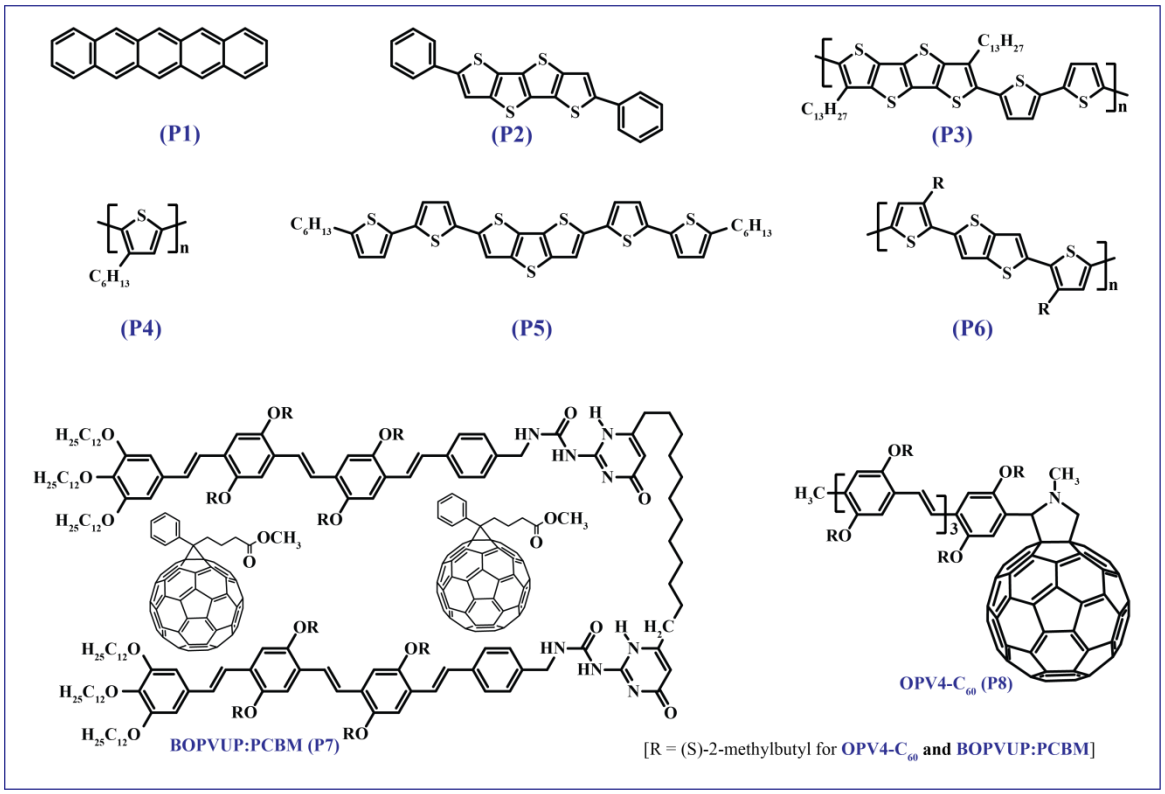

Figure 1.17: Examples of p-type semiconductors with molecular structure.

1.5.3 Ambipolar Semiconductor

Ambipolar semiconductors are the class of semiconductors which can transport both holes and electrons depending upon the applied voltage. The design principle for n-type organic semiconductor is also applicable to develop ambipolar materials. One main criteria to make an ambipolar material is to decrease the LUMO energy levels with the help of electron withdrawing group with simultenious balancing of HOMO energy level which can favour hole injection. For example, core-substituted naphthalenediimide containing copolymer PNDI-T(Bz)T exhibited ambipolar charge transport properties with electron mobility of 0.05 cm^2/Vs and hole mobility up to 0.03 cm^2/Vs.[157] There are several other examples for ambipolarity in organic semiconducting materials, which are not delved upon in the present thesis work.

1.6 Aim of the Thesis

The detailed discussion presented in this chapter clearly suggest the potential of the rylenediimide and oligo (*p*-phenylene vinylene) for different electronic applications. Many supramolecular π-conjugated architectures were made from the basic building blocks of NDI, PDI and OPV, which were used for applications in devices like sensors and OLEDs, in addition to eliciting fundamental understanding of processes involved in energy transfer, host-guest interaction etc,. Along with π-π interaction, hydrogen bonding (H-bonding) is also an important tool for constructing one dimensional (1D) structures which can help in improving charge carrier mobility along the self-assembled molecular stacks of the respective π-conjugated molecules. The role of the H-bonding in charge transport mechanism of a supramolecular π-conjugated system is not fully understood. Though the solution processability is very poor for small molecular system, small molecules based on PDI or NDI have exhibited better device performances as compared to their polymeric analogues. In general, main chain conjugated polymers are very easy to solution process and are used extensively in devices, but they typically exhibit low mobility with respect to their small molecular analogue. Device performances can also be developed by attaching the active π-conjugated molecule to the side chain of a comb polymer or block copolymer through covalent attachment. However, this approach is difficult in terms of their synthesis since the π-conjugated molecules have limited solubility in common organic solvents. The covalently linked sidechain can also reduce the chain mobility of the polymer which restricts the packing of the attached π-conjugated

molecules required for better charge carrier mobility. This problem can be overcome by attaching the small π-conjugated molecules as a pendant group to a polymer backbone via noncovalent hydrogen bonding interaction or electrostatic interaction. In this regards, sidechain polymers based on PDI, NDI or OPV still do not find much application in electronic devices. Therefore, it is important to develop new strategies to get high performance and cost effective p-type, n-type or p-n type polymeric materials for different electronic applications.

The present thesis work is mainly focused on the design, synthesis and investigation of new categories of supramolecular sidechain polymers based on PDI, NDI and OPV to understand the effect of hydrogen bonded self-assembly in the charge transport properties for the applications in optoelectronics. More specifically, this dissertation mainly targets the detailed investigation of the structure property relationship in supramolecular comb polymers based on PDI, NDI and OPV. Varieties of small molecules were synthesised based on PDI, NDI and OPV to make the supramolecular structure and studied the effect of molecular packing, thin film morphology in charge transport properties. These objectives were carried out in four different chapters.

The first chapter explains the hydrogen bonded complex formation of unsymmetrically substituted n-type naphthalenemonoimide (NMI) and naphthalenediimide (NDI) small molecule with polybenzimidazole. Large area (3cm x 3cm) transparent free standing film was made from Polybenzimidazole-NMI composite. The complex showed nano structure morphology upon observation under TEM imaging. Detailed studies were carried out to understand molecular packing and thin film morphology of the supramolecular composites. Polybenzimidazole-NMI and Polybenzimidazole-NDI composites showed n-type mobility in SCLC and OFET measurement respectively. However, the observed electron mobility was not so promising for further applications, therefore a different polymer backbone - namely P4VP was chosen as the polymer template for complexation, which was taken up in the next chapter. P4VP was complexed with various types of derivatives based on PDI, NDI and OPV small molecules. The third working chapter explains the improvement in charge carrier mobility in P4VP-PDI and P4VP-NDI supramolecular crosslinked polymer network which was made via noncovalent H-bonded interaction among the –OH group of rylenediimides and nitrogen atom of P4VP. This particular work involved the synthesis of symmetric perylenediimide and naphthalenediimide with free –OH group at the termini.

Supramolecular crosslinked polymer networks were made by complementary hydrogen bonding of symmetric rylenebisimides with P4VP. Detailed studies were done to understand the microstructure and thin film morphology of the supramolecularly crosslinked polymer networks. SCLC measurement for both rylenediimide complexes showed 2 orders increment in the electron mobility with respect to their small molecular counterpart. The fourth chapter details the design and synthesis of donor OPV and acceptor PDI molecules to construct donor-acceptor nano structures in the P4VP polymer backbone. The complex formation was confirmed with the help of FT-IR and ^{1}H NMR spectroscopic techniques. Small angle X-ray scattering (SAXS) and wide angle X-ray diffraction (WXRD) techniques were used for understanding packing of the donor-acceptor mixed complexes. TEM studies showed the lamellar arrangement of donor-acceptor in the P4VP polymer backbone. The mixed donor-acceptor complex achieved reasonably high hole mobility (μ_h) which was measured by SCLC method. In the last chapter nanostructured supramolecular donor-acceptor assembly was made without the aid of any templating polymer. This nano organization was formed when an unsymmetrically functionalized oligo(p-phenylenevinylene) (OPVM-OH) was complexed with unsymmetrical N-substituted pyridine functionalized perylenediimide (UPBI-Py). The resultant supramolecular complex was subjected to photo polymerization with an UV spot curing setup. SAXS and WXRD were recorded to understand the molecular packing of the donor-acceptor small molecular complex as well as supramolecular polymer complex. The nanoscale organization of the donor/acceptor could be visualized using the TEM imaging. The supramolecular complex exhibited a higher order of electron mobility with respect to its pristine state. Thus, a versatile method was developed to construct nano structure of suitably functionalized donor and acceptor materials with improvement in photocurrent response. Chapter six gives an overall conclusion and summary of the thesis work.

1.7 References

1. Cuevas, J. C.; Scheer, E. *Molecular Electronics an Introduction to Theory and Experiment*. 2010.

2. Shirakawa, H.; Louis, E. J.; MacDiarmid, A. G.; Chiang, C. K.; Heeger, A. J. *J. Chem. Soc. Chem. Commun.* **1977**, 578–580.

3. Blochwitz, J.; Pfeiffer, M.; Fritz, T.; Leo, K.; Blochwitz, J.; Pfeiffer, M.; Fritz, T.; Leo, K. *Appl. Phys. Lett.* **1998**, *73*, 729–731.

4. Hamada, Y.; Kanno, H.; Tsujioka, T.; Takahashi, H.; Usuki, T.; Hamada, Y.; Kanno, H.; Tsujioka, T.; Takahashi, H. *Appl. Phys. Lett.* **1999**, *75*, 1682–1684.

5. Kim, W. H.; Mäkinen, A. J.; Nikolov, N.; Shashidhar, R.; Kim, H.; Kafafi, Z. H.; Nikolov, N.; Shashidhar, R.; Kim, H.; Kafafi, Z. H. *Appl. Phys. Lett.* **2002**, *80*, 3844–3846.

6. Lamansky, S.; Djurovich, P.; Murphy, D.; Abdel-razzaq, F.; Lee, H.; Adachi, C.; Burrows, P. E.; Forrest, S. R.; Thompson, M. E. *J. Am. Chem. Soc.* **2001**, *123*, 4304–4312.

7. Bao, Z.; Dodabalapur, a; Lovinger, a J. *Appl. Phys. Lett.* **1996**, *69*, 4108–4110.

8. Dimitrakopoulos, C. D.; Brown, A. R.; Pomp, A. *J. Appl. Phys.* **1996**, *80*, 2501.

9. Garnier, F.; Hajlaoui, R.; Yassar, A.; Srivastava, P. *Science.* **1994**, *265*, 1684–1686.

10. Meijer, E. J.; de Leeuw, D. M.; Setayesh, S.; van Veenendaal, E.; Huisman, B. H.; Blom, P. W. M.; Hummelen, J. C.; Scherf, U.; Kadam, J.; Klapwijk, T. M. *Nat. Mater.* **2003**, *2*, 678–682.

11. Rost, C.; Gundlach, D. J.; Karg, S.; Rieß, W. *J. Appl. Phys.* **2004**, *95*, 5782–5787.

12. Sirringhaus, H. *Adv. Mater.* **2005**, *17*, 2411–2425.

13. Zen, A.; Pflaum, J.; Hirschmann, S.; Zhuang, W.; Jaiser, F.; Asawapirom, U.; Rabe, J. P.; Scherf, U.; Neher, D. *Adv. Funct. Mater.* **2004**, *14*, 757–764.

14. Bundgaard, E.; Krebs, F. C. *Sol. Energy Mater. Sol. Cells* **2007**, *91*, 954–985.

15. Dang, M. T.; Hirsch, L.; Wantz, G. *Adv. Mater.* **2011**, *23*, 3597–3602.

16. Dhanabalan, A.; van Duren, J. K. J.; van Hal, P. a; van Dongen, J. L. J.; Janssen, R. a J. *Adv. Funct. Mater.* **2001**, *11*, 255–262.

17. Kim, J. S.; Park, Y.; Lee, D. Y.; Lee, J. H.; Park, J. H.; Kim, J. K.; Cho, K. *Adv. Funct. Mater.* **2010**, *20*, 540–545.

18. Li, C.; Liu, M.; Pschirer, N. G.; Baumgarten, M.; Muellen, K. *Chem. Rev.* **2010**, *110*, 6817–6855.

19. Sonar, P.; Fong Lim, J. P.; Chan, K. L. *Energy Environ. Sci.* **2011**, *4*, 1558–1574.

20. Wöhrle, D.; Meissner, D. *Adv. Mater.* **1991**, *3*, 129–138.

21. Burroughes, J. H.; Bradley, D. D. C.; Brown, A. R.; Marks, R. N.; Mackay, K.; Friend, R. H.; Burns, P. L.; Holmes, A. B. *Nature* **1990**, *347*, 539–541.

22. Brabec, Christoph J., Sariciftci, Serdar N., Hummelen, J. C. *Adv. Funct. Mater.* **2001**, *11*, 15–26.

23. Sariciftci, N. S.; Braun, D.; Zhang, C.; Srdanov, V. I.; Heeger, A. J.; Stucky, G.; Wudl, F. *Appl. Phys. Lett.* **1993**, *62*, 585–587.

24. Sariciftci, N. S.; Smilowitz, L.; Heeger, A. J.; Wudl, F. *Science* **1992**, *258*, 1474–1476.

25. Smilowitz, L.; Sariciftci, N. S.; Wu, R.; Gettinger, C.; Heeger, A. J.; Wudl, F. *Phys. Rev. B* **1993**, *47*, 13835–13842.

26. Heeger, A. J. *Chem. Soc. Rev.* **2010**, *39*, 2354.

27. Kozlov, V. G.; Bulović, V.; Burrows, P. E.; Forrest, S. R. *Nature* **1997**, *389*, 362–364.

28. Kranzelbinder, G.; Leising, G. *Reports Prog. Phys.* **2000**, *63*, 729.

29. McGehee, M. D.; Heeger, A. J. *Adv. Mater.* **2000**, *12*, 1655–1668.

30. Peterson, O. G.; Tuccio, S. A.; Snavely, B. B. *Appl. Phys. Lett.* **1970**, *17*, 245–247.

31. Riechel, S.; Lemmer, U.; Feldmann, J.; Berleb, S.; Mückl, a G.; Brütting, W.; Gombert, a; Wittwer, V. *Opt. Lett.* **2001**, *26*, 593–595.

32. Schäfer, F. P.; Schmidt, W.; Volze, J. *Appl. Phys. Lett.* **1966**, *9*, 306–309.

33. Schneider, D.; Rabe, T.; Riedl, T.; Dobbertin, T.; Kröger, M.; Becker, E.; Johannes, H. H.; Kowalsky, W.; Weimann, T.; Wang, J.; Hinze, P.; Gerhard, A.; Stössel, P.; Vestweber, H. *Adv. Mater.* **2005**, *17*, 31–34.

34. Shank, C. V.; Dienes, A.; Trozzolo, A. M.; Myer, J. A. *Appl. Phys. Lett.* **1970**, *16*, 405–407.

35. Wegmann, G.; Schweitzer, B.; Hopmeier, M.; Oestreich, M.; Giessen, H.; Mahrt, R. F. *Phys. Chem. Chem. Phys.* **1999**, *1*, 1795–1800.

36. Buryak, A.; Severin, K. *J. Am. Chem. Soc.* **2005**, *127*, 3700–3701.

37. Ekanayake, E. M. I. M.; Preethichandra, D. M. G.; Kaneto, K. *Biosens. Bioelectron.* **2007**, *23*, 107–113.

38. Lee, J.-S.; Kim, H. K.; Feng, S.; Vendrell, M.; Chang, Y.-T. *Chem. Commun.* **2011**, *47*, 2339–2341.

39. Miranda, O. R.; You, C. C.; Phillips, R.; Kim, I. B.; Ghosh, P. S.; Bunz, U. H. F.; Rotello, V. M. *J. Am. Chem. Soc.* **2007**, *129*, 9856–9857.

40. Phillips, R. L.; Kim, I. B.; Tolbert, L. M.; Bunz, U. H. F. *J. Am. Chem. Soc.* **2008**, *130*, 6952–6954.

41. Phillips, R. L.; Miranda, O. R.; You, C.-C.; Rotello, V. M.; Bunz, U. H. F. *Angew. Chemie, Int. Ed.* **2008**, *47*, 2590–2594.

42. Zhu, C.; Yang, Q.; Liu, L.; Lv, F.; Li, S.; Yang, G.; Wang, S. *Adv. Mater.* **2011**, *23*, 4805–4810.

43. Ankah, G. N.; Büchele, P.; Poulsen, K.; Rauch, T.; Tedde, S. F.; Gimmler, C.; Schmidt, O.; Kraus, T. *Org. Electron.* **2016**, *33*, 201–206.

44. Baeg, K. J.; Binda, M.; Natali, D.; Caironi, M.; Noh, Y. Y. *Adv. Mater.* **2013**, *25*, 4267–4295.

45. Kim, Y.; Ballarotto, M.; Park, D.; Du, M.; Cao, W.; Lee, C. H.; Herman, W. N.; Romero, D. B. *Appl. Phys. Lett.* **2007**, *91*, 193510.

46. Manna, E.; Xiao, T.; Shinar, J.; Shinar, R. *Electronics* **2015**, *4*, 688-722.

47. Hong, J. P.; Park, A. Y.; Lee, S.; Kang, J.; Shin, N.; Yoon, D. Y. *Appl. Phys. Lett.* **2008**, *92*, 12–15.

48. Kim, C. S.; Lee, S.; Gomez, E. D.; Anthony, J. E.; Loo, Y. L. *Appl. Phys. Lett.* **2008**, *93*, 91–94.

49. Dailey, S.; Feast, W. J.; Peace, R. J.; Sage, I. C.; Till, S.; Wood, E. L. *J. Mater. Chem.* **2001**, *11*, 2238–2243.

50. Haino, T. *Polym. J.* **2012**, *45*, 1–21.

51. Hill, J. P.; Shrestha, L. K.; Ishihara, S.; Ji, Q.; Ariga, K. *Molecules* **2014**, *19*, 8589–8609.

52. Krieg, E.; Bastings, M. M. C.; Besenius, P.; Rybtchinski, B. *Chem. Rev.* **2016**, *16*, 2414–2477.

53. Wang, L.; Lin, J.; Zhang, X. *Polym. (United Kingdom)* **2013**, *54*, 3427–3442.

54. Zhao, Y.; Thorkelsson, K.; Mastroianni, A. J.; Schilling, T.; Luther, J. M.; Rancatore, B. J.; Matsunaga, K.; Jinnai, H.; Wu, Y.; Poulsen, D.; Fréchet, J. M. J.; Alivisatos, a P.; Xu, T. *Nat. Mater.* **2009**, *8*, 979–985.

55. Rotzoll, R.; Mohapatra, S.; Olariu, V.; Wenz, R.; Grigas, M.; Dimmler, K.; Shchekin, O.; Dodabalapur, A. *Appl. Phys. Lett.* **2006**, *88*, 2004–2007.

56. Coropceanu, V.; Cornil, J.; Silva, D.; A, D.; Olivier, Y.; Silbey, R.; Bredas, J. L.; da Silva Filho, D. A.; Brédas, J.-L. *Chem. Rev.* **2007**, *107*, 926–952.

57. Gross, M.; Muller, D.; Nothofer, H.; Scherf, U.; Neher, D.; Brauchle, C.; Meerholz, K. *Nature* **2000**, *405*, 661–665.

58. Molapo, K. M.; Ndangili, P. M.; Ajayi, R. F.; Mbambisa, G.; Mailu, S. M.; Njomo, N.; Masikini, M.; Baker, P.; Iwuoha, E. I. **2012**, *7*, 11859–11875.

59. Bredas, J. L. and G. B. S. *Acc. Chem. Res.* 1985, *18*, 309–315.

60. Zou, L.; Savvate'ev, V.; Booher, J.; Kim, C. H.; Shinar, J. *Appl. Phys. Lett.* **2001**, *79*, 2282–2284.

61. Kim, N. H.; Kim, Y. H.; Yoon, J. A.; Lee, S. Y.; Ryu, D. H.; Wood, R.; Moon, C. B.; Kim, W. Y. *J. Lumin.* **2013**, *143*, 723–728.

62. Pope, M.; Kallmann, H. P.; Magnante, P. *J. Chem. Phys.* **1963**, *38*, 2042.

63. Bryant, P.; Brown, R. *Phys Review Letters.* **1990**, *65*, 1523–1526.

64. Tang, C. W.; Vanslyke, S. A. *Appl. Phys. Lett.* **1987**, *51*, 913–915.

65. Yang, Y. *MRS Bull.* **1997**, 31–38.

66. Zaumseil, J.; Sirringhaus, H. *Chem. Rev.* **2007**, *107*, 1296–1323.

67. Katz, H. E.; Bao, Z. *J. Phys. Chem. B* **2000**, *104*, 671–678.

68. Williams, R. *J. Chem. Phys.* **1960**, *32*, 1505–1514.

69. Tress, W.; Petrich, A.; Hummert, M.; Hein, M.; Leo, K.; Riede, M. *Appl. Phys. Lett.* **2011**, *98*, 063301.

70. Lessmann, R.; Hong, Z.; Scholz, S.; Maennig, B.; Riede, M. K.; Leo, K. *Org. Electron. physics, Mater. Appl.* **2010**, *11*, 539–543.

71. Blom, P. W. M.; Mihailetchi, V. D.; Koster, L. J. A.; Markov, D. E. *Adv. Mater.* **2007**, *19*, 1551–1566.

72. Liang, Y.; Xu, Z.; Xia, J.; Tsai, S. T.; Wu, Y.; Li, G.; Ray, C.; Yu, L. *Adv. Mater.* **2010**, *22*, 135–138.

73. Park, S. H.; Roy, A.; Beaupre, S.; Cho, S.; Coates, N.; Moon, J. S.; Moses, D.; Leclerc, M.; Lee, K.; Heeger, A. J. *Nat. Photonics* **2009**, *3*, 297–303.

74. Law, M.; Greene, L. E.; Johnson, J. C.; Saykally, R.; Yang, P. *Nat. Mater.* **2005**, *4*, 455–459.

75. Chiba, Y.; Islam, A.; Watanabe, Y.; Komiya, R.; Koide, N.; Han, L. *Japanese J. Appl. Physics, Part 2 Lett.* **2006**, *45*, 23–26.

76. Hagfeldt, A.; Boschloo, G.; Sun, L.; Kloo, L.; Pettersson, H. *Chem. Rev.* **2010**, *110*, 6595–6663.

77. Grätzel, M. *J. Photochem. Photobiol. C Photochem. Rev.* **2003**, *4*, 145–153.

78. Wei, D. *J. Mol. Sci.* **2010**, *11*, 1103–1113.

79. Mathew, S.; Yella, A.; Gao, P.; Humphry-Baker, R.; Curchod, B. F. E.; Ashari-Astani, N.; Tavernelli, I.; Rothlisberger, U.; Nazeeruddin, M. K.; Grätzel, M. *Nat. Chem.* **2014**, *6*, 242–247.

80. He, X.; Cao, B.; Hauger, T. C.; Kang, M.; Gusarov, S.; Luber, E. J.; Buriak, J. M. *ACS Appl. Mater. Interfaces* **2015**, *7*, 8188–8199.

81. Roncali, J.; Leriche, P.; Blanchard, P. *Adv. Mater.* **2014**, *26*, 3821–3838.

82. Zhang, Q.; Kan, B.; Liu, F.; Long, G.; Wan, X.; Chen, X.; Zuo, Y.; Ni, W.; Zhang, H.; Li, M.; Hu, Z.; Huang, F.; Cao, Y.; Liang, Z.; Zhang, M.; Russell, T. P.; Chen, Y. *Nat. Photonics* **2014**, *9*, 35–41.

83. Scharber, M. C.; Sariciftci, N. S. *Prog. Polym. Sci.* **2013**, *38*, 1929–1940.

84. Günes, S.; Neugebauer, H.; Sariciftci, N. S. *Chem. Rev.* **2007**, *107*, 1324–1338.

85. Dennler, G.; Scharber, M. C.; Brabec, C. J. *Adv. Mater.* **2009**, *21*, 1323–1338.

86. Ma, W.; Yang, C.; Gong, X.; Lee, K.; Heeger, A. J. *Adv. Funct. Mater.* **2005**, *15*, 1617–1622.

87. Li, G.; Shrotriya, V.; Huang, J.; Yao, Y.; Moriarty, T.; Emery, K.; Yang, Y. *Nat. Mater.* **2005**, *4*, 864–868.

88. Herrikhuyzen, J. v.; Syamakumari, a; Schenning, a. P. H. J.; Meijer, E. W. *J. Am. Chem. Soc.* **2004**, *126*, 10021–10027.

89. You, J.; Dou, L.; Yoshimura, K.; Kato, T.; Ohya, K.; Moriarty, T.; Emery, K.; Chen, C.-C.; Gao, J.; Li, G.; Yang, Y. *Nat. Commun.* **2013**, *4*, 1446.

90. Holliday, S.; Ashraf, R. S.; Wadsworth, A.; Baran, D.; Yousaf, S. A.; Nielsen, C. B.; Tan, C.-H.; Dimitrov, S. D.; Shang, Z.; Gasparini, N.; Alamoudi, M.; Laquai, F.; Brabec, C. J.; Salleo, A.; Durrant, J. R.; McCulloch, I. *Nat. Commun.* **2016**, *7*, 11585.

91. Lira-Cantu, M.; Krebs, F. C. *Sol. Energy Mater. Sol. Cells* **2006**, *90*, 2076–2086.

92. Kumar, S.; Nann, T. *J. Mater. Res.* **2004**, *19*, 1990–1994.

93. Granstrom, M.; Petritsch, K.; Arias, a C.; Lux, a; Andersson, M. R.; Friend, R. H. *Nature* **1998**, *395*, 257–260.

94. Kietzke, T.; Hörhold, H-H.; Neher, D. *Chem. Mater.* **2005**, *17*, 6532–6537.

95. Mayer, A. C.; Scully, S. R.; Hardin, B. E.; Rowell, M. W.; McGehee, M. D. *Mater. Today* **2007**, *10*, 28–33.

96. Chi, D.; Qu, S.; Wang, Z.; Wang, J. *J. Mater. Chem. C* **2014**, *2*, 4383–4387.

97. Hoppe, H.; Niggemann, M.; Winder, C.; Kraut, J.; Hiesgen, R.; Hinsch, A.; Meissner, D.; Sariciftci, N. S. *Adv. Funct. Mater.* **2004**, *14*, 1005–1011.

98. Zhang, Q.; Cirpan, A.; Russell, T. P.; Emrick, T. *Macromolecules* **2009**, *42*, 1079–1082.

99. Zhang, X.; Lu, Z.; Ye, L.; Zhan, C.; Hou, J.; Zhang, S.; Jiang, B.; Zhao, Y.; Huang, J.; Zhang, S.; Liu, Y.; Shi, Q.; Liu, Y.; Yao, J. *Adv. Mater.* **2013**, *25*, 5791–5797.

100. Zhou, E.; Cong, J.; Wei, Q.; Tajima, K.; Yang, C.; Hashimoto, K. *Angew. Chemie - Int. Ed.* **2011**, *50*, 2799–2803.

101. Zhou, E.; Cong, J.; Zhao, M.; Zhang, L.; Hashimoto, K.; Tajima, K. *Chem. Commun.* **2012**, *48*, 5283.

102. Earmme, T.; Hwang, Y. J.; Murari, N. M.; Subramaniyan, S.; Jenekhe, S. A. *J. Am. Chem. Soc.* **2013**, *135*, 14960–14963.

103. Hwang, Y. J.; Ren, G.; Murari, N. M.; Jenekhe, S. A. *Macromolecules* **2012**, *45*, 9056–9062.

104. Kim, J. Y.; Lee, K.; Coates, N. E.; Moses, D.; Nguyen, T.; Dante, M.; Heeger, A. J. *Science* **2007**, *317*, 222–226.

105. Lund, J.; Larsen, T. *Nature Photonics* **2006**, *6*, 153-161.

106. Forrest, S. *MRS Bull.* **2012**, *37*, 552–553.

107. Rand, B. P.; Genoe, J.; Heremans, P.; Poortmans, J. *Prog. Photovolt Res. Appl.* **2007**, *15*, 659–676.

108. Huang, Y.; Kramer, E. J.; Heeger, A. J.; Bazan, G. C. *Chem. Rev.* **2014**, *114*, 7006–7043.

109. Yu, G.; Gao, J.; Hummelen, J. C.; Wudl, F.; Heeger, A. J. *Science* **1995**, *270*, 1789–1791.

110. Ye, L.; Zhang, S.; Zhao, W.; Yao, H.; Hou, J. *Chem. Mater.* **2014**, *26*, 3603–3605.

111. Kokil, A.; Yang, K.; Kumar, J. *J. Polym. Sci. Part B Polym. Phys.* **2012**, *50*, 1130–1144.

112. Wang, C.; Dong, H.; Li, H.; Zhao, H.; Meng, Q.; Hu, W. *Cryst. Growth Des.* **2010**, *10*, 4155–4160.

113. Salleo, A. *Mater. Today* **2007**, *10*, 38–45.

114. Antolini, L.; Horowitz, G.; Kouki, F.; Garnier, F. *Adv. Mater.* **1998**, *10*, 382–385.

115. da Silva Filho, D. A.; Kim, E. G.; Brédas, J. L. *Adv. Mater.* **2005**, *17*, 1072–1076.

116. Singh, T. B.; Erten, S.; Günes, S.; Zafer, C.; Turkmen, G.; Kuban, B.; Teoman, Y.; Sariciftci, N. S.; Icli, S. *Org. Electron. physics, Mater. Appl.* **2006**, *7*, 480–489.

117. Madhavan, N. Small-Molecule Organic Semiconductors. April 01, **2002**, 49–56.

118. Wen, Y.; Liu, Y. *Adv. Mater.* **2010**, *22*, 1331–1345.

119. Anthony, J. E.; Facchetti, A.; Heeney, M.; Marder, S. R.; Zhan, X. *Adv. Mater.* **2010**, *22*, 3876–3892.

120. de Leeuw, D. M.; Simenon, M. M. J.; Brown, a. R.; Einerhand, R. E. F. *Synth. Met.* **1997**, *87*, 53–59.

121. Brédas, J. L.; Beljonne, D.; Coropceanu, V.; Cornil, J. *Chem. Rev.* **2004**, *104*, 4971–5003.

122. Murphy, A. R.; Fréchet, J. M. J.; Fre, J. M. J. *Chem. Rev.* **2007**, *107*, 1066–1096.

123. Zhang, X. H.; Domercq, B.; Kippelen, B. *Appl. Phys. Lett.* **2007**, *91*, 2005–2008.

124. Dey, A.; Kalita, A.; Iyer, P. K. *ACS Appl. Mater. Interfaces* **2014**, *6*, 12295−12301.

126. Laquindanum, J. G.; Katz, H. E.; Dodabalapur, A.; Lovinger, A. J. *J. Am. Chem. Soc.* **1996**, *118*, 11331–11332.

127. Shukla, D.; Nelson, S. F.; Freeman, D. C.; Rajeswaran, M.; Ahearn, W. G.; Meyer, D. M.; Carey, J. T. *Chem. Mater.* **2008**, *20*, 7486–7491.

128. Jung, B. J.; Sun, J.; Lee, T.; Sarjeant, A.; Katz, H. E. *Chem. Mater.* **2009**, *21*, 94–101.

129. Polander, L. E.; Tiwari, S. P.; Pandey, L.; Seifried, B. M.; Zhang, Q.; Barlow, S.; Risko, C.; Brédas, J.-L.; Kippelen, B.; Marder, S. R.; Brédas, J. L. *Chem. Mater.* **2011**, *23*, 3408–3410.

130. Deng, P.; Yan, Y.; Wang, S.-D.; Zhang, Q. *Chem. Commun.* **2012**, *48*, 2591.

131. Yoo, B.; Jung, T.; Basu, D.; Dodabalapur, A.; Jones, B. A.; Facchetti, A.; Wasielewski, M. R.; Marks, T. J. *Appl. Phys. Lett.* **2006**, *88*, 10–13.

132. Jones, B. A.; Ahrens, M. J.; Yoon, M. H.; Facchetti, A.; Marks, T. J.; Wasielewski, M. R. *Angew. Chemie - Int. Ed.* **2004**, *43*, 6363–6366.

133. Jones, B. A.; Facchetti, A.; Wasielewski, M. R.; Marks, T. J. *J. Am. Chem. Soc.* **2007**, *129*, 15259–15278.

134. Molinari, A. S.; Alves, H.; Chen, Z.; Facchetti, A.; Morpurgo, A. F. *J. Am. Chem. Soc.* **2009**, *131*, 2462–2463.

135. Chesterfield, R. J.; McKeen, J. C.; Newman, C. R.; Ewbank, P. C.; da Silva Filho, D. a.; Brédas, J.-L.; Miller, L. L.; Mann, K. R.; Frisbie, C. D. *J. Phys. Chem. B* **2004**, *108*, 19281–19292.

136. Malenfant, P. R. L.; Dimitrakopoulos, C. D.; Gelorme, J. D.; Kosbar, L. L.; Graham, T. O.; Curioni, A.; Andreoni, W. *Appl. Phys. Lett.* **2002**, *80*, 2517–2519.

137. Guo, X.; Facchetti, A.; Marks, T. J. *Chem. Rev.* **2014**, *114*, 8943–9012.

138. Krebs, F. C. *Sol. Energy Mater. Sol. Cells* **2009**, *93*, 394–412.

139. Babel, A.; Jenekhe, S. A. *J. Am. Chem. Soc.* **2003**, *125*, 13656–13657.

140. Zhan, X.; Tan, Z.; Domercq, B.; An, Z.; Zhang, X.; Barlow, S.; Li, Y.; Zhu, D.; Kippelen, B.; Marder, S. R. *J. Am. Chem. Soc.* **2007**, *129*, 7246–7247.

141. Mikroyannidis, J. A.; Stylianakis, M. M.; Sharma, G. D.; Balraju, P.; Roy, M. S. *J. Phys. Chem. C* **2009**, *113*, 7904–7912.

142. Guo, X.; Kim, F. S.; Seger, M. J.; Jenekhe, S. A.; Watson, M. D. *Chem. Mater.* **2012**, *24*, 1434–1442.

143. Yan, H.; Chen, Z.; Zheng, Y.; Newman, C.; Quinn, J. R.; Dötz, F.; Kastler, M.; Facchetti, A. *Nature* **2009**, *457*, 679–686.

144. Durban, M. M.; Kazarinoff, P. D.; Luscombe, C. K. *Macromolecules* **2010**, *43*, 6348–6352.

145. Lindner, S. M.; Thelakkat, M. *Macromolecules* **2004**, *37*, 8832–8835.

146. Eckhardt, H.; Shacklette, L. W.; Jen, K. Y.; Elsenbaumer, R. L. *J. Chem. Phys.* **1989**, *91*, 1303.

147. Micaroni, L.; Nart, F. C.; Hümmelgen, I. A. *J. Solid State Electrochem.* **2003**, *7*, 55–59.

148. Wu, W.; Liu, Y.; Zhu, D. *Chem. Soc. Rev.* **2010**, *39*, 1489–1502.

149. Fong, H. H.; Pozdin, V. a; Amassian, A.; Malliaras, G. G.; Smilgies, M.; He, M.; Gasper, S.; Zhang, F.; Sorensen, M. *Polymer (Guildf).* **2008**, *4*, 1–7.

150. Sirringhaus, H.; Brown, P. J.; Friend, R. H.; Nielsen, M. M.; Bechgaard, K.; Langeveld-Voss, B. M. W.; Spiering, a. J. H.; Janssen, R. a. J.; Meijer, E. W.; Herwig, P.; de Leeuw, D. M. *Nature* **1999**, *401*, 685–688.

151. Iosip, M. D.; Destri, S.; Pasini, M.; Porzio, W.; Pernstich, K. P.; Batlogg, B. *Synth. Met.* **2004**, *146*, 251–257.

152. McCulloch, I.; Heeney, M.; Bailey, C.; Genevicius, K.; Macdonald, I.; Shkunov, M.; Sparrowe, D.; Tierney, S.; Wagner, R.; Zhang, W.; Chabinyc, M. L.; Kline, R. J.; McGehee, M. D.; Toney, M. F. *Nat. Mater.* **2006**, *5*, 328–333.

153. Yu, G.; Gao, J.; Hummelen, J. C.; Wudl, F.; Heeger, A. J. *Science* **1995**, *270*, 1789-1791.

154. El-ghayoury, A.; Schenning, A. P. H. J.; Hal, P. A. Van.; Duren, J. K. J. Van; Janssen, Â. A. J.; Meijer, E. W. *Angew. Chem. Int. Ed.* **2001**, *40*,3660–3663.

155. Peeters, E.; van Hal, P. A.; Knol, J.; Brabec, C. J.; Sariciftci, S. N.; Hummelen, J. C.; Janssen, R. A. J. *J. Phys. Chem. B* **2000**, *104*, 10174–10190.

156. Olsen, B. D.; Jang, S.; Lu, J. M.; Segalman, R. A. *Macromolecules* **2006,** *39,* 4469-4479.

157. Gu, C.; Hu, W.; Yao, J.; Fu, H. *Chem. Mater.* **2013**, *25*, 2178–2183.

Chapter 2

Poly(benzimidazole)/ Naphthalene-imide Semiconducting Composite by Complementary Hydrogen Bonding.

2.1 Abstract

Composites of unsymmetrically substituted n-type naphthalenemonoimide (**NMI**) and naphthalenediimide (**NDI**) with polybenzimidazole (**PBImz**) were formed with the help of supramolecular interaction like hydrogen bonding, π-π interaction etc. The resultant composites were subjected to FT-IR and ^{1}H NMR spectroscopic analysis for the confirmation of composite formation. Wide angle X-ray diffraction (WXRD) was recorded to understand the microstructure of the polymer composites. Thin film morphology of **NMI** and **NDI** composites with polybenzimidazole were clearly visualized with the help of transmission electron microscopy (TEM) which showed composite nanoparticle with size range of 100-200 nm. The composite made from **NMI** and polybenzimidazole (**PBImz-NMI**) formed transparent free standing film over a large area with semiconducting characteristics. The effect of self-organization of donor acceptor assembly on bulk mobility was measured via SCLC method. **PBImz-NMI** composite showed space charge limited current (SCLC) mobility in the order of 10^{-7} cm^2/Vs, which was similar to that of the pristine naphthalenemonoimide (**NMI**) alone.

2.2 Introduction

Polymeric materials are in high demand for large area optoelectronic and other energy related applications due to their mechanical flexibility and solution processability.[1-13] On the other hand, small-molecule organic semiconductors are known to exhibit high charge carrier mobility.[14-23] They have the ability to pack more precisely and in well-defined molecular motifs. The improved charge carrier mobility is accounted for by high level of crystallinity. However, the processing is not simple and scalable to large area electronics. For example, the state of art mobility achieved in single crystal of small molecules is not possible to reproduce in large array of electronic device due to formation of grain boundaries in thin film which limits charge transport.[24-27] There may also be another issue of thin film uniformity. Polymers are known to form uniform film with very less device to device variation over large area. However, inherent disorder and poor crystallinity in polymeric materials tend to give lower charge carrier mobility. Therefore, the composite of small molecule/polymer to combine the electrical properties of small molecule and processability of polymer offers promising route to achieve desired optoelectronic material. The composite of organic semiconducting molecule (p-type or n-type) with polymer matrix by supramolecular interaction is an emerging strategy which showed promising performance in optoelectronic devices.[28-32] The naphthalenediimide containing small molecules are extensively used as n-type semiconductor due to their high electron affinity and charge carrier mobility. In this study, polybenzimidazole (**PBImz**) was chosen as the polymer matrix to embed naphthalenemonoimide (**NMI**) and naphthalenediimide (**NDI**) small molecules. Polybenzimidazole (**PBImz**) belongs to the heterocyclic rigid polymer family which exhibits high thermal, mechanical and chemical stability.[33-36] Moreover, **PBImz** has excellent film forming capability and its solution casted membrane finds several commercial applications. For example, acid doped **PBImz** membrane has become very popular solid polymer electrolyte in fuel cell application due to their high ionic (proton) conductivity.[37-39] Additionally, **PBImz** has been extensively used as matrix to dope highly conducting materials such as graphene and carbon nanotube.[40,41] In this chapter, we have explored the use of commercially important **PBImz** polymer to form supramolecular composite with n-type naphthalenemonoimide with one terminal substituted with 2-ethyl hexyl amine (**NMI**) and naphthalenediimide (**NDI**) with one terminal substituted with 2-ethyl hexyl and –N–H at the other termini. The imidazole linkage of **PBImz** possess proton donor (N-H) moiety which exhibited hydrogen bonding interaction with (C=O) group of **NMI** and formed freestanding

supramolecular composite film. The evidences of supramolecular interaction between **PBImz-NMI** and **PBImz-NDI** in composite were obtained by FTIR and NMR. Nano structure of the composite **PBImz-NMI** and **PBImz-NDI** were confirmed by transmission electron microscope (TEM) measurement. XRD analysis was performed to understand the microstructure of both the composites. The semiconducting nature of composite was characterized by SCLC measurement.

2.3 Experimental

2.3.1 Materials:

All the chemicals were purchased from Aldrich and used as received. Analytical grade solvents were used for the synthesis and used after drying. Procedure for the synthesis of the unsymmetrical naphthalenemonoimide (**NMI**), naphthalenediimide (**NDI**) and polybenzimidazole (**PBImz**) are given in scheme 2.1a, 2.1b and 2.1c.

2.3.2 Sample Preparation:

Both small molecules – **NMI** and **NDI** and polymer **PBImz** were dried at 110 °C in vacuum oven for 3 days. **NMI** and **NDI** were mixed separately with **PBImz** in dry DMSO and then the resultant solutions were heated up to 60 °C and stirred for 24 hours at this temperature. After completion of 24 hours, solvent was removed by slow evaporation of DMF at 75 °C on a petri dish. The resultant supramolecular polymer composites were dried further in vacuum oven at 80 °C for 3 days. The dried complexes were stored in desiccator.

2.3.3 Instrumentation Techniques:

Infrared spectra were collected for all the samples using a Bruker α-T spectrophotometer in the range of 4000-400 cm^{-1}. Supramolecular polymer composites **PBImz-NMI** and **PBImz-NDI** were mixed with KBr to make pellets. ^{1}H NMR and ^{13}C NMR spectra were recorded in DMSO-d_6 using Bruker AVAENS 400 MHz spectrophotometer. Chemical shifts (δ) are reported in ppm at 298 K, with trace amount of tetramethylsilane (TMS) as internal standard. MALDI-TOF analysis was carried out on a Voyager-De-STRMALDI-TOF (Applied Biosystems, Framingham, MA, USA) instrument equipped with 337 nm pulsed nitrogen laser used for desorption and ionization. The data was collected in reflector mode with an accelerating voltage of 25 kV. Micromolar solutions of the compound in DMF was mixed with 2,5-dihydroxy benzene (DHB) matrix and spotted on stainless steel MALDI plate and dried well. Wide Angle X-ray Diffractograms (WXRD)

was obtained using a Rigaku, MicroMax-007HF with high intensity Microfocus rotating anode X-ray generator. All the samples were recorded in the (2θ) range of 3–50 degrees and data was collected with the help of Control Win software. A Rigaku, R-axis IV^{++} detector was employed in wide-angle experiments. The radiation used was CuKα (1.54 Å) with a Ni filter, and the data collection was carried out using an Aluminium holder. Transmission Electron microscopy (TEM) was done using an FEI-Tecnai^{TM}-F20 electron microscope operating at 200 kV. The thermal stability of the PBImz and all composites with pristine NMI and NDI were analysed using PerkinElmer STA-6000 thermogravimetric analyser (TGA) under a nitrogen atmosphere from 40–800 °C at a heating rate of 10 °C/min.

2.3.4 SCLC Device Fabrication:

Electron only mobility was measured via SCLC method. The glass substrate was cleaned in distilled water, detergent, deionised water, acetone and isopropyl alcohol for 10-15 min each with ultrasonication. Cleaned glass substrates were dried in oven at 100 °C about 60 min. Al/polymer composite/Al diode configuration was used for the measurement of electron mobilities of the polymer composites and pristine molecules. Supramolecular polymer composites were dissolved in DMSO and filtered through PTFE membrane (0.45 micron) and clear solution was then dropcast on Al coated glass substrate to measure electron mobility. The drop casted substrates were annealed on a hot plate at 70 °C for 45 min followed by drying in vacuum at 10^{-1} mbar pressure for 3 hrs. On top of the active layer, Al layer (100 nm thick) was deposited by thermal evaporation in vacuum chamber at 10^{-6} mbar for electron-only device with the help of a shadow mask. The current and voltage (J-V) were measured using an Agilent semiconductor parameter analyser model 4156 C and semiprobe probe station. The Mott-Gurney law was used to extract the electron mobility as follows:

$$J = \varepsilon_0 \varepsilon_r \mu \frac{9V^2}{8L^3}$$

Where ε_0 = permittivity of the free space (8.854 x 10^{-12} F/m); ε_r = relative dielectric constant of the thin film which is assumed to be 3; μ = charge carrier (hole and electron) mobility; V = voltage drop across the device and L = thickness of the organic composites layer.

2.3.5 Synthesis:

(i) Synthesis of Naphthalenemonoimide (NMI):

1, 4, 5, 8-Naphthalenetetracarboxylic dianhydride (NDA) (5 gm; 1.86 x 10^{-2} mol) and zinc acetate ($Zn(OAc)_2$) (0.41 gm; 1.86 x 10^{-3} mol) were taken in a one neck round bottom (RB) flask. N, N-Dimethylacetamide (DMAc) (350 ml) was added to that resultant solid mixture. Resultant dispersed solution was heated further to 120 °C. 2-Ethylhexyl amine (3.05 ml; 1.86 x 10^{-2} mol) was added to that resultant solution at 120 °C and stirred further for 2 h at this temperature. After 2 h, DMAc was distilled off with the help of vacuum at 120 °C. After distillation of DMAc, methanol was added to that pasty mass in RB flask and stirred for 3-4 h at room temperature. The resultant solution was filtered off with suction filtration method. Solid brown powder was obtained which was further purified by column chromatography, where silica (mesh size - 100:200) was used as a stationary phase and dichloromethane: hexane (50: 50) mixture as a mobile phase. Yield = 60%. Melting Point = 115 °C. FT-IR (KBr Palate, cm^{-1}) = 3121, 3085, 3046, 2961, 2923, 2861, 1971, 1792, 1761, 1708, 1668, 1625, 1579, 1513, 1448, 1374, 1332, 1284, 1238, 1182, 1152, 1097, 1024, 924, 883, 805, 762, 707, 661. ^{1}H NMR (400 MHz, DMSO-d_6, δ): 8.69 (s, 4H); 4.00 (d, 2H); 1.85 (m, 1H); 1.27 (m, 8H); 0.88 (t, 6H) ppm. ^{13}C NMR (400 MHz, DMSO-d_6, δ): 162.71, 159.66, 131.81, 130.51, 129.20, 128.46, 126.98, 126.10, 123.72, 43.75, 37.19, 30.08, 28.04, 23.52, 22.38, 13.87, 10.41 ppm. MALDI-TOF MS (Calcd m/z 379); Found m/z – 380.19 [M+1], 402 [M+Na], 418 [M+K]. Elemental analysis calculated (%): C 69.64, H 5.58, N 3.69; found: C 69.24, H 5.12, N 4.13.

(i) Synthesis of Naphthalenediimide (NDI):

Naphthalenemonoimide (**NMI**) (500 mg) was added into a solution of ammonium hydroxide (NH4OH) (33 v/v %, 30 mL) at room temperature (r.t). The resultant dispersed solution was stirred for 4-5 hours at room temperature. After finishing the reaction, the solid precipitate was filtered through vacuum and washed thoroughly by large excess of water. The shiny powder was further dried in vacuum oven at 80 °C for 3 days. Yield = > 90 %. Melting Point = > 200 °C. FT-IR (KBr Palate, cm^{-1}) = 3169, 3122, 3065, 2951, 2923, 2853, 1691, 1650, 1575, 1516, 1444, 1373, 1333, 1262, 1230, 1187, 1085, 1057, 1019, 988, 953, 891, 855, 803, 765, 689, 645. ^{1}H NMR (400 MHz, DMSO-d_6, δ): 12.11 (s, 1H) 8.66 (dd, 4H); 4.00 (d, 2H); 1.85 (m, 1H); 1.27 (m, 8H); 0.88 (t, 6H) ppm. MALDI-TOF MS (Calcd m/z 378.16); Found m/z – 378.55 [M]. Elemental analysis calculated (%): C 69.83, H 5.86, N 7.40; found: C 69.28, H 5.85, N 7.66.

(iii) Synthesis of Polybenzimidazole (PBImz):

Polyphosphoric acid (PPA) was used to synthesise **PBImz** by solution polycondensation method. PPA was used as a condensation agent as well as polymerization solvent.[33, 42] A three-necked flask was taken fitted with an overhead stirrer with nitrogen (N_2) inlet and $CaCl_2$ drying tube. 150 g of PPA was taken in the three neck flask and the flask temperature was increased slowly to 120 °C. 3, 3'-Diaminobenzidine (DAB) (5.0 g, 2.33 x 10^{-2} mol) was added to PPA and stirred for an hour. Dicarboxylic acid (3.87 gm, 2.33 x 10^{-2} mol) was added to that resultant viscous mixture. Temperature of the reaction mixture was slowly raised to 170 °C and stirred further for 5 h at this temperature. Again temperature was further increased to 200 °C and stirred for 12 h. After completion of the polymerization, viscous solution was added to stirred water. The resultant polymer fiber was washed thoroughly with water till the pH became near to neutral. The fibrous polymer was dipped in 10% aqueous $NaHCO_3$ for overnight to extract any small amounts of acid left in the polymer. Afterwards the polymer fiber was again washed with fresh water until the pH became neutral. The resultant polymer was further stirred in acetone for 12 h to extract the water. Acetone washed polymer was put in vacuum oven for 72 h at 110 °C. The final **PBImz** polymer was characterized by ^{1}H and ^{13}C NMR, FT-IR spectroscopic techniques. Molecular weight was determined with the help of viscosity measurement procedure. Yield = 60%. FT-IR (KBr Palate, cm^{-1}) = 3610, 3399, 3144, 3050, 2956, 2893, 2525, 2321, 1960, 1883, 1618, 1533, 1437, 1407, 1372, 1282, 1227, 1174, 1101, 968, 955, 901, 856, 798, 689. ^{1}H NMR (400 MHz, DMSO-d_6, δ): 13.27 (s, 1H); 9.16 (t, 1H); 8.31 (m, 2H); 8.03 (s, 1H); 7.84-7.61 (m, 6H) ppm. ^{13}C NMR (400 MHz, DMSO-d_6, δ): 151.41, 144.58, 143.18, 135.97, 134.56, 130.99, 129.69, 121.79, 119.18, 117.02, 111.83, 109.54 ppm. Molecular weight of **PBImz** (Viscosity measurement method, Solvent used conc. H_2SO_4), $\mathbf{M_w} \cong 98000$ (with respect to $\boldsymbol{\eta_{red}}$ =1.704).

(iv) Synthesis of Composite (PBI-NMI)$_{1:0.5}$:

PBImz (2 mole) and **NMI** (1 mole) were taken in a one necked RB flask under nitrogen (N_2) atmosphere. Dry DMSO was added to the solid mixture and heated up to 65 °C and stirred further for 24 h at this temperature under N_2 atmosphere. After composite formation solvent was evaporated on hot plate and dry film was kept in vacuum oven at 80 °C for 3 days. Dry film was used further for characterization.

(v) Synthesis of Composite (PBImz-NMI)$_{1:1}$:

1 mole each of **PBImz** and **NMI** were taken and procedure was same as described above.

(vi) Synthesis of Composite (PBImz-NMI)$_{1:2}$:

1 mole of **PBImz** and 2 moles of **NMI** were taken and followed the same procedure as described above.

(vii) Synthesis of Composite (PBImz-NDI)$_{1:0.5}$:

2 moles of **PBImz** and 1 mole of **NDI** were taken and followed the same procedure as described above for the Synthesis of Composite **(PBImz-NMI)$_{1:0.5}$.**

(viii) Synthesis of Composite (PBI-NDI)$_{1:1}$:

1 mole each of **PBImz** and **NDI** were taken and followed the same procedure as described above.

(ix) Synthesis of Composite (PBImz-NDI)$_{1:2}$:

1 mole of **PBImz** and 2 moles of **NDI** were taken and followed the same procedure as described above.

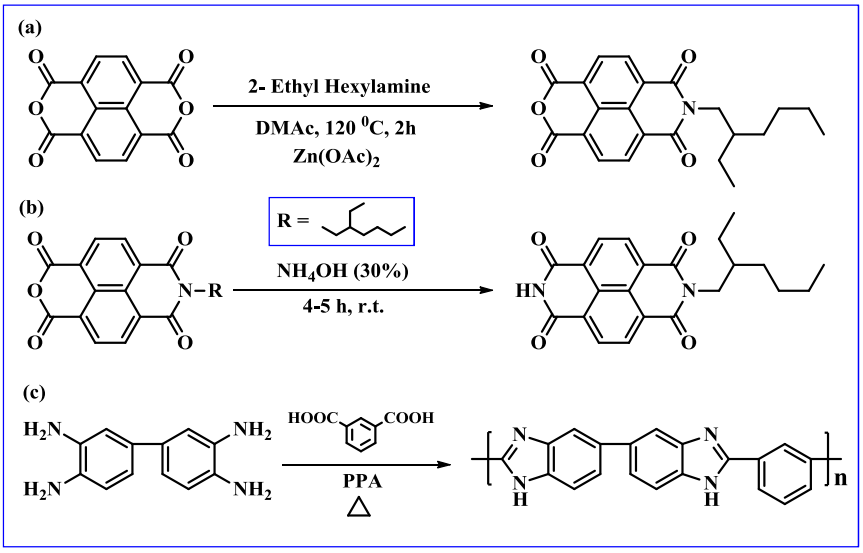

Scheme 2.1: Synthesis of (a) **NMI**, (b) **NDI** and (c) **PBImz**

2.4 Results and Discussion

2.4.1 Synthesis and Characterization

NMI, **NDI** and **PBImz** were synthesised as depicted in scheme 2.1. The detailed synthetic procedures are given in section 2.3.5. As shown in scheme 2.2, the 1:1 composites were prepared by dissolving equal mole ratios of **PBImz** and **NMI** or **NDI** in dry dimethyl sulfoxide (DMSO). The resultant solution was heated and stirred at 65 °C for 24 h under nitrogen (N_2) atmosphere. The hot solution was filtered into petri dish; the free standing composite film was obtained after complete evaporation of DMSO at 75 °C. The composites incorporating higher and lower content of **NMI** and **NDI** (1:2 and 1:0.5) were also prepared. However, the higher **NMI** and **NDI** containing composites (1:2) were brittle in nature compared to 1:1 and 1:0.5. The **NMI/NDI** small molecules were structurally characterized by ^{1}H NMR (figure 2.1a, 2.1b) and FT-IR spectroscopy and the purity was confirmed from the elemental analysis. ^{1}H NMR spectra of all the composites, **PBImz**, **NMI** and **NDI** were recorded at room temperature by dissolving in deuterated dimethyl sulfoxide (DMSO-d_6). Figure 2.2 shows the expanded ^{1}H NMR spectra of 1:0.5, 1:1 and 1:2 composite named as **(PBImz-NMI)$_{1:0.5}$**, **(PBImz-NMI)$_{1:1}$**, **(PBImz-NMI)$_{1:2}$** along with **NMI** and **PBImz**. The polymer **PBImz** exhibited bunch of proton signals in the aromatic region at 9.16 (singlet), 8.31 (multiplet), 8.30 (singlet), 7.84 (multiplet), 7.64 (multiplet) ppm.[43], whereas **NMI** showed single peak at 8.69 ppm corresponding to the aromatic core proton. Upon composite formation the ^{1}H NMR spectra of **(PBImz-NMI)$_{1:1}$** showed considerable peak broadening compared to **PBImz** and **NMI** alone,

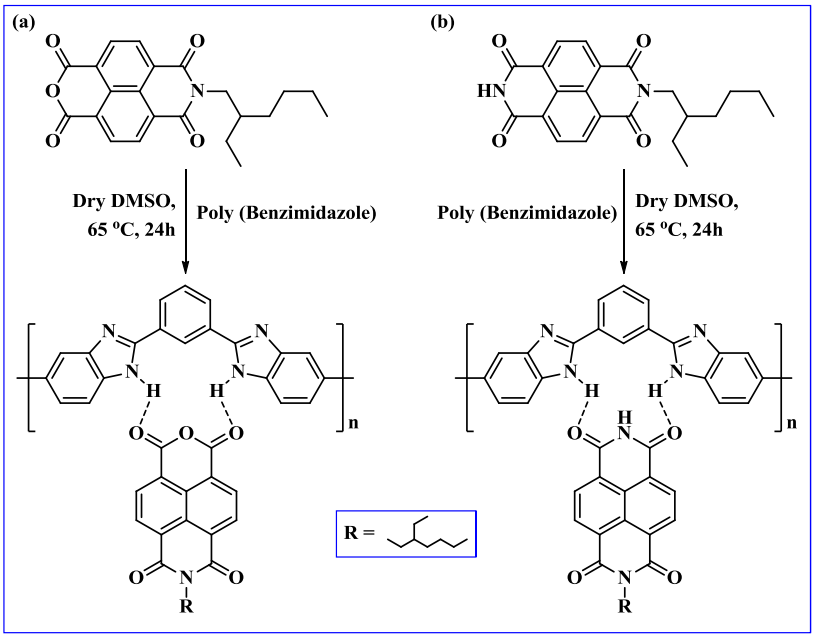

Scheme 2.2: Preparation of (a) **PBImz-NMI** and (b) **PBImz-NDI** composites.

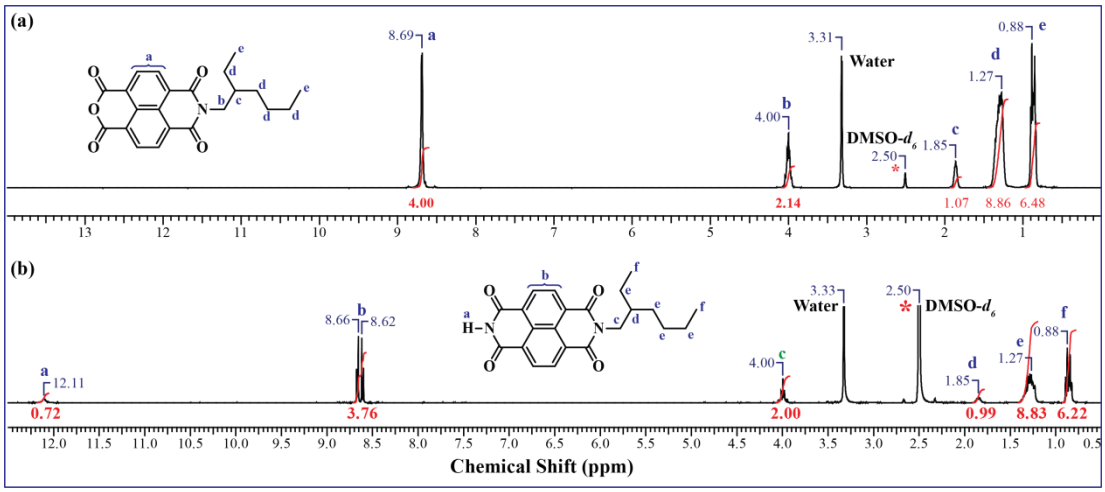

Figure 2.1: ^{1}H NMR spectra of (a) **NMI** and (b) **NDI** in DMSO-d_6.

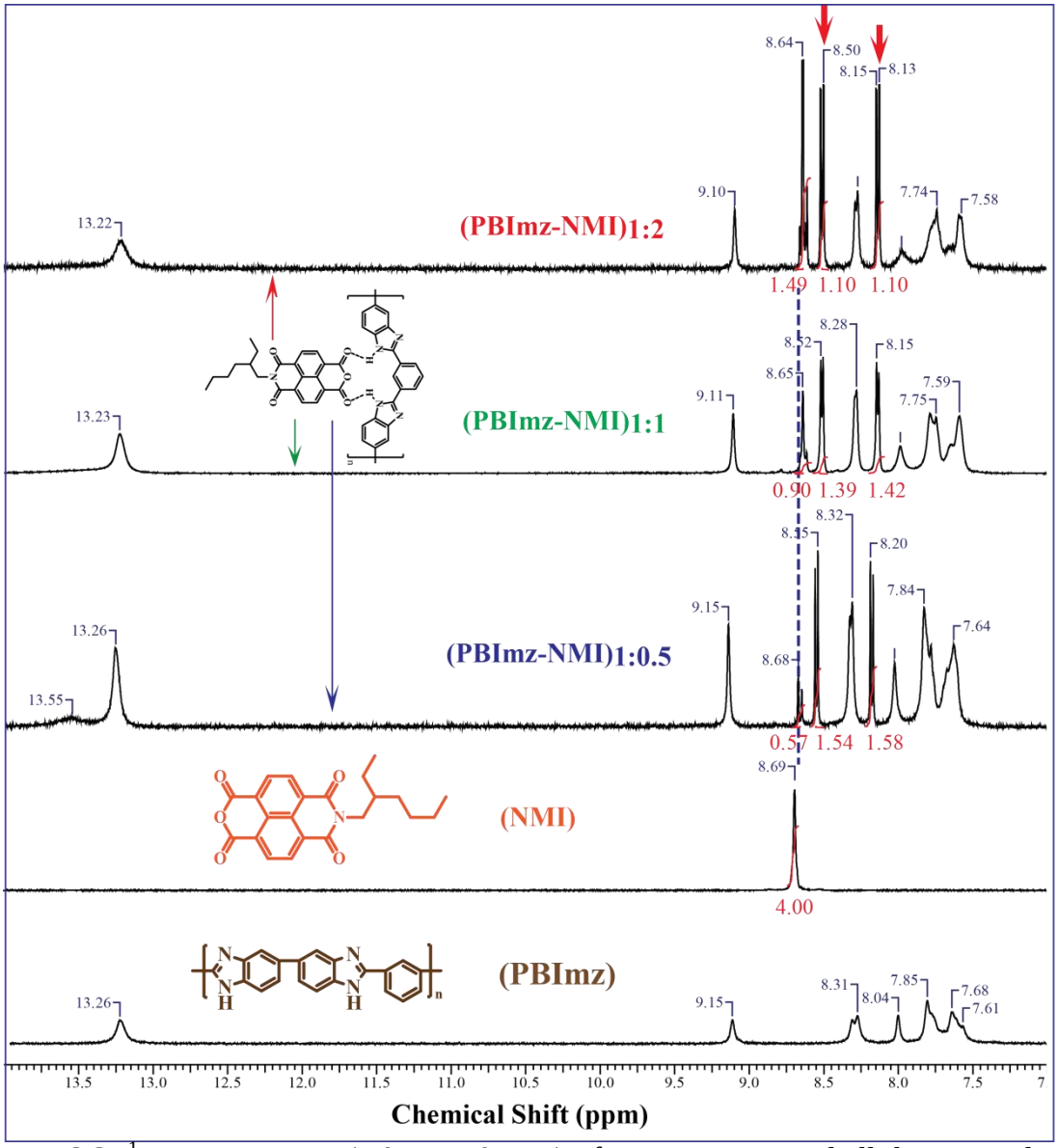

Figure 2.2: ^{1}H NMR spectra (7.0 to 14.0 ppm) of **PBImz**, **NMI** and all three complexes **(PBImz-NMI)$_{1:0.5}$**, **(PBImz-NMI)$_{1:1}$** and **(PBImz-NMI)$_{1:2}$**.

which indicated that successful composite formation has occurred in solution. Furthermore, two new high intensity peaks appeared in the spectrum at 8.56 (doublet) and 8.19 (doublet) ppm. Composite **(PBImz-NMI)$_{1:2}$** and **(PBImz-NMI)$_{1:3}$** also exhibited similar behaviour like **(PBImz-NMI)$_{1:1}$**. These two new peaks in composite could be assigned to aggregates of **NMI** which occurred due to interaction of **NMI** in **PBImz** matrix through hydrogen bonding. The inner aromatic core proton of aggregated **NMI** appeared at lower ppm (8.56 and 8.19) value compared to free **NMI** (8.69 ppm). Moreover, the number of aromatic protons of **NMI** (4 protons) at 8.69 ppm were drastically reduced with concomitant increase in number of protons for aggregated **NMI** which confirmed the existence of more aggregated **NMI** species in composite. The above evidence clearly confirmed the formation of **NMI/PBImz** composite through hydrogen bonding which was stable in solution. **PBImz-NDI** composites did not exhibit the same kind of behaviour like **NMI/PBImz** composite. Figure 2.3 compares the expanded ^{1}H NMR spectra of 1:0.5 [**(PBImz-NDI)$_{1:0.5}$**], 1:1 [**(PBImz-NDI)$_{1:1}$**] and 2:1 [**(PBImz-NDI)$_{1}$**

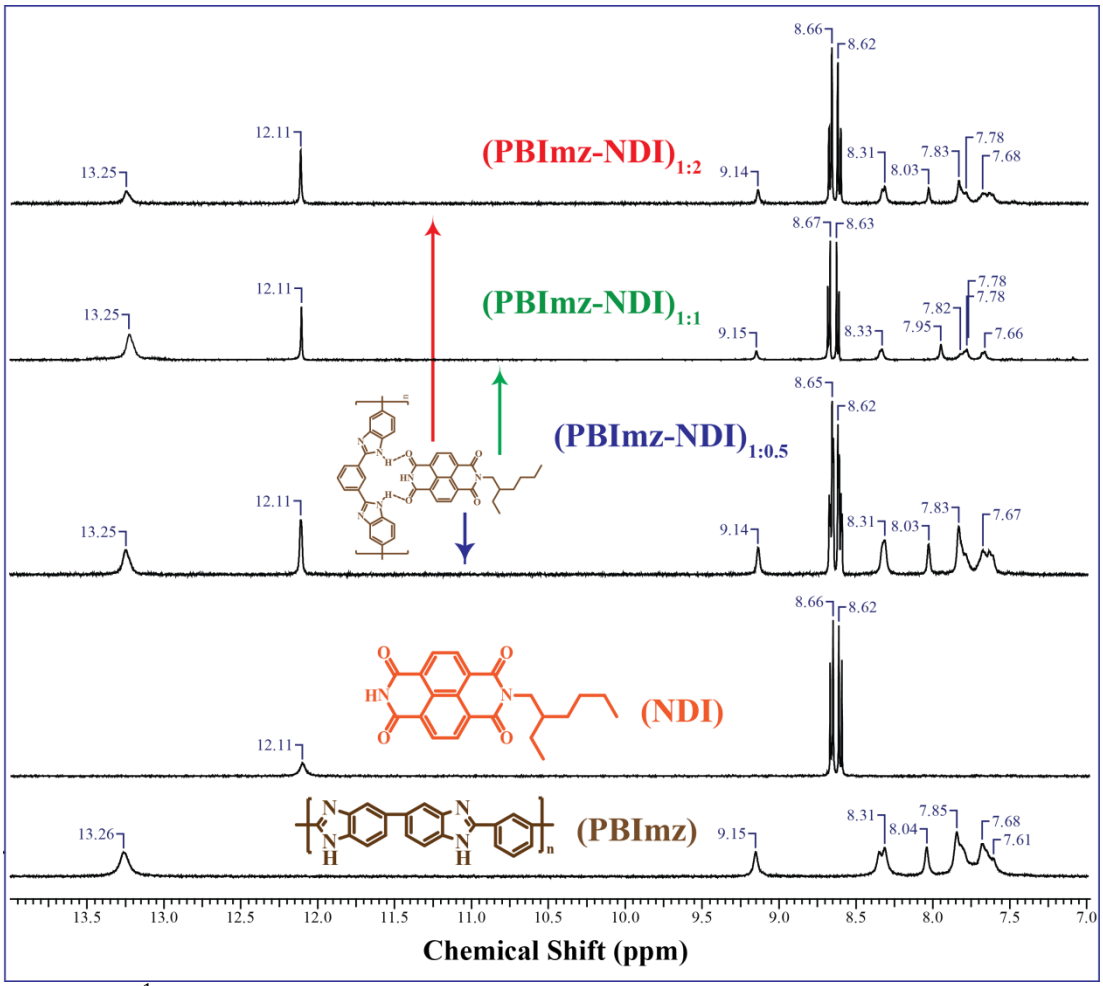

Figure 2.3: ^{1}H NMR spectra (7.0 to 14.0 ppm) of **PBImz**, **NDI** and all three complexes **(PBImz-NDI)$_{1:0.5}$**, **(PBImz-NDI)$_{1:1}$** and **(PBImz-NDI)$_{1:2}$**.

$_{:2}$] composites along with pristine **NDI** and **PBImz**. The aromatic protons of **NDI** appeared at 8.66 ppm as doublet of doublet which remained intact after composite formation between **NDI** and **PBImz**. None of the three composites showed any significant changes in the spectra. No peak corresponding to **NDI** aggregates appeared upon complex formation as was observed for the NMI complex. This clearly indicated that with little variation in structure from **NMI** to **NDI** the interaction pathway with **PBImz** has been changed significantly.

To obtain further insight into the supramolecular interaction between **PBImz-NMI** and **PBImz-NDI** composites in solid state, the composite films were characterized by FT-IR spectroscopy. Figure 2.4a and 2.4b shows the FT-IR spectra of **PBImz**, **NMI** and all three composites **(PBImz-NMI)$_{1:0.5}$**, **(PBImz-NMI)$_{1:1}$** and **(PBImz-NMI)$_{1:2}$**. FT-IR spectra of **NMI** showed four major peaks at 1793 cm^{-1}, 1761 cm^{-1}, 1708 cm^{-1} and 1668 cm^{-1} in the functional group region for (C=O) stretching vibration. They were assigned as belonging to two types of carbonyl groups present in **NMI**; the high frequency peaks at 1793 cm^{-1} and 1761 cm^{-1} were assigned for the (C=O) group of anhydride linkage and the lower frequency peaks at 1708 cm^{-1} and 1668 cm^{-1} corresponded to (C=O) group of imide linkage. The parent polymer **PBImz** did not have IR absorption in the functional group region (1800 cm^{-1} to 1650 cm^{-1}). The anhydride carbonyl groups of **NMI** was more accessible to form hydrogen bonding with (N-H) moiety of **PBImz** as compared to the more sterically hindered (2-ethylhexyl) imide carbonyl. As expected, upon composite formation the peaks corresponding to anhydride carbonyl (1793 cm^{-1} and 1761 cm^{-1}) shifted to lower frequency (1787 cm^{-1} and 1751 cm^{-1}) in **(PBImz-NMI)$_{1:1}$** composite, whereas peaks at 1708 cm^{-1} and 1668 cm^{-1} for imide carbonyl did not shift reasonably which confirmed the selective interaction of anhydride carbonyl group with **PBImz**. Similar results were also obtained for other composites incorporating lower and higher amounts of **NMI**; **(PBImz-NMI)$_{1:0.5}$** and **(PBImz-NMI)$_{1:2}$** as depicted in figure 2.4a. The supramolecular interaction in composite was further analysed by monitoring N-H stretching frequency of **PBImz** between 3600-3000 cm^{-1} (figure 2.4b). As shown in figure 2.4b, **PBImz** exhibited two absorption for N-H stretching frequency; one broad absorption at 3144 cm^{-1} for intermolecular hydrogen bonded N-H group and another relatively sharp absorption at 3410 cm^{-1} for free N-H group[44], **NMI** did not show absorption in this region (3144 cm^{-1} and 3410 cm^{-1}). Interestingly, the N-H peak for self-associated **PBImz** (intermolecular hydrogen bonding) disappeared in composite which gave clear evidence for interaction of imide (N-H) with **NMI**. Figure 2.4c and 2.4d

compares the FT-IR spectra of all three **PBImz-NDI** composites along with **PBImz** and **NDI**. FT-IR spectra of **NDI** showed two major absorption at 1691 cm^{-1}, 1649 cm^{-1} in the functional group region for (C=O) stretching vibration. Upon composite formation the peaks corresponding to imide carbonyl (1691 cm^{-1} and 1649 cm^{-1}) shifted to higher frequency (1698 cm^{-1} and 1659 cm^{-1}) in all three composites of **PBImz** and **NDI**. Similarly, N-H stretching frequency of **PBImz** between 3600-3000 cm^{-1} (figure 2.4d) showed a shift in absorption for free N-H stretching vibration (3410 cm^{-1}) in IR spectrum.

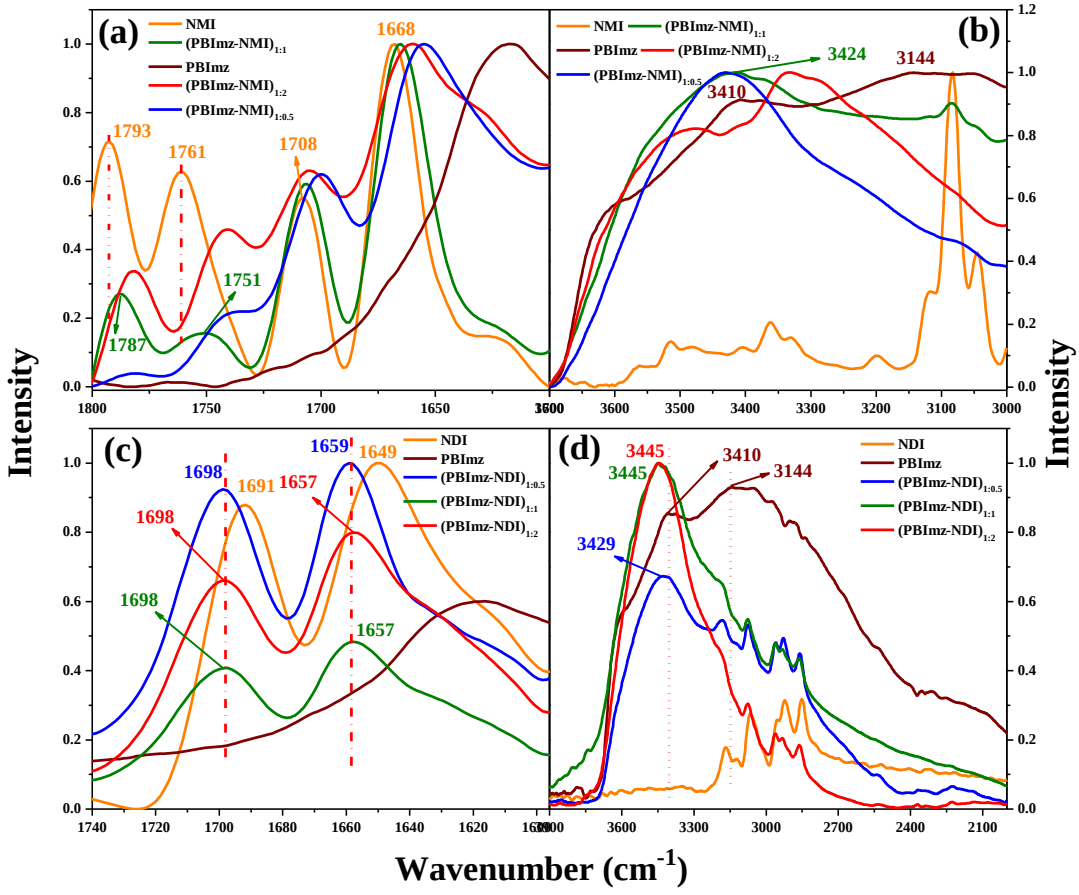

Figure 2.4: Comparison of FT-IR of (a-b) **NMI**, **(PBImz-NMI)$_{1:0.5}$**, **(PBImz-NMI)$_{1:1}$** and **(PBImz-NMI)$_{1:2}$** and (c-d) **NDI**, **(PBImz-NDI)$_{1:0.5}$**, **(PBImz-NDI)$_{1:1}$** and **(PBImz-NDI)$_{1:2}$** with **PBImz**.

Intermolecular hydrogen boding is known to impart inherent rigidity to **PBImz** chain. However, upon disruption of self-association of **PBImz** by interaction with **NMI** or **NDI**, the composites lost rigidity which was evident from thermogravimetric analysis (TGA). The TGA curve shown in figure 2.5a for composites **(PBImz-NMI)$_{1:0.5}$**, **(PBImz-NMI)$_{1:1}$** and **(PBImz-NMI)$_{1:2}$** depicts the decomposition occurring at relatively lower

temperature than pristine **PBImz**. Similarly, all three composites made from **PBImz** and **NDI** showed a decrease in decomposition temperature compared to pristine **PBImz** in TGA analysis (figure 2.5b).

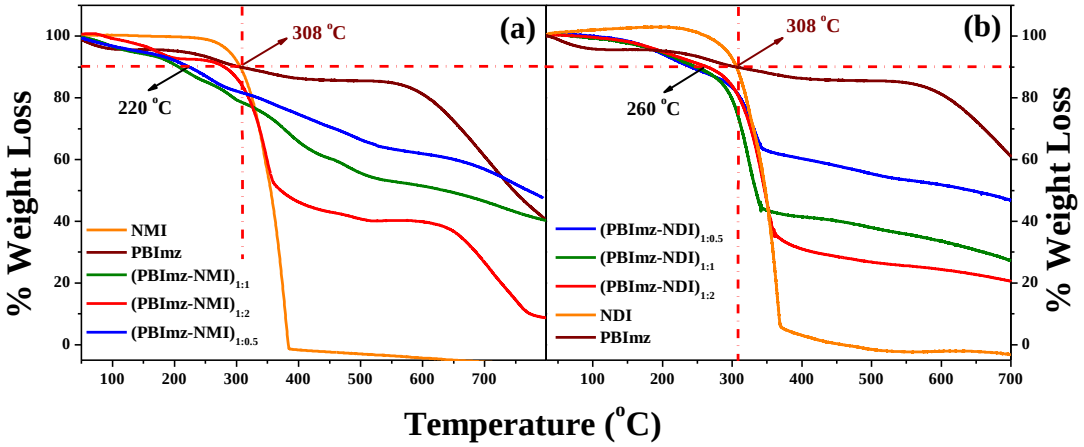

Figure 2.5: Thermogravimetric analysis of **PBImz**, (a) **NMI**, **(PBImz-NMI)$_{1:0.5}$**, **(PBImz-NMI)$_{1:1}$** and **(PBImz-NMI)$_{1:2}$** and (b) **NDI**, **(PBImz-NDI)$_{1:0.5}$**, **(PBImz-NDI)$_{1:1}$** and **(PBImz-NDI)$_{1:2}$**.

2.4.2 Micro Structure Analysis

Molecular packing and crystalline nature of composite was analysed by wide angle X-ray diffraction (WXRD). The measurement was carried out for the free standing films of all composites and **PBImz** whereas the powder WXRD was recorded for **NMI** and **NDI**. Figure 2.6a shows the 1D WXRD patterns of all composites of **NMI** with **PBImz** along with **PBImz** and **NMI**. **NMI** (Figure 2.6a) and **NDI** (Figure 2.6b) showed multiple and intense peaks in WXRD which indicated their high crystalline nature. On the other hand, **PBImz** exhibited typical amorphous nature which was evident from the broad peak at 2θ ≅ 20° in WXRD. However, the composite showed relatively high intense peaks in WXRD. It showed two major peaks, out of which the new peak that appeared at 2θ ≅ 25° was not present in pristine **NMI** and accounted for strong π-π interaction between **NMI** aromatic cores in composite. It is to be noted that the hydrogen bond association between **PBImz** and **NMI** drove the **NMI** core to form large aggregates in composite via π-π stacking. Furthermore, low *d* spacing value (3.38 Å; 2θ = 26.34) calculated for π-π stacking distance in 1:1 composite indicated better electronic coupling between **NDI** cores. The composite incorporating lower and higher content of **NMI** showed π-π stacking peak along with slight change in *d* spacing value (3.36 Å and 3.43 Å at 2θ = 26.51° and 25.93°). The WXRD pattern obtained for **PBImz-NDI** complexes showed

similar kind of diffraction pattern with pristine **NDI** molecule (figure 2.6b). All the three composites **(PBImz-NDI)$_{1:0.5}$**, **(PBImz-NDI)$_{1:1}$** and **(PBImz-NDI)$_{1:2}$** showed multiple diffraction peaks in the WXRD window which confirmed their crystalline nature. However, π-π stacking was not observed (encircled region in figure 2.6b) in **PBImz-NDI** composites as well as pristine **NDI** molecule. This clearly indicated that strong π-π interaction was present in **PBImz-NMI** composite which helped it to form better aggregates of **NMI** in the **PBImz** backbone whereas, it was absent in **PBImz-NDI** composite system.

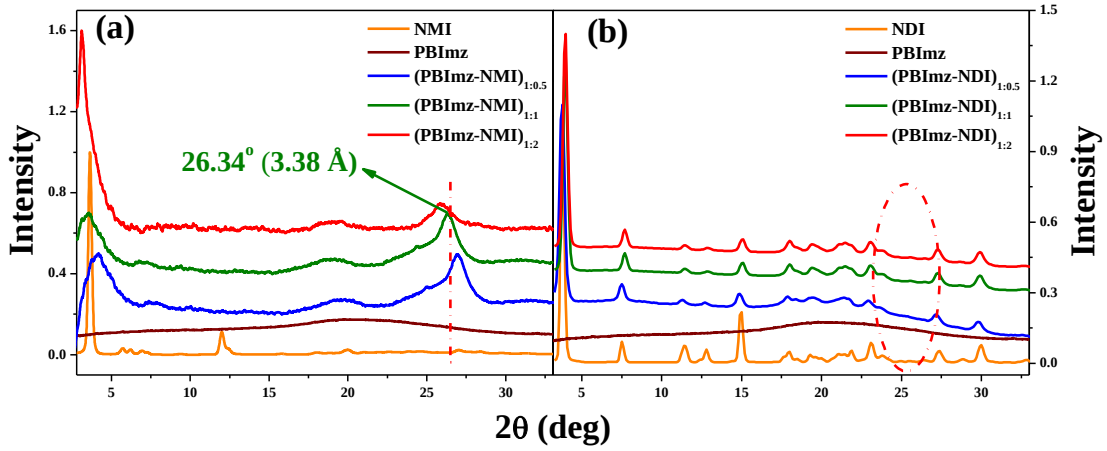

Figure 2.6: WXRD pattern of **PBImz**, (a) **NMI**, **(PBImz-NMI)$_{1:0.5}$**, **(PBImz-NMI)$_{1:1}$** and **(PBImz-NMI)$_{1:2}$** and (b) **NDI**, **(PBImz-NDI)$_{1:0.5}$**, **(PBImz-NDI)$_{1:1}$** and **(PBImz-NDI)$_{1:2}$**.

2.4.3 Thin Film Morphology

Microstructures formed within the composites were characterized by transmission electron microscopy (TEM). Samples were dropcast from DMSO solution (1 mg/ml) onto copper grids. Figure 2.7 and figure 2.8 depicts the TEM images of all **PBImz-NMI** and **PBImz-NDI** composites along with pristine **NMI**, **NDI** and **PBImz** on copper grid. The samples were air dried followed by drying in vacuum oven at 75 °C for 12 h to remove all traces of solvent. **NMI** and **NDI** showed large plate like crystalline morphology (figure 2.8e-f and figure 2.8g-h). On the other hand, all the **PBImz-NMI** composites **(PBImz-NMI)$_{1:0.5}$**, **(PBImz-NMI)$_{1:1}$** and **(PBImz-NMI)$_{1:2}$** exhibited uniform nano-spherical morphology (figure 2.7a-l), whereas **PBImz-NDI** composites exhibited fused spherical

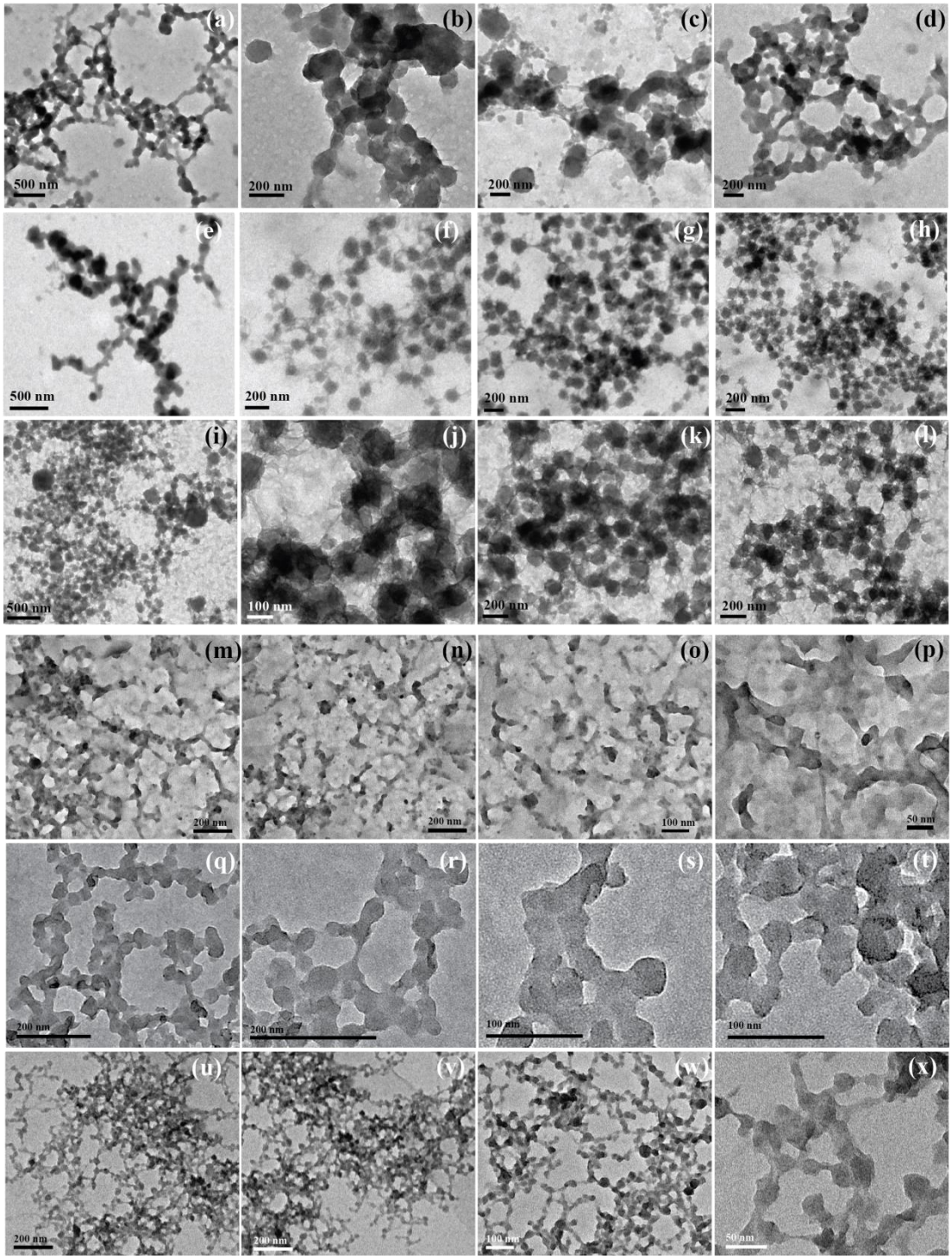

Figure 2.7: TEM images of (a-d) **(PBImz-NMI)$_{1:0.5}$**, (e-h) **(PBImz-NMI)$_{1:1}$**, (i-l) **(PBImz-NMI)$_{1:2}$**, (m-p) **(PBImz-NDI)$_{1:0.5}$**, (q-t) **(PBImz-NDI)$_{1:1}$** and (u-x) **(PBImz-NDI)$_{1:2}$** dropcast from DMSO.

morphology (figure 2.7m-x) under TEM. The nano-sphere exhibited average size of ~ 30-100 nm in all **PBImz-NMI** and **PBImz-NDI** composites. The formation of nano-spheres in **PBImz-NMI** composite was accounted by hydrogen bonding interaction and

self-aggregation of **NMI** core due to π-π stacking. The significant change in morphology for all the composites compared to their respective pristine state confirmed the formation of hydrogen bonded composites between small molecule (**NMI** or **NDI**) and **PBImz**.

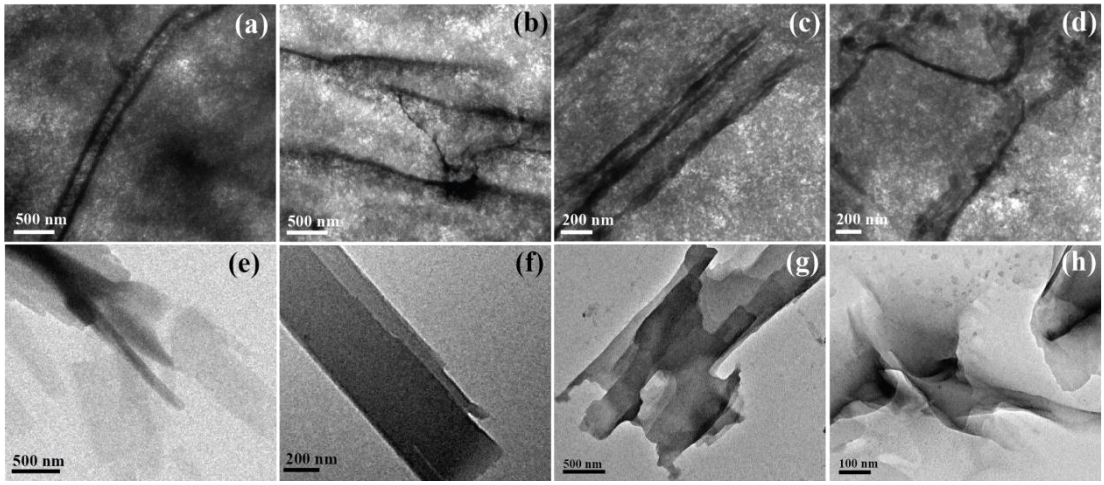

Figure 2.8: TEM images of (a-d) **PBImz**, (e-f) **NMI** and (g-h) **NDI** dropcast from DMSO.

2.4.4 Charge Carrier Mobility Using Space Charge Limited Current (SCLC) Measurements

The semiconducting behaviour of nano-composites was characterized by measuring the bulk electron conductivity. Electron mobility was measured via space charge limited current (SCLC) method with device configuration **Al/ active layer/ Al** structure. Samples (pristine **NMI/NDI** and the corresponding supramolecular complexes) were prepared from DMF at a concentration of 12 mg/ml, filtered through PTFE (0.45 μm) membrane and drop cast directly on the aluminium coated substrate to get smooth films with average thickness of ~ 1.5-2.0 microns. An average of 3 to 4 devices were prepared and used for measurement for each individual samples. The summary of device parameters including film thickness and maximum and average electron mobility obtained from SCLC are given in table 2.1. The measurement was done for **(PBImz-NMI)$_{1:1}$** composite and **NMI** small molecule whereas, **(PBImz-NDI)$_{1:1}$** composite short circuited as they did not form uniform films on the aluminium coated substrate. Therefore, OFET measurement was carried out for **NDI** and **(PBImz-NDI)$_{1:1}$** composite. OFET was fabricated with device configuration **Au/ active layer/ polystyrene/ SiO_2/ Si** structure. The **(PBImz-NDI)$_{1:1}$** composite showed the OFET mobility in the order of 10^{-5} cm^2/Vs (table 2.2) which is one

order less with respect to pristine **NDI** small molecule. The **(PBImz-NMI)$_{1:1}$** composite and **NMI** were drop casted from DMSO and sandwiched between two aluminium electrodes. The obtained J-V characteristics are shown in figure 2.9 and values are tabulated in table 2.1. **NMI** small molecule exhibited very poor film forming ability; however few devices could be measured, which showed average SCLC electron mobility in the order of 10^{-7} cm^2/Vs. The composite **(PBImz-NMI)$_{1:1}$** showed good film forming ability over a large area and exhibited electron mobility of 1 x 10^{-7} cm^2/Vs, which clearly demonstrated that **NMI** small molecule transferred its semiconducting nature to 1:1 polymer composite while retaining the electron mobility in the order of 10^{-7} cm^2/Vs. Pristine **NDI** exhibited mobility in the range of 10^{-4} cm^2/Vs (OFET) whereas pristine **NMI** exhibited mobility in the order of 10^{-7} cm^2/Vs (SCLC) only. However, it is not correct to compare mobilities measured by different techniques as it is known that OFET tends to give higher numbers compared to SCLC.[45, 46] Although both **NMI** and **NDI** formed composites with **PBImz**, based on evidences from ^{1}H NMR, XRD etc., **NMI/PBImz** formed better composites with good film forming property compared to **NDI/PBImz** composites. Therefore, **NMI/PBImz** composites exhibited mobility of the same order as the pristine **NMI**, which was not observed with the **NDI/PBImz** composites.

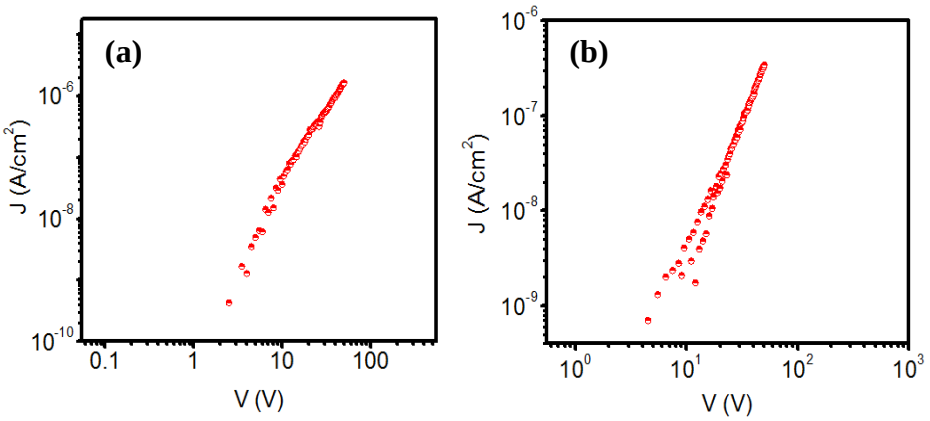

Figure 2.9: J-V characteristics for electron only mobility of (a) **NMI** and (b) **(PBImz-NMI)$_{1:1}$** composite.

Table 2.1: Summary of device parameters of **(PBImz-NMI)$_{1:1}$** composite and **NMI**.

Electron only device with Al/ active layer/ Al			
Sample Name	**Maximum mobility $\mu_{e,max}$ [cm^2/Vs]**	**Average mobility $\mu_{e,avg}$ [cm^2/Vs]**	**Film Thickness [micron]**
NMI	5.3 x 10^{-7}	1.2 x 10^{-7}	1.5-2.0
(PBImz-NMI)$_{1:1}$	1.0 x 10^{-7}	1.0 x 10^{-7}	1.6-2.0

Table 2.2: OFET characteristics of **(PBImz-NDI)$_{1:1}$** composite and **NDI**.

Electron only device with Au/ active layer/ polystyrene/ SiO_2/ Si			
Sample Name	**Linear regime $\mu_{e,max}$ ($\mu_{e,avg}$) [cm^2/Vs]**	**Saturetion regime $\mu_{e,max}$ ($\mu_{e,avg}$) [cm^2/Vs]**	**I_{ON}/I_{OFF}**
NDI	8.5 x 10^{-4} (6.28 x 10^{-4})	7.1 x 10^{-4} (4.28 x 10^{-4})	5.8 x 10^5
(PBImz-NDI)$_{1:1}$	4.7 x 10^{-5} (2.5 x 10^{-5})	7.7 x 10^{-5} (5.1 x 10^{-5})	3.5 x 10^4

2.5 Conclusion

In conclusion, a polymer composite comprising of electrically active **NMI** and **NDI** small molecule into **PBImz** matrix via supramolecular interaction was demonstrated. FTIR results showed the evidences of intermolecular hydrogen bonding between **PBImz** and **NMI** and **NDI**. Strong π-π stacking interaction occurring between **NMI** core drove the self-assembly within composites which were stable from solution to solid state. TEM images showed formation of uniform nano-spherical morphology. **PBImz/NMI** nano-composite was capable to form large area free standing film with semiconducting property. To the best of our knowledge this is the first demonstration of using commercially important **PBImz** polymer to from composite with organic semiconducting molecule. The semiconducting property could be further improved by applying this strategy to form composites of other wide range rylenemonoimides including perylenemonoimide with **PBImz**.

2.6 References

1. Cao, W.; Li, J.; Chen, H.; Xue, J. *J. Photonics Energy* **2014**, *4*, 40990.

2. Guo, X.; Liu, X.; Lin, F.; Li, H.; Fan, Y.; Zhang, N. *Sci. Rep.* **2015**, *5*, 10569.

3. Lee, J.; Han, A. R.; Yu, H.; Shin, T. J.; Yang, C.; Oh, J. H. *J. Am. Chem. Soc.* **2013**, *135*, 9540–9547.

4. Liu, Y.; Xie, Y.; Liu, Y.; Song, T.; Zhang, K.-Q.; Liao, L.; Sun, B. *Semicond. Sci. Technol.* **2015**, *30*, 104004.

5. Luo, C.; Kyaw, A. K. K.; Perez, L. A.; Patel, S.; Wang, M.; Grimm, B.; Bazan, G. C.; Kramer, E. J.; Heeger, A. J. *Nano Lett.* **2014**, *14*, 2764–2771.

6. Marder, S. R.; Kippelen, B.; Jen, A. K.-Y.; Peyghambarian, N. *Nature* **1997**, *388*, 845–851.

7. Mariani, P.; Vesce, L.; Di Carlo, A. *Semicond. Sci. Technol* **2015**, *30*, 104003.

8. Nathan, A.; Ahnood, A.; Cole, M. T.; Lee, S.; Suzuki, Y.; Hiralal, P.; Bonaccorso, F.; Hasan, T.; Garcia-Gancedo, L.; Dyadyusha, A.; Haque, S.; Andrew, P.; Hofmann, S.; Moultrie, J.; Chu, D.; Flewitt, A. J.; Ferrari, A. C.; Kelly, M. J.; Robertson, J.; Amaratunga, G. A. J.; Milne, W. I. *Proc. IEEE* **2012**, *100*, 1486–1517.

9. Ong, B. S.; Wu, Y. L.; Liu, P.; Gardner, S. *J. Am. Chem. Soc.* **2004**, *126*, 3378–3379.

10. Schroeder, B. C.; Chiu, Y.-C.; Gu, X.; Zhou, Y.; Xu, J.; Lopez, J.; Lu, C.; Toney, M. F.; Bao, Z. *Adv. Electron. Mater.* **2016**, *2*, 1600104.

11. Xiao, S.; Liu, C.; Chen, L.; Tan, L.; Chen, Y. *J. Mater. Chem. A* **2015**, *3*, 22316–22324.

12. Zhao, Y.; Zhao, X.; Zang, Y.; Di, C. A.; Diao, Y.; Mei, J. *Macromolecules* **2015**, *48*, 2048–2053.

13. Zhu, B.; Wang, H.; Leow, W. R.; Cai, Y.; Loh, X. J.; Han, M. Y.; Chen, X. *Adv. Mater.* **2016**, *28*, 4250–4265.

14. Halik, M.; Klauk, H.; Zschieschang, U.; Schmid, G.; Radlik, W.; Ponomarenko, S.; Kirchmeyer, S.; Weber, W. *J. Appl. Phys.* **2003**, *93*, 2977–2981.

15. Hamilton, R.; Smith, J.; Ogier, S.; Heeney, M.; Anthony, J. E.; McCulloch, I.; Veres, J.; Bradley, D. D. C.; Anthopoulos, T. D. *Adv. Mater.* **2009**, *21*, 1166–1171.

16. Katz, H. E.; Bao, Z.; Gilat, S. L. *Acc. Chem. Res.* **2001**, *34*, 359–369.

17. Lee, S.; Koo, B.; Shin, J.; Lee, E.; Park, H.; Kim, H. *Appl. Phys. Lett.* **2006**, *88*, 2004–2007.

18. Li, Y. N.; Sonar, P.; Murphy, L.; Hong, W. *Energy Environ. Sci.* **2013**, *6*, 1684–1710.

19. Lin, Y.; Li, Y.; Zhan, X. *Chem. Soc. Rev.* **2012**, *41*, 4245.

20. Mas-Torrent, M.; Rovira, C. C. *Chem. Soc. Rev.* **2008**, *37*, 827–838.

21. Sun, Y.; Welch, G. C.; Leong, W. L.; Takacs, C. J.; Bazan, G. C.; Heeger, A. J. *Nat. Mater.* **2011**, *11*, 44–48.

22. Takimiya, K.; Shinamura, S.; Osaka, I.; Miyazaki, E. *Adv. Mater.* **2011**, *23*, 4347–4370.

23. Yoon, S.; Cho, J.; Yu, S. H.; Son, H. J.; Chung, D. S. *Org. Electron.* **2016**, *34*, 28–32.

24. Horowitz, G.; Hajlaoui, M. E.; Hajlaoui, R. *J. Appl. Phys.* **2000**, *87*, 4456.

25. Jimison, L. H.; Toney, M. F.; McCulloch, I.; Heeney, M.; Salleo, A. *Adv. Mater.* **2009**, *21*, 1568–1572.

26. Salleo, A. *Mater. Today* **2007**, *10*, 38–45.

27. Schön, J. .; Kloc, C.; Batlogg, B. *Org. Electron.* **2000**, *1*, 57–64.

28. Narayan, R.; Kumar, P.; Narayan, K. S.; Ashe, S. K. *J. Mater. Chem. C* **2014**, *2*, 6511–6519.

29. Narayan, R.; Kumar, P.; Narayan, K. S.; Asha, S. K. *Adv. Funct. Mater.* **2013**, *23*, 2033–2043.

30. Rancatore, B. J.; Mauldin, C. E.; Tung, S. H.; Wang, C.; Hexemer, A.; Strzalka, J.; Fréchet, J. M. J.; Xu, T. *ACS Nano* **2010**, *4*, 2721–2729.

31. Saibal, B.; Chithiravel, S.; Asha, S. K. *J. Polym. Sci. Part A Polym. Chem.* **2016**, *54*, 2403–2412.

32. Saibal, B.; Ashar, A. Z.; Devi, R. N.; Narayan, K. S.; Asha, S. K. *ACS Appl. Mater. Interfaces* **2014**, *6*, 19434−19448.

33. Board, E.; Long, L. T. E.; Voit, T. B. *Advances in Polymer Science* **2008**, 63-124.

34. Guo, C.; Zhou, L.; Lv, J. *Polym. Polym. Compos.* **2013**, *21*, 449–456.

35. Li, Q.; Jensen, J. O.; Savinell, R. F.; Bjerrum, N. J. *Prog. Polym. Sci.* **2009**, *34*, 449–477.

36. Tsur, Y.; Levine, H. H.; Levy, M. **1974**, *12*, 1515–1529.

37. Jones, D. J.; Rozière, J. *J. Memb. Sci.* **2001**, *185*, 41–58.

38. Smitha, B.; Sridhar, S.; Khan, A. A. *J. Memb. Sci.* **2005**, *259*, 10–26.

39. Xiao, L.; Zhang, H.; Jana, T.; Scanlon, E.; Chen, R.; Choe, E. W.; Ramanathan, L. S.; Yu, S.; Benicewicz, B. C. *Fuel Cells* **2005**, *5*, 287–295.

40. Suryani; Chang, C.-M.; Liu, Y.-L.; Lee, Y. M. *J. Mater. Chem.* **2011**, *21*, 7480–7486.

41. Wang, Y.; Shi, Z.; Fang, J.; Xu, H.; Yin, J. *Carbon* **2011**, *49*, 1199–1207.

42. Xiao, L.; Zhang, H.; Scanlon, E.; Ramanathan, L. S.; Choe, E.-W.; Rogers, D.; Apple, T.; Benicewicz, B. C. *Chem. Mater.* **2005**, *17*, 5328–5333.

43. Ainla, A. 2006, 1-43.

44. Musto, P.; Karasz, F. E.; MacKnight, W. J. *Macromolecules* **1991**, *24*, 4762–4769.

45. Tanase, C.; Meijer, E. J.; Blom, P. W. M.; De Leeuw, D. M. *Phys. Rev. Lett.* **2003**, *91*, 21660(1-4).

46. Mueller, C. J.; Singh, C. R.; Fried, M.; Huettner, S.; Thelakkat, M. *Adv. Funct. Mater.* **2015**, *25*, 2725–2736.

Chapter 3

Improved Charge Carrier Mobility in Liquid Crystalline Supramolecular Crosslinked Polymer Complexes of Ditopic Rylenebisimides and P4VP

3.1 Abstract

Pentadecyl phenol substituted ditopic hydrogen bonding acceptors perylenebisimide and naphthalenebisimide (**PBI-PDP** and **NBI-PDP**) were synthesised to form supramolecular crosslinked network with poly(4-vinyl pyridine) (P4VP). The pristine **PBI-PDP** was grown as single crystals from DCM-MeOH (dichloromethane-methanol) mixture at room temperature, which revealed a $P2_1$ space group. Single crystal assembly of **PBI-PDP** did not show any π-π interaction as the alkyl chains of pentadecyl phenol shielded the aromatic perylene core from both sides. Thermotropic liquid crystalline phase was observed for **NBI-PDP**, whereas both **NBI-PDP** and **PBI-PDP** exhibited lyotropic liquid crystalline behaviour in tetrahydrofuran (THF). The liquid crystalline phases were characterized by differential Scanning Calorimeter (DSC), polarized light microscopy (PLM) and X-ray diffraction (XRD) studies. Supramolecular crosslinked polymer networks (**P4VP-PBI** and **P4VP-NBI**) made from hydrogen bonding interaction of **PBI-PDP** or **NBI-PDP** with P4VP preserved the liquid crystalline phases in THF. Thin film morphology revealed the presence of layer structure of **P4VP-PBI** and **P4VP-NBI** complexes dropcasted from DMF. The charge carrier mobility was measured for the P4VP complexes via space charge limited current (SCLC) measurement technique which showed a two order increase in the electron mobility with respect to their pristine states.

3.2 Introduction

Solution processable nanostructured functional materials are the building blocks for organic and large area electronics. Organic semiconducting materials based on small molecules have many advantages over their polymeric analogue like high purity, well defined structure and strong tendency to crystallize. Therefore it is highly desirable to develop polymeric materials with better organization of the desired semiconductors to improve the device performance. Noncovalent interactions like hydrogen bonding is one of the important approaches to build a supramolecular polymer network with the help of crosslinkable building blocks.[1-7] Multifunctional small molecules with complimentary functionalities or polymers with supramolecular interacting sites can be the building blocks to make various types of supramolecular structures. Poly(4-vinyl pyridine) is one of the most studied polymer as a building block to form various types of hierarchical structures via noncovalent interaction.[8-16] P4VP is also known to form thermoreversible supramolecular polymer gels with the help of noncovalent interaction through the lone pair of pyridine nitrogen.[17] In most of the cases, supramolecular polymer gels are subjected to test their thermoreversibilities, self-healing abilities etc.[18-21] Less number of reports are there for the supramolecular bulk materials with respect to soft supramolecular gel networks made from the noncovalent interactions. Self-assembly of P4VP with π-conjugated small molecules clearly depicted an enhancement in charge carrier mobility with respect to their pristine small molecular state.[11, 22, 23] Multiple site of interaction between P4VP backbone and semiconducting small molecule helps to build a highly ordered supramolecular polymer network.

Liquid crystalline ordering allows the semiconducting material to self-organize into 2D and 3D arrangements which can improve processability and self-healing properties.[24] The effect of self-assembly on their liquid crystalline phase was explored for the interaction between P4VP and small liquid crystalline molecules.[25-29] The supramolecular polymer network made up of P4VP and ditopic liquid crystalline semiconducting molecule is a very interesting system to study the effect of self-assembly on both liquid crystalline properties as well as charge carrier mobility. In the present chapter, a supramolecular mesogenic crosslinked polymer network was made by hydrogen bonding interaction of symmetric rylenebisimides (**PBI-PDP** and **NBI-PDP**) with Poly(4-vinyl pyridine) (P4VP). This particular work involves the synthesis of symmetric perylenebisimide and naphthalenebisimide with free –OH group at the termini. Mono functionalized Rylenebisimides are well known to form P4VP-rylenebisimide

supramolecular complex with the help of directional hydrogen bonding and π-π interaction which results in lamellar organization with many fold increase in the charge carrier mobility with respect to their pristine small molecular state.[11, 22] The **PBI-PDP** and **NBI-PDP** (the ditopic hydrogen bond donor) acted as supramolecular crosslinking agent to P4VP (the multiple hydrogen bond acceptor) backbone. Solution state mixing of the ditopic hydrogen bond donor (**PBI-PDP** or **NBI-PDP**) and acceptor (P4VP) produced the supramolecular crosslinked polymer network. Complex formation was confirmed by FT-IR spectroscopy. Both the **PBI-PDP** and **NBI-PDP** exhibited mesomorphic behavior which further helped to understand the packing ability of the semiconducting mesogen in supramolecular crosslinked polymer networks. Detailed DSC, POM and XRD were undertaken to understand the packing behavior and micro structure of the supramolecular polymer networks. Transmission electron microscopy (TEM) was used to study the thin film morphology of supramolecular polymer network. The effect of self-organization on bulk mobility was measured via SCLC which showed electron mobility in the order of 10^{-3} and 10^{-4} cm^2/Vs, which were two orders higher in magnitude compared to the pristine rylenebisimide molecules.

3.3 Experimental

3.3.1 Materials:

All the chemicals were purchased from Aldrich and used as received. Analytical grade solvents were used for the synthesis and used after drying. Procedure for the synthesis of the symmetrical perylenebisimide (**PBI-PDP**) and naphthalenebisimide (**NBI-PDP**) are given in scheme 3.1a and scheme 3.1b.

3.3.2 Sample Preparation:

Both small molecules – **PBI-PDP** and **NBI-PDP** and polymer P4VP were dried at 60 °C in vacuum oven for 2 days. **PBI-PDP** and **NBI-PDP** were mixed separately with P4VP in dry DMF and then the resultant solutions were heated up to 55 °C and stirred for 24 hours at this temperature. After completion of 24 hours, solvent was removed by slow evaporation of DMF at 65 °C on a petri dish. The resultant supramolecular polymer complexes were dried further in vacuum oven at 60 °C for 2 days. The dried complexes were stored in desiccator.

3.3.3 Instrumentation Techniques:

Infrared spectra were collected for all the samples using a Bruker α-T spectrophotometer in the range of 4000-400 cm^{-1}. Supramolecular polymer complexes **P4VP-PBI** and **P4VP-NBI** were mixed with KBr to make pellets. ^{1}H NMR spectra were recorded in $CDCl_3$ using Bruker AVAENS 400 MHz spectrophotometer. Chemical shifts (δ) are reported in ppm at 298 K, with trace amount of tetramethylsilane (TMS) as internal standard. MALDI-TOF analysis was carried out on a Voyager-De-STRMALDI-TOF (Applied Biosystems, Framingham, MA, USA) instrument equipped with 337 nm pulsed nitrogen laser used for desorption and ionization. The data was collected in reflector mode with an accelerating voltage of 25 kV. Micromolar solutions of the compound in THF was mixed with 2,5-dihydroxy benzene (DHB) matrix and spotted on stainless steel MALDI plate and dried well. Gel permeation chromatography (GPC) of all samples were performed using Viscotek VE 1122 pump, Viscotek VE 3580 RI detector and Viscotek VE 3210 UV/vis detector in tetrahydrofuran (THF) as a solvent, using polystyrene as standards. Wide Angle X-ray Diffractogram (WXRD) was obtained using a Rigaku, MicroMax-007HF with high intensity Microfocus rotating anode X-ray generator. All the samples were recorded in the (2θ) range of 3–50 degrees and data was collected with the help of Control Win software. A Rigaku, R-axis IV^{++} detector was employed in wide-angle experiments. The radiation used was CuKα (1.54 Å) with a Ni filter, and the data collection was carried out using an Aluminium holder. Transmission Electron microscopy (TEM) was done using an FEI-Tecnai^{TM}-F20 electron microscope operating at 200 kV. The thermal stability of the **PBI-PDP** and **NBI-PDP** were analysed using PerkinElmer STA-6000 thermogravimetric analyser (TGA) under a nitrogen atmosphere from 40–800 °C at a heating rate of 10 °C/min. Differential Scanning colorimetry was done in TA Q10 machine. Indium standard was used to calibrate the DSC instrument before measurement of the sample. Typically 2-3 mg of the powdered **NBI-PDP** sample was taken in an aluminium pan and subjected to DSC analysis at 10 °C /min heating and cooling rates in the temperature range -50 °C to 300 °C under nitrogen (N_2) atmosphere.

3.3.4 SCLC Device Fabrication:

Electron only mobility was measured via SCLC method. The glass substrate was cleaned in distilled water, detergent, deionised water, acetone and isopropyl alcohol for 10-15 min each with ultrasonication. Cleaned glass substrates were dried in oven at 100 °C for about 60 min. Al/active layer/Al diode configuration was used for the measurement of electron

mobilities of the supramolecularly crosslinked polymers and pristine molecules. Supramolecular crosslinked polymers were dissolved in DMF and filtered through PTFE membrane (0.45 micron) and clear solution was then dropcast on Al coated glass substrate to measure electron mobility. The drop casted substrates were annealed on a hot plate at 60 °C for 30 min followed by drying in vacuum at 10^{-1} mbar pressure for 3 hrs. On top of the active layer, Al layer (100 nm thick) was deposited by thermal evaporation in vacuum chamber at 10^{-6} mbar for electron-only device with the help of a shadow mask. The current and voltage (J-V) were measured using an Agilent semiconductor parameter analyser model 4156 C and semiprobe probe station. The Mott-Gurney law was used to extract the electron mobility as follows:

$$J = \varepsilon_0 \varepsilon_r \mu \frac{9V^2}{8L^3}$$

Where ε_0 = permittivity of the free space (8.854 x 10^{-12} F/m); ε_r = relative dielectric constant of the thin film which is assumed to be 3; μ = charge carrier (hole and electron) mobility; V = voltage drop across the device and L = thickness of the organic composite layer.

3.3.5 Synthesis:

(i) Synthesis of Pentadecyl phenol substituted symmetrical PBI-PDP:

(a) Synthesis of 4-amino-3-pentadecyl phenol:

3-pentadecylphenol (10 gm), potassium hydroxide (10 gm) and 95% ethyl alcohol (80 mL) were taken together into a one-necked, round-bottom flask and cooled to 4 °C. To the resultant reaction mixture diazonium chloride prepared from sulphanilic acid dihydrate was added dropwise at 4 °C. The reaction mixture was stirred further for 2 hours at that temperature and then heated up to 75 °C. A saturated solution of sodium dithionite (25 gm) was added to the red dye solution at 75 °C. The reaction mixture was stirred further for 30 minutes till the colour changed to orange. After 30 minutes, 80 mL acetic acid was added to that and refluxed for 1 hour. The resultant reaction mixture was poured into crushed ice and then the solid product was filtered by vacuum. The solid product was dried in vacuum oven at 50 °C for 2-3 hours. Yield: 75%. FT-IR (ATR eco ZnSe, cm^{-1}): 3434, 3349, 3298, 1644, 1583, 1419, 1336, 912,730, 678. ^{1}H NMR (200 MHz, $CDCl_3$, δ): 7.22 (d, 1H), 6.56-6.44 (m, 2H), 2.68 (t, 2H), 1.63 (t, 2H), 1.37–1.21 (m, 24H), 0.87 (t, 3H) ppm. ^{13}C NMR (200 MHz, $CDCl_3$, δ): 147.9, 138.1, 125.9, 118.0,

111.9, 30.5, 29.9, 23.2, 14.7 ppm. MALDI-TOF MS (Calcd Mol Wt: 319.29); found Mol Wt: 320.37 [M+1].

(b) Synthesis of PBI-PDP:

Perylene bis anhydride (PBA) (10 gm; 2.55 x 10^{-2} mole) was taken in a one necked round bottom (RB) flask with 0.5 gm of zinc acetate [$Zn(OAc)_2$]. 150 gm Imidazole was added to that. The resultant mixture was heated upto 160 °C and then 4-amino 3-pentadecylphenol (16.29 gm; 5.09 x 10^{-2} mole) was added to the molten reaction mixture and further stirred for 12 hour at 160 °C (Scheme 3.1a) under nitrogen (N_2) atmosphere. After 12 hr, the reaction mixture was allowed to cool down to room temperature and then 2N HCL was added followed by stirring at room temperature for another 5-6 h. The dark red precipitate was filtered through vaccum filtration assembly and washed throughly with water and methanol. The solid mass was dried and purified through column chromatography using dichloromethane-methanol (DCM-MeOH = 98-2) as a mobile phase. Yield = 55%. Melting Point >300 °C. FT-IR (ATR eco ZnSe, cm^{-1}) = 3349, 2919, 2849, 1700, 1656, 1587, 1501, 1457, 1434, 1400, 1354, 1297, 1251, 1177, 1127, 1092, 1021, 964, 861, 811, 750, 721. ^{1}H NMR(400 MHz, $CDCl_3$+TFA, δ): 8.89 (m, 8H); 6.88 – 7.10 (m, 6H); 2.37 (t, 4H); 1.51 (t, 4H); 1.19 – 1.08 (m, 48H); 0.84 (t, 6H).^{13}C NMR(400 MHz, $CDCl_3$+TFA, δ): 164.86, 159.98, 159.56, 159.14, 158.72, 156.23, 142.09, 135.67, 133.03, 129.79, 126.69, 125.61, 124.07, 122.80, 118.83, 116.91, 115.99, 114.41, 113.16, 110.33, 67.26, 31.89, 31.02, 29.66, 24.33, 22.65, 14.03 ppm. MALDI-TOF MS (Calcd Mol Wt: 995.33); Found Mol Wt: 995.42 [M], 1018.42 [M+Na], 1034.29 [M+K]. Single crystal was obtained for this compound and data will be given in later section of the chapter.

(c) Synthesis of NBI-PDP:

Naphthalenebisanhydride (NBA) (10 gm; 3.73 x 10^{-2} mole) was taken in a one necked round bottom (RB) flask with 0.5 gm of zinc acetate [$Zn(OAc)_2$], and 150 mL dimethyl acetamide (DMAc) was added to it. The resultant mixture was heated upto 120 °C and then 4-amino 3-pentadecylphenol (23.83 gm; 7.46 x 10^{-2} mole) was added to that reaction mixture and further stirred for 12 hour at 120 °C (Scheme 3.1b) under nitrogen (N_2) atmosphere. After 12 hr, the reaction mixture was allowed to cool down to room temperature and DMAc was removed by vacuum distillation. Methanol was added to the dark brown precipitate and stirred for 2-3 hour. The precipitate was filtered by vaccum filtration assembly and washed throughly with methanol. The solid mass was dried and purified through combi flash column chromatography using dichloromethane-methanol

(DCM-MeOH = 98-5) as a mobile phase. Yield = 60%. Melting Point = 280 °C. FT-IR (ATR eco ZnSe, cm^{-1}) = 3360, 3319, 2918, 2851, 1709, 1658, 1581, 1497, 1448, 1344, 1297, 1243, 1201, 1085, 1031, 979, 870, 830, 761, 707. ^{1}H NMR(400 MHz, $CDCl_3$, δ): 8.86 (m, 8H); 6.76 – 7.04 (m, 6H); 5.40 (s, 2H); 2.37 (t, 4H); 1.53 (t, 4H); 1.11 – 1.22 (m, 48H); 0.86 (t, 6H).^{13}C NMR(400 MHz, $CDCl_3$, δ): 163.13, 156.44, 147.14, 141.76, 131.57, 129.63, 126.98, 125.82, 116.77, 114.30, 31.90, 31.15, 29.66, 29.34, 22.68, 14.10, 11.30ppm. MALDI-TOF MS (Calcd Mol Wt: 871.55); Found Mol Wt: 872.43 [M+1], 894.29 [M+Na].

(ii) Synthesis of P4VP-Rylenebisimide complex:

Rylenebisimides (1 mol ratio) and P4VP (2 mol ratio) were taken in a two necked round bottom (RB) flask and charged with nitrogen (N_2). Dry dimethyl formamide (DMF) was added to the solid mixture. The resultant solution mixture was heated upto 55 °C and stirred further for 24 hours at this temperature (shown in scheme 3a and 3b). After complex formation, DMF was removed by heating and the powder was dried further in vacuum oven for one day at 60 °C. Finally the dried powder was used for further characterization.

3.4 Results and Discussion

3.4.1 Synthesis and Characterization

The ditopic hydrogen bond donors, 3-pentadecylphenol group substituted symmetrical perylenebisimide and symmetric naphthalenebisimide were synthesized as described in section 3.3.5 (a) and 3.3.5 (b). The ditopic perylene and naphthalenebisimide molecules were named as **PBI-PDP** and **NBI-PDP** respectively. Detailed structural characterization of **PBI-PDP** including ^{1}H and ^{13}C NMR spectra and MALDI-TOF are shown in figure 3.1a, 3.1b and 3.2a. Similarly, structural characterization of **NBI-PDP** including ^{1}H and ^{13}C NMR and MALDI-TOF are shown in figure 3.1c, 3.1d and 3.2b. The high level of purity of **NBI-PDP** was confirmed by the single peak in gel permeation chromatography (GPC) (figure 3.2c).

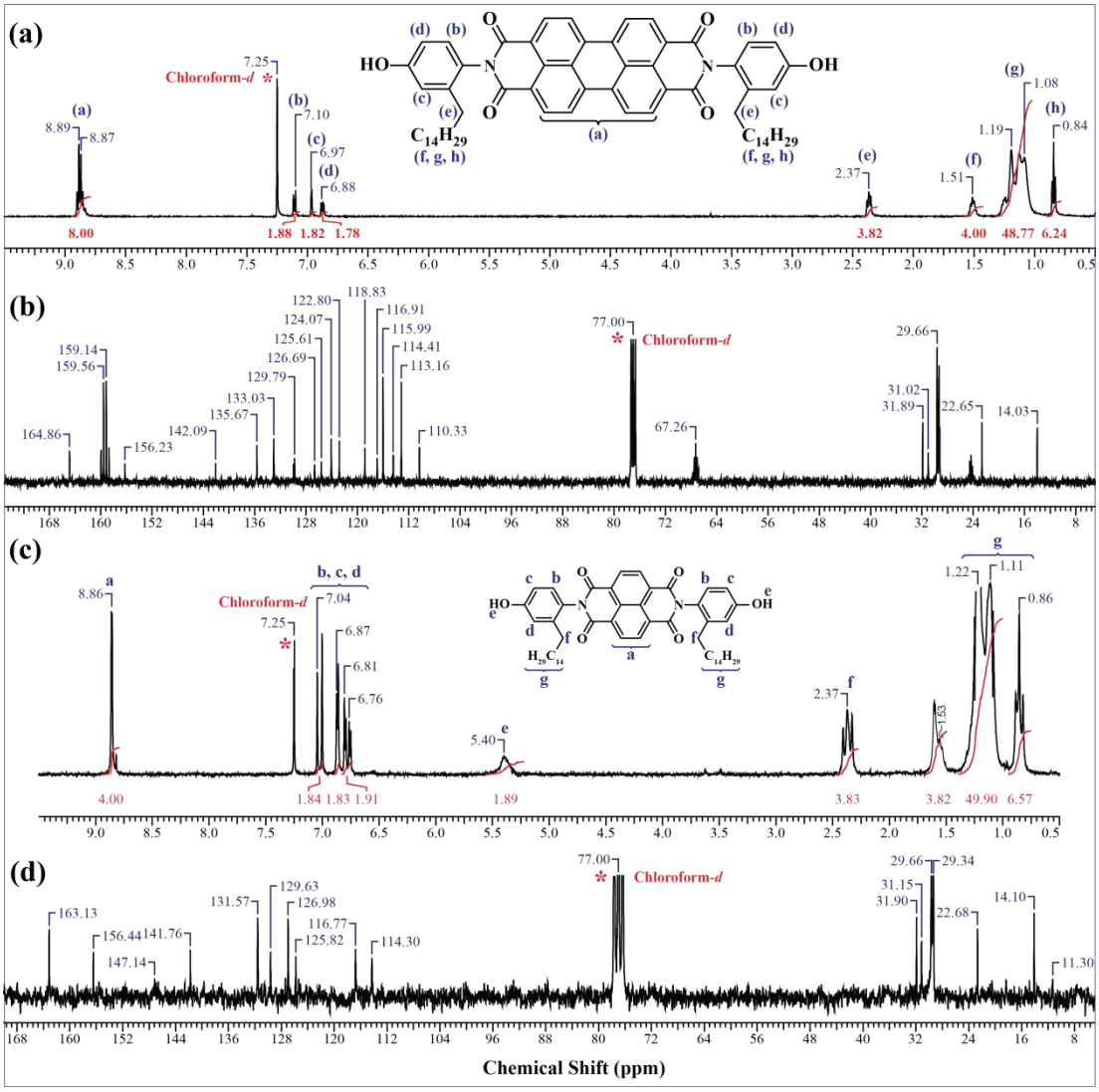

Figure 3.1: (a) ^{1}H and (b) ^{13}C NMR spectra of **PBI-PDP** in $CDCl_3$+TFA and (c) ^{1}H and (d) ^{13}C NMR spectra of **NBI-PDP** in $CDCl_3$.

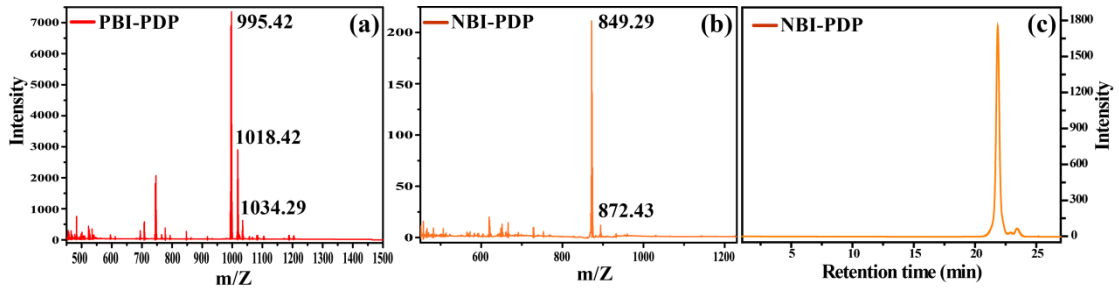

Figure 3.2: MALDI-TOF spectra of (a) **PBI-PDP** and (b) **NBI-PDP** and (c) Gel permeation Chromatography of **NBI-PDP** recorded in THF.

Thermogravimetric ananlysis (TGA) was performed (30 °C to 800 °C under nitrogen atmosphere) for **PBI-PDP** and **NBI-PDP** for the study of their thermal stability. Figure

3.3 shows the high thermal stability of both rylenebisimides up to 400 °C. **PBI-PDP** could be grown as a single crystal in DCM-methanol (98:2) mixture. It showed a space group of $P2_1$ with cell parameters a = 10.3523(5); b = 15.8324(8); c = 18.6542(9) and α = 90.00; β = 114.671(4); γ = 90.00. Figure 3.5 represents the single crystal structure of **PBI-**

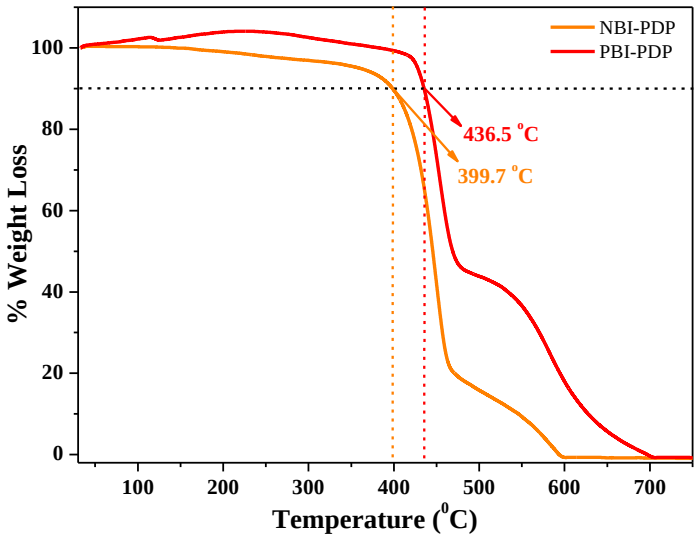

Figure 3.3: Thermogravimetric ananlysis (TGA) of **PBI-PDP** and **NBI-PDP**

PDP (molecular length 22.42 Å). It could be seen from figure 3.4a that the C15 alkyl chain masked the aromatic core of the **PBI-PDP** from either side. The distance between perylene core was found to be 10.35 Å and 18.65 Å along 'a' and 'c' direction respectively. The packing along 'a', 'b'and 'c' direction clearly indicated the absence of π-π interaction between aromatic cores of the **PBI-PDP** molecule. Attempts in growing the single crystals of **NBI-PDP** was unsuccessful. However, powder X-ray diffraction data could be made use of to explore the bulk packing in **NBI-PDP** as detailed in later se-

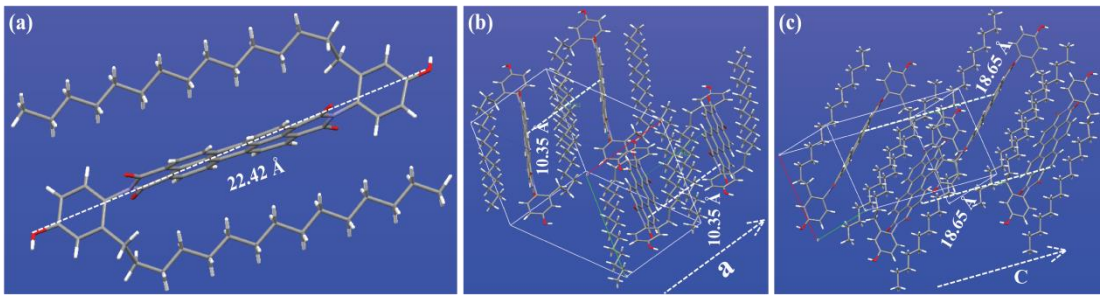

Figure 3.4: Single crystal structure of **PBI-PDP** (a) single molecule (b) packing along 'a' direction (c) packing along 'c' direction.

ction. Supramolecular crosslinked polymer complexes were prepared by mixing of rylenebisimide (1 mole) with P4VP (2 moles) in mimimum amount of dry N, N-dimethyl formamide (DMF) as described in section 3.3.2 (Scheme 3.2a and 3.2b). The complexes were named as **P4VP-PBI** and **P4VP-NBI**.

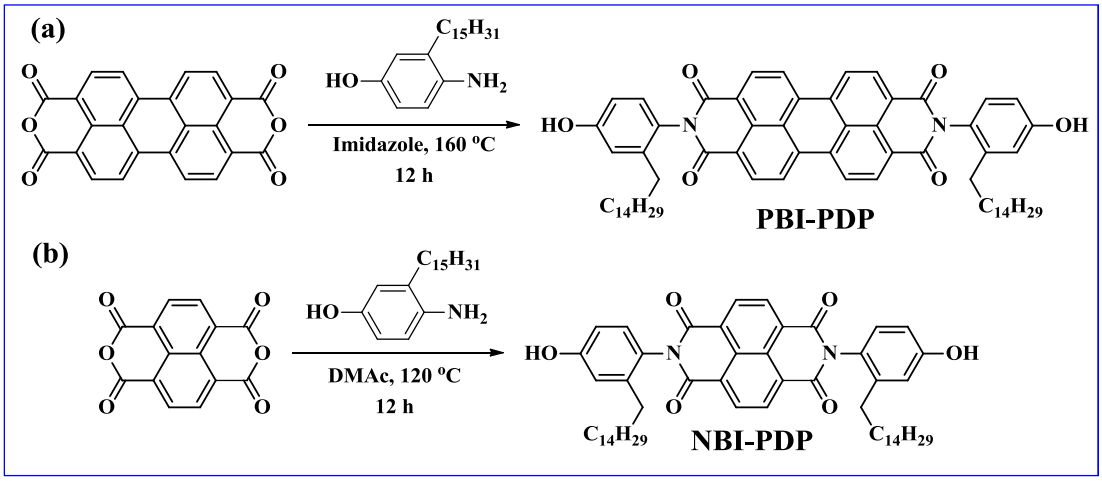

Scheme 3.1: Synthesis of (a) **PBI-PDP** and (b) **NBI-PDP**

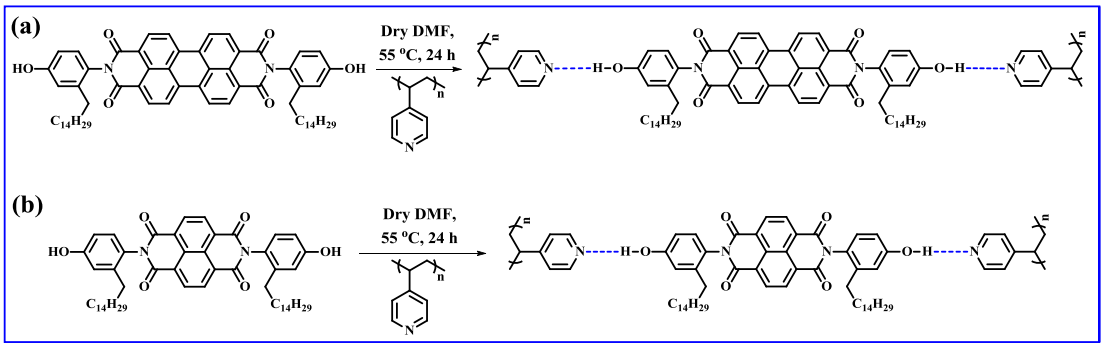

Scheme 3.2: Preparation of supramolecular polymer complexes (a) **P4VP-PBI** complex and (b) **P4VP-NBI** complex.

The formation of supramolecular complex was confirmed by FT-IR spectroscopy. There are many evidences where FT-IR was used for the confirmation of hydrogen bonds between the nitrogen atom of P4VP and phenolic -OH group on pentadecyl phenol [P4VP(PDP)$_x$)].[15, 32] Two pyridine stretching vibrational bands at 993 cm^{-1} (ν_1 vibration band)[33] and 1413 cm^{-1} [33] are generally examined for the confirmation of hydrogen bond in this system. Figure 3.5 compares the FT-IR spectra (1 weight % on KBr pellet) of pristine **PBI-PDP**, **NBI-PDP** and their supramolecular polymer complex along with P4VP. Both the pristine rylenebisimide molecules did not show IR absorption at 993 cm^{-1}. The free pyridine absorption peak at 993 cm^{-1} was shifted to higher wave number (1009 cm^{-1} and 1016 cm^{-1} respectively) for both the **P4VP-PBI** and **P4VP-NBI** complexes. Similar kind

of shifts in pyridine stretching vibration (characteristic of hydrogen bonded pyridine) were demostrated for the supramolecular polymer complex formed between P4VP and unsymmetrical perylenebisimide.[22]

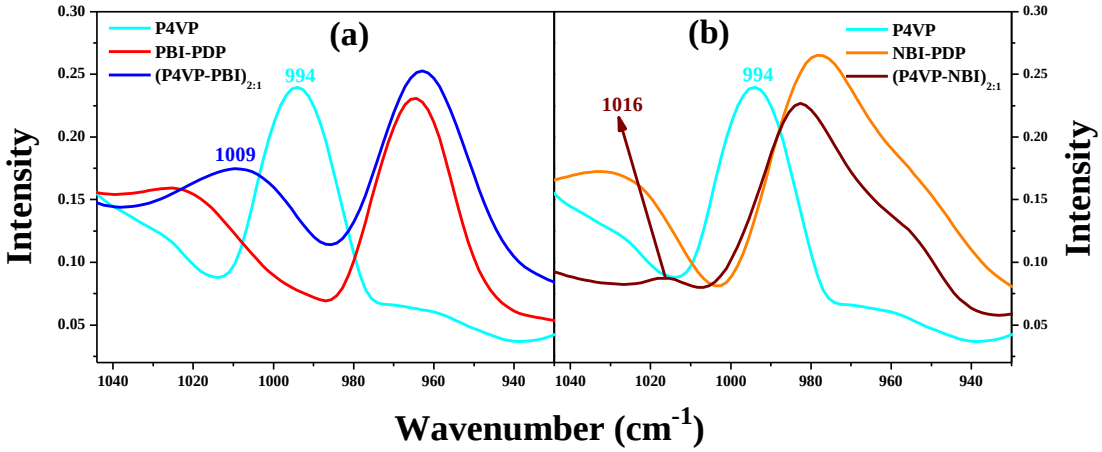

Figure 3.5: Comparison of the FT-IR spectra of the complexes with the pristine molecules (a) **P4VP-PBI** complex and (b) **P4VP-NBI** complex in the region 930 – 1044 cm^{-1}.

3.4.2 Microstructure Analysis

Wide angle X-ray diffraction data was collected in the range 2θ = 3 -30° for the powder samples of the pristine rylenebisimides as well as the corresponding complexes with P4VP to get a better insight of the micro structure of the complexes. P4VP is amorphous in nature, and had only two broad diffraction in WXRD region.[11] Figure 3.6 compares the WXRD pattern of **PBI-PDP** and **P4VP-PBI** (figure 3.6a) and **NBI-PDP** and **P4VP-NBI** (figure 3.6b). Several numbers of sharp diffraction peaks were observed for **PBI-PDP** molecule in the entire 2θ region (2θ = 3-33°), whereas no of peaks were reduced significantly in **P4VP-PBI** polymer complex. Inset of figure 3.6a exhibited the first diffraction peak (negligable intensity) at 2θ = 3.96° (d = 22.29 Å). However, it was prominant in the samples dropcast from THF (discussed later on). A comparison of WXRD pattern between powder sample of **PBI-PDP** and simulated XRD pattern obtained from the single crystal data is shown in figure 3.7, which clearly shows the absence of diffraction peaks at 2θ range from 3-8°. This clearly indicated that the bulk powder of **PBI-PDP** had mixed phases present - the single crystal phase as well as the phase obtained from THF. The first order reflection of **PBI-PDP** was observed at a 'd' spacing of 22.29 Å which was shifted to d = 24.27 Å (2θ = 3.64°) after complex formation with P4VP. One new diffraction peak at 2θ = 21.65° (d = 4.1 Å) (arrow mark

in figure 3.6a) appeared for the **P4VP-PBI** complex, which could be assigned for the π- π stacking distance of the **PBI-PDP** aromatic core.

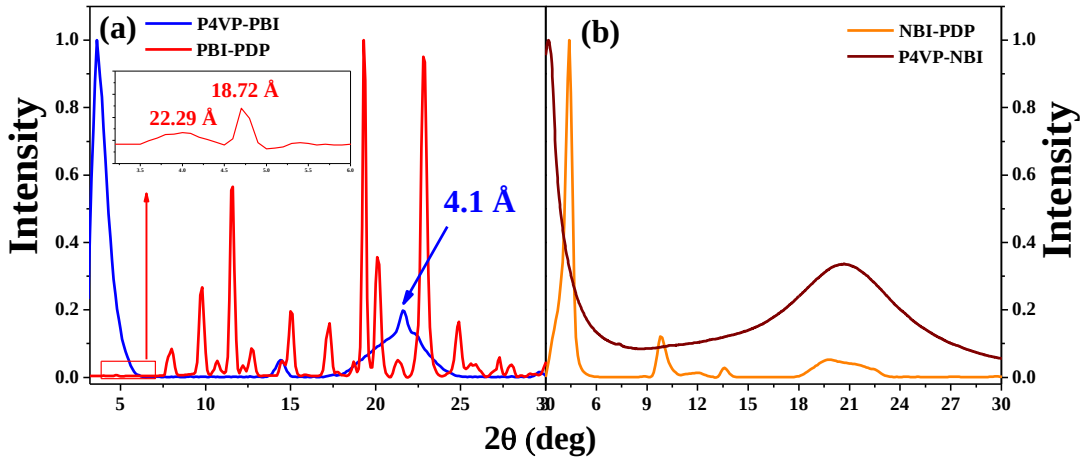

Figure 3.6: WXRD of (a) **PBI-PDP**, **P4VP-PBI** complex and (b) **NBI-PDP**, **P4VP-NBI** complex in powder state.

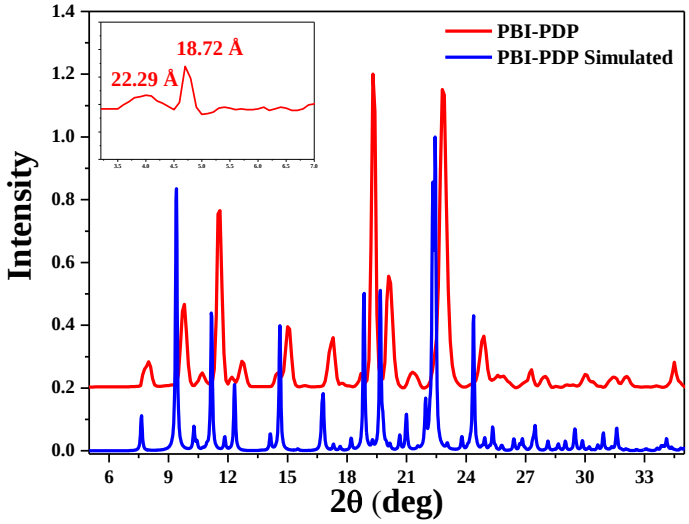

Figure 3.7: Comparison of WXRD plot of **PBI-PDP** in powder state and generated from single crystal XRD.

Figure 3.6b compares the WXRD pattern of **NBI-PDP** and **P4VP-NBI** complex. The first diffraction peak appeared at 2θ = 4.39° (d = 20.07Å) for pristine **NBI-PDP**, which was shifted to higher 'd' spacing [2θ = 3.14° (d = 28.08 Å)] in **P4VP-NBI** complex. Thus both the rylenebisimide molecules exhibited an expansion upon complexation indicating the unfolding of the P4VP polymer chains and its intercalation into the rylenebisimide domains to accommodate hydrogen bonding at either ends of the ditopic rylenebisimides.

The rylenebisimide molecules with long alkyl substitution are known to show mesogenic behaviour. Better charge transport could be observed for a liquid crystalline semiconductor if the liquid crystalline character could be retained until room temperature. Differential scanning calorimetric (DSC) analysis was performed to understand the thermotropic phase behavior. **PBI-PDP** was unable to show the thermotropic behaviour because of its very high melting point (> 400 °C). The lower analogue **NBI-PDP** had a melting point ~ 280 °C due to its lower extent of rigidity compared to **PBI-PDP** molecule. Figure 3.8 represents the second heating and first cooling cycles in the DSC thermogram of **NBI-PDP**. The heating cycle showed a sharp melting at 287 °C with an

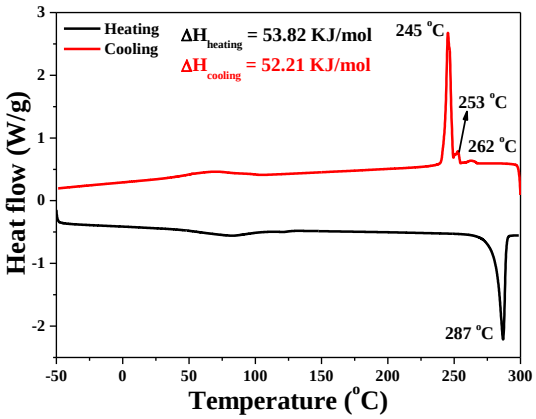

Figure 3.8: DSC thermogram of **NBI-PDP** in the second heating and cooling cycle at 10 °C min^{-1} under nitrogen atmosphere.

enthalpy value of 53.82 KJ/mol, while multiple transitions were observed in the cooling cycle. The multiple transition in cooling cycle indicated the presence of liquid crystalline phases. Total enthalpy calculated for heating and cooling cycle were 53.82 KJ/mol and 52.21 KJ/mol respectively. Focal conic or spherulitic type textures was observed in the PLM images collected for the thermotropic liquid crystalline phases of **NBI-PDP** molecule (figure 3.9) which was stable up to room temperature from the isotropic melt. Since the melting transition of 280 °C was too high to be beneficial for aligning the sample in the liquid crystalline order on a device substrate, alternate strategies for attaining the liquid crystalline order was sought out. Another type of liquid crystalline ordering known as lyotropic liquid crystal phase can be achieved by dissolving the mesogen in suitable solvent instead of temperature. Various solvent systems were tried to attain the lyotropic phases for both rylenebisimide molecules and it was observed that tetrahydrofuran (THF) was the suitable solvent which could bring out the lyotropic order-

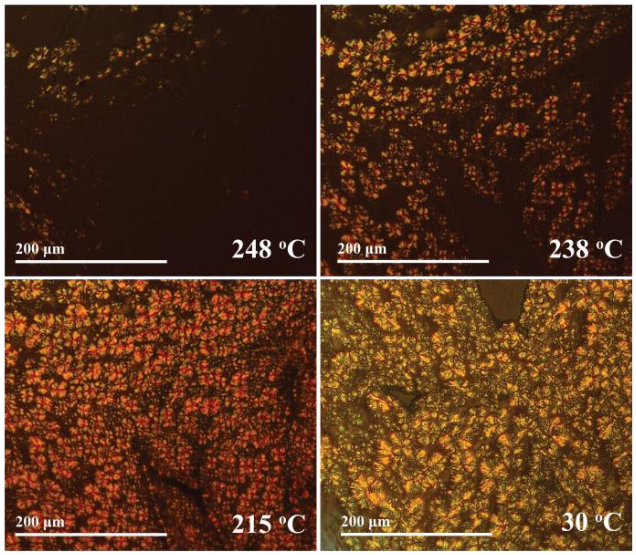

Figure 3.9: Polarized light microscopic images of **NBI-PDP** (under crossed polarizer) at various temperatures.

ing in **PBI-PDP** and **NBI-PDP**. **NBI-PDP** (5 weight % solution in THF) showed birefringent phases under polarized light microscope (PLM) (figure 3.10a-d). The lytropic phase of **NBI-PDP** was found to be stable even after slow evaporation of the solvent. WXRD data was collected for both lyotropic (THF dropcast sample) and thermotropic (the solid obtained at room temperature upon cooling from its isotropic state) liquid crystal phases of **NBI-PDP**. A comparison of WXRD pattern of **NBI-PDP** in the thermal

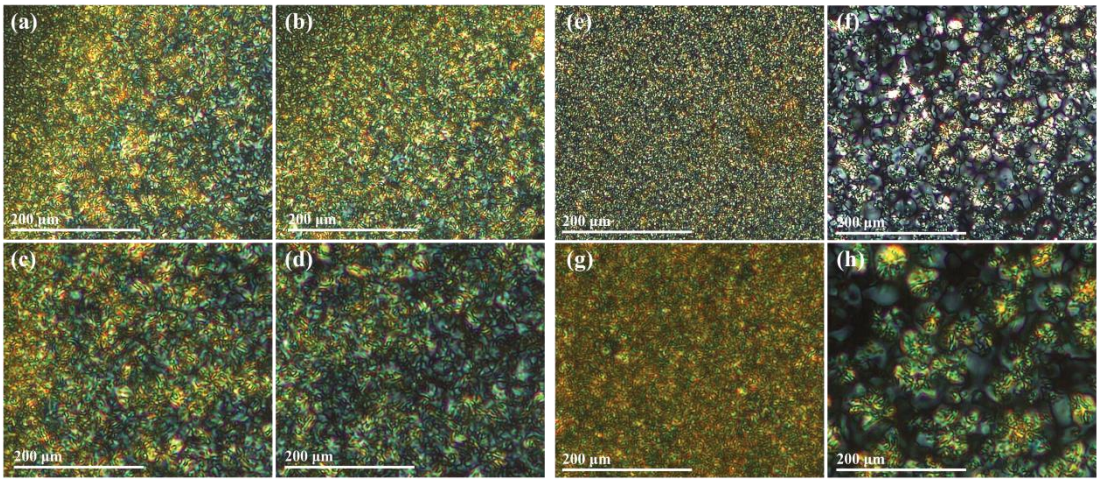

Figure 3.10: Polarized light microscopic images (under crossed polarizer) of 5 weight % solution of (a-d) **NBI-PDP** and (e-h) **P4VP-NBI** complex in THF.

and lyotropic mesophases along with the as-solvent drop cast powder is depicted in figure 3.11 in the range 2θ = 5-30°. The inset compares their first order reflection. Thermotropic sample exhibited layered ordering with d spacing 26.69 Å; 13.85 Å; 9.34 Å (ratio of 1: 1/2 : 1/3: 1/ 4) (2θ = 3.31°; 6.38°; 9.47°) in WXRD pattern. The lyotropic sample also showed the presence of several sharp peaks with layered ordering at 2θ = 3.43°; 6.67°; 10.25° with d spacing = 25.72 Å; 13.23 Å; 8.61 Å. Unlike the as-solvent

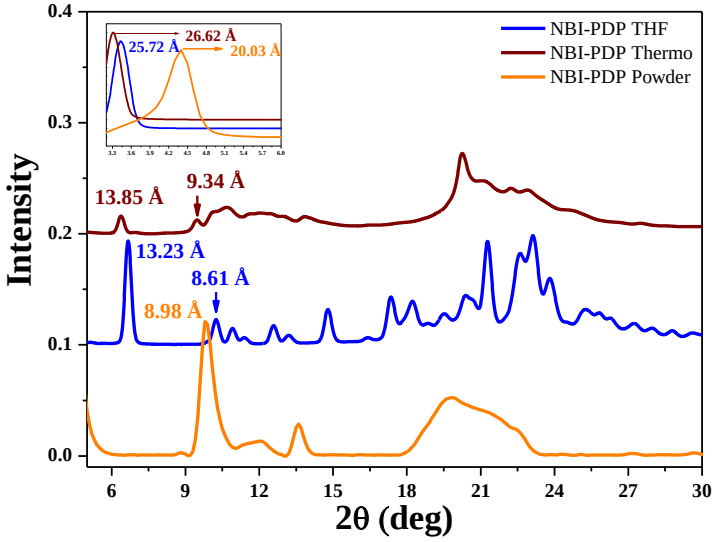

Figure 3.11: Comparison of WXRD plot of **NBI-PDP** in powder state (**NBI-PDP** Powder), drop casted from THF (**NBI-PDP** THF) and cooled after melting (**NBI-PDP** Thermo).

recrystallized sample, the WXRD pattern of thermotropic and THF dropcasted sample were very similar. Sharp reflections were also observed in the wide angle region in the 2θ = 18-25° range, which usually reflects the ordering of the alkyl chains. Smectic liquid crystals are characterized by the layered ordering and they exhibit large enthalpies of transition in their DSC thermogram. However, the lower ordered smectic phases like SmA and SmC generally show only a diffuse halo in the wide angle region, whereas some higher ordered Smectic phases are known to exhibit several peaks in their XRD pattern due to more regular packing of mesogens.[34, 35] Therefore, the layered LC phase exhibited by **NBI-PDP** could be attributed to higher ordered Smectic phase.[36] Figure 3.10e-h shows the lyotropic textures obtained for **P4VP-NBI** from THF. Figure 3.12a compares the WXRD pattern of **NBI-PDP** and **P4VP-NBI** dropcast from THF solutions. It could be seen that **P4VP-NBI** also exhibited layered ordering with sharp reflections at 2θ = 3.27°; 6.36°; 9.47° corresponding to d spacing of 27.05 Å; 13.89 Å; 9.33 Å respectively. A

sharp peak was observed around 2θ = 20.91° corresponding to d spacing of 4.24 Å, which could be attributed to the π-π stacking interaction of the naphthalene aromatic cores. Significantly, this peak was absent in the WXRD pattern of **P4VP-NBI** prepared from DMF (figure 3.6b).

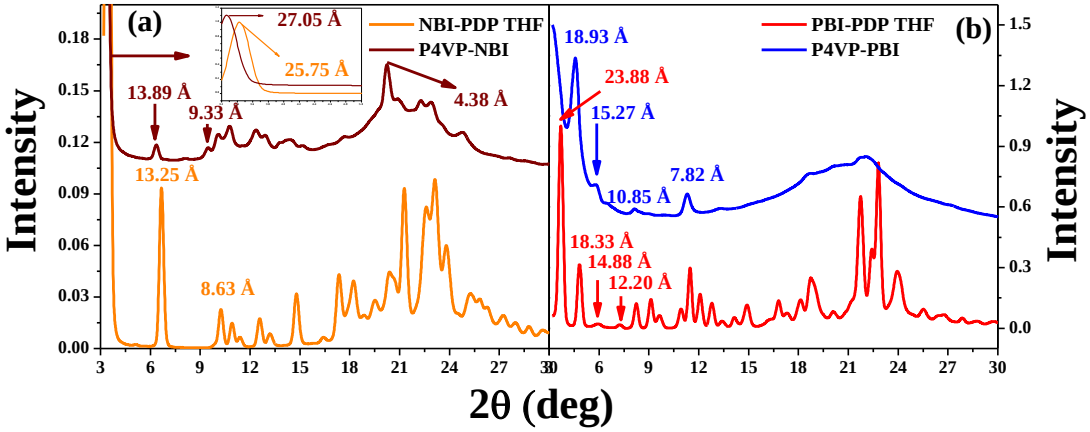

Figure 3.12: WXRD of (a) **NBI-PDP**, **P4VP-NBI** complex and (b) **PBI-PDP**, **P4VP-PBI** complex from THF drop casted film (5 wt. % solution in THF).

Pristine **PBI-PDP** as well as its supramolecular complex **P4VP-PBI** in THF exhibited birefringence, as shown in figure 3.13. Figure 3.12b compares the WXRD pattern for THF dropcast samples of **PBI-PDP** and **P4VP-PBI**. Diffraction pattern of **PBI-PDP** showed reflections at 2θ = 3.70°, 4.82°, 7.24° and 8.24° corresponding to 'd' spacing of 23.88 Å, 18.33 Å, 12.20 Å, 10.69 Å with π-π stacking at 2θ = 21.74° (d = 4.09

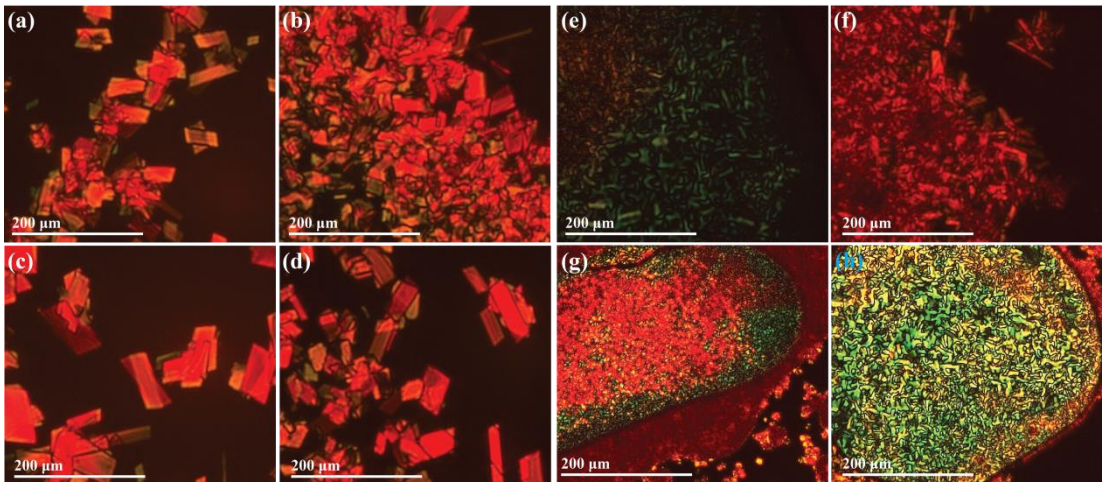

Figure 3.13: Polarized light microscopic images (under crossed polarizer) of 5 weight % solution (a-d) **PBI-PDP** and (e-h) **P4VP-PBI** in THF.

Å). The layered organization that was observed in pristine **NBI-PDP** was not observed in **PBI-PDP** (THF). On the other hand, the WXRD pattern of the **P4VP-PBI** complex showed peaks at 27.58 Å, 15.05 Å, 10.86 Å and 7.82 Å, which were in the approximate ratio of 1: 1/2: 1/3: 1/ 4. This confirmed the lamellar ordering in the PBI supramolecular complex. The π-π stacking peak which was observed at d spacing of 4.1 Å for the PBI supramolecular complex dropcast from DMF (figure 3.6a), was surprisingly not so prominent in the organization from THF.

3.4.3 Thin Film Morphology

Thin film morphology of the supramolecular polymer complexes were examined by tran-

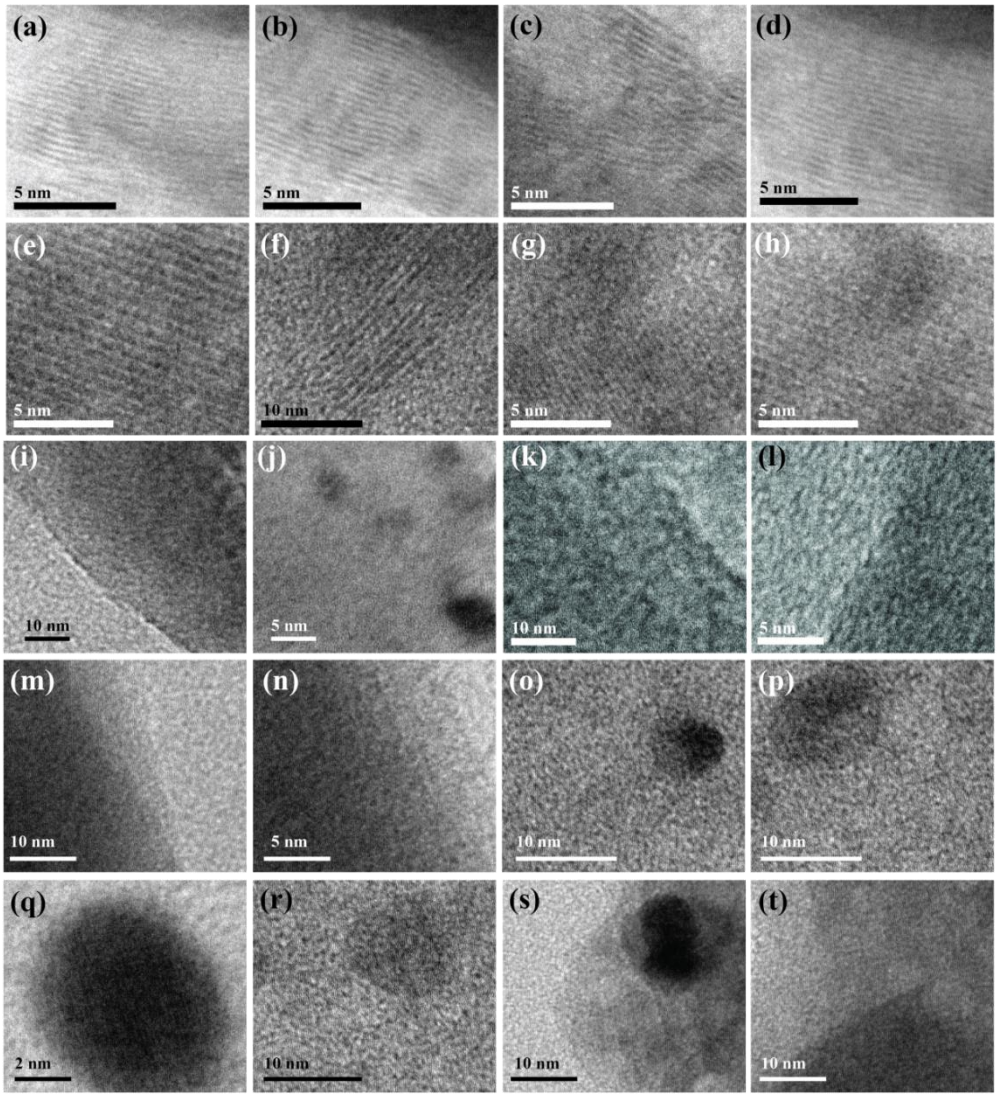

Figure 3.14: TEM images of (a-d) **P4VP-PBI** complex, (e-h) **P4VP-NBI** complex (i-j) **PBI-PDP** and (k-l) **NBI-PDP** dropcast from DMF and (m-n) **PBI-PDP**, (o-p) **NBI-PDP**, (q-r) **P4VP-PBI** complex and (s-t) **P4VP-NBI** complex dropcast from THF.

smission electron microscopy (TEM) imaging. Samples were dropcast from DMF as well as THF solution (2 mg/ml) onto copper grids. Figure 3.14a-l and figure 3.14m-t depicts the TEM images dropcast from DMF and THF respectively. The samples were air dried followed by drying in vacuum oven at 55 °C for 12 h to remove all traces of solvent, following which they were stained with the help of iodine vapor to improve the contrast of the image.[37] Figure 3.14a-d and figure 3.14e-h show the layered morphology with alternate dark and light lines in the < 10 nm length scale obtained for **P4VP-PBI** and **P4VP-NBI** respectively. This observation was in confirmation with the layered structure obtained from WXRD also. Neither the pristine rylenebisimides nor the amorphous P4VP exhibited any specific morphology under identical conditions.

3.4.4 Charge Carrier Mobility of Complexes: Space Charge Limited Current (SCLC) Measurements

Electron mobility was measured via space charge limited current (SCLC) method with device configuration **Al/ active layer/ Al** structure. Samples (pristine rylenebisimides and the corresponding supramolecular complexes) were prepared from DMF at a concentration of 8 mg/ml, filtered through PTFE (0.45 μm) membrane and dropcast directly on the aluminium coated substrate to get smooth films with average thickness of ~1.9-2.4 microns. An average of 3 to 4 devices were prepared and used for measurement of each individual sample. The summary of device parameters including film thickness and maximum and average electron mobility obtained from SCLC are given in table 3.1.

Table 3.1: Summary of device parameters

Electron only device with Al/ active layer/ Al			
Sample Name	**Maximum mobility $\mu_{e,max}$ [cm^2/Vs]**	**Average mobility $\mu_{e,avg}$ [cm^2/Vs]**	**Film Thickness [micron]**
UPBI-PDP	2.12 x 10-5	9.77x10-6	1.9
P4VP- PBI Complex	1.17 x 10-3	1.03 x 10-3	2.4
NBI-PDP	3.27 x 10-6	2.85 x 10-6	2.2
P4VP-NBI Complex	2.20 x 10-4	1.65 x 10-4	2.4

Figure 3.15a-d depicts the J-V characteristics of **PBI-PDP**, **NBI-PDP**, and **P4VP-PBI** and **P4VP-NBI** complexes. An average electron transport mobility of 9.77 x 10^{-6} cm^2/Vs (~1 x 10^{-5} cm^2/Vs) was obtained for the pristine **PBI-PDP**, which was enhanced by two orders of magnitude to 1.03 x 10^{-3} cm^2/Vs in **P4VP-PBI**. The pristine **NBI-PDP**

exhibited an average electron mobility of 2.85 x 10^{-6} cm^2/Vs. In the supramolecular complex **P4VP-NBI**, the average electron mobility value was enhanced by an order of two to 1.65 x 10^{-4} cm^2/Vs. Thus, both the supramolecular crosslinked polymer networks exhibited higher mobilities compared to the pristine rylenebisimides. This observation is in line with our own previous observation of enhancement in mobility upon supramolecular complex formation of unsymmetrical perylenebisimide with P4VP.[22] Since the supramolecular complexes exhibited liquid crystalline ordering upon solvent treatment with THF, SCLC mobility measurements were attempted for THF dropcast samples. Samples and devices were prepared under similar conditions as that from DMF. Unfortunately **PBI-PDP** and its complex did not give uniform films, which could be used for SCLC device studies. **NBI-PDP** and **P4VP-NBI**, exhibited mobility values of 4.60 x 10^{-6} cm^2/Vs and 2.16 x 10^{-4} cm^2/Vs respectively, which were very similar to the values obtained from DMF.

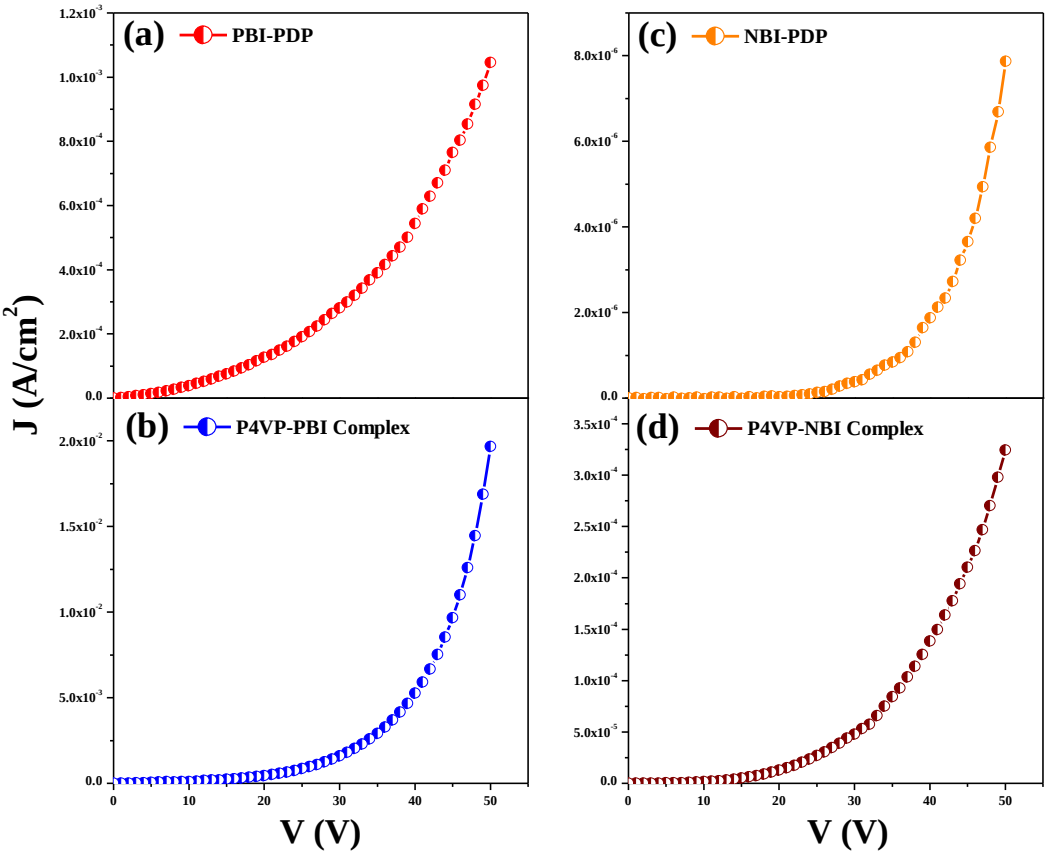

Figure 3.15: J-V characteristics for electron only mobility of (a) **PBI-PDP** (b) **P4VP-PBI** complex (c) **NBI-PDP** (d) **P4VP-NBI** complex.

The poor electron mobility value for pristine **PBI-PDP** could be justified from the orientation of the C15 alkyl chains across the perylene aromatic core on either side, almost insulating the π-electron cloud. The intercalation of the P4VP chains upon hydrogen bond induced network formation stretched the **PBI-PDP** molecule (increase in d spacing of the first order peak observed in WXRD by ~ 2 Å upon complexation), reorienting the alkyl chains and facilitating the π-π interaction. This was clearly reflected in the SCLC mobility values which showed a two-fold increase.

3.5 Conclusions

Supramolecularly crosslinked polymer networks were developed between commercially available polymer –P4VP and ditopic rylenebisimides with the help of hydrogen bonding interaction between the nitrogen atom on P4VP and hydroxyl moieties on rylenebisimides. The complexations were confirmed by FT-IR studies and bulk structure was analyzed using WXRD. Thin film morphology (TEM) revealed the layer structure formation in supramolecular polymer networks. Mesomorphic behavior observed in the pristine molecules was retained in the complexes **P4VP-PBI** and **P4VP-NBI** which was confirmed by POM and WXRD. It is expected that multiple sites of interaction, as is possible along the P4VP polymer backbone, can make up for the lack of strong individual point sites of interaction,[23] resulting in overall improvement in alignment. The WXRD studies of the complexes versus pristine systems clearly demonstrated stretching of the rylenebisimide molecules due to hydrogen bonded intercalation of P4VP polymer chains. This was manifested as a two fold increase of electron transport ability; μ_e = 1.03 x 10^{-3} cm^2/Vs for P4VP-PBI compared to μ_e ~ 1.0 x 10^{-5} cm^2/Vs for pristine PBI derivative. Compared to a covalently crosslinked donor acceptor polymer network, which would have remained intractable, the solution processable supramolecular crosslinks allowed for the dynamic behavior and mesomorphic properties to be retained after crosslinking.

3.6 References

1. Voorhaar, L.; Hoogenboom, R. *Chem. Soc. Rev.* **2016**, *45*, 4013 – 4031.

2. Rossowab, T.; Seiffert, S. *Polym. Chem.* **2014**, *5*, 3018 – 3029.

3. Seiffert, S.; Sprakel, J. *Chem. Soc. Rev.* **2012**, *41*, 909 – 930.

4. Patra, D.; Ramesh, M.; Sahu, D.; Padhy, H.; Chu, C-W.; Wei, K-H.; Lin, H-C. *Polymer* **2012**, *53*, 1219 – 1228.

5. Shibata, M.; Kimura, Y.; Yaginuma, D. *Polymer* **2004**, *45*, 7571–7577.

6. Xu, D.; Hawk, J. L.; Loveless, D. M.; Jeon, S. L.; Craig, S. L. *Macromolecules* **2010**, *43*, 3556–3565.

7. Hackelbusch, S.; Rossow, T.; van Assenbergh, P.; Seiffert, S. *Macromolecules* **2013**, *46*, 6273−6286.

8. Mäki-Ontto, R.; de Moel, K.; Polushkin, E.; van Ekenstein, G. A.; ten Brinke, G.; Ikkala, O. *Adv. Mater.* **2002**, *14*, 357-361.

9. Kuo, S-W.; Lin, C-L.; Chang, F-C. *Polymer* **2002**, *43*, 3943-3949.

10. de Moel, K.; Mäki-Ontto, R.; Stamm, M.; Ikkala, O.; ten Brinke, G. *Macromolecules* **2001**, *34*, 2892-2900.

11. Narayan, R.; Kumar, P.; Narayan, K. S.; Asha, S. K. *J. Mater. Chem. C* **2014**, *2*, 6511–6519.

12. Ikkala, O.; Ruokolainen, J.; Torkkeli, M.; Tanner, J.; Serimaa, R.; ten Brinke, G. *Colloids Surfaces A* **1999**, *147*, 241–248.

13. Wu, S.; Bubeck, C. *Macromolecules* **2013**, *46*, 3512−3518.

14. Tran, H.; Gopinadhan, M.; Majewski, P. W.; Shade, R.; Steffes, V.; Osuji, C. O.; Campos, L. M. *ACS Nano* **2013**, *7*, 5514–5521.

15. Luyten, M. C.; van Ekenstein, G. O. R. A.; ten Brinke, G.; Ruokolainen, J.; Ikkala, O.; Torkkeli, M. Serimaa, R. *Macromolecules* **1999**, *32*, 4404-4410.

16. Rancatore, B. J.; Mauldin, C. E.; Tung, S-H.; Wang, C.; Hexemer, A.; Strzalka, J.; Fréchet, J. M. J.; Xu, T. *ACS Nano* **2010,** *4*, 2721–2729.

17. Noro, A.; Matsushima, S.; He, X.; Hayashi, M.; Matsushita, Y. *Macromolecules* **2013**, *46*, 8304−8310.

18. Noro, A.; Matsushita, Y.; Lodge, T. P. *Macromolecules* **2008**, *41*, 5839-5844.

19. Leia, Y.; Lodge, T. P. *Soft Matter* **2012**, *8*, 2110–2120.

20. Zhan, J.; Zhang, M.; Zhou, M.; Liu, B.; Chen, D.; Liu, Y.; Chen, Q.; Qiu, H.; Yin, S. *Macromol. Rapid Commun.* **2014**, *35*, 1424−1429.

21. Zhang, M.; Xu, D.; Yan, X.; Chen, J.; Dong, S.; Zheng, B.; Huang, F. *Angew. Chem.* **2012**, *124*, 7117 –7121.

22. Narayan, R.; Kumar, P.; Narayan, K. S.; Asha, S. K. *Adv. Funct. Mater.* **2013**, *23*, 2033–2043.

23. Saibal, B.; Chithiravel, S.; Asha. S. K. *J Polym Sci Part A: Polym Chem.* **2016**, *54*, 2403–2412.

24. Bushby, R. J.; Kelly, S. M.; O'Neill, M (Eds.). *Liquid Crystalline Semiconductors. Materials, properties and applications.Springer Series in Material Science* **2013**, *Vol.169*.

25. Ikkala, O.; Ruokolainen, J.; ten Brinke, G.; Torkkeli, M.; Serimaa. R. *Macromolecules* **1995**, *28*, 7088-7094.

26. Ouskova, E.; Vapaavuori, J.; Kaivola, M. *Optical Materials Express* **2011**, *1*, 1463-1470.

27. Li, J.; Ou, X.; Sims, S.; Li, W.; Wu, L. *RSC Adv.* **2014**, *4*, 56998–57008.

28. Bazuin, C. G.; Brandys, F. A. *Chem. Mater.* **1992**, *4*, 970-972.

29. Bazuin, C. G.; Brandys, F. A.; Eve, T. M.; Plante, M. *Macromol. Symp.* **1994**, *84*,183-196.

30. Saibal, B.; Ashar, A. Z.; Devi, R. N.; Narayan, K. S.; Asha, S. K. *ACS Appl. Mater. Interfaces* **2014**, *6*, 19434–19448.

31. Bhavsar, G. A.; Asha, S. K. *Chem. Eur. J.* **2011**, *17*, 12646 – 12658.

32. Ruotsalainen, T.; Torkkeli, M.; Serimaa, R.; Mäkelä, T.; Mäki-Ontto, R.; Ruokolainen, J.; ten Brinke, G.; Ikkala, O. *Macromolecules* **2003**, *36*, 9437-9442.

33. Groppo, E.; Uddin, M. J.; Zavorotynska, O.; Damin, A.; Vitillo, J. G.; Spoto, G.; Zecchina, A. *J. Phys. Chem. C* **2008,** *112*, 19493–19500.

34. Nardele, C. G.; Asha, S. K. *J. Phys. Chem. B* **2014**, *118*, 1670−1684.

35. Xie, H-L.; Jie, C-K.; Yu, J-Q.; Liu, X-B.; Zhang, H-L.; Shen, Z.; Chen, E-Q.; Zhou, Q. F. *J. Am. Chem. Soc.* **20 10**, *132*, 8071–8080.

36. Kapernaum, N.; Knecht, F.; Hartley, C. S.; Roberts, J. C.; Lemieux, R. P.; Giesselmann, F. *J. Org. Chem.* **2012**, *8*, 1118–1125.

37. Huang, W-H.; Chen, P-Y.; Tung, S-H. *Macromolecules* **2012**, *45*, 1562−1569.

Chapter 4

P4VP and Oligo(Phenylenevinylene)-Perylenebisimide Mixed Donor-Acceptor Supramolecular Comb Polymer Complexes with Improved Charge Carrier Mobility

This chapter has been adapted from following publication

B. Saibal, S. Chithiravel and S. K. Asha. *J. Polym. Sci. Part A: Polym. Chem.* **2016**, *54*, 2403–2412.

4.1 Abstract

Random donor-acceptor (D-A) supramolecular comb polymers were formed when hydroxyl functionalized donor and acceptor small molecules based on Oligo(Phenylenevinylene) (named **OPVCN-OH**) and Perylenebisimide (named **UPBI-PDP**) respectively, were complexed with Poly(4-vinyl pyridine) (P4VP). A series of random D-A supramolecular comb polymers were formed by varying the ratios of **UPBI-PDP** and **OPVCN-OH** with P4VP. A 100 % P4VP-donor polymer complex (**P4VP(OPV$_{1.00}$)**) and a 100 % P4VP-acceptor polymer complex (**P4VP(UPBI$_{1.00}$)**) were also synthesized and characterized. Complex formation was confirmed by FT-IR and ^{1}H NMR spectroscopy. Solid state structural studies carried out using small angle X-ray scattering (SAXS) and wide angle X-ray diffraction (WXRD) experiments revealed altered packing of the D and A molecules in the complexes. Transmission electron microscopy (TEM) images showed lamellar structures in the < 10 nm scale for the **P4VP(OPV$_{1.00}$)**, **P4VP(UPBI$_{1.00}$)** and mixed P4VP (D-A) complexes. The effect of the nanoscopic D-A self-assembly on the bulk mobility of the materials was probed using SCLC measurements. The mixed D-A random complexes exhibited ambipolar charge transport characteristics with higher values for the average bulk hole mobility estimate. **P4VP(OPV$_{0.25}$ + UPBI$_{0.75}$)** exhibited an average hole mobility in the order of 10^{-2} cm^2 V^{-1}s^{-1} and electron mobility 10^{-5}cm^2 V^{-1}s^{-1}.

4.2 Introduction

Noncovalent interactions like the hydrogen bonding and ionic interactions have been used to develop 'bottle-brush' polymeric structures between linear polymers and small surfactant molecules.[1, 2] Poly(4-vinyl pyridine) (P4VP) is the most widely studied polymer that has been explored for the hydrogen bonding interactions of the pyridine nitrogen with aromatic hydroxyl or carboxyl units of small surfactant molecules.[3-15] Most of these studies focused on the self-organization in the bulk state.[13-15] In the recent years this self-assembly has been utilized to bring together π-conjugated molecules in a 'supramolecular comb polymer' architecture with promising improvements in their charge carrier mobilities. For instance, our research group successfully demonstrated complexation of hydroxyl functionalized perylene and naphthalenebisimides with P4VP resulting in lamellar organization of the 'n' type rylenebisimides in the 5-10 nm domain range, with improved conductance.[16, 17] The bulk structure of the supramolecular comb polymer complex analyzed using small and wide angle X-ray diffraction revealed retention of the highly crystalline nature of the rylenebisimide molecules despite its self-assembly within the amorphous confines of the P4VP polymer chains. This self-assembly approach of small π-conjugated molecules with P4VP has thus demonstrated its effectiveness in the preparation of functional n- type semiconducting polymeric materials that exhibited crystallinity and processability along with high charge transport mobilities suitable for application in optoelectronics. Other examples of self-assembly of P4VP with π conjugated organic semiconducting materials include those reported by Xu et al. where oligothiophene was self-assembled with PS-b-P4VP.[18] One of the main objectives in the organic semiconducting material research is the ability to assemble donor (D) and acceptor (A) π-conjugated materials in the nanoscopic length scale that promotes increased charge separation as well as long range pathway for charge transport to the respective electrodes. In the last decade, when the organic optoelectronic research was in the initial stages, a lot of interest was focused on the self-assembly approach to assemble small molecules or oligomers of donor and acceptor molecules.[19-23] Noted among them was the approach of incorporating complementary hydrogen bonding moieties like the imide and ureido pyrimidinone (UPI) pair into donor-acceptor (D-A) pairs like perylenebisimide (PBI acceptor) and oligo(p-phenylenevinylene) (OPV donor) introduced by Meijer et al.[22, 23] The melamine-barbiturate/cyanurate and diaminopyrimidine-thymine pairs also were studied in this pursuit for D-A nano self-assembly.[24, 25] Although the

association constant for these complementary hydrogen bonding D-A pairs were very high, they were plagued by formation of homo-stacks of the donor or acceptor leading to unwanted aggregation and macro phase separation and poor device performance. Sometimes, non-ideal lateral organization of the co-aggregated donor and acceptor aromatic units on the substrate surface was also believed to be the cause of the poor device performance. Organogels based on π conjugated donor[26, 27] and acceptor semiconducting molecules[28, 29] also have been tested for their ability to form 'self-sorted' p-n junction nanowires; however besides an efficient photoresponse no other device performance of such systems have been reported.[30] Compared to the large number of reports on small molecule based D-A self-assembly, those based on self-assembled polymeric D-A systems are very few. Blends of PBI with P3HT have been studied for their ambipolar charge transport characteristics in thin film field effect transistors.[31]

The P4VP based donor-acceptor assembly is expected to overcome the issue of processability while retaining the crystalline ordering of the donor and acceptor small molecules, which is considered as one of the major drawbacks of high molecular weight conjugated polymers. Although high molecular weight conjugated polymers afford processability, they are generally amorphous or exhibit improper ordering of their crystalline domains thereby limiting the mobility of charge carriers. The present work highlights random D-A supramolecular comb polymers formed between donor molecules based on OPV (named **OPVCN-OH**) and acceptor molecules based on PBI (named **UPBI-PDP**), which were designed with hydroxyl moieties at one of their termini to form complexes with P4VP. A series of random D-A supramolecular comb polymers were formed by varying the ratios of **UPBI-PDP** and **OPVCN-OH** with P4VP. Complex formation was confirmed by FT-IR and ^{1}H NMR spectroscopy; solid state supramolecular structural characterization was carried out by small angle X-ray scattering (SAXS) and wide angle X-ray diffraction (WXRD) experiments. A D-A small molecular complex was also formed without P4VP so as to compare the self-organizing behavior of the D-A assembly in the presence and absence of the templating polymer. Transmission electron microscopy (TEM) was used to determine thin film morphology of the supramolecular D-A polymer complexes as well as the D-A small molecule complex. The effect of the nanoscopic D-A self-assembly on the bulk mobility of the material was probed using SCLC measurements. The random D-A supramolecular comb polymers exhibited

lamellar organization in the size range < 10 nm as confirmed by TEM images and improved electron and hole transport ability compared to the pristine molecules.

4.3 Experimental

4.3.1 Materials:

Aldrich chemicals required for the synthesis were used as received. All solvents used were of analytical grade and were carefully dried before use. Procedure for the synthesis of the unsymmetrical oligo(*p*-phenylenevinylene) (**OPVCN-OH**) is described in section **4.3.4**.

4.3.2 Instrumentation Techniques:

The details of the instrumentation techniques used for the characterization of the small molecules and complexes like the FTIR spectroscopy, ^{1}H NMR, MALDI-TOF, Wide Angle X-ray Diffractograms (WXRD), Transmission Electron microscopy (TEM) and Gel Permeation Chromatography (GPC) were exactly identical as explained in chapter 2 and chapter 3. Small angle X-ray scattering (SAXS) was employed to investigate the phase behavior of the complexes. The scattering experiments were conducted on a three pinhole collimated Bruker Nanostar machine equipped with rotating copper anode, operating at 45 kV and 100 mA providing characteristic Kα radiation of 1.54 Å. The measurements were carried out in the normal resolution mode having a q range of 0.011–0.2 $Å^{-1}$. The bulk sample was taken in between two Kaptan film. The scattered data was collected using a 2-D Histar detector and later converted from 2D to 1D by azimuthal averaging using Bruker software. 1D data presented after background subtraction is plotted as I v/s q, where $q = (4\pi/\lambda) \sin\theta$, λ is the wavelength of the incident X-rays and 2θ is the scattering angle. A Perkin-Elmer Lambda 35 UV spectrophotometer was used for measuring absorption spectrum. Steady-state fluorescence studies and time-resolved fluorescence lifetime measurements were conducted on a Horiba Jobin Yvon Fluorolog 3 spectrophotometer having a 450 W Xenon lamp. The steady-state emission and fluorescence lifetime decay analysis were carried out in DMF as well as in thin film drop casted from DMF. Throughout the experiments, emission and excitation slit width was maintained at 1 nm, and the data were obtained in "S1/R1" mode.

4.3.3 SCLC Device Fabrication:

The ITO and glass substrate was cleaned in distilled water, detergent, deionised water, acetone and isopropyl alcohol for 10 min each with ultrasonication. The cleaned substrates were kept in oven at 100 °C for 45 min. The SCLC mobilities of the pristine and composites films were determined using the following diode configuration for hole-

only device ITO/PEDOT:PSS/active layer/Au and for electron only device Al/polymer/Al sandwiched structures. Composites solutions were drop casted from DMF (Dimethylformamide) on ITO/PEDOT:PSS (for hole mobility) and Al (for electron mobility). The drop casted substrates were annealed on a hot plate at 60°C for 30 min followed by drying in vacuum at 10^{-1} mbar pressure for 3 hrs to completely remove the solvent. 100 nm Au and Al layer were deposited for hole-only and electron-only device respectively through a shadow mask on top of the composite layers by thermal evaporation in vacuum chamber at 10^{-6} mbar. The current and voltage (J-V) were measured using an Agilent semiconductor parameter analyser model 4156 C and semiprobe probe station. The hole and electron mobility was determined by fitting the J-V curve into the Mott-Gurney law.

$$J = \varepsilon_0 \varepsilon_r \mu (9V^2/8L^3)$$

Where ε_0 is the permittivity of the free space (8.854 x 10^{-12} F/m), ε_r is the relative dielectric constant of the thin film which is assumed to be 3 (a typical value for organic semiconductor) μ is the charge carrier (hole and electron) mobility, V is the voltage drop across the device and L is the thickness of the organic composites layer.

4.3.4 Synthesis

(i) Synthesis of Unsymmetrical OPVCN-OH:

(a) Synthesis of para-MEM-oxy benzaldehyde:

Para hydroxy benzaldehyde (0.5 gm; 4.1x10^{-3} mol) and dry THF was taken in a one necked round bottom flask and kept under nitrogen (N_2) atmosphere. In another two necked round bottom flask, sodium hydride (NaH) (0.19gm; 8.2x10^{-3} mol) was taken under N_2 atmosphere to which dry THF was added. The para hydroxy benzaldehyde (solution in THF) was then added to the NaH/THF solution under N_2 atmosphere, under ice-cold condition. 2-Ethoxymethoxy ethylene chloride (MEM-Cl) (0.71mL; 6.15 mol) was added to the resultant reaction mixture under N_2 atmosphere. After addition the reaction was brought to room temperature and stirred for further 12 hr. The crude mixture was purified using column chromatography (10 % Pet ether Ethyl acetate mixture). Yield = 70 %. FT-IR (ATR eco ZnSe, cm^{-1}) = 2883, 2821, 2739, 1686, 1598, 1580, 1503, 1453, 1426, 1394, 1366, 1308, 1229, 1158, 1099, 1027, 970, 830, 757, 731, 657. ^{1}H NMR (200 MHz, $CDCl_3$, δ): 9.92 (s, 1H; CHO), 7.90-7.83 (td, 2H; CH), 7.22-2.17 (td, 2H; CH), 5.38 (s, 1H), 3.86 (m, 2H), 3.59 (m, 2H), 3.39 (s, 3H) ppm.

(b) Synthesis of Phosphonium salt of Methyl 4-(bromomethyl) benzoate:

Methyl 4-(bromomethyl) benzoate (1gm; $4.0x10^{-3}$ mol) was taken in a one necked round bottom flask to which was added the reagent triethylphosphite, $P(OEt)_3$ (1.03mL; $6.0x10^{-3}$ mol). The reaction mixture was heated to 130-140 ^oC in an oil bath under N_2 atmosphere and stirred for 24 hr. Vacuum distillation was done to remove the excess $P(OEt)_3$. Yield > 95 %. FT-IR (ATR eco ZnSe, cm^{-1}) = 3455, 2985, 2913, 1717, 1611, 1437, 1277, 1243, 1185, 1106, 1018, 955, 866, 807, 764, 700, 633. ^1H NMR (200 MHz, $CDCl_3$, δ): 7.96 (d, 2H); 7.34 (d, 2H); 3.97 (m, 4H); 3.86 (s, 3H); 3.21 (d, 2H); 1.19 (t, 6H) ppm.

(c) Synthesis of MEM-UOPV2-COOMe (Wittig Horner Reaction):

NaH (0.38 gm; $1.56x10^{-2}$ mol) was taken in a two necked round bottom flask under nitrogen atmosphere. Phosphonate ester of Methyl 4-(bromomethyl) benzoate (0.73 gm; $2.4x10^{-3}$ mol) and Para MEM-oxy benzaldehyde (0.5 gm; $2.4x10^{-3}$ mol) were taken in another one necked round bottom flask under N_2 atmosphere. Dry THF was added to both round bottom flasks under N_2 atmosphere. The mixture of aldehyde and phosphonium salt was added to the NaH under N_2 atmosphere at 0 ^oC. After addition the resultant reaction mixture was stirred for 1-2 hr. After removing the ice bath the reaction was further stirred for 12 hr. After completion of the reaction (which was followed by thin layer chromatography - TLC), the product was purified by crystallization from cold methanol (MeOH). Yield = 25 %. Melting Point = 115 ^0C. FT-IR (ATR eco ZnSe, cm^{-1}) = 3407, 2922, 2852, 2813, 2063, 1932, 1712, 1592, 1507, 1433, 1368, 1277, 1243, 1167, 1105, 962, 874, 841, 811, 763, 718, 696, 665, 638. ^1H NMR (200 MHz, $CDCl_3$, δ): 8.02-6.95 (m, 10H); 5.29 (s, 2H); 3.91 (s, 3H); 3.81 (m, 2H); 3.53 (m, 2H); 3.37 (s, 3H) ppm. ^{13}C NMR (200 MHz, $CDCl_3$, δ): 166.89, 157.35, 142.07, 130.64, 129.97, 128.54, 128.00, 126.04, 116.46, 93.34, 71.56, 67.69, 59.00, 52.01 ppm. MALDI-TOF MS (Calcd m/z 342.38); Found m/z – 341.89 [M], 364.87 [M+Na], 381.17 [M+K].

(d) Reduction of MEM-UOPV2-COOMe by Lithium Aluminium Hydride (LAH):

LAH (0.08 gm; $2.2x10^{-3}$ mol) was taken in a two necked round bottom flask under N_2 atmosphere. MEM-OPV2-COOMe (0.3 gm; 8.8 $x10^{-4}$ mol) was dissolved in dry THF under N_2 atmosphere. MEM-OPV2-COOMe solution in THF was added to the LAH under N_2 atmosphere at 0 ^oC. After addition, ice bath was removed and stirred further for 6-7 hr at room temperature and reaction followed by TLC. After completion of the reaction the product was obtained as a white crystalline material, giving single spot in TLC and used as such for the next step. Yield > 95 %. Melting Point = 130 ^oC. FT-IR (ATR eco ZnSe, cm^{-1}) = 3290, 3021, 2922, 2872, 2854, 2812, 1680, 1599, 1574, 1511,

1454, 1415, 1365, 1297, 1244, 1200, 1162, 1111, 1029, 988, 967, 828, 777, 725, 638, 608. ^{1}H NMR (200 MHz, $CDCl_3$, δ): 7.50-6.92 (m, 10H); 5.28 (s, 2H); 4.69 (s, 2H); 3.83 (m, 2H); 3.55 (m, 2H); 3.37 (s, 3H) ppm. ^{13}C NMR (200 MHz, $CDCl_3$, δ): 156.85, 139.93, 136.92, 131.15, 128.08, 127.61, 127.30, 126.39, 116.39, 93.36, 71.54, 67.61, 65.02, 58.95, 29.64 ppm. MALDI-TOF MS (Calcd m/z 314.37); Found m/z – 314.10 [M], 337.08 [M+Na], 353.38 [M+K].

(e) Synthesis of MEM-UOPV2-CHO:

MEM-OPV2-CH_2OH (0.15gm; $4.8x10^{-4}$ mol), MnO_2 (0.21 gm; $2.4x10^{-3}$ mol) (activated), $KMnO_4$ (0.076 gm; $4.8x10^{-3}$ mol) were taken in a one necked round bottom flask. Dry DCM was added to the solid mixture under N_2 atmosphere and stirred for 48 hr at room temperature. The product was passed through sintered funnel with cilate. The final product was obtained as a green colored solid and used as such without further purification for the next step. Yield > 95 %. Melting Point = 60 ^{0}C. FT-IR (ATR eco ZnSe, cm^{-1}) = 3029, 2922, 2853, 2732, 1745, 1691, 1593, 1564, 1508, 1457, 1419, 1388, 1304, 1219, 1163, 1100, 983, 875, 830, 801, 732, 703, 653, 624. ^{1}H NMR (200 MHz, $CDCl_3$, δ): 10.00 (s, 1H); 7.89-7.02 (m, 10H); 5.32 (s, 2H); 3.85 (m, 2H); 3.58 (m, 2H); 3.40 (s, 3H) ppm.

(f) Synthesis of 4-(Bromo methyl) benzonitrile:

4-(Hydroxy methyl) benzonitrile (2.0 gm; $1.5x10^{-2}$ mol) and carbon tetra bromide (CBr_4) (5.5 gm; $1.65x10^{-2}$ mol) were taken in a two neck round bottom flask and triphenyl phosphine (PPh_3) (4.3 gm; $1.65x10^{-3}$ mol) was taken in a solid addition funnel. Dry DCM was added to the solid mixture under N_2 atmosphere. PPh_3 was added slowly by solid addition funnel at room temperature. The resultant reaction mixture was stirred further for 8 hr at room temperature and reaction followed by TLC. The product was purified through silica column with pet ether and ethyl acetate (5 %) as mobile phase. Yield > 95 %. FT-IR (ATR eco ZnSe, cm^{-1}) = 3359, 2963, 2922, 2853, 2220, 1931, 1643, 1501, 1411, 1262, 1223, 1094, 841, 805, 728, 687. ^{1}H NMR (200 MHz, $CDCl_3$, δ): 7.66 (d, 2H); 7.51 (d, 2H); 4.47 (s, 2H) ppm.

(g) Synthesis of phosphonate ester of 4-(Bromo methyl) benzonitrile:

4-(Bromo methyl) benzonitrile (0.44 gm; $2.22x10^{-3}$ mol) was taken in a one necked round bottom flask to which was added the reagent tryethylphosphite, $P(OEt)_3$ (0.76 mL; $4.45x10^{-3}$ mol). This reaction mixture was heated to 130-140 ^{o}C in an oil bath under N_2 atmosphere and stirred for 24 hr. Vacuum distillation was done to remove the excess $P(OEt)_3$. Yield > 95 %. FT-IR (ATR eco ZnSe, cm^{-1}) = 3451, 2985, 2914, 2228,

1608, 1505, 1449, 1397, 1234, 1163, 1097, 1018, 956, 855, 784, 727. ^{1}H NMR (200 MHz, $CDCl_3$, δ): 7.52 (d, 2H); 7.30 (d, 2H); 3.98 (m, 4H); 3.16 (d, 2H); 0.99 (t, 6H) ppm.

(h) Synthesis of MEM-UOPV3-CN:

NaH (0.45 gm; $1.87x10^{-2}$ mol) was taken in a two necked round bottom flask under nitrogen atmosphere. MEM-OPV2-CHO (0.9 gm; $2.88x10^{-3}$ mol) and Phosphonate ester of 4-(Bromo methyl) benzonitrile (1.21 gm; $2.88x10^{-3}$ mol) were taken in a one necked round bottom flask under N_2 atmosphere. Dry THF was added to both round bottom flask under N_2 atmosphere. The mixture of aldehyde and phosphonium salt was added to the NaH under N_2 atmosphere at 0 ^{o}C. After addition, the resultant reaction mixture was stirred for 1-2 hr. After removing the ice bath the reaction was further stirred for 12 hr. After completion of the reaction (followed by TLC) the product was purified by column chromatography (silica as stationary phase) (Petether:DCM = 50:50). Yield = 80 %. Melting Point > 200 ^{0}C. FT-IR (ATR eco ZnSe, cm^{-1}) = 3385, 3016, 2925, 2879, 2809, 2215, 1592, 1509, 1458, 1419, 1301, 1245, 1168, 1113, 1023, 969, 834. ^{1}H NMR (200 MHz, $CDCl_3$, δ): 7.66-6.93 (m, 14H); 5.29 (s, 2H); 3.28 (m, 2H); 3.56 (m, 2H); 3.37 (s, 3H) ppm. ^{13}C NMR (200 MHz, $CDCl_3$, δ): 157.08, 141.88, 137.99, 135.21, 132.47, 131.99, 131.03, 128.71, 127.76, 127.26, 126.70, 126.32, 119.04, 116.46, 110.43, 93.39, 71.59, 67.68, 59.01 ppm. MALDI-TOF MS (Calcd m/z 411.49); Found m/z – 411.05 [M].

(i) Synthesis of OPVCN-OH:

(0.1 gm; 2.43×10^{-4} mole) MEM-UOPV3-CN (this compound was synthesised using reported procedure)[1]was taken in a one necked round bottom (RB) flask. It was dissolved in dicholoro methane (DCM) at room temperature. Trifluoro acetic acid (TFA) (0.14 gm; 1.21×10^{-3} mole) was added to it and stirred for 24 hr at room temperature. After 24 hr, the reaction mixture was filtered through whatman filter paper and washed several times with DCM. The product was dried and soxhlet extraction was done using chloroform ($CHCl_3$) for 7 days to remove unreacted precursor (MEM-UOPV3-CN). The pure product was dried again in vaccum oven for 48 hr at a temperature of 55 °C. Then this dried product was used for further studies. Yield = 80 %. Melting Point > 200 °C. FT-IR (ATR eco ZnSe, cm^{-1}) = 3397, 3355, 3192, 3092, 3032, 2951, 2900, 2835, 2322, 2245, 1927, 1922, 1835, 1791, 1734, 1677, 1642, 1590, 1517, 1453, 1422, 1362, 1349, 1285, 12134, 1221, 1173, 1107, 969, 876, 840, 723, 625. ^{1}H NMR(400 MHz, $CDCl_3$, δ): 7.80-6.75 (m, 16H) ppm.^{13}C NMR(400 MHz, $CDCl_3$, δ): 157.49, 142.04, 137.87, 135.03, 132.66, 131.97, 128.99, 128.03, 127.41, 127.07, 126.47, 126.26, 124.61, 119.12, 116.39,

115.61, 109.29 ppm. MALDI-TOF MS (Calcd Mol Wt: 323.38); found Mol Wt: 323.34 [M], 361.96 [M+K], HRMS in acetonitrile for $C_{23}H_{17}ON$ (calcd m/z: 323.1310); Found m/z: 323.1308.

(ii) Synthesis of unsymmetrical perylenebisimide UPBI-PDP:

(a) Synthesis of 4-amino-3-pentadecyl phenol:

This particular synthesis was described in chapter 3 in section 3.3.5 (a). Yield: 75 %. FT-IR (ATR eco ZnSe, cm^{-1}): 3434, 3349, 3298, 1644, 1583, 1419, 1336, 912,730, 678. ^{1}H NMR (200 MHz, $CDCl_3$, δ): 7.22 (d, 1H), 6.56-6.44 (m, 2H), 2.68 (t, 2H), 1.63 (t, 2H), 1.37–1.21 (m, 24H), 0.87 (t, 3H) ppm. ^{13}C NMR (200 MHz, $CDCl_3$, δ): 147.9, 138.1, 125.9, 118.0, 111.9, 30.5, 29.9, 23.2, 14.7 ppm. MALDI-TOF MS (Calcd Mol Wt: 319.29); found Mol Wt: 320.37 [M+1].

(b) Synthesis of symmetrical 2-ethylhexyl perylenebisimide molecule:

PTCDA (10 gm, 2.55 x 10^{-2} mole), 2-ethyl-1-hexylamine (6.59 gm, 5.09 x 10^{-2} mole) and 0.5 gm $Zn(OAc)_2$ were taken in a round bottom flask, and N,N'-Dimethylacetamide (DMAc) (~ 500 ml) was added to it. The resultant solution was stirred for 10-12 hours at 110 °C. After completion of the reaction, DMAc was removed by vacuum distillation and HCL (400mL, 2N) was added to the solid mixture and stirred for 3-4 hr. The resultant solution was filtered using vacuum filtration and the dark red precipitate was washed thoroughly with water and methanol. This solid mass was dried in air and further dried in vacuum oven at 110 °C. Yield: 95 %. FT-IR (ATR eco ZnSe, cm^{-1}): 2957, 2929, 2852, 1710, 1657, 1602, 1577, 1514, 1448, 1334, 1252, 1185, 1088, 1022, 794, 744, 648. ^{1}H NMR (200 MHz, $CDCl_3$, δ): 8.62 (m, 8H), 4.13(m, 4H), 1.21 (m, 2H), 0.97-0.86 (t, 12H), 1.46-1.30 (m, 16H) ppm. ^{13}C NMR (200 MHz, $CDCl_3$, δ): 160.1, 135.9, 131.1, 129.6, 48.0, 36.7, 32.0, 29.6, 23.2, 15.1 ppm. MALDI-TOF MS (Dithranol matrix); (Calcd Mol Wt: 614.77); found Mol Wt: 615.89 [M+1].

(c) Synthesis of mono 2-ethylhexyl unsymmetrical perylene imide anhydride:

Symmetrical ethylhexyl perylenebisimide (6.0 gm, 9.76 x 10^{-3} mole) was dispersed in 170 mL tertiary butanol (t-BuOH) and refluxed with solid KOH (5.48 gm, 9.76 x 10^{-2} mole) until the solution turned wine red color. The hot reaction mixture was slowly cooled to room temperature and stirred further with 100 mL acetic acid (AcOH) and 300 mL 2N HCl for 3-4 hours. The reaction mixture was filtered and washed thoroughly with water until the filtrate was neutral. This solid mass was dried further in vacuum oven at 120 °C for 24 hours. The product was purified by column chromatography (silica as a stationary phase) ($CHCl_3$/ Acetic acid 10:1). Yield: 55 %.

FT-IR (ATR eco ZnSe, cm^{-1}): 2958, 2936, 2853, 1775, 1736, 1712, 1660, 1600, 1583, 1509, 1450, 1333, 1253, 1185, 1090, 1020, 795, 744, 649. ^{1}H NMR (200 MHz, $CDCl_3$ + TFA, 298K) δ: 8.79 (m, 8H), 4.13 (m, 2H), 1.96 (m, 1H), 1.47-1.30 (m, 16H), 0.95-0.86 (t, 6H) ppm. ^{13}C NMR (200 MHz, $CDCl_3$+ TFA) δ: 161.0, 150.1, 131.5, 130.1, 130.0, 124.1, 56.3, 32.0, 29.9, 27.1, 25.2, 22.9, 15.2 ppm. MALDI-TOF MS (Dithranol matrix); (Calcd Mol Wt: 503.54); found Mol Wt: 526.44 [M+Na].

(d) Synthesis of unsymmetrical perylenebisimide UPBI-PDP:

The unsymmetrical imide-anhydride perylene (5 gm, 9.93 x 10^{-3} mole), 4-amino-3-pentadecylphenol (4.76 gm, 1.49 x 10^{-2} mole) and 0.3 gram $Zn(OAc)_2$ were taken in a single necked round bottom flask along with 35 gram of imidazole. The resultant solid mixture was heated up to 160 °C and stirred further for 8 hours at that temperature under N_2 atmosphere. After completion, reaction mixture was cooled down to room temperature and stirred further with 2N HCl for 4-5 hours. The dark red precipitate was filtered under vacuum and washed repeatedly with water and methanol and dried in vacuum oven at 120 °C. Column chromatography was used to purify the product (silica as a stationary phase) ($CHCl_3$ as mobile phase). Yield: 60 %. M.P.: 320 °C. FT-IR (ATR eco ZnSe, cm^{-1}): 3367, 3110, 3048, 2970, 2938, 2867, 1707, 1664, 1595, 1504, 1468, 1445, 1407, 1356, 1305, 1259, 1186, 1100, 1026, 977, 862, 810, 750, 724, 636. ^{1}H NMR (200 MHz, $CDCl_3$, δ): 8.73-8.58 (m, 8H), 6.70–7.15 (m, 3H), 4.16 (m, 2H), 2.38 (t, 2H), 1.96 (m, 1H), 0.81-1.43 (m, 43H) ppm. ^{13}C NMR (200 MHz, $CDCl_3$, δ): 166.5, 165.6, 162.3, 157.1, 156.0, 145.1, 134.7, 131.3, 130.9, 128.5, 125.7, 126.2, 121.6, 114.3, 106.5, 54.9, 33.1, 32.0, 30.1, 28.1, 22.6, 14.8. MALDI-TOF MS (Dithranol matrix); (Calcd Mol Wt: 805.05); found Mol Wt: 806.46 [M+1], 828.45 [M+Na].

4.3.5 Sample Preparation:

The donor and acceptor small molecules - **OPVCN-OH** and **UPBI-PDP** were dried at 60 °C in vacuum oven for 2 days. The random D-A complexes were prepared by first dissolving **OPVCN-OH** and **UPBI-PDP** in dry DMF followed by addition of required amount of P4VP in DMF. The resultant solution was stirred at 55 °C for 24 h. Afterwards the solvent was slowly evaporated on a petri dish on a hot plate at 65 °C and dried further in vacuum oven at 65 °C for 2 days. The dried complex was stored in desiccator. Apart from the mixed D-A complexes, the 100 % complex of donor

(**OPVCN-OH**) and acceptor (**UPBI-PDP**) with P4VP were also prepared by maintaining the same reaction conditions as described above.

4.4 Results and Discussion

4.4.1 Synthesis and Characterization

The acceptor molecule - **UPBI-PDP** based on unsymmetrical perylenebisimide was designed with one side hydrogen bondable unit and synthesized as described in section 4.3.4. The donor molecule – **OPVCN-OH** based on oligo(*p*-phenylene vinylene) (OPV) was designed with cyanide (CN) group at one end and hydrogen bondable hydroxyl unit at the other termini. It was synthesized as mentioned in section 4.3.4. The structure of **OPVCN-OH** was confirmed based on ^{1}H and ^{13}C NMR, MALDI-TOF (Figure-4.1a, b and 4.2a) measurements and purity was confirmed by single peak in the size exclusion chromatogram (SEC recorded in DMF, Figure 4.2b). Figure 4.1a shows the labeled proton NMR spectra of **OPVCN-OH**. Due to poor solubility in chloroform, the ^{1}H NMR spectra of **OPVCN-OH** was recorded in deuterated dimethyl sulfoxide (DMSO-d_6). The OPV aromatic protons appeared in the range 7.80-6.75 ppm. The structure and purity of **UPBI-PDP** was confirmed by ^{1}H NMR, MALDI-TOF and gel permeation chromatography as shown in figure 4.3, 4.4a, 4.4b respectively. Supramolecular complexes of **OPVCN-OH** and **UPBI-PDP** with P4VP were prepared by dissolving

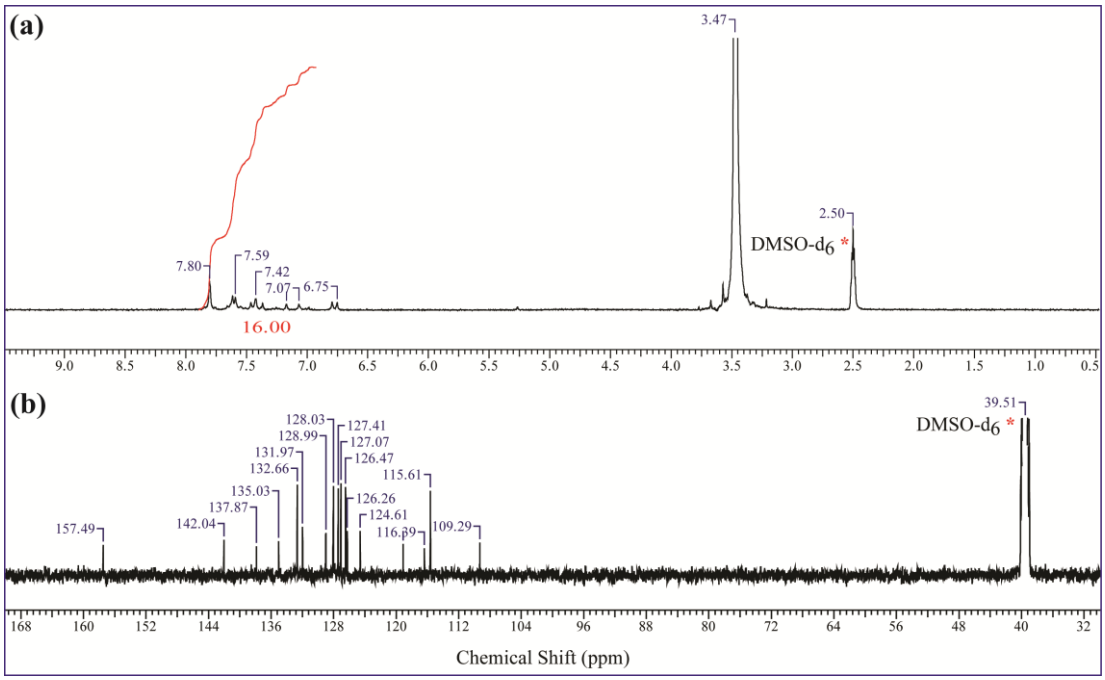

Figure 4.1: (a) ^{1}H NMR and (b) ^{13}C NMR spectra of **OPVCN-OH** in DMSO-d_6.

various molar ratios of **OPVCN-OH**, **UPBI-PDP** and P4VP in minimum amount of dry N, N-dimethyl formamide (DMF), stirring at 55 °C for 24 h (Scheme 4.1), followed by heating to remove solvent and further drying in vacuum at 55 °C for 48 h. For the D-A

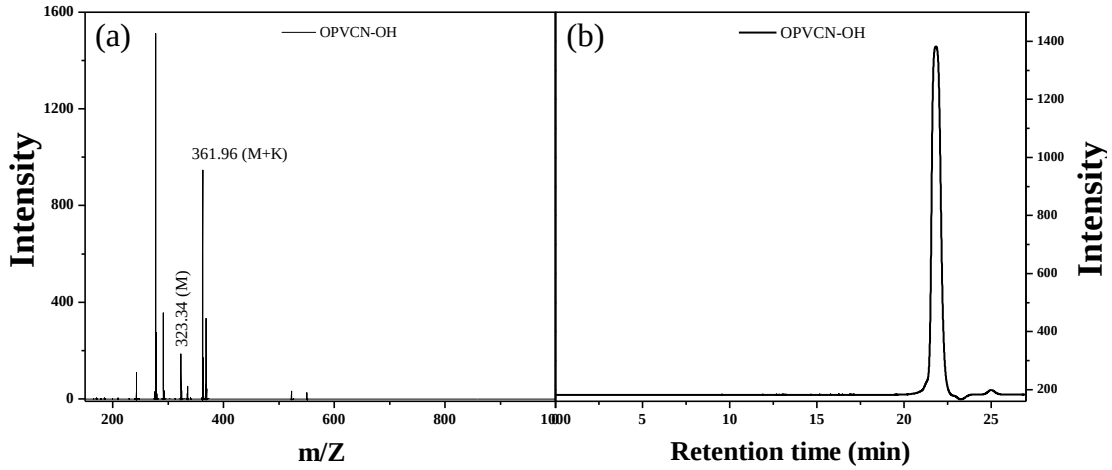

Figure 4.2: (a) MALDI-TOF and (b) Gel permeation Chromatography **(**recorded in DMF) of **OPVCN-OH**

random supramolecular comb polymer complexes, the total molar ratio of **OPVCN-OH + UPBI-PDP** was fixed to be 1.00, which was complexed with 1.00 molar equivalent of P4VP. Thus, **P4VP(OPV$_{0.25}$ + UPBI$_{0.75}$)**, **P4VP(OPV$_{0.50}$ + UPBI$_{0.50}$)** and **P4VP(OPV$_{0.75}$ + UPBI$_{0.25}$)** were prepared (note that for reasons of simplification, the name **OPVCN-OH** and **UPBI-PDP** have been shortened to OPV and UPBI respectively in the complexes).

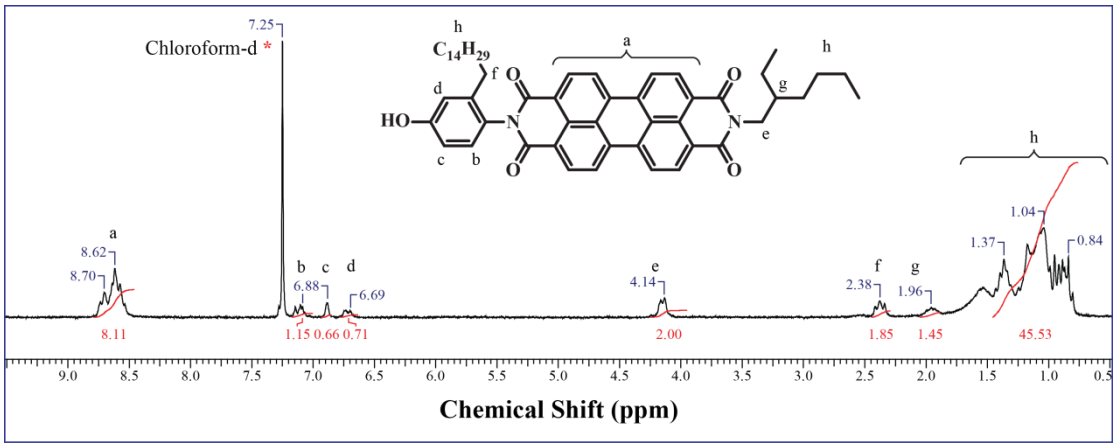

Figure 4.3: (a) ^{1}H NMR spectra of **UPBI-PDP** in $CDCl_3$.

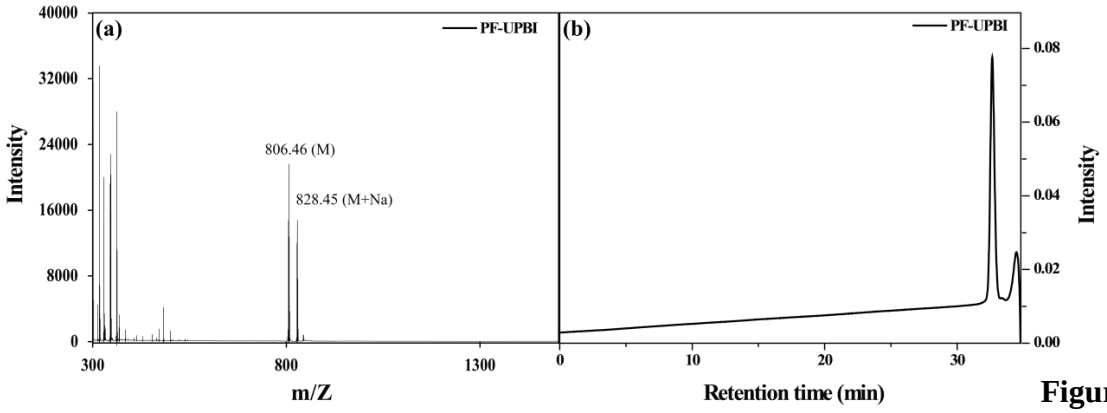

Figure 4.4: (a) MALDI-TOF and (b) Gel permeation Chromatography **(**recorded in THF) of **UPBI-PDP**

The subscripts in all complexes denoted the theoretical molar ratio of **UPBI-PDP** and **OPVCN-OH** with P4VP polymer. A 1:1 complex of **OPVCN-OH** with P4VP i.e., **P4VP(OPV$_{1.00}$)** was also prepared following the same procedure, but without **UPBI-PDP**. The complementary 100 % acceptor-P4VP complex **P4VP(UPBI$_{1.00}$)** was also freshly prepared and the data has been included in the discussions for sake of comparison. Although **OPVCN-OH** had very poor or no solubility in chloroform, its complexes with P4VP were completely soluble in chloroform; therefore structural characterization using proton NMR spectra in $CDCl_3$ was possible. The improved solubility could be considered as preliminary evidence for complex formation. A 1:1 (molar) donor-acceptor complex of

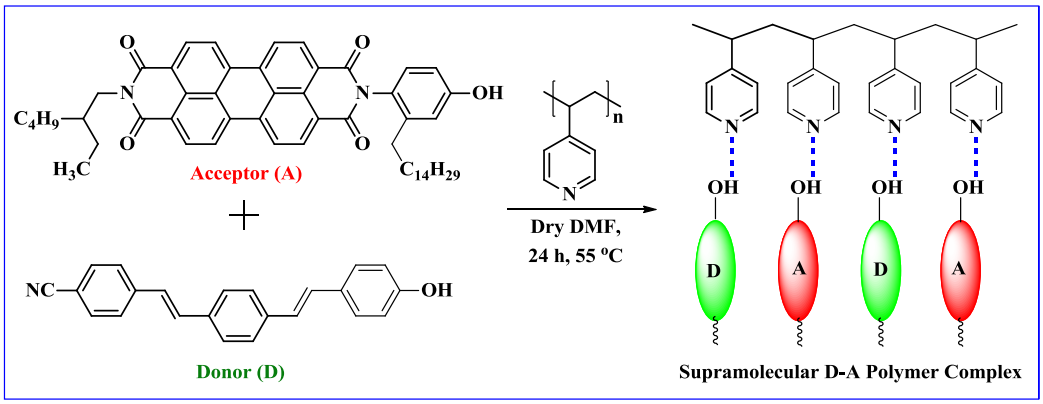

Scheme 4.1: Synthesis of supra molecular polymer complexes **P4VP(OPV$_x$+UPBI$_y$)**, where 'x' and 'y' = 1.0, 0.75, 0.50, 0.25, 0.00 and 'x+y' = 1.

D and A alone without P4VP was prepared **(OPV$_{0.50}$ + UPBI$_{0.50}$)** following the same experimental procedure as that for the **P4VP(OPV$_{0.50}$ + UPBI$_{0.50}$)** complex except that P4VP was not added. Figure 4.5 compares the proton NMR spectra of P4VP and

P4VP(OPV$_{1.00}$) in $CDCl_3$, where the spectrum of **OPVCN-OH** in DMSO-d_6 also was included for comparison. P4VP exhibited two broad NMR signals at 6.38 and 8.32 ppm corresponding to four aromatic protons of pyridine ring, which showed an upfield shift to

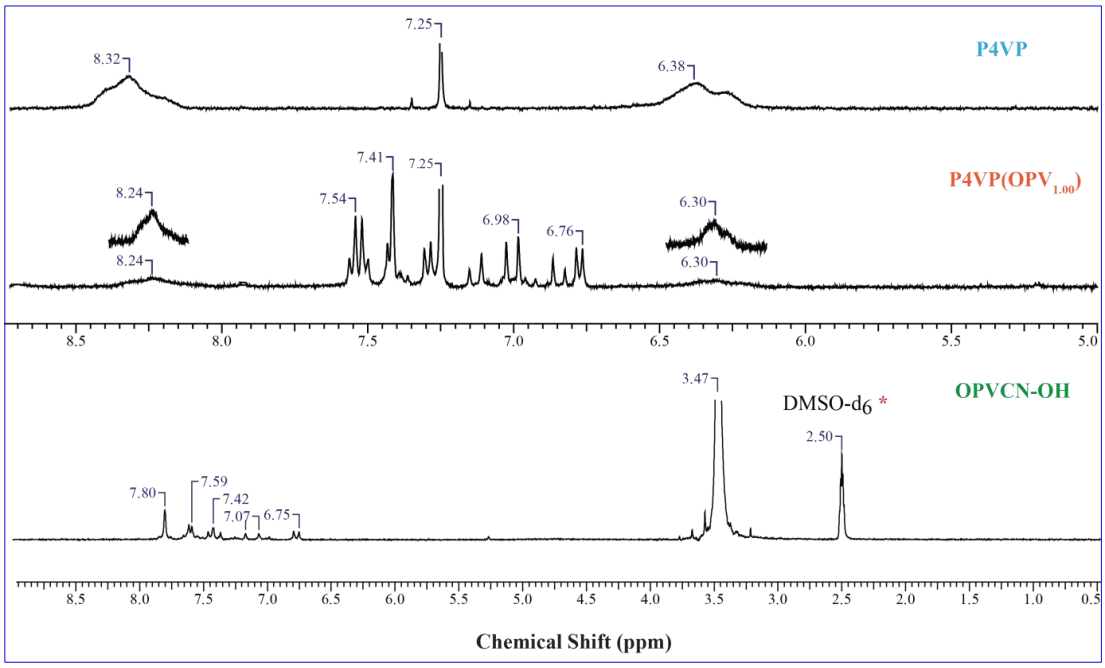

Figure 4.5: ^{1}H NMR spectra of **OPVCN-OH** in DMSO-d_6; P4VP(OPV$_{1.00}$) and P4VP in $CDCl_3$.

6.30 and 8.24 ppm upon complex formation. Figure 4.6 compares the expanded aromatic region (6-9.5 ppm) in the proton NMR spectra of the small molecule D-A complex as well as the mixed D-A complexes with P4VP and both the 100 % complexes - **P4VP(UPBI$_{1.00}$)** and **P4VP(OPV$_{1.00}$)** recorded in $CDCl_3$ at a concentration of ~4 mg/mL (the full range NMR spectra are given in Figure 4.7). The proton NMR spectra of the 100 % acceptor-P4VP complex **P4VP(UPBI$_{1.00}$)** at high concentrations (15 mg/mL) exhibited broadening of the aromatic peaks of the perylene along with upfield chemical shift compared to the pristine **UPBI-PDP** molecule. Considering the lower solubility of the mixed complexes, the proton NMR spectra of **P4VP(UPBI$_{1.00}$)** was also recorded at lower concentrations at which the changes in chemical shift were not so obvious. The effect of the presence of **UPBI-PDP** on the chemical shift of **OPVCN-OH** could be very clearly traced from the proton NMR spectra of the D-A complexes. For instance, **OPVCN-OH** had sharp peaks in the region 7.38-7.54 ppm in its 100% complex with P4VP- **P4VP(OPV$_{1.00}$)**, where **UPBI-PDP** did not exhibit any peaks. A significant downfield shift was observed for these peaks, in the mixed complexes, which are traced

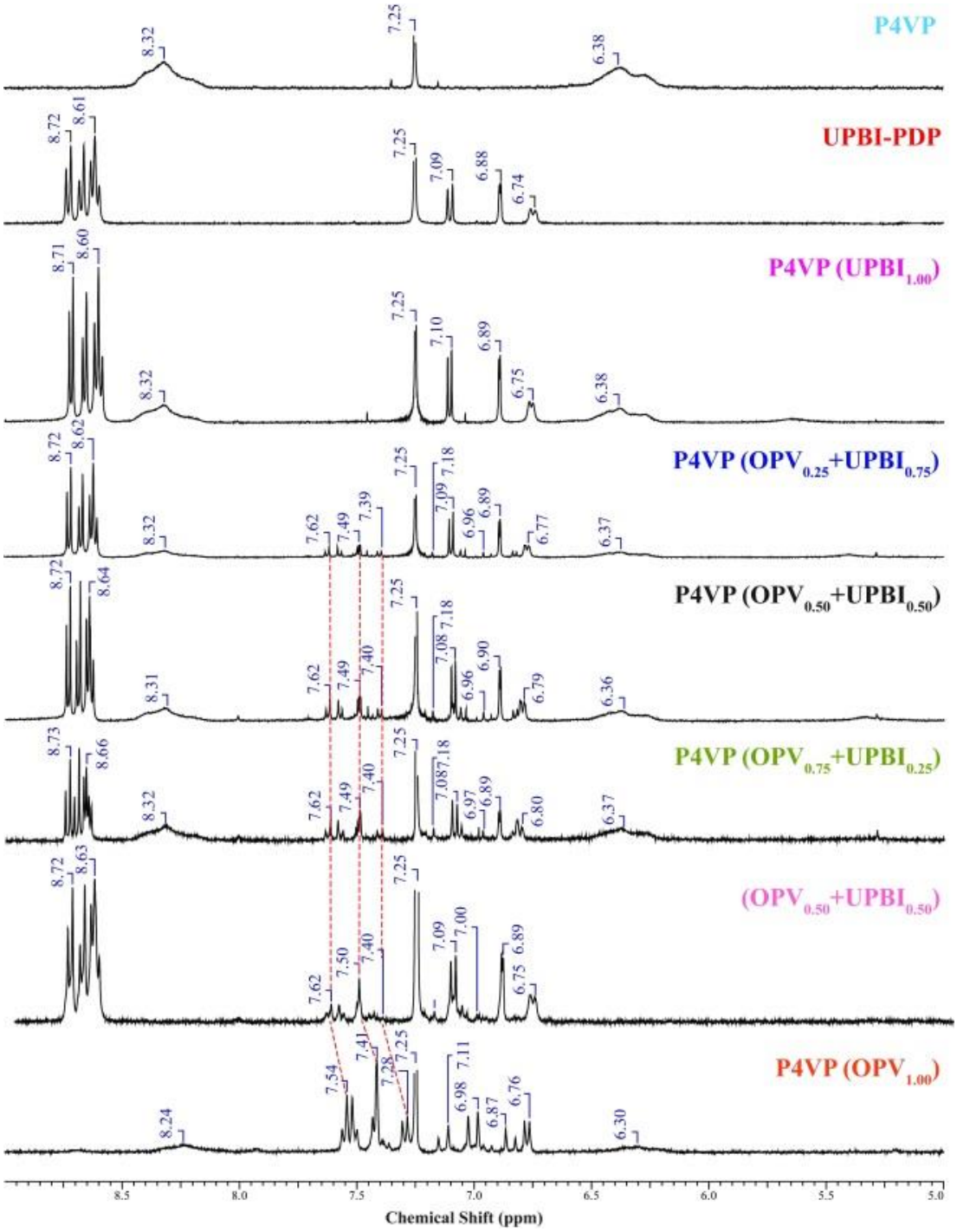

Figure 4.6: Expanded aromatic region in the ^{1}H NMR spectra of complexes in $CDCl_3$; concentration ~4 mg/mL.

by dotted lines in the figure 4.6. Addition of 25 mole % **UPBI-PDP** into **P4VP(OPV$_{1.00}$)** resulted in a downfield shift of the peaks at 7.54, 7.41 and 7.28 ppm to 7.62, 7.49 and 7.40 ppm respectively. Similar shifts were observed for the aromatic proton peaks corresponding to the pentadecyl phenol moiety of **UPBI-PDP** at 6.75 ppm; however the

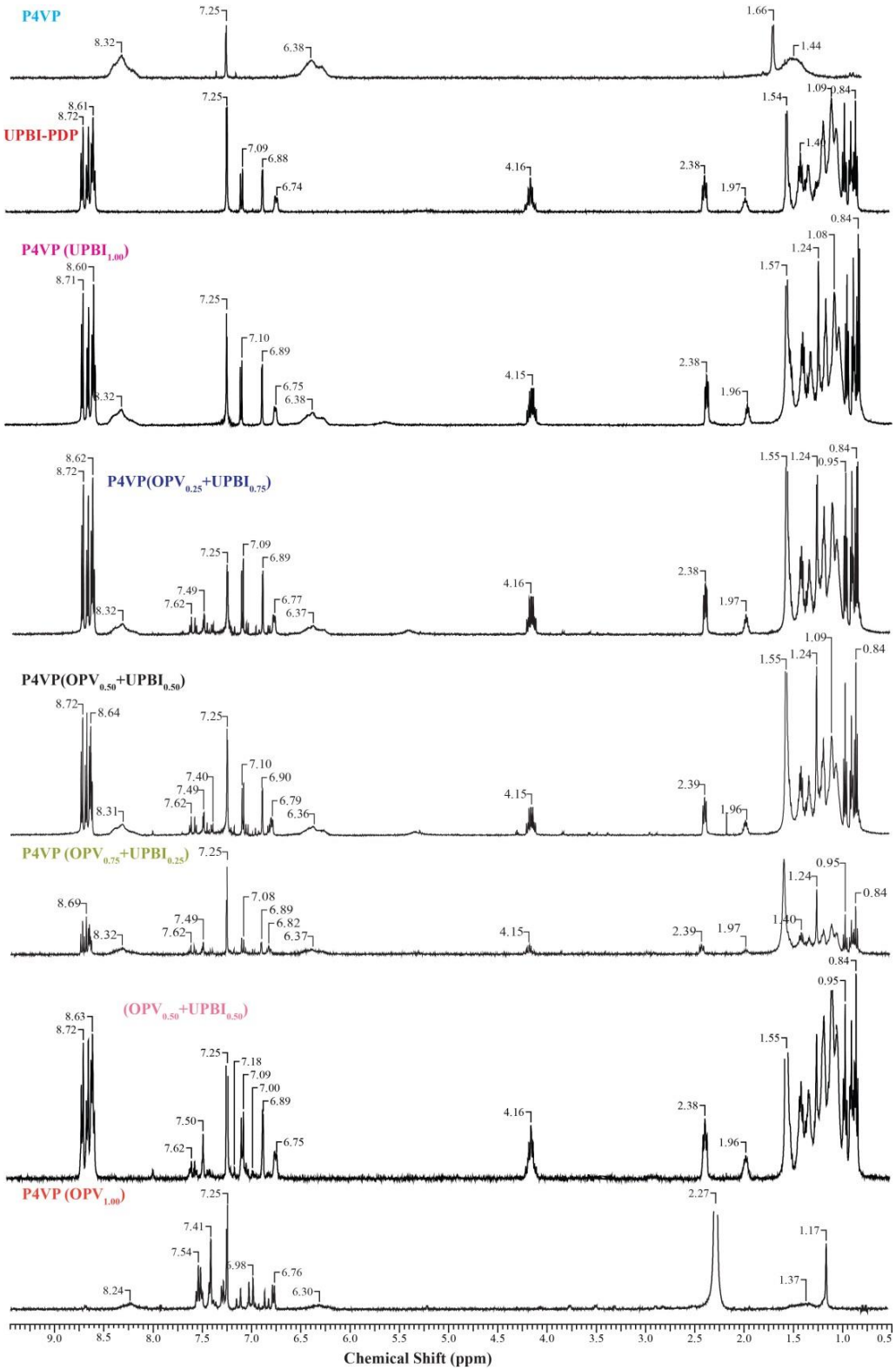

Figure 4.7: Comparison of ^{1}H NMR spectra (0.50-9.50 ppm) of all complexes with P4VP.

peaks below 7.25 ppm were overlaid by peaks from both **UPBI-PDP** and **OPVCN-OH** making it difficult to assign the peaks clearly. It was noticeable that the OPV protons

exhibited similar shifts in its small molecule complex with perylenebisimide even in the absence of P4VP. Comparing the proton NMR spectra of **($OPV_{0.50}$ + $UPBI_{0.50}$)** with that of **P4VP($OPV_{0.50}$ + $UPBI_{0.50}$)**, the proton shifts were similar in both spectra, except for the lower intensity for the OPV protons in the former due to the comparatively lower solubility of **OPVCN-OH**. In all its complexes irrespective of small molecule or polymeric, the entire aromatic protons of **OPVCN-OH** were affected by the presence of the **UPBI-PDP**. In contrast, only the pentadecyl phenol moiety seemed to register the presence of the rigid aromatic molecules of **OPVCN-OH** with the perylene aromatic protons remaining almost unaffected in the mixed complexes. This could be due to the fact that the pentadecyl phenol moiety and the perylene aromatic core were out of plane (90°) with respect to each other.

Formation of the complex could also be confirmed by FTIR spectroscopy. In general, the absorption at 993 cm^{-1} in **P4VP** is assigned to the pyridine ring stretching vibration (ν_1 vibrational band).[32] Figure 4.8a compares the expanded region from 1020-959 cm^{-1} in the normalized FTIR spectra of P4VP, **OPVCN-OH** and **P4VP($OPV_{1.00}$)** highlighting the shift in the pyridine ring stretching vibration upon complex formation. Pristine **OPVCN-OH** and **UPBI-PDP** did not have any peaks in this region. Upon complex formation a shift to higher frequency (997 cm^{-1}) was observed for the pyridine ring stretching band. Similar shifts to higher frequency were also observed in the case of the mixed complexes. P4VP has other characteristic pyridine vibrational bands at 1556 cm^{-1}, 1490 cm^{-1} etc, which were shifted or altered in the complexes as shown in figure 4.8b and 4.8c; however these regions were complicated by characteristic vibrations of **OPVCN-OH** and **UPBI-PDP** also. The shift in the hydroxyl band of the phenolic moiety can also be examined to trace the hydrogen bonding interaction. Feng-Chih Chang et.al studied the hydrogen bonding interaction between P4VP and Novalac type phenolic resin, which is known to contain free phenol groups using FTIR spectroscopy.[33] They observed the free phenolic stretching band as a shoulder at 3525 cm^{-1} and a broad band centered at 3450 cm^{-1} was observed from hydrogen bonded hydroxyl band in the phenolic resin. Upon interaction with pyridine units from P4VP, this hydroxyl band shifted further to lower wavenumbers at 3250 cm^{-1}. The average hydrogen bonding strength for the pyridine / phenolic interaction is higher compared to phenolic/phenolic interaction. Figure 4.8d shows the expanded region from 4000-2800 cm^{-1} in the FTIR spectra of all mixed D-A complexes (including 100 % complex of **OPVCN-OH** and **UPBI-PDP**) along with

their pristine molecules **OPVCN-OH** and **UPBI-PDP**. The spectrum of P4VP also is included for comparison. **OPVCN-OH** showed a sharp band at 3349 cm^{-1} (phenolic/phenolic) with a shoulder at 3394 cm^{-1} (free hydroxyl). In the 100 % complex with P4VP, an overall broadening was observed in this range; however a sharp peak was noticeable at 3324 cm^{-1}. The pristine **UPBI-PDP** did not exhibit two peaks in the 4000-2800 cm^{-1} range; only a single sharp band was observed at 3378 cm^{-1}. In its 100 % complex with P4VP, a shift was observed to lower wavenumber at 3364 cm^{-1}. In the mixed complexes, the peak position of the broad hydroxyl band was observed (figure 4.8d) in between that for the pristine **UPBI-PDP** and **OPVCN-OH** molecules.

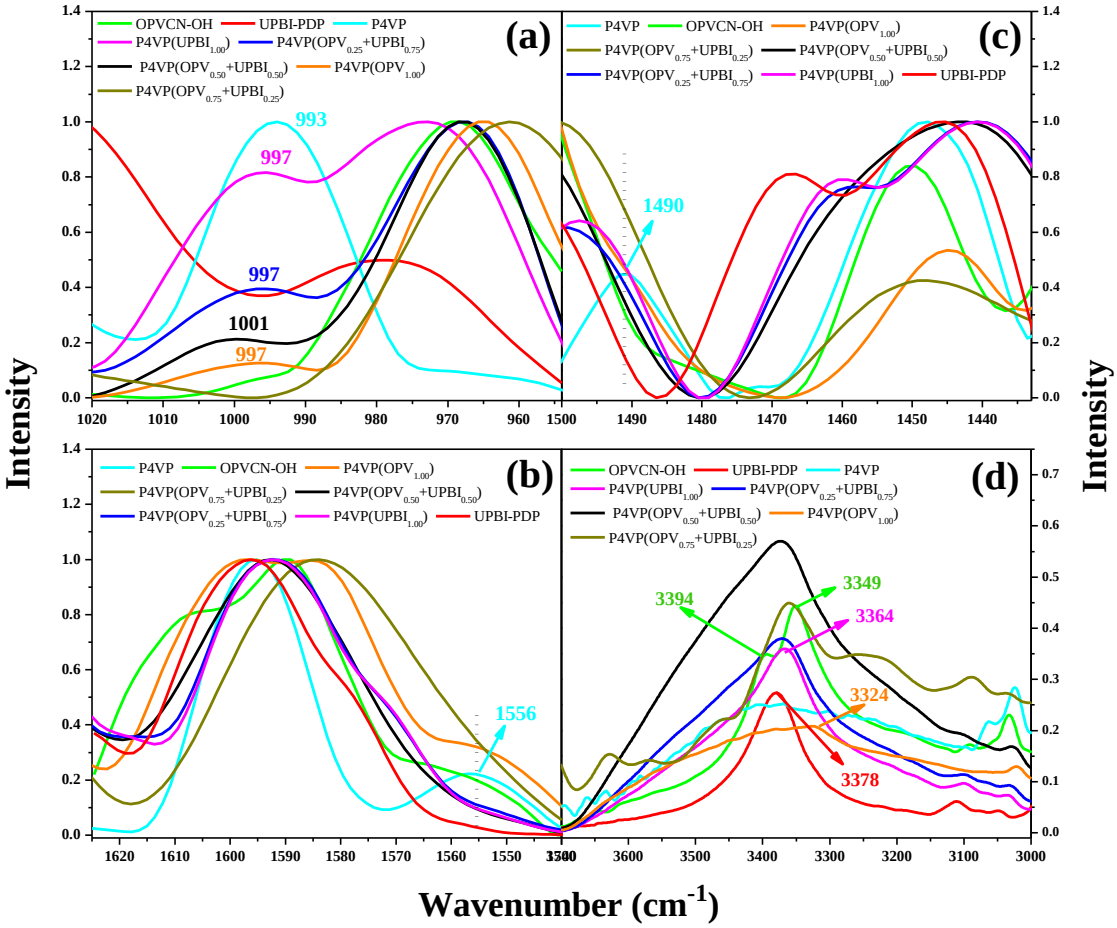

Figure 4.8: FT-IR spectra of **OPVCN-OH**, **UPBI-PDP** and all complexes with P4VP.

4.4.2 Absorption and Emission in Thin Films

Solutions of the pristine donor and acceptor molecules were prepared in DMF as solvent maintaining 0.1 OD at the absorption maxima of the OPV molecule i.e. 380 nm or 525 nm for the PBI molecule. Thin films also were prepared by drop casting from DMF, where the concentration was maintained at 2 mg/mL. Figure 4.9a shows the normalized

absorption spectra of the pristine donor and acceptor molecules in DMF solution as well as in the form of thin drop cast films. In solution **OPVCN-OH** exhibited absorption maximum at 380 nm, which was blue shifted to 330 nm in the film indicating aggregation.[34, 35] **UPBI-PDP** exhibited typical features of perylenebisimide absorption with peaks at 525, 490 and 459 nm in DMF solution. However, in thin film drop cast from DMF, the pattern was totally different with blue shifted peak maxima and presence of additional red shifted peak. The aggregation pattern of **UPBI-PDP** in thin film exhibited features of both H (blue shifted 0-0 absor-

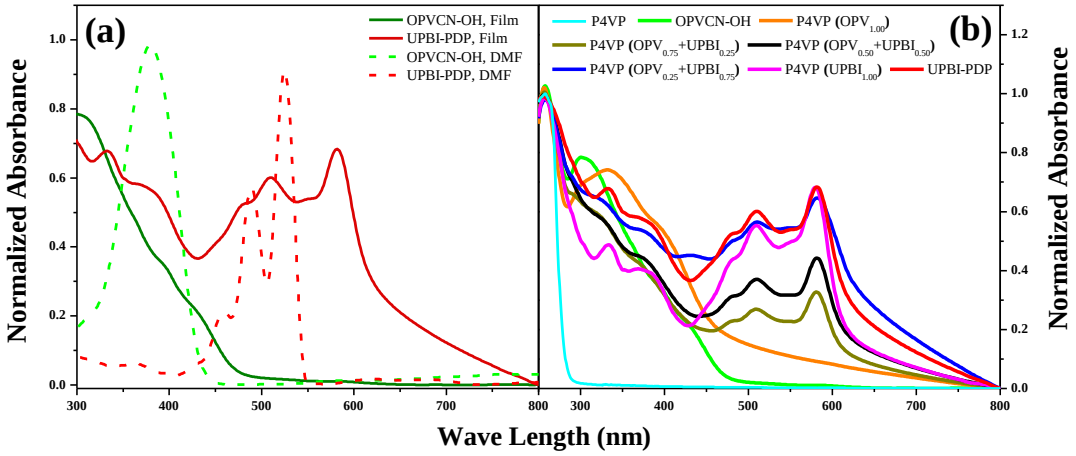

Figure 4.9: Normalized absorption spectra of (a) **OPVCN-OH** and **UPBI-PDP** in DMF solution (straight line) as well as in thin drop cast films (dotted line). (b) drop cast films (from DMF) of P4VP, **OPVCN-OH**, **UPBI-PDP** and all complexes with P4VP

ption band) and J (appearance of new red shifted bands around 560 and 580 nm) type aggregates.[36-38] However, we have attributed it to H type aggregates based on elaborate solution studies involving variable temperature absorption studies etc, which were reported previously.[39] The absorption spectra of drop cast films of the 100 % P4VP complexes of the donor and acceptor as well as that for the mixed D-A complexes are shown in figure 4.9b. Since the mobility measurements and powder XRD data (to be discussed later on) were taken for samples in the solid state, the photophysical data of the various complexes in film form is presented here. The absorption spectrum of P4VP alone is included in the figure 4.9b for the sake of comparison. The absorption spectra of the mixed D-A complexes indicated similar features as that of the pristine molecules, with no charge transfer band present indicating absence of any interaction between the donor and acceptor in the ground state. In thin films all the mixed complexes indicated aggregated nature for both donor and acceptor units. Figure 4.10 shows the emission spectra of films

of all D-A P4VP complexes along with that of **OPVCN-OH** and **UPBI-PDP**. Figure 4.10d shows the emission with peak around 510-520 nm and 500 nm for **OPVCN-OH** and **P4VP(OPV$_{1.00}$)** respectively upon excitation at 330 nm. Figure 4.10e and figure 4.10f shows the excitation of **UPBI-PDP** and **P4VP(UPBI$_{1.00}$)** at the OPV absorption wavelength of 330 nm, exhibiting intense emission indicating that selective excitation of the donor was not possible in the mixed D-A complexes. Aggregated perylene emission beyond 600 nm was observed upon excitation at 330 nm. Direct excitation of perylene chromophore ~ 500 nm also resulted in the aggregate emission with peak maximum at 607 nm with almost similar intensity as that for the indirect excitation at 330 nm. Figure 4.10a-10c compares the emission from the mixed D-A complexes upon excitation at the

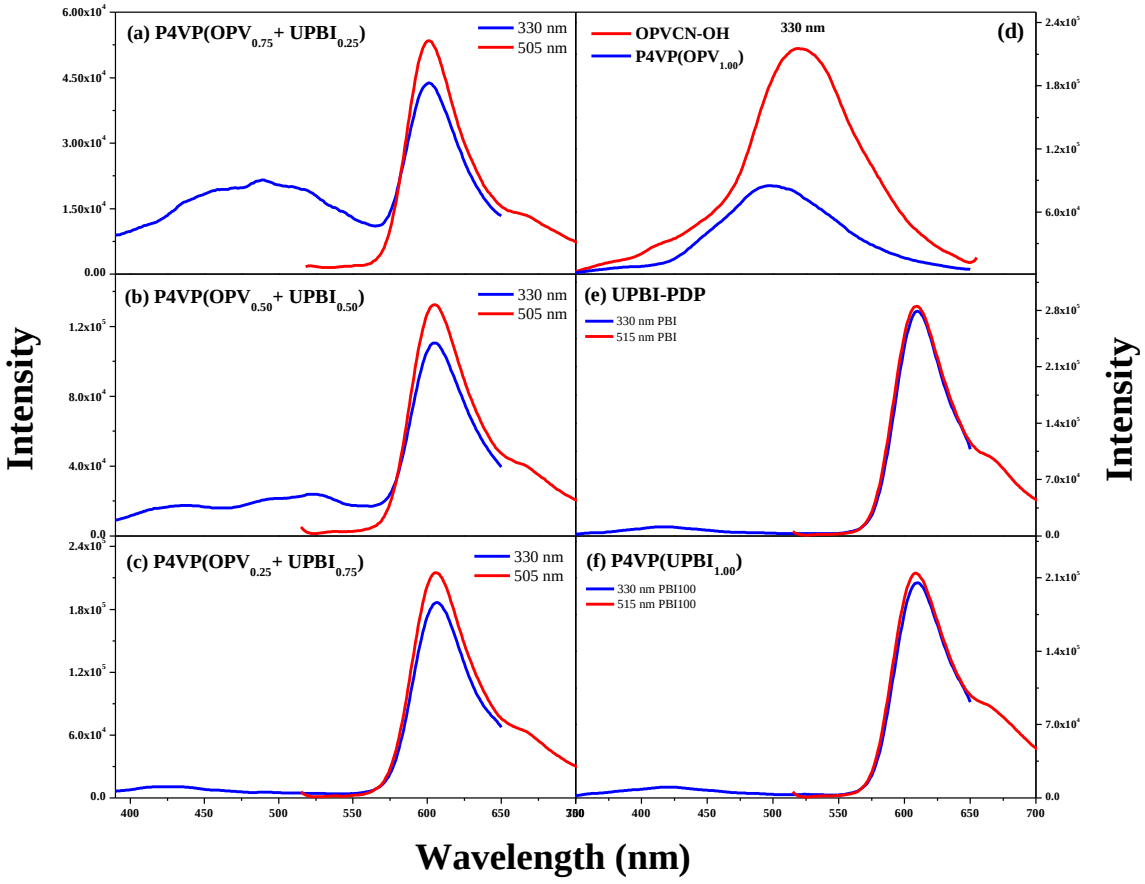

Figure 4.10: Fluorescence spectra of (a) **P4VP(OPV$_{0.75}$ + UPBI$_{0.25}$)**, (b) **P4VP(OPV$_{0.50}$ + UPBI$_{0.50}$)**, (c) **P4VP(OPV$_{0.25}$ + UPBI$_{0.75}$)**, (d) **OPVCN-OH**, **P4VP(OPV$_{1.00}$)**, (e) **UPBI-PDP** and (f) **P4VP(UPBI$_{1.00}$)** recorded as thin films drop cast from DMF excited at different wavelengths.

OPV absorption wavelength (330 nm) and at the perylene absorption wavelength ~ 500 nm. Direct excitation at the perylene absorption wavelength ~ 500 nm resulted in

aggregate emission beyond 600 nm for all the mixed D-A complexes. Upon excitation at 330 nm, aggregate emission of perylene was observed beyond 600 nm for the complex with lowest OPV content i.e. **P4VP(OPV$_{0.25}$ + UPBI$_{0.75}$)**. As the OPV amount increased, OPV emission in the 400 – 550 nm region also increased as observed in **P4VP(OPV$_{0.50}$ + UPBI$_{0.50}$)**, and **P4VP(OPV$_{0.75}$ + UPBI$_{0.25}$)**.

4.4.3 WXRD Analysis

Micro structure analysis of the complexes was done by both wide angle X-ray diffraction (WXRD) and small angle X-ray scattering (SAXS) in powder state at room temperature in the range 2θ = 0.1-35°. Figure 4.11 show the SAXS scattering plot for all the complexes along with that of P4VP and both pristine D and A molecules. **UPBI-PDP** had a first order peak at q = 0.1901 Å^{-1}, while **OPVCN-OH** had a first order peak of low intensity at q = 0.1516 Å^{-1}. These maxima of **OPVCN-OH** and **UPBI-PDP** corresponded to 'd' spacing of 41.42 Å and 33.03Å respectively. The peak at d spacing 41.42 Å corresponding to **OPVCN-OH** was completely absent in **P4VP(OPV$_{1.00}$)** as well as the mixed D-A complexes. Figure 4.12 shows the WXRD

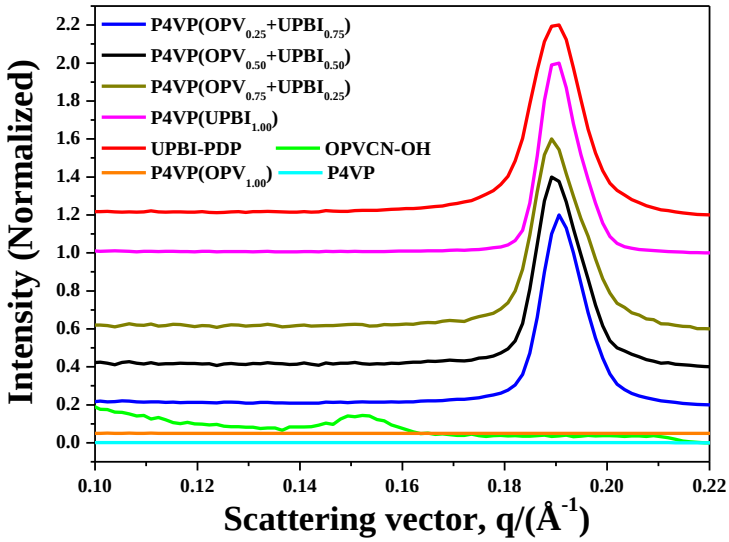

Figure 4.11: SAXS pattern of different complexes with P4VP: **P4VP(UPBI$_{1.00}$)**; **P4VP(OPV$_{0.25}$+UPBI$_{0.75}$)**; **P4VP(OPV$_{0.50}$+UPBI$_{0.50}$)**; **P4VP(OPV$_{0.75}$+UPBI$_{0.25}$)**; **P4VP(OPV$_{1.00}$)**.

plot covering the wide angle region 2θ = 2-33° of all complexes. Both **OPVCN-OH** and **UPBI-PDP** were crystalline with several sharp peaks in the entire region of 2θ = 2-33°, whereas P4VP was completely amorphous in nature.[16] Figure 4.12a shows the expanded 2θ region from 2-6.5°, to get a clear view of the 2θ < 3° range. The first diffraction peak

at 2θ = 2.10° (d = 41.96 Å) (observed at q = 0. 1516 $Å^{-1}$ in the SAXS plot) for pristine **OPVCN-OH** was partially cut in the WXRD. The observation of the disappearance of the first peak of **OPVCN-OH** at 2θ = 2.10° (d = 41.96 Å) upon complex formation in **P4VP(OPV$_{1.00}$)** from SAXS was confirmed in the WXRD pattern also. The first diffraction for **P4VP(OPV$_{1.00}$)** was observed at 2θ = 3.59° (d = 24.57 Å). The SAXS exp-

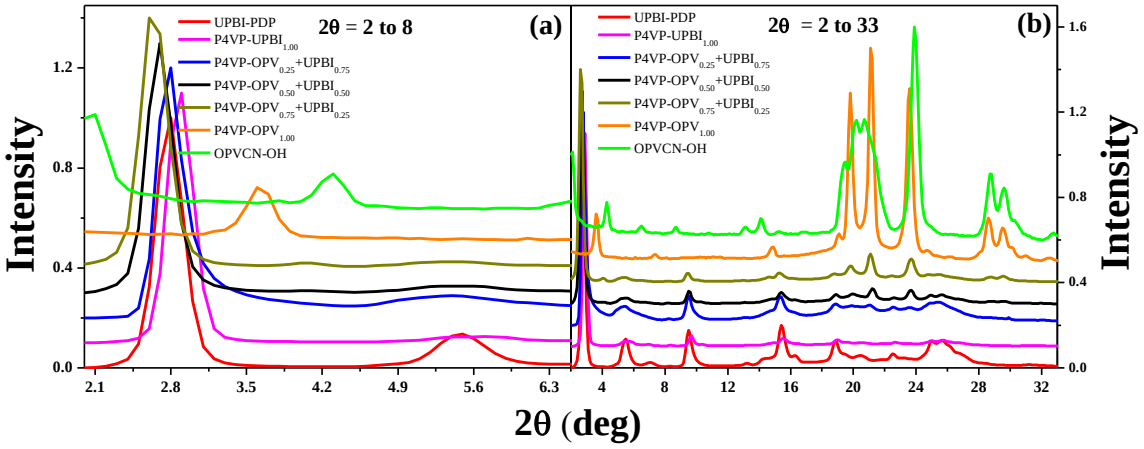

Figure 4.12: WXRD of **OPVCN-OH**, **UPBI-PDP** and different complexes with P4VP: **P4VP(UPBI$_{1.00}$)**; **P4VP(OPV$_{0.25}$+UPBI$_{0.75}$)**; **P4VP(OPV$_{0.50}$+UPBI$_{0.50}$)**; **P4VP(OPV$_{0.75}$+UPBI$_{0.25}$)**; **P4VP(OPV$_{1.00}$)**. (a) 2θ = 2-6.5° and (b) 2θ = 2-33°.

eriment had confirmed the absence of any reflection below 2θ = 2°. Comparing the plots for **OPVCN-OH** and **P4VP(OPV$_{1.00}$)**, (figure 4.13a) it could be seen that the peak positions were altered for the latter in the entire 2θ = 2-35° region. **OPVCN-OH** showed a sharp high intense reflection at 2θ = 23.92° (*d* = 3.71 Å), which could be considered as

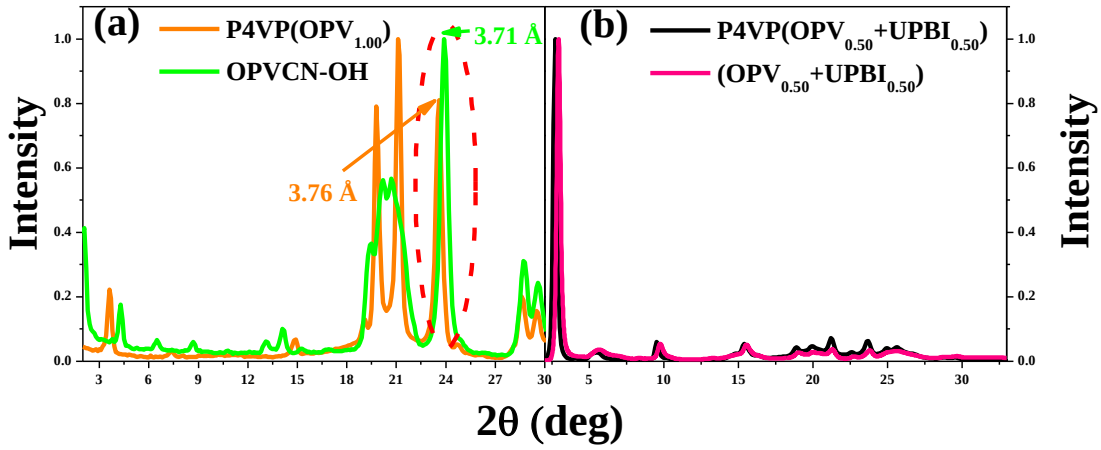

Figure 4.13: (a) Comparison of WXRD plot of **OPVCN-OH** and **P4VP(OPV$_{1.00}$)**. (b) Comparison of WXRD plot of (**OPV$_{0.50}$ + UPBI$_{0.50}$**) with P4VP(**OPV$_{0.50}$ + UPBI$_{0.50}$**).

the π-π stacking length in the crystal lattice[40] (as indicated by arrow in figure 4.13a). Complex formation with P4VP altered the crystal packing of **OPVCN-OH**, as indicated by the altered peak pattern in **P4VP(OPV$_{1.00}$)**. The π-π stacking distance increased to *d* = 3.76 Å (2θ = 23.62°) indicated by the dotted circle in figure 4.13a, to accommodate the polymer chains of P4VP. The Figure 4.12 also shows the diffraction pattern for all the mixed D-A complexes. The low angle region in the WXRD pattern of the mixed complexes was dominated by the intense reflection corresponding to **UPBI-PDP**, which showed a gradual increase in d spacing from 30.29 Å to 33.32 Å in going from the 100 % PBI complex **P4VP(UPBI$_{1.00}$)** to the mixed complex with highest OPV content i.e. **P4VP(OPV$_{0.75}$ + UPBI$_{0.25}$)**. This reflection lay in between that of the pristine **UPBI-PDP** and **OPVCN-OH** molecules of 31.49 Å to 41.96 Å respectively. The peak pattern of the mixed D-A complexes were not a simple sum of the reflections of the individual pristine D or A molecule, but were shifted compared to either of the parent molecules. For instance, the π-π stacking distance of *d* = 3.71 Å in **OPVCN-OH** increased to *d* = 3.76 Å (2θ = 23.64°) in the mixed D-A complexes. The altered powder XRD pattern in the mixed D-A complexes indicated altered packing which was not only influenced by the polymer chains but also by the presence of each other. The fact that the packing of the donor and acceptor were affected by the presence of each other even in the absence of P4VP could be established by studying the WXRD data of the **(OPV$_{0.50}$ + UPBI$_{0.50}$)**, which did not have the polymer template of P4VP. Figure 4.13b compares the WXRD pattern of **(OPV$_{0.50}$ + UPBI$_{0.50}$)** with that of **P4VP(OPV$_{0.50}$ + UPBI$_{0.50}$)**. Although peak patterns were similar, small shift was observed in the d spacing for the peak corresponding to the perylene bisimide at *d* = 30.03 Å (2θ = 2.94°). This indicated that the packing of the molecules were affected by the presence of each other. The table 4.1(a-h) gives the d spacing calculated for all the complexes and pristine molecules. It could be seen from the data in the table that the peak positions for **(OPV$_{0.50}$ + UPBI$_{0.50}$)** was different compared to **P4VP(OPV$_{0.50}$ + UPBI$_{0.50}$)** as well as pristine **OPVCN-OH** and **UPBI-PDP**. The notable observation from the WXRD pattern of the mixed D-A complexes was the retention of the crystalline nature of the donor and acceptor components in all of them despite the presence of the amorphous P4VP chains. It has generally been understood with small surfactant molecule-P4VP complexes that, upon interaction with the polymer back bone, the small surfactant molecules can restrict the polymer chain motion and influence the overall packing.[15] Diffraction packing distances are affected by the perfect

balance between the polymer chain and interactive surfactant. Additionally, tabulating the d spacing in the complexes indicated a layered periodicity as detailed in the Table 4.1. Among the different complexes, the 100 % P4VP-donor complex - **P4VP(OPV$_{1.00}$)** exhibited the highest periodic structure (up to 5th order). TEM images (to be discussed below) also confirmed the clear lamellar structure of all complexes.

Table 4.1: Wide angle X-ray diffraction (WXRD) data os (a) **UPBI-PDP**, (b) **OPVCN-OH** and different complexes with P4VP: (c) **P4VP(UPBI$_{1.00}$)**, (d) **P4VP(OPV$_{1.00}$)**, (e) **P4VP(OPV$_{0.25}$+UPBI$_{0.75}$)**, (f) **P4VP(OPV$_{0.75}$+UPBI$_{0.25}$)**, (g) **P4VP(OPV$_{0.50}$+UPBI$_{0.50}$)**, (h) **(OPV$_{0.50}$+UPBI$_{0.50}$)**.

(a) UPBI-PDP			**(b) OPVCN-OH**		
Sl No	**2θ (deg)**	**d-Spacing (Å)**	**Sl No**	**2θ (deg)**	**d-Spacing (Å)**
1	2.80	31.49	1	2.10	41.96
2	5.49	16.06	2	4.29	20.56
3	7.10	12.44	3	6.53	13.52
4	9.51	9.29	4	8.76	10.08
5	13.22	6.69	5	13.10	6.75
6	14.39	6.15	6	14.15	6.25
7	15.45	5.73	7	15.29	5.79
8	16.35	5.42	8	19.54	4.54
9	18.88	4.69	9	20.20	4.39
10	19.51	4.54	10	20.73	4.28
11	20.45	4.34	11	23.92	3.71
12	22.56	3.94	12	28.74	3.10
13	24.99	3.56	13	29.66	3.01
14	25.69	3.46	14	30.37	2.94
15	26.17	3.40	15	32.78	2.73
16	26.77	3.33	--	--	--

(c) P4VP(UPBI$_{1.00}$)			(d) P4VP(OPV$_{1.00}$)		
Sl No	**2θ (deg)**	**d-Spacing (Å)**	**Sl No**	**2θ (deg)**	**d-Spacing (Å)**
1	2.91	30.29	1	3.59	24.57
2	5.44	16.21	2	7.36	11.99
3	5.81	15.21	3	14.89	5.94
4	8.40	10.51	4	19.11	4.64
5	9.69	9.12	5	19.85	4.47
6	14.92	5.93	6	21.17	4.19
7	15.50	5.71	7	23.62	3.76
8	16.38	5.40	8	24.71	3.59
9	19.00	4.67	9	28.66	3.11
10	19.58	4.53	10	29.53	3.02
11	20.55	4.32	11	30.15	2.96
12	22.70	3.91	12	31.02	2.88
13	25.00	3.56	13	32.56	2.74
14	25.71	3.46	--	--	--
15	26.75	3.33	--	--	--

(e) P4VP(OPV$_{0.25}$+UPBI$_{0.75}$)			(f) P4VP(OPV$_{0.75}$+UPBI$_{0.25}$)		
Sl No	**2θ (deg)**	**d-Spacing (Å)**	**Sl No**	**2θ (deg)**	**d-Spacing (Å)**
1	2.91	30.29	1	3.59	24.57
2	5.43	16.26	2	4.06	21.76
3	8.25	10.70	3	5.51	16.01
4	9.55	9.25	4	8.23	10.73
5	13.16	6.72	5	9.45	9.35
6	15.36	5.78	6	14.64	6.04
7	18.93	4.68	7	15.32	5.77
8	19.87	4.46	8	18.82	4.71
9	21.13	4.20	9	19.79	4.48
10	22.62	3.93	10	21.10	4.20
11	23.64	3.76	11	22.51	3.95
12	24.98	3.56	12	23.68	3.75
13	25.45	3.49	13	24.80	3.58
--	--	--	14	25.47	3.49
--	--	--	15	28.83	3.09
--	--	--	16	29.60	3.01

(g) P4VP($OPV_{0.50}$+$UPBI_{0.50}$)			(h) ($OPV_{0.50}$+$UPBI_{0.50}$)		
Sl No	**2θ (deg)**	**d-Spacing (Å)**	**Sl No**	**2θ (deg)**	**d-Spacing (Å)**
1	2.92	30.26	1	2.94	30.03
2	4.09	21.56	2	4.49	19.65
3	5.55	15.92	3	5.59	15.80
4	6.88	12.83	4	7.26	12.18
5	8.41	10.50	5	8.38	10.55
6	9.59	9.21	6	9.73	9.09
7	10.33	8.55	7	10.59	8.35
8	13.14	6.73	8	14.13	6.26
9	14.84	5.96	9	13.32	6.64
10	15.40	5.75	10	14.44	6.13
11	16.29	5.43	11	15.51	5.71
12	18.89	4.69	12	16.51	5.37
13	19.97	4.44	13	19.01	4.67
14	21.20	4.18	14	19.92	4.45
15	22.58	3.93	15	20.47	4.34
16	23.64	3.76	16	22.66	3.92
17	24.98	3.56	17	23.79	3.74
18	25.61	3.47	18	24.82	3.58
19	26.67	3.34	19	25.58	3.48
20	28.90	3.08	20	27.13	3.28
21	29.57	3.02	21	28.79	3.10
--	--	--	22	29.73	3.00

4.4.4 Thin Film Morphology

Thin film morphology of all complexes was analyzed by transmission electron microscopy (TEM). All the complexes were drop cast (1 mg/ml) on copper (Cu) TEM grids from dimethylformamide (DMF) as a solvent. Selective staining of the **P4VP** polymer was done with the help of iodine (I_2) vapor to get better contrast.[41] Figure 4.14 shows nice lamellar morphology on TEM grids in the length scale of < 5 nm. The dark line corresponded to **P4VP** polymer backbone selectively stained by I_2 vapor and the bright line corresponded to **OPVCN-OH** and **UPBI-PDP** molecules. The statistically averaged line thickness of the dark and bright lines in TEM images of the complexes was determined from the histogram of instrument software, which is given in table 4.2. It

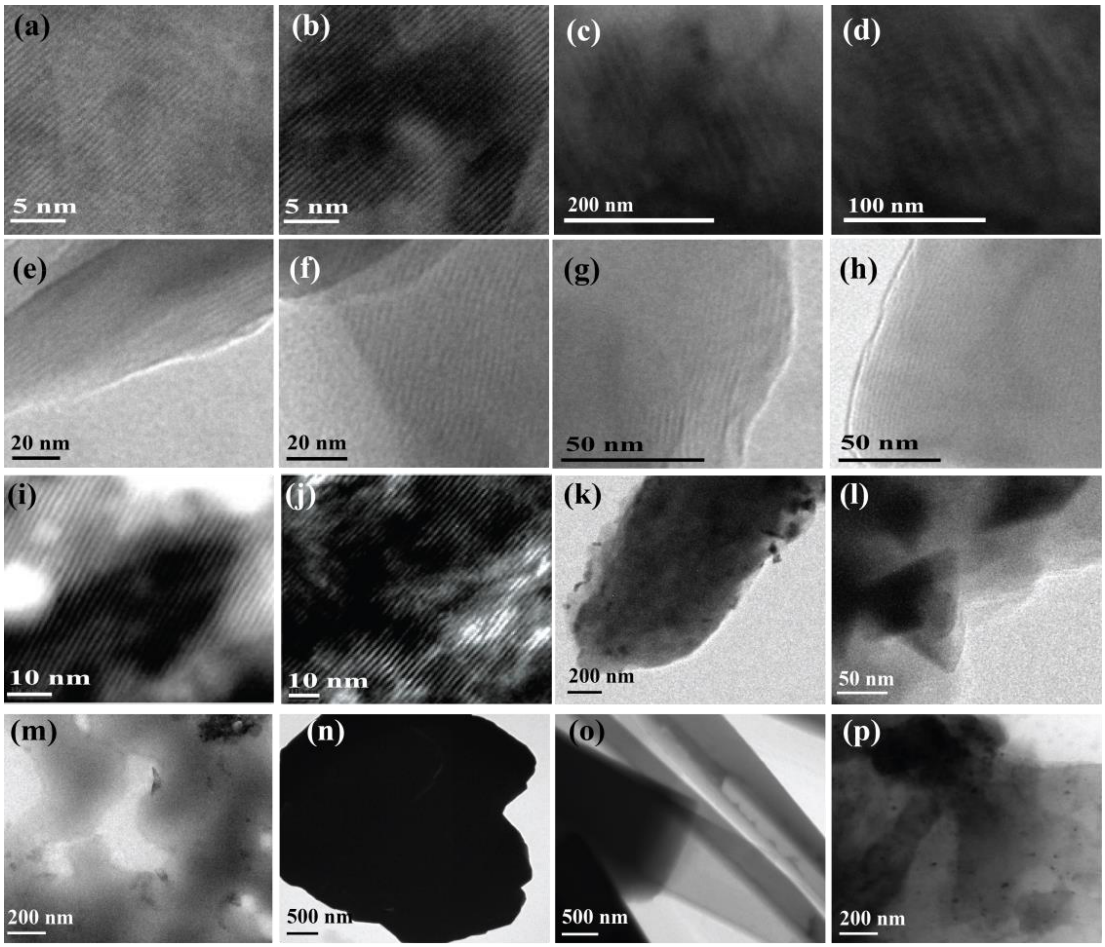

Figure 4.14: TEM images of (a-b) **P4VP(OPV$_{1.00}$)**, (c-d) **P4VP(OPV$_{0.75}$+UPBI$_{0.25}$)**, (e-f) **P4VP(OPV$_{0.50}$+UPBI$_{0.50}$)**, (g-h) **P4VP(OPV$_{0.25}$+UPBI$_{0.75}$)**, (i-j) **P4VP(UPBI$_{1.00}$)**[16] (Reproduced with permission from the publisher), (k-l) **(OPV$_{0.50}$+UPBI$_{0.50}$)**, (m-n) **OPVCN-OH**, (o-p) **UPBI-PDP**.

showed good agreement with the d spacing values obtained from the WXRD data. The **P4VP(OPV$_{1.00}$)** complex showed average line width of 44 ± 15 Å from the TEM images, which correlated very well with the 'd' spacing of pristine **OPVCN-OH** (41.96 Å). The

Table 4.2: d-spacing values of all complexes from TEM.

Compound Name	Average d-spacing (Å)
P4VP(OPV$_{1.00}$)	44
P4VP(OPV$_{0.75}$+UPBI$_{0.25}$)	98
P4VP(OPV$_{0.50}$+UPBI$_{0.50}$)	25
P4VP(OPV$_{0.25}$+UPBI$_{0.75}$)	26

mixed D-A complexes **P4VP(OPV$_{0.25}$+UPBI$_{0.75}$)** and **P4VP(OPV$_{0.50}$+UPBI$_{0.50}$)** gave line widths of 26 ± 3 Å and 25 ± 3 Å, which were close to the d spacing of 31.53 Å and 30.26 Å respectively observed for the complexes from WXRD. The WXRD data of the D-A complexes had indicated that the pattern was dominated by the intense reflection corresponding to **UPBI-PDP**. For the complex **P4VP(OPV$_{0.75}$+UPBI$_{0.25}$)**, the lines in the TEM images crisscrossed or appeared overlaid so that calculation of the average line width became difficult. In the TEM images, P4VP alone did not show any definite morphology. Both monomers **OPVCN-OH** and **UPBI-PDP** also did not exhibit any characteristic morphology under identical conditions. Similarly, **(OPV$_{0.50}$+UPBI$_{0.50}$)** also did not exhibit any specific morphology upon being dropcast on TEM grids under identical conditions as that for the complexes with P4VP. Figures 4.14k-l, 4.14m-n and 4.14o-p shows the TEM images of **(OPV$_{0.50}$+UPBI$_{0.50}$)**, **OPVCN-OH** and **UPBI-PDP** respectively, drop cast from DMF solution.

4.4.5 Charge Carrier Mobility using Space Charge Limited Current (SCLC) Measurements

The electron as well as hole mobility of the donor-acceptor polymer complex was determined using space charge limited current (SCLC) measurements of electron only (**Al/ active layer/ Al structure**) and hole only (**ITO/ PEDOT:PSS/Active layer/Au**) devices respectively. All samples were dissolved in DMF and drop cast directly on the substrate to afford films of average thickness ~1.2 – 2 microns. An average of 4-5 devices was prepared for each sample. All J-V characteristics for electron and hole mobility are given in the figure 4.15 and figure 4.16 respectively. The electron mobility of the pristine acceptor **UPBI-PDP** was determined in an electron only device having the configuration **Al/ active layer/ Al structure**. Table 4.3 gives the summary of device parameters including the film thickness and maximum and average bulk electron and hole mobility estimates with standard deviation. Pristine **UPBI-PDP** formed uniform films and devices were made with average thickness of 1.5 – 2 microns. The average electron mobility from the SCLC measurements was estimated to be 2.28 x 10^{-4} cm^2 $V^{-1}s^{-1}$. The 100 % complex of **UPBI-PDP** with P4VP - **P4VP(UPBI$_{1.00}$)** exhibited average mobility which was an order higher at 1.99 x $10^{-3}cm^2$ $V^{-1}s^{-1}$. Introduction of **OPVCN-OH** into the P4VP-UPBI complex resulted in reduction of average bulk electron mobility estimate to ~ $10^{-5}cm^2$ $V^{-1}s^{-1}$ in **P4VP(OPV$_{0.25}$ + UPBI$_{0.75}$)** and **P4VP(OPV$_{0.50}$ + UPBI$_{0.50}$)**. **P4VP(OPV$_{0.75}$ + UPB**

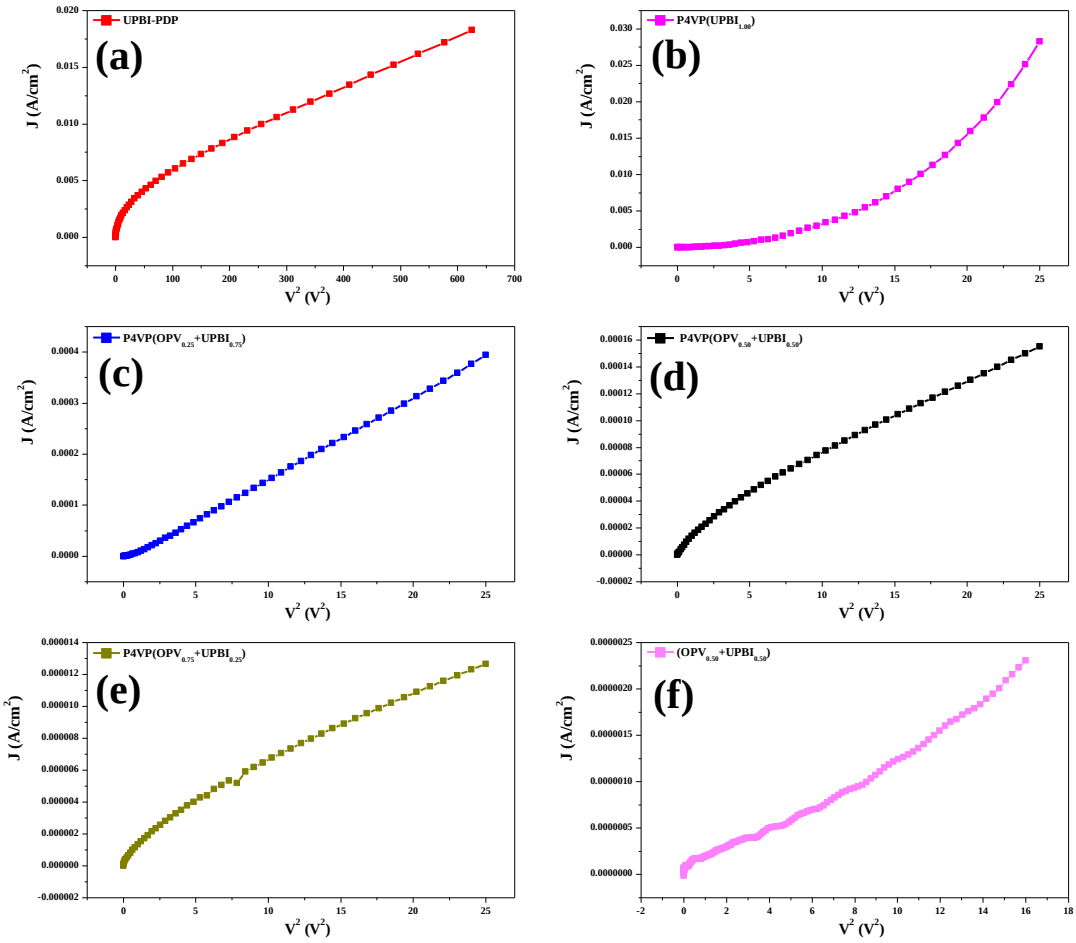

Figure 4.15: J-V characteristics for electron only mobility of (a) **UPBI-PDP** (b) **P4VP(UPBI$_{1.00}$)** (c) **P4VP(OPV$_{0.25}$+UPBI$_{0.75}$)** (d) **P4VP(OPV$_{0.50}$+UPBI$_{0.50}$)** (e) **P4VP(OPV$_{0.75}$+UPBI$_{0.25}$)** (f) **(OPV$_{0.50}$+UPBI$_{0.50}$)**.

I$_{0.25}$) exhibited average electron mobilities of 3.7 x 10^{-7} cm^2 $V^{-1}s^{-1}$. It should be mentioned here that the complexes with higher OPV content exhibited poor film forming ability. This fact along with the reduced amounts of the 'n' type material could be attributed as the reason for the reduced average bulk electron carrier mobility for the complexes with higher donor component. Note that the thin films of the complexes did not reflect poor film-forming tendencies as they formed nice lamellar morphologies as observed in the TEM images of all the complexes. The pristine **OPVCN-OH** as well as its 100 % complex with P4VP- (**P4VP-OPV$_{1.00}$)** did not form good quality thick films which could be used for the SCLC device measurements. Therefore, the hole-transport ability was estimated only for the three D-A complexes - **P4VP(OPV$_{0.25}$ + UPBI$_{0.75}$)**, **P4VP(OPV$_{0.50}$ + UPBI$_{0.50}$)** and **P4VP(OPV$_{0.75}$ + UPBI$_{0.25}$)** using the device configuration **ITO/PEDOT:**

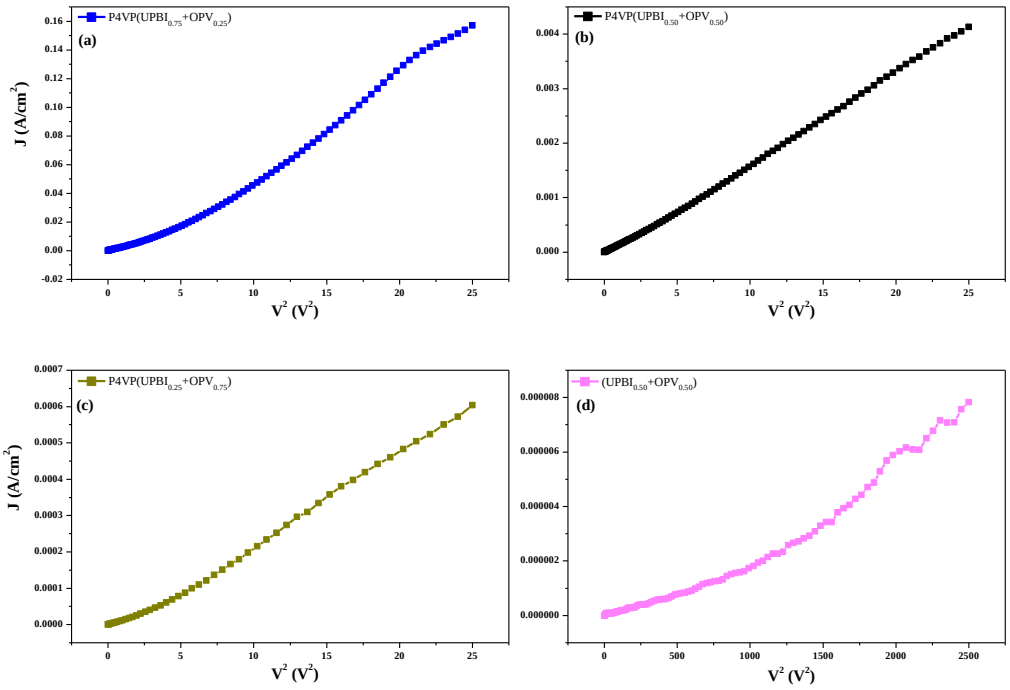

Figure 4.16: J-V characteristics for hole only mobility of (a) **P4VP(OPV$_{0.25}$+UPBI$_{0.75}$)** (b) **P4VP(OPV$_{0.50}$+UPBI$_{0.50}$)** (c) **P4VP(OPV$_{0.75}$+UPBI$_{0.25}$)** (d) **(OPV$_{0.50}$+UPBI$_{0.50}$)**.

PSS/Active layer/Au. Reasonably high average hole-mobility estimate of 1.19 x 10^{-2}cm^2 V^{-1}s^{-1} (one of the highest values reported for oligo(phenylene vinylene) based donor systems) was obtained for the complex with high perylene content **P4VP(OPV$_{0.25}$ + UPBI$_{0.75}$)**. Thus, the donor-acceptor complex **P4VP(OPV$_{0.25}$ + UPBI$_{0.75}$)** exhibited both electron and hole transport mobilities of average values 8.58 x 10^{-5}cm^2 V^{-1}s^{-1} and 1.19 x 10^{-2}cm^2 V^{-1}s^{-1} respectively. The hole mobilities of **P4VP(OPV$_{0.50}$ + UPBI$_{0.50}$)** and **P4VP(OPV$_{0.75}$ + UPBI$_{0.25}$)** complexes were 1.25 x 10^{-3}cm^2 V^{-1}s^{-1} and 3.71 x 10^{-4} cm^2 V^{-1}s^{-1} respectively. The fact that hole mobility of the complex decreased with increasing OPV content was rather contradictory; a probable reason for this anomalous observation could be the poor film (thick) forming capability of complexes with higher OPV content. The role of P4VP in enabling good film processability became evident from the mobility data for the D-A complex without P4VP. The average bulk electron and hole mobilities for **(OPV$_{0.50}$ + UPBI$_{0.50}$)** were 1.08 x 10^{-5}cm^2 V^{-1}s^{-1} and 1.17 x 10^{-6}cm^2 V^{-1}s^{-1} respectively. Although the electron mobilities were in the similar order compared to **P4VP(OPV$_{0.50}$ + UPBI$_{0.50}$)** the hole mobility was three orders lower. In fact the hole mobility was the lowest among all the samples studied. In these D-A systems, the most critical factor seems to be the influence that the presence of each (D or A) has on the ordering of the other in the active layer. In the P4VP-PBI/OPV supramolecular comb polymers that we

Table 4.3: Summary of device parameters

Electron only device with Al/ active layer/ Al				
Sample Name	**Maximum mobility $\mu_{e,max}$ (cm^2/Vs)**	**Average mobility $\mu_{e,avg}$ (cm^2/Vs)**	**Standard deviation**	**Film Thickness (micron)**
UPBI-PDP	4.0×10^{-4}	2.3×10^{-4}	$\pm 0.9 \times 10^{-4}$	1.5 – 2
P4VP- $UPBI_{1.00}$	3.4×10^{-3}	1.9×10^{-3}	$\pm 0.9 \times 10^{-3}$	0.9
P4VP($OPV_{0.25}$ + $UPBI_{0.75}$)	1.1×10^{-4}	8.6×10^{-5}	$\pm 1.7 \times 10^{-5}$	1.2
P4VP($OPV_{0.50}$ + $UPBI_{0.50}$)	5.5×10^{-5}	3.4×10^{-5}	$\pm 1.0 \times 10^{-5}$	1.3
P4VP($OPV_{0.75}$ + $UPBI_{0.25}$)	5.4×10^{-7}	3.7×10^{-7}	$\pm 1.5 \times 10^{-7}$	2
($OPV_{0.50}$+ $UPBI_{0.50}$)	1.3×10^{-5}	1.1×10^{-5}	$\pm 0.2 \times 10^{-5}$	1.5 - 2
Hole only device with ITO/ PEDOT:PSS/ active layer/ Au				
Sample Name	**Maximum mobility $\mu_{h,max}$ (cm^2/Vs)**	**Average mobility $\mu_{h,avg}$ (cm^2/Vs)**	**Standard deviation**	**Film Thickness (micron)**
P4VP($OPV_{0.25}$ + $UPBI_{0.75}$)	1.4×10^{-2}	1.2×10^{-2}	$\pm 0.2 \times 10^{-2}$	1.1
P4VP($OPV_{0.50}$ + $UPBI_{0.50}$)	1.7×10^{-3}	1.3×10^{-3}	$\pm 0.4 \times 10^{-3}$	1.2
P4VP($OPV_{0.75}$ + $UPBI_{0.25}$)	4.5×10^{-4}	3.7×10^{-4}	$\pm 0.9 \times 10^{-4}$	1.0
($OPV_{0.50}$+ $UPBI_{0.50}$)	2.3×10^{-6}	1.2×10^{-6}	$\pm 0.6 \times 10^{-6}$	1.3

have examined, the hole transport was found to be more dominant compared to the electron transport for all the various D and A combinations. Two order reduction in electron mobility was observed in going from **P4VP($UPBI_{1.00}$)** to **P4VP($OPV_{0.25}$ + $UPBI_{0.75}$)** upon incorporation of 25 mole percentage of OPV units, which suggested disruption of ordered PBI domains in the latter due to introduction of **OPVCN-OH**. However, its hole carrier mobility was the highest, suggesting that the small amounts of **OPVCN-OH** were better organized among larger domains of PBI. In fact, among the three P4VP mixed D-A complexes, **P4VP($OPV_{0.25}$ + $UPBI_{0.75}$)**, had the best hole and electron mobility.

4.5 Conclusions

A self-assembly route for assembling donor and acceptor π conjugated molecules onto high molecular weight commercially available polymer like poly(4-vinyl pyridine) (P4VP) to afford materials with improved charge transport capabilities was presented. Hydroxyl functionalized oligo(phenylenevinylene) (OPV) and perylenebisimide (PBI) as donor and acceptor respectively were complexed with P4VP via hydrogen bonding

interaction. Unlike the strong, multiple hydrogen bonded motifs with large association constants introduced in D-A molecules previously explored in literature, the hydrogen bonding interaction of pyridine-hydroxyl pair is weak. Although improved charge carrier mobilities have been reported for strongly hydrogen bonded D-A systems compared to their non-hydrogen bonded counterparts, their solar cell performance have mostly been poor.[42, 43] This has been attributed to unwanted aggregation and phase separation in these strongly interacting systems. Although the pyridine-hydroxyl group interaction between P4VP and donor OPV and acceptor PBI derivatives reported in the current work was weak in nature, the multiple sites of interaction on the templating polymer backbone was successful in achieving a lamellar organization in the domain range < 10 nm. The visual evidence for donor – acceptor self-assembly in the domain range < 10 nm could be obtained from TEM images. P4VP not only acted as a supramolecular comb polymer template but also provided processability to the complex. The clear evidence of the important role of P4VP in this donor- acceptor assembly was highlighted by the performance of a donor-acceptor alone complex without P4VP – (**($OPV_{0.50}$ + $UPBI_{0.50}$)**). The film forming ability of **($OPV_{0.50}$ + $UPBI_{0.50}$)** was very poor and the SCLC mobility showed very poor electron and hole mobility compared to the analogous donor- acceptor complex with P4VP – (**P4VP($OPV_{0.50}$ + $UPBI_{0.50}$)**). The bulk mobility estimate from SCLC device studies showed that hole transport was more favored in the P4VP mixed donor-acceptor complex. The higher hole carrier mobility compared to electron carrier mobility in mixed D-A complexes with higher acceptor component could be attributed to better film quality afforded by the improved packing of both the donor and acceptor when the amount of D was less.

4.6 References

1. Ruokolainen, J.; ten Brinke, G.; Ikkala, O.; Torkkeli, M.; Serimaa, R. *Macromolecules* **1996**, *29*, 3409-3415.
2. Valkama, S.; Lehtonen, O.; Lappalainen, K.; Kosonen, H.; Castro, P.; Repo, T.; Torkelli, M.; Serimaa, R.; ten Brinke, G.; Leskelä M.; Ikkala, O. *Macromol. Rapid Commun.* **2003**, *24*, 556-560.
3. Arulkashmir, A.; Mahale, R. Y.; Dharmapurikar, S. S.; Jangid, M. K.; Krishnamoorthy, K. *Polym. Chem.* **2012**, *3*, 1641-1646
4. Wu, S.; Shi, F.; Zhang, Q.; Bubeck, C. *Macromolecules* **2009**, *42*, 4110–4117.
5. Tai-Shen, H.; Shiang-Lin, D.; Ke-Ying, S.; Jin-Long, H. *J. Mater. Chem. C***2014**, *2*, 4828-4834
6. Guerlain, C.; Piogé, S.; Detrembleur, C.; Fustin, C-A.; Gohy, J-F. *J. Polym. Sci. Part A: Polym. Chem.* **2015,** *53*, 459–467.
7. Hardeman, T.; Willot, P.; De Winter, J.; Josse, T.; Gerbaux, P.; Shestakova, P.; Nies, E.; Koeckelberghs, G. *J. Polym. Sci. Part A: Polym. Chem.* **2014,** *52*, 804–809.
8. Priimagi, A.; Vapaavuor, J.; Rodriguez, F. J.; Faul, C. F. J.; Heino, M. T.; Ikkala, O.; Kauranen, M.; Kaivola, M. *Chem. Mater.* **2008,** *20*, 6358–6363
9. Saccone, M.; Dichiarante, V.; Forni, A.; Goulet-Hanssens, A.; Cavallo, G.; Vapaavuori, J.; Terraneo, G.; Barrett, C. J.; Resnati, G.; Metrangolo, P.; Priimagi, A. *J. Mater. Chem. C* **2015**, *3*, 759-768.
10. Wu, S.; Bubeck, C. *Macromolecules***2013**, *46*, 3512−3518
11. Sary, N.; Richard, F.; Brochon, C.; Leclerc, N.; Lévêque, P.; Audinot, J.-N.; Berson, S.; Heiser, T.; Hadziioannou, G.; Mezzenga, R. *Adv. Mater.* **2010**, *22*, 763–768.
12. del Barrio, J.; Blasco, E.; Oriol, L.; Alcal, R.; Sánchez-Somolinos, C. *J. Polym. Sci. Part A: Polym. Chem.* **2013**, *51*, 1716–1725.
13. Ruokolainen, J.; ten Brinke, G.; Ikkala, O. *Adv. Mater.* **1999**, *11*, 777-780.
14. Soininen, A. J.; Rahikkala, A.; Korhonen, J. T.; Kauppinen, E. I.; Mezzenga, R.; Raula, J.; Ruokolainen, J. *Macromolecules* **2012**, *45*, 8743−8751.
15. Lai, T.-Y.; Cheng, C.-Y.; Cheng, W.-Y.; Lee, K.-M.; Tung, S.-H. *Macromolecules* **2015**, *48*, 717−724.
16. Narayan, R.; Kumar, P.; Narayan, K. S.; Asha, S. K. *Adv. Funct. Mater.* **2013**, *23*, 2033–2043.

17. Narayan, R.; Kumar, P.; Narayan, K. S.; Asha, S. K. *J. Mater. Chem. C* **2014**, *2*, 6511-6519.
18. Rancatore, B. J.; Mauldin, C. E.; Tung, S-H.; Wang, C.; Hexemer, A.; Strzalka, J.; Fréchet, J. M. J.; Xu, T. *ACS Nano* **2010,***4*, 2721–2729.
19. Sary, N.; Rubatat, L.; Brochon, C.; Hadziioannou, G.; Mezzenga, R. *Macromolecular Symposia* **2008**, *268*, 28-32.
20. Schoonbeek, F. S.; van Esch, J. H.; Wegewijs, B.; Rep, D. B. A.; de Haas, M. P.; Klapwijk, T. M.; Kellogg, R. M.; Feringa, B. L. *Angew. Chem. Int. Ed.* **1999**, *38*, 1393-1397.
21. Chu, C.-C.; Raffy, G.; Ray, D.; Guerzo, A. D.; Kauffmann, B.; Wantz, G.; Hirsch, L.; Bassani, D. M. *J. Am. Chem. Soc.* **2010**, *132*, 12717-12723.
22. Jonkheijm, P.; Stutzmann, N.; Chen, Z.; de Leeuw, D. M.; Meijer, E. W.; Schenning, A. P. H. J.; Würthner, F. *J. Am. Chem. Soc.* **2006**, *128*, 9535–9540.
23. Würthner, F.; Chen, Z.; Hoeben, F. J. M.; Osswald, P.; You, C.-C.; Jonkheijm, P.; v. Herrikhuyzen, J.; Schenning, A. P. H. J.; van der Schoot, P. P. A. M.; Meijer, E. W.; Beckers, E. H. A.; Meskers, S. C. J.; Janssen, R. A. J. *J. Am. Chem. Soc*. **2004**, *126*, 10611-10618.
24. Seki, T.; Maruya, Y.; Nakayama, K.-i.; aratsu, T.; Kitamura, A.; Yagai, S. *Chem. Commun.* **2011**, *47*, 12447–12449.
25. Patra, D.; Ramesh, M.; Sahu, D.; Padhy, H.; Chu, C.-W.; Wei, K.-H.; Lin, H.-C. *Polymer* **2012**, *53*, 1219-1228.
26. Srinivasan, S.; Babu, S. S.; Praveen, V. K.; Ajayaghosh, A. *Angew. Chem. Int. Ed.* **2008**, *47*, 5746 –5749.
27. Ajayaghosh, A.; George, S. J.; Praveen, V. K. *Angew. Chem. Int. Ed.* **2003**, *42*, 332-335.
28. Sugiyasu, K.; Fujita, N.; Shinkai, S. *Angew. Chem. Int. Ed.* **2004**, *43*, 1229 – 1229.
29. Li, X.-Q.; Stepanenko, V.; Chen, Z.; Prins, P.; Siebbeles, L. D. A.; Würthner, F. *Chem. Commun.* **2006**, 3871–3873.
30. Sugiyasu, K.; Kawano, S.-i.; Fujita, N.; Shinkai, S. *Chem Mater.* **2008**, *20*, 2863-2865.

31. Puniredd, S. R.; Kiersnowski, A.; Battagliarin, G.; Zajaczkowski, W.; Wong, W. W. H.; Kirby, N.; Mullen, K.; Pisula, W. *J. Mater. Chem., C* **2013**, *1*, 2433-2440.
32. Groppo, E.; Uddin, M. J.; Zavorotynska, O.; Damin, A.; Vitillo, J. G.; Spoto, G.; Zecchina, A. *J. Phys. Chem. C* **2008,** *112*, 19493–19500.
33. Kuo, S-W.; Lin, C-L.; Chang, F-C. *Polymer* **2002**, *43*, 3943-3949.
34. Zhao, Y-Z.; Zhang, Z-L.; Li, Y.; Liu, X-Q.; Liu, S-M.; Yu, J-K.; Zhang, H-Q. *Chinese Chemical Letters* **2014**, *25*, 99–103.
35. Whitten, D. G. *Acc. Chem. Res.* **1993**, *26*, 502–509.
36. Gómez, R.; Veldman, D.; Blanco, R.; Seoane, C.; Segura, J. L.; Janssen, R. A. J. *Macromolecules* **2007,** *40*, 2760-2772.
37. Schmidt, C. D.; Böttcher, C.; Hirsch, A. *Eur. J. Org. Chem.* **2009**, *31*, 5337–5349.
38. Shao, C.; Grüne, M.; Stolte, M.; Würthner, F. *Chem. Eur. J.* **2012,***18*, 13665-13677.
39. Narayan, R.; Asha, S. K. *J. Mater. Chem. C* **2013**, *1*, 5925-5934.
40. George, S. J.; Ajayaghosh, A. *Chem. Eur. J.* **2005**, *11*, 3217 – 3227.
41. Ruokolainen, J.; Tanner, J.; Ikkala, O.; ten Brinke, G.; Thomas, E. L. *Macromolecules* **1998**, *31*, 3532-3536.
42. El-Ghayoury, A.; Schenning, A. P. H. J.; van Hal, P. A.; van Duren, J. K. J.; Janssen, R. A. J.; Meijer, E. W. *Angew. Chem. Int. Ed.* **2001**, *40*, 3660-3663.
43. Xiao, Z.; Sun, K.; Subbiah, J.; Ji, S.; Jones, D. J.; Wong, W. W. H. *Sci. Rep.* **2014**, *4*, 1-8.

Chapter 5

Nanostructured Donor-Acceptor Self Assembly with Improved Photoconductivity

This chapter has been adapted from following publication

B. Saibal, A. Z. Ashar, R. Nandini Devi, K. S. Narayan, S. K. Asha. *ACS Appl. Mater. Interfaces* **2014**, *6*, 19434−19448.

5.1 Abstract

Nanostructured supramolecular donor-acceptor assemblies were formed when an unsymmetrical N-substituted pyridine functionalized perylenebisimide (**UPBI-Py**) was complexed with oligo(*p*-phenylenevinylene) (**OPVM-OH**) complementarily functionalized with hydroxyl unit and polymerizable methacrylamide unit at the two termini. The resulting supramolecular complex **[UPBI-Py (OPVM-OH)]$_{1.0}$** upon polymerization by irradiation in presence of photoinitiator formed well-defined supramolecular polymeric nanostructures. Self-assembly studies using fluorescence emission from thin film samples showed that subtle structural changes occurred on the OPV donor moiety following polymerization. The 1:1 supramolecular complex showed red-shifted aggregate emission from both OPV (~ 500 nm) and PBI (~640 nm) units, whereas the OPV aggregate emission was replaced by intense monomeric emission (~ 430 nm) upon polymerizing the methacrylamide units on the **OPVM-OH**. The bulk structure was studied using wide angle X-ray diffraction (WXRD). Complex formation resulted in distinct changes in the cell parameters of **OPVM-OH**. In contrast, a physical mixture of 1 mole each of **OPVM-OH** and **UPBI-Py** prepared by mixing the powdered solid samples together showed only a combination of reflections from both parent molecules. Thin film morphology of the 1:1 molecular complex as well as the supramolecular polymer complex showed uniform lamellar structures in the domain range < 10 nm. The donor-acceptor supramolecular complex **[UPBI-Py (OPVM-OH)]$_{1.0}$** exhibited space charge limited current (SCLC) with a bulk mobility estimate an order of magnitude higher accompanied by a higher photoconductivity yield compared to the pristine **UPBI-Py**. This is a very versatile method to obtain spatially defined organization of n and p-type semiconductor materials based on suitably functionalized donor and acceptor molecules resulting in improved photocurrent response using self-assembly.

5.2 Introduction

The bottom-up self-assembly of donor-acceptor semiconducting materials is a very challenging task that is being pursued by researchers worldwide.[1-8] Well-defined and reproducible nanoscale assemblies of donor-acceptor semiconducting materials are crucial for several devices in the optoelectronic applications.[1-4] From the perspective of device applications, it is highly desirable to translate the self-assembly of small molecules to processable polymers, which is a non-trivial task. A promising approach in this regard has been the one pioneered by the group of Ikkala and ten Brinke et. al to form hierarchical architectures of small surfactant molecules with block copolymers.[9-12] Recently, we reported well defined nano organization of n-type semiconductors based on perylenebisimide with the polymer poly(4-vinyl pyridine) (P4VP), resulting in lamellar structures in the domain range of 5-10 nm with a clear trend of higher conductance compared to the pristine PBI molecule.[13] Ting Xu and Fréchet et al attached suitably functionalized p-type organic semiconductor - oligothiophene to P4VP resulting in solution processable nanostructured semiconductor composites with charge carrier mobilities comparable to the existing semiconductors already used in OPV devices.[14, 15] Both these approaches took aid of the self-assembly afforded by the nanoscale phase separation of the small molecule and preformed polymer. There are several interesting articles in literature whereby the larger length scale phase separation afforded by block copolymers were combined with the small length scale phase separation of small molecules and mesogens to obtain higher degree of organization.[16-22] The critical challenge however is to replicate the success achieved independently for the donor (D) or acceptor (A) alone materials in an effective donor-acceptor combination where the wide D-A interface would afford increased charge separation and at the same time provide long range pathway for transport of the generated charges to the respective electrodes. The increasing numbers of research articles along this direction is proof to the fact that this is a rich area with scope for further exploitation.[23, 24]

In the present work we report the self-assembly of complementarily functionalized donor and acceptor materials based on oligo(p-phenylenevinylene) (OPV) and perylenebisimide (PBI) respectively. The aim here was to assemble the donor and acceptor molecules so as to increase the interface between them in the domain of 5-10 nm and then translate the self-assembly of the small molecules to that of the polymer, at the same time retaining the crystallinity of the small molecules. This challenging task required design of tailor-made donor and acceptor small molecules with built-in

capabilities for spontaneous self-assembly as well as functionalities to aid in further hierarchical organization via polymerization. Towards this end the donor molecule based on oligo(p-phenylenevinylene) was functionalized with hydrogen bondable hydroxyl moiety at one end and polymerizable methacrylamide units at the other termini. The acceptor molecule based on perylenebisimide was functionalized with complementary pyridine units at one terminus and solubilizing branched alkyl chains at the other termini. The 1:1 donor-acceptor complex was further subjected to photopolymerization in presence of photoinitiator. The complex formation and polymerization were followed in the bulk by FTIR and in solution using proton NMR spectroscopy. Photophysical studies involving UV Vis absorption and fluorescence emission were studied in solution as well as in thin film samples to understand the self-assembly between the donor and acceptor units in the 1:1 supramolecular complex as well as its polymer. Bulk structure analyses were conducted by wide angle X-ray diffraction (WXRD) experiments. The thin film morphology of the 1:1 donor-acceptor complex and its supramolecular polymer was investigated using TEM imaging which showed the presence of lamellar organization of donor-acceptor nanostructures in the length scale of 5-10 nm. Systematic investigation of the effect of improved self-assembly on the photocurrent response of the materials was also undertaken. The study presented here is a viable route towards semiconducting donor-acceptor materials with crystallinity and processability affording better photoinduced charge separation.

5.3 Experimental Section

5.3.1 Materials:

All chemicals were purchased from Aldrich and used as received. All solvents used were of analytical grade and carefully dried before use. Synthetic procedure to prepare the unsymmetrical oligo(*p*-phenylenevinylene) (**OPVM-OH**) and unsymmetrical N-substituted Perylenebisimide (**UPBI-Py**) is given in section 5.3.4.

5.3.2 Instrumentation Techniques:

The details of the instrumentation techniques used for the characterization of the small molecules, complexes and polymer complexes like the FTIR spectroscopy, ^{1}H NMR, ^{13}C NMR, MALDI-TOF, Gel permeation chromatography (GPC), Wide Angle X-ray Diffractograms (WXRD), Small angle X-ray scattering (SAXS), Transmission Electron microscopy (TEM), absorption and fluorescence studies were exactly identical as explained in chapter 2 and chapter 4. HRMS (ESI) were recorded on ORBITRAP mass analyser (Thermo Scientific, Q Exactive). Mass spectra were measured with ESI

ionization in MSQ LCMS mass spectrometer. Elemental analysis was done by Thermofinnigan flash EA 1112 series CHNS analyser. The photo polymerization was performed with DYMAX Blue Wave 75 watt short arc mercury vapor lamp as light source with an output wavelength in the range 280-450 nm. The fluorescence lifetime studies were carried out for samples drop cast as films from DMF. Nano LED of 370 nm was used for fluorescence lifetime measurements and data was collected at 450 nm (OPV) and 625 nm (PBI). The decay curves were obtained by the time correlated single photon counting (TCSPC) technique. Fluorescence lifetime values were determined by deconvoluting the data with exponential decay using DAS6 decay analysis software. The quality of fit was judged by fitting parameters such as $\chi^2 \approx 1$, as well as the visual inspection of the residuals and autocorrelations.

5.3.3 SCLC Device Fabrication:

SCLC mobility and AC photocurrent measurements were performed on ITO/polymer (complex)/Al sandwiched structures. Polymer / complex solution was drop casted from ODCB (Ortho dichlorobenzene) on cleaned ITO (sheet resistance 15 Ωsq^{-1}). Aluminum top contacts with thickness of 80 nm and area ~ 6×10^{-2} cm^2 were thermally evaporated on to the polymer through shadow mask, at the rate of 1 Å/sec and under pressure of 5×10^{-6} mbar. Thickness of the polymer coatings (1-4 μm) were measured using Dektak surface profiler. SCLC and photocurrent measurements were carried out while keeping device in vacuum (10^{-3} mbar). Incident light from Tungsten –halogen source was modulated at 20 Hz and the photocurrent was measured using a lock-in Amplifier (Stanford SR830). The data was normalized to incident photon density using a commercial calibrated photodiode under similar experimental conditions.

5.3.4 Synthesis:

(i) Synthesis of Hydroxyl Methacrylic amide Unsymmetrical OPV3 (OPVM-OH):

(a) Synthesis of MEM-UOPV3-CN:

The synthesis of **MEM-UOPV3-CN** was already described in Section 4.3.4 (i) Synthesis of unsymmetrical **OPVCN-OH** (a) to (h) (chapter 4)

(b) Synthesis of MEM-UOPV3-CH_2NH_2:

LAH (0.14 gm; $3.66\text{x}10^{-3}$ mol) was taken in a two necked round bottom flask under N_2 atmosphere. MEM-OPV3-CN (0.5 gm; $1.22\text{x}10^{-3}$ mol) was dissolved in dry THF under N_2 atmosphere. MEM-OPV3-CN solution in THF was added to the LAH under N_2 atmosphere at 0 ^oC. After addition ice bath was removed and stirred further for

7-8 hr at room temperature and the reaction was monitered by TLC. After completion of the reaction green coloured material was obtained. The resultant was used as such for the next reaction. Yield > 95 %. Melting Point > 200 ^{0}C. FT-IR (ATR eco ZnSe, cm^{-1}) = 3369, 3270, 2922, 2855, 1601, 1510, 1457, 1419, 1374, 1243, 1168, 1109, 1002, 970, 833, 753, 720. ^{1}H NMR (200 MHz, $CDCl_3$, δ): 7.48-6.92 (m, 14H); 5.28 (s, 2H); 4.69 (d, 2H); 3.87-3.57 (m, 4H); 3.37 (s, 3H) ppm.

(c) Synthesis of MEM- Methacrylic amide Unsymmetrical OPV3 (MEM-UOPV3-MAm):

Methacrylic acid (0.02 gm; 2.4x10^{-4} mol) was taken in a two necked round bottom flask with EDCl (0.12 gm; 6.0x10^{-4} mol) and dry DCM under nitrogen atmosphere. MEM-OPV3-CH_2NH_2 (0.1 gm; 2.4x10^{-4} mol) and DMAP (0.006 gm; 4.8x10^{-5} mol) were taken in a one neck round bottom flask under N_2 atmosphere and then dry DCM was added. This resultant solution was added to the two necked round bottom flask under N_2 atmosphere in ice cold condition. After addition, ice bath was removed and further stirred for 48 hr and the reaction was monitored by TLC. The compound was purified by column chromatography (DCM:MeOH = 99.5:0.5). Yield = 55 %. Melting Point > 200 ^{0}C. FT-IR (ATR eco ZnSe, cm^{-1}) = 3297, 2957, 2923, 2859, 1720, 1653, 1612, 1544, 1513, 1432, 1366, 1303, 1253, 1164, 1096, 1006, 970, 798, 704, 659. ^{1}H NMR (200 MHz, $CDCl_3$, δ): 7.51-7.00 (m, 14H); 5.73 (s, 1H); 5.36 (s, 1H); 5.28 (s, 2H); 4.52 (d, 2H); 3.82 (m, 2H); 3.56 (m, 2H); 3.38 (s, 3H); 1.99 (s, 3H) ppm. ^{13}C NMR (200 MHz, DMSO-d_6, δ): 203.40, 167.48, 164.23, 155.38, 154.49, 149.85, 127.52, 126.30, 118.12, 114.85, 107.96, 93.36, 71.69, 67.48, 59.11, 47.83, 17.99 ppm. MALDI-TOF MS (Calcd m/z 483.59); Found m/z – 483.89 [M], 506.62 [M+Na], 522.25 [M+K].

(d) Synthesis of Hydroxyl Methacrylic amide Unsymmetrical OPV3 (OPVM-OH):

MEM-OPV3-MAm (0.41 gm; 8.4x10^{-4} mol) was taken in a two necked round bottom flask under N2 atmosphere. Dry DCM was added to the R.B flask followed by trifluro acetic acid (0.32 mL; 4.19x10^{-3}mol). This resultant reaction mixture was further stirred for 48 hr at room temperature. After completion of reaction DCM was evaporated by rota vap and reprecipited from methanol to get the pure product. Yield = 50 %. Melting Point > 200 ^{0}C. FT-IR (KBr Pallate, cm^{-1}) = 3831, 3476, 3317, 3021, 2880, 2819, 1653, 1597, 1547, 1518, 1429, 1359, 1327, 1230, 1171, 1109, 1062, 1016, 966, 834, 785, 709, 659. ^{1}H NMR (400 MHz, DMSO-d_6, δ): 8.51 (t, 1H); 7.56-6.75 (m, 16H); 5.73 (s, 1H); 5.37 (s, 1H); 4.34 (d, 2H); 1.89 (s, 3H) ppm. ^{13}C NMR (200 MHz, DMSO-d_6, δ): 202.50, 167.44, 163.28, 157.34, 156.19, 147.95, 127.51, 126.32, 119.22, 115.55, 108.76,

46.72, 18.67 ppm. MALDI-TOF MS (Calcd m/z 395.19); Found m/z – 395.90 [M+1]. HRMS in Acetonitrile (Calcd m/z 395.19); Found m/z – 396.19 [M+1], 418.18 [M+Na], 434.15 [M+K].

(ii) Synthesis of Octyl dodecyl Aminopyridyl unsymmetrical Perylenebisimide (UPBI-Py):

(a) Synthesis of 2-Octyl-dodecyl ethyl bromide:

Triphenyl phosphine (PPh_3) (61.5 gm; 0.23 mol) was taken in a three necked round bottom flask in DCM and purged with N_2 for 15 minutes followed by addition of bromine (12 mL; 0.23 mol). 2-octyl-dodecyl ethanol (70 mL; 0.23 mol) was added drop wise to that reaction mixture. The resultant reaction mixture was stirred for overnight under N_2 atmosphere. After completion of reaction DCM was evaporated. The product was purified with the help of column chromatography using hexane as a mobile phase. Yield = 90%. ^{1}H NMR (200 MHz, $CDCl_3$, δ): 4.68 (s, 2H); 1.99 (t, 1H); 1.27 (m, 38H); 0.88 (t, 3H) ppm.

(b) Synthesis of N-(2-octyl-dodecyl) phthalimide:

K-phthalimide (13.2 gm; $7.6x10^{-2}$ mol) and 2-octyl-dodecyl bromide (25.0 gm; $6.92x10^{-2}$ mol) were taken in a two necked round bottom flask. Dry DMF was added to the solid mixture under N_2 atmosphere. The resultant reaction mixture was stirred for 16 hr at 90 ^{o}C. After completion of reaction reaction mixture was extracted with DCM repeatedly. The combined organic layer was washed with 0.2 N KOH solution and then washed with saturated ammonium chloride solution and dried over sodium sulphate. The product was purified by column chromatography, DCM-Hexane (70:30) as a mobile phase. Yield = 60%. ^{1}H NMR (200 MHz, $CDCl_3$, δ): 7.81-7.71 (m, 4H); 3.57 (d, 2H); 1.86 (s, 1H); 1.22 (m, 38H); 0.86 (t, 6H) ppm.

(c) Synthesis of 2-octyl-dodecyl ethyl amine:

N-(2-octyl-dodecyl) phthalimide (28.0 gm; $6.5x10^{-2}$ mol)and hydrazine hydrate (16.39 gm; 0.33 mol) were taken in a one necked round bottom flask containing methanol. The reaction mixture was stirred for 18 hr at 95 ^{o}C. After completion of the reaction, methanol was evaporated and DCM was added. DCM solution was washed with 10% KOH solution. Aqueous layers were combined and extracted with DCM. The combined organic layer was washed with brine solution and dried over sodium sulphate. Yield = 50%. FT-IR (ATR eco ZnSe, cm^{-1}) = 3296, 2920, 2854, 1668, 1543, 1460, 1378, 1305, 1042, 722. ^{1}H NMR (200 MHz, $CDCl_3$, δ): 2.57 (t, 2H); 1.24 (m, 38H); 0.86 (t, 6H) ppm.

(d) Synthesis of bisOctyl dodecyl Perylene bismide (OD-SPBI):

Perylene dianhydride (5.0 gm; $1.27x10^{-2}$ mol) and Octyl dodecyl amine (8.35gm; $2.81x10^{-2}$ mol) were taken in a one necked round bottom flask and dimethylacetamide (DMAc) was added. The resultant reaction mixture was heated to 90 ^{o}C and stirred for 12 hr. After completion of reaction, DMAc was vacuum distilled off at 100 ^{o}C. The solid product was washed with methanol. Yield > 95%. FT-IR (ATR eco ZnSe, cm^{-1}) = 3465, 3116, 2923, 2853, 1769, 1695, 1654, 1590, 1506, 1438, 1403, 1341, 1301, 1242, 1152, 1122, 1084, 1020, 857, 808, 742, 640. ^{1}H NMR (200 MHz, $CDCl_3$, δ): 8.63-8.50 (m, 8H); 3.83 (d, 4H); 1.99 (m, 2H); 1.32-1.19 (m, 64H); 0.83 (t, 12H) ppm.

(e) Synthesis of Mono Octyl dodecyl unsymmetrical Perylene imide anhydride:

Octyl dodecyl symmetrical Perylenebismide (8.0 gm; $8.4x10^{-3}$mol) and t-butanol (25 ml per mmol of perylene imide anhydride) were taken in a one necked round bottom flask and heated up to 90 ^{o}C. KOH (~2.4 gm; $4.2x10^{-2}$ mol) was added at 90 ^{o}C and after 20 min aceticacid was added to the reaction mixture followed by 2 hr stirring. After that 2N HCL was added to the resultant mixture and washed with water until acid free. The product was purified by column using DCM as a mobile phase. Yield = 30%. Melting Point > 200 ^{0}C. FT-IR (ATR eco ZnSe, cm^{-1}) = 3071, 2919, 2851, 1763, 1733, 1692, 1651, 1586, 1505, 1456, 1437, 1402, 1378, 1347, 1315, 1237, 1145, 1120, 1071, 1010, 854, 804, 731, 634. ^{1}H NMR (200 MHz, $CDCl_3$, δ): 8.74-8.64 (m, 8H); 4.15 (d, 2H); 2.00 (m, 1H); 1.34-1.20 (m, 32H); 0.83 (t, 6H) ppm. ^{13}C NMR (200 MHz, $CDCl_3$, δ): 184.31, 177.64, 173.22, 163.69, 159.14, 136.26, 132.18, 131.42, 126.36, 123.87, 123.02, 119.47, 69.13, 62.47, 52.99, 44.74, 36.63, 31.72, 30.03, 29.63, 29.33, 26.51, 26.03, 22.65, 14.09 ppm. MALDI-TOF MS (Calcd m/z 671.86); found m/z – 672.66 [M+1].

(f) Synthesis of Octyl dodecyl Aminopyridyl unsymmetrical Perylene bisimide (UPBI-Py):

Mono Octyl dodecyl unsymmetrical Perylene imide anhydride (0.76 gm; $1.12x10^{-3}$ mol), 4-aminopyridine (0.16 gm; $1.68x10^{-3}$ mol), imidazole (6-7 gm per 1 gm of unsymmetrical perylene imide anhydride) and catalytic amount of zinc acetate (0.076 gm; $1.12x10^{-4}$) were taken in a one necked round bottom flask under N_2 atmosphere and heated up to 160 ^{o}C followed by stirring for 12 hr at that temperature. After completion of reaction 2 N HCL was added and finally product was purified by column chromatography using DCM-Methanol (1:3) mixture as a mobile phase. Yield = 55 %. Melting Point > 200 ^{0}C. FT-IR (KBr Pallate, cm^{-1}) = 3415, 2959, 2922, 2856, 1704, 1661, 1590, 1490, 1457, 1433, 1396, 1355, 1255, 1190, 1158, 1125, 1076, 966, 932, 857, 813, 776, 740,

697, 643. ^{1}H NMR (400 MHz, $CDCl_3$, δ): 8.88 (d, 2H); 8.69-8.45 (m, 8H); 7.42 (d, 2H); 4.14 (d, 2H); 1.99 (m, 1H); 1.33-1.20 (m, 32H); 0.83 (t, 6H) ppm. ^{13}C NMR (200 MHz, $CDCl_3$, δ): 163.22, 162.53, 151.12, 134.75, 133.48, 131.50, 130.84, 129.48, 127.70, 125.98, 124.09, 123.33, 122.70, 31.87, 29.31, 26.46, 22.64, 14.07 ppm. MALDI-TOF MS (Calcd m/z 747.40); found m/z – 748.52 [M+1].

(iii) Synthesis of 1:1 complex:

Unsymmetrical oligo(*p*-phenylenevinylene) (**OPVM-OH**) and unsymmetrical N-substituted perylenebisimide (**UPBI-Py**) were kept in vacuum oven for 2 days at 60 °C. 1:1 complex **[UPBI-Py (OPVM-OH)]$_{1.0}$** was prepared from dry THF solution, where 1.0 denoted the number of PBI molecules per OPV molecule (theoretically). **OPVM-OH** was first dissolved in THF to which required amount of **UPBI-Py** was added and the solution was stirred at 60 °C for 24 h. The solvent was slowly evaporated on a petri dish placed on a hot plate at 60 °C and dried further in vacuum oven at 65 °C for 2 days. After 2 days, the dried complex was stored in desiccator. To get the supramolecular polymer complex **[UPBI-Py Poly(OPVM-OH)]$_{1.0}$**, the dried **[UPBI-Py (OPVM-OH)]$_{1.0}$** complex was dissolved in dry THF. 0.2 equivalents of 2,2-diethoxyacetophenone as photoinitiator was added to it and the solution irradiated for 15-min using DYMAX Blue Wave 75 light source. The solvent was evaporated on a hot plate at 60 °C and washed with hexane to remove unreacted photoinitiator. Thereafter the sample was dried in vacuum oven at 65 °C for 2 days and stored in desiccator.

(iv) Thermal Polymerization

20 mg (1.7 x10^{-4} moles) [UPBI-Py (OPVM-OH)]$_{1.0}$ was taken in a round bottom flask with 3 ml of dry THF. 0.4 mg (3.4 x10^{-5} moles) of BPO was added and polymerization carried out at 65 °C under nitrogen atmosphere. After 24 hr the polymer was worked up by removing the solvent, washing the precipitate with hexane and drying under vacuum oven. ^{1}H NMR (400 MHz, $CDCl_3$, δ): 8.91 (d, 2H); 8.68 (m, 8H); 8.06 (d, 2H); 7.51-6.65 (m, 16H), 5.72 (s, 1H); 5.36 (s, 1H), 4.50 (s, 2H); 4.13 (d, 2H), 2.34 (m, 1H); 1.26 (m, 32H); 0.87 (t, 6H) ppm.

(v) Synthesis of Complex [UPBI-Py$_{2.0}$ (OPVM-OH)$_{1.0}$]:

UPBI-Py (1.34 x 10^{-4} moles) and OPVM-OH (6.68 x 10^{-5} moles) were taken together in a two necked round bottom flask. Dry THF was added to that in N_2 environment and stirred for 24 h at 55 ^{o}C. After 24 hr THF was evaporated on petridish and dried further in vaccum oven at 55 ^{o}C for 48 hr and used further as such. ^{1}H NMR

(400 MHz, $CDCl_3$, δ): 8.94 (d, 2H); 8.74 (m, 8H); 8.04 (d, 2H); 7.40-6.99 (m, 16H); 5.42 (s, 1H); 5.19 (s, 1H); 4.56 (d, 2H); 4.14 (d, 2H); 2.32 (m, 1H); 1.41-1.10 (m, 32H); 0.87 (m, 9H) ppm.

(vi) Synthesis of Complex [UPBI-$Py_{1.0}$ $(OPVM\text{-}OH)_{2.0}$]:

UPBI-Py (1.34×10^{-4} moles) and OPVM-OH (2.67×10^{-4} moles) were taken together in a two necked round bottom flask. Dry THF was added to that in N_2 environment and stirred for 24 h at 55 ^oC. After 24 hr THF was evaporated on petridish and dried further in vaccum oven at 55 ^oC for 48 hr and used further as such. ^1H NMR (400 MHz, $CDCl_3$, δ): 8.94 (d, 2H); 8.75 (m, 8H); 8.06 (d, 2H); 7.42-7.00 (m, 16H); 5.77 (s, 1H); 5.41 (s, 1H); 4.53 (d, 2H); 4.16 (d, 2H); 2.35 (m, 1H); 1.41-1.11 (m, 32H); 0.88 (m, 9H) ppm.

5.4 Results and Discussion

5.4.1 Synthesis and Characterization

The donor molecule **OPVM-OH** based on oligo(p-phenylenevinylene) (OPV) was synthesized as shown in Scheme 5.1 with polymerizable methacrylamide groups at one end and hydrogen bondable hydroxyl unit at the other termini. The acceptor molecule **UPBI-Py** based on unsymmetrical N-substituted perylenebisimide (PBI) was synthesized in reasonable yield and purity following the procedure shown in Scheme 5.2. The donor and acceptor molecules were subjected to repeated column chromatographic purification to obtain the final molecules in extremely pure form. The structure was confirmed by proton NMR (Figure 5.1), MALDI-TOF (Figure 5.2a, b) and purity was confirmed by HRMS/elemental analysis and size exclusion chromatogram (SEC) (Figure 5.2c). Figure 5.1 shows the labelled proton NMR spectra of the OPV and PBI molecules. Due to poor solubility in chloroform, the 1H NMR spectra of **OPVM-OH** was recorded in dimethyl sulfoxide (DMSO-d_6). The OPV aromatic protons as well as vinylic protons appeared in the range 7.56-6.75 ppm and the methacrylic protons appeared as two singlets at 5.73 and 5.37 ppm. In the proton NMR spectra of **UPBI-Py**, the eight aromatic protons of perylene core appeared as four doublets in the region 8.64-8.43 ppm, while the aromatic protons of the pyridine ring appeared as doublets at 8.87 and 7.42 ppm.

The supramolecular assembly of n-type organic semiconductor perylenebisimide (PBI) with p-type organic semiconductor oligo(p-phenylenevinylene) (OPV), involving non-covalent secondary interactions such as hydrogen-bonding and π-π stacking interactions were investigated. The complex was prepared by dissolving 1:1 molar ratio

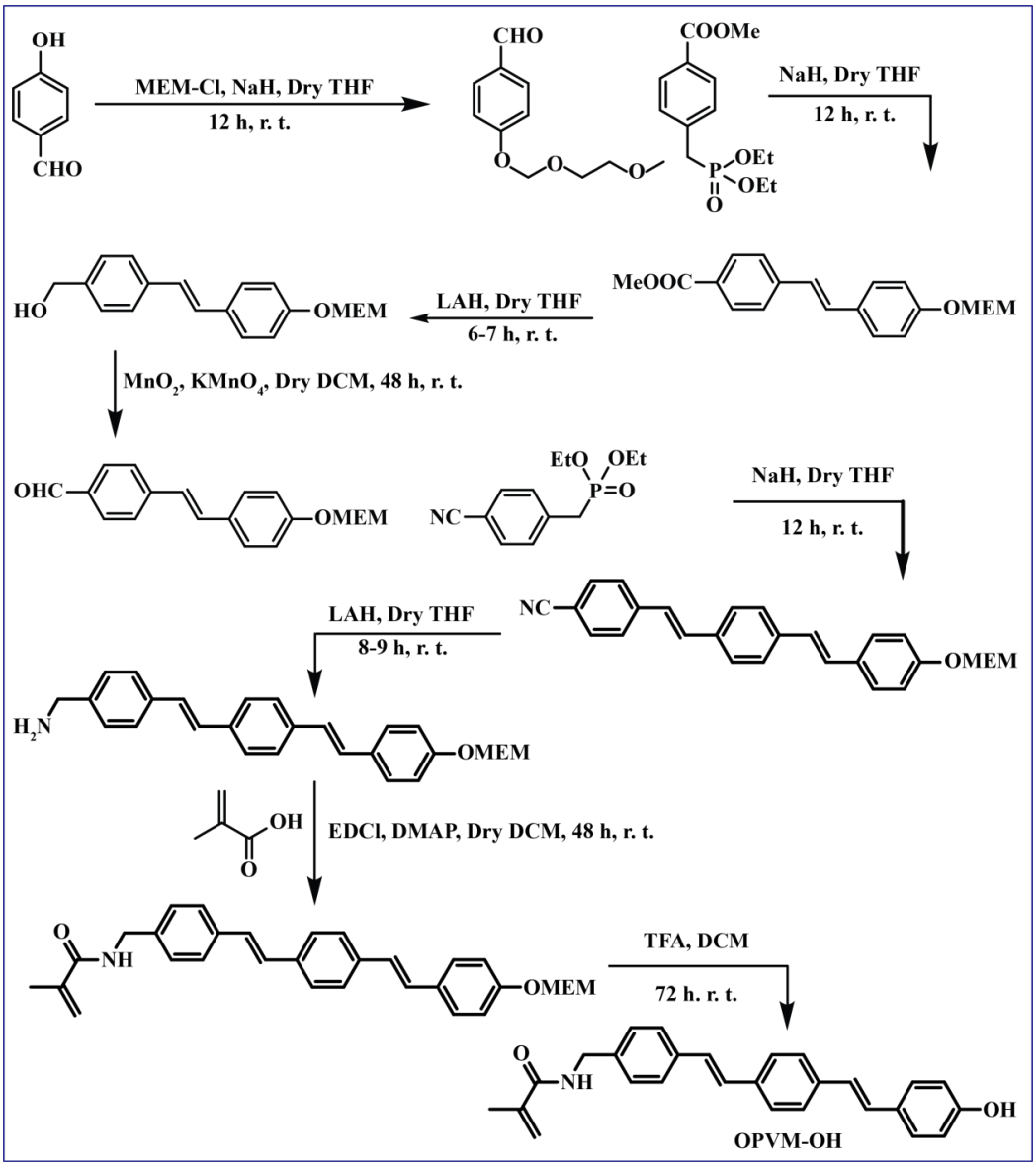

Scheme 5.1: Synthesis of hydroxyl functionalized oligo(*p*-phenylenevinylene) methacrylamide (**OPVM-OH**)

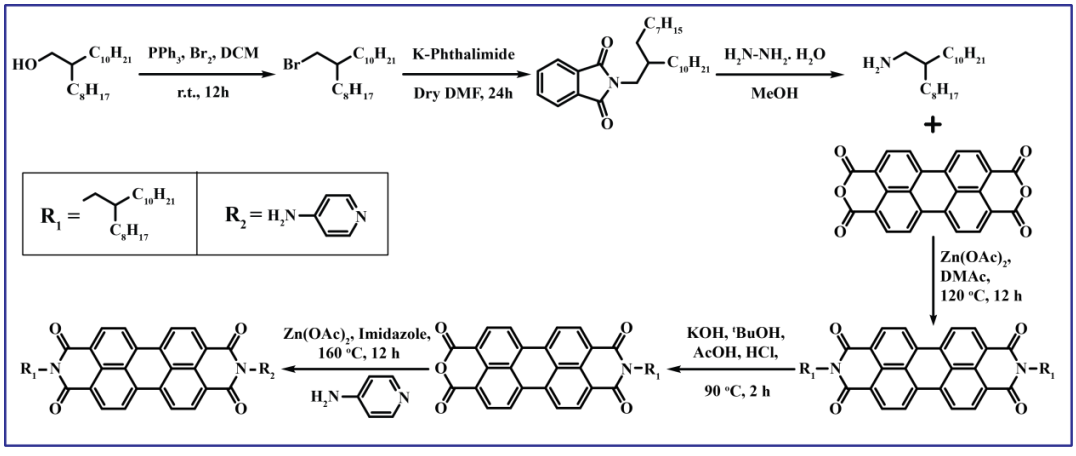

Scheme 5.2: Synthesis of unsymmetrical perylenebisimide **UPBI-Py**.

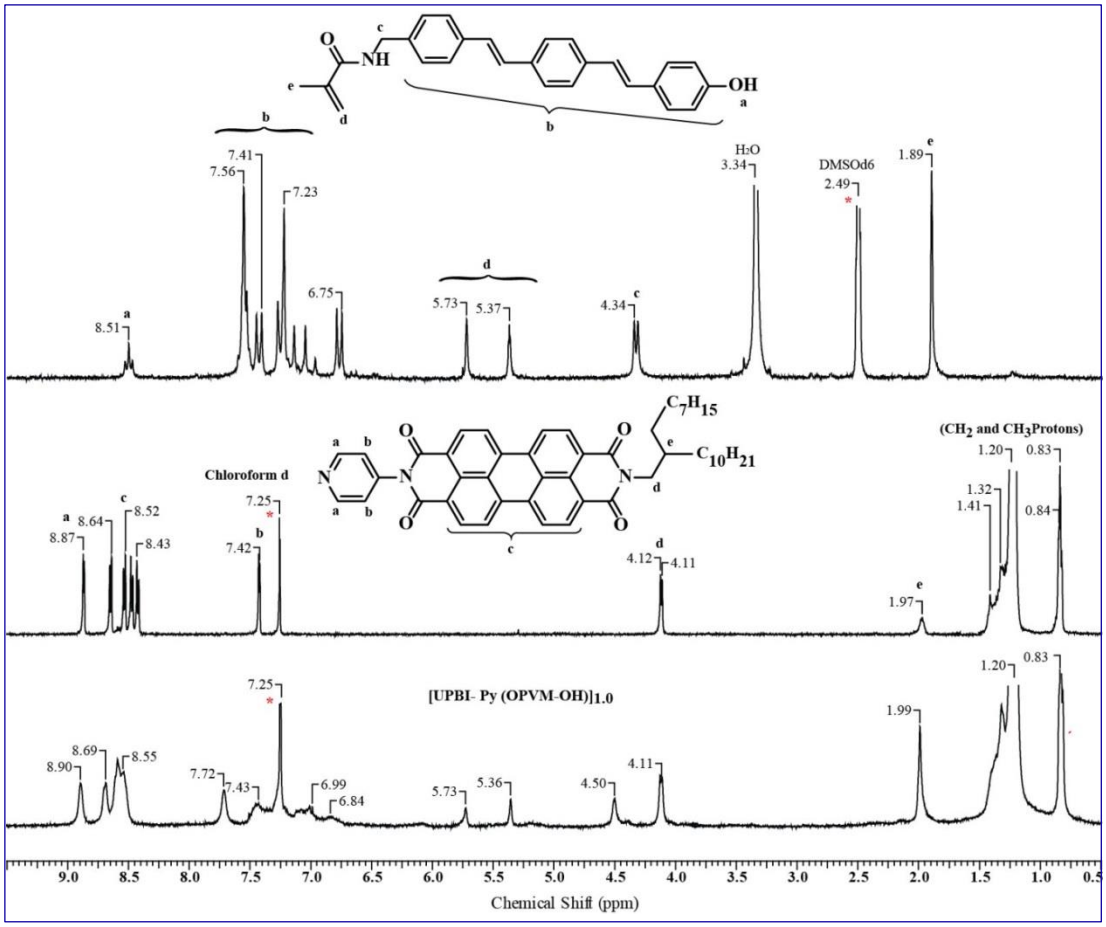

Figure 5.1: Comparison of the ^{1}H NMR spectra of **OPVM-OH** (recorded in DMSO-d_6)**, UPBI-Py** and the 1:1 complex **[UPBI-Py (OPVM-OH)]$_{1.0}$** recorded in $CDCl_3$ at 25 °C.

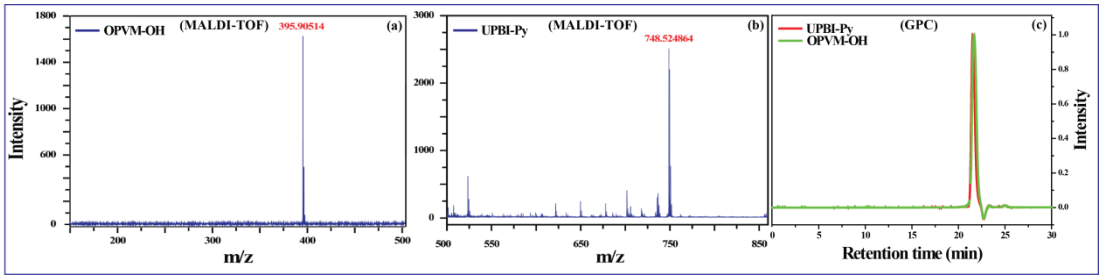

Figure 5.2: MALDI-TOF of (a) **OPVM-OH;** (b) **UPBI-Py** and (c) GPC of **UPBI-Py** and **OPVM-OH**.

of **UPBI-Py** and **OPVM-OH** in dry tetrahydrofuran (THF) as solvent, stirring at 60 °C for 24 h, followed by removal of solvent by heating (scheme 5.3). The complex was named **[UPBI-Py (OPVM-OH)]$_{1.0}$**, where 1.0 denoted the theoretical 1:1 ratio of **UPBI-**

Py and **OPVM-OH**. Successful complex formation was indicated by the improved solubility of the complex compared to the respective pure components. Detailed structural

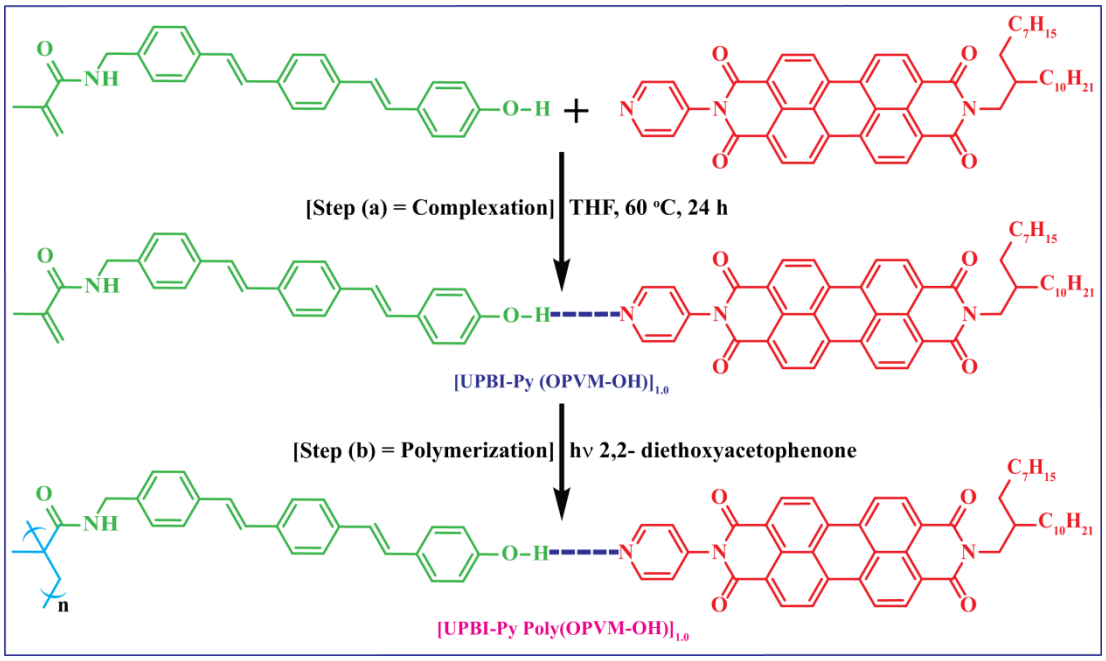

Scheme 5.3: Structure of complex **[UPBI-Py (OPVM-OH)]$_{1.0}$** formed by the unsymmetrical **UPBI-Py** with **OPVM-OH** [Step (a) complexation] and Photo polymerization of the 1:1 complex **[UPBI-Py (OPVM-OH)]$_{1.0}$** to yield **[UPBI-Py Poly(OPVM-OH)]$_{1.0}$** [Step (b) polymerization].

characterization of the complex was carried out using proton NMR spectroscopy (figure 5.1) in deuterated chloroform, in which the complex was now soluble, in contrast to the poor solubility of **OPVM-OH**. The amino pyridine aromatic ring protons at 8.87 ($H_{\alpha\text{-Py}}$) and 7.42 ($H_{\beta\text{-Py}}$) ppm in **UPBI-Py**[25] shifted down field to 8.90 and 7.72 ppm respectively upon complex formation. The down field shift of the inner pyridine protons from 7.42 to 7.72 ppm was rather surprising. A two-dimensional correlation spectroscopy (COSY) experiment on **[UPBI-Py (OPVM-OH)]$_{1.0}$** in $CDCl_3$+DMSO-d_6 showed a cross coupling of the two peaks at 7.72 and 8.90 ppm confirming that they were indeed the aromatic protons of the pyridine ring of **UPBI-Py**. An overall broadening of all the peaks was also surprisingly observed in the complex.

The formation of the complex was traced by FTIR spectroscopy also. The pyridine ring in **UPBI-Py** has a symmetric ring stretching vibration at 1093 cm^{-1}.[26] In general, the nitrogen atom in pyridine derivatives like 4-vinyl pyridine, has a pyridine breathing mode ~ 996 cm^{-1}.26 The absorption at 1093 cm^{-1} in **UPBI-Py** was assigned to the pyridine ring stretching vibration based on comparison with a symmetric

perylenebisimide molecule having only alkyl substitution on both termini, which lacked the absorption at 1093 cm^{-1} (Figure 5.3a). After complexation, a shift to higher wave-

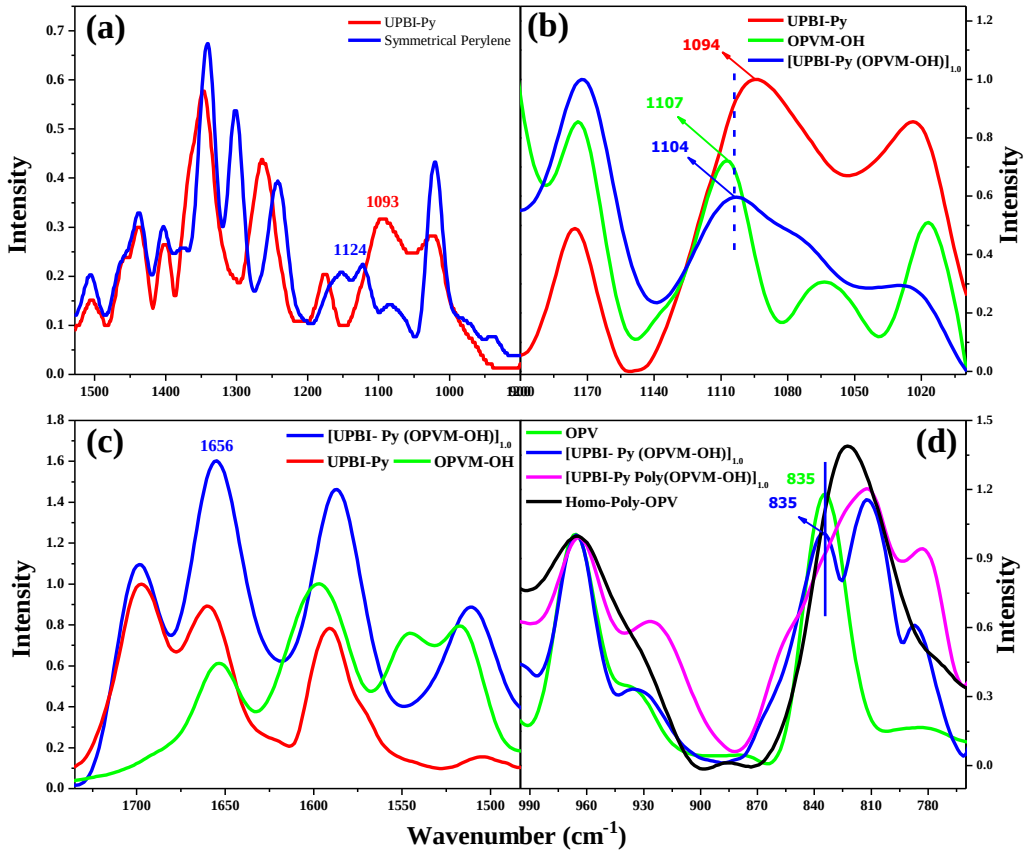

Figure 5.3: Comparison of FT-IR of: (a) **UPBI-Py** and **SPBI;** (b-c) **UPBI-Py, OPVM-OH** and 1:1 complex **[UPBI-Py (OPVM-OH)]$_{1.0}$**; (d) **OPVM-OH**, **homo Poly(OPVM-OH),** 1:1 complex **[UPBI-Py (OPVM-OH)]$_{1.0}$** and supramolecular polymer complex **[UPBI-Py Poly(OPVM-OH)]$_{1.0}$**

number (1105 cm^{-1}) was observed upon hydrogen bonding interaction with the phenol unit of **OPVM-OH** (Figure 5.3b). Other characteristic pyridine C=N symmetric stretching vibration at 1271 cm^{-1} and 1511 cm^{-1} were difficult to trace due to considerable overlap from other OPV stretching vibrations. Hydrogen bonding interaction of the >C=O group in the amide linkage in **OPVM-OH** was ruled out as this stretching vibration at 1656 cm^{-1} (Figure 5.3c) remained unchanged upon complex formation clearly indicating its lack of participation in any non-covalent interaction.

5.4.2 Polymerization

The photoinduced polymerization of the 1:1 OPV-PBI complex was carried out in the presence of photoinitiator 2,2 diethoxyacetophenone. A dry THF solution of the

complex (10 mg in 3 mL) with 0.2 equiv of photoinitiator was irradiated for 15 min using a DYMAX Blue Wave 75 light source (Scheme 5.3 [Step (b)]). Afterward, the solvent was removed; the residue washed with hexane to remove the photoinitiator and then the sample was analysed using FTIR as well as proton NMR spectroscopic techniques. The same photopolymerization experiment was repeated under identical conditions for the OPV molecule **OPVM-OH** also. Upon evaporation of the solvent THF at the end of 15 min of irradiation, followed by hexane washing, a film of the homopolymer **poly(OPVM-OH)** was obtained. This homo polymer of OPV was completely insoluble in common organic solvents such as chloroform, dimethylformamide (DMF) and THF. Hence structural characterization using proton NMR spectroscopy was unfortunately not possible. However, the FTIR spectra was recorded of the solid homopolymer sample and compared with that of the supramolecular polymer complex. The supramolecular polymer complex is represented as **[UPBI-Py poly(OPVM-OH)]$_{1.0}$** to indicate that the polymerization occurred on the **OPVM-OH** moiety. The disappearance of the characteristic methacrylate double bond at 836 cm^{-1} was followed using FTIR spectra.[27,28] Figure 5.3d compares the expanded normalized FTIR spectra of solid samples of the complex before and after photopolymerization along with that of **OPVM-OH**. The spectra were normalized at 965 cm^{-1} corresponding to OPV vibrations, where UPBI-Py did not have any absorbance. The peak at 836 cm^{-1} was clearly observable in the 1:1 complex **[UPBI-Py (OPVM-OH)]$_{1.0}$** but was reduced in intensity in the supramolecular polymer complex **[UPBI-Py poly(OPVMOH)]$_{1.0}$**. In the polymer, a broad peak at 812 cm^{-1} corresponding to **UPBI-Py** was observed. It was difficult to trace the extent of polymerization from the FTIR spectra due to the close overlap of other peaks.

An attempt was made to characterize the supramolecular complex and polymer using gel permeation chromatography (GPC). The Figure 5.4a compares the gel permeation chromatograms of the **[UPBI-Py (OPVM-OH)]$_{1.0}$** and **[UPBIPy poly(OPVM-OH)]$_{1.0}$** along with that of **UPBI-Py** and **OPVM-OH** recorded in THF − a solvent in which all the samples were soluble. The difference in molar mass between **UPBI-Py** and **OPVM-OH** was not so large so that their chromatograms overlapped to a large extent with very narrow time difference in their elution. The SEC chromatograms of **[UPBI-Py (OPVM-OH)]$_{1.0}$** and **[UPBI-Py poly(OPVMOH)]$_{1.0}$** were broader and appeared in between that of the starting components. GPC is expected to differentiate a mixture of two different compounds provided they differ considerably in their masses.

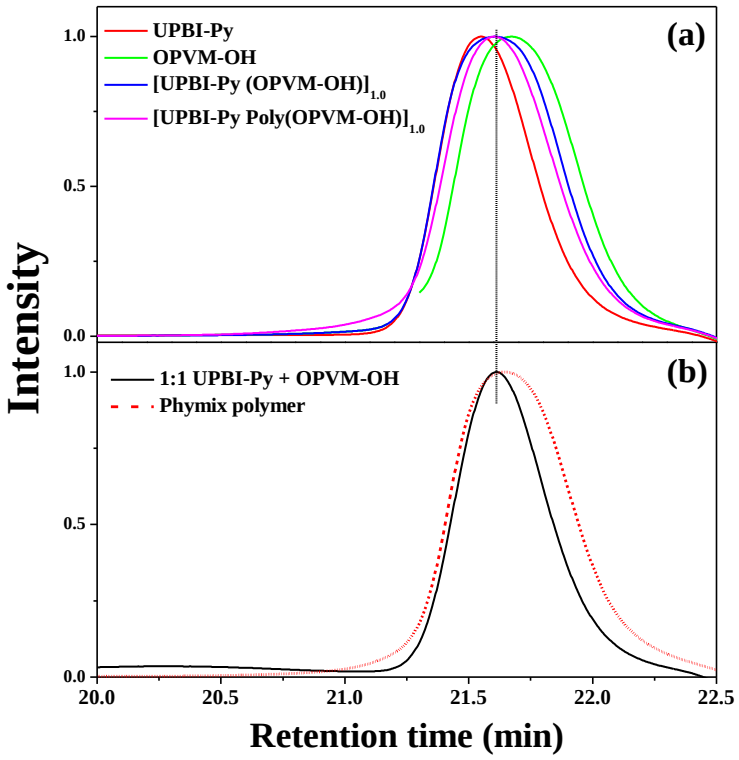

Figure 5.4: GPC of (a) **UPBI-Py, OPVM-OH, [UPBI-Py (OPVM-OH)]$_{1.0}$** and **[UPBI-Py poly(OPVM-OH)]$_{1.0}$** (b) 1:1 Physical mixture of **UPBI-Py** and **OPVM-OH**, polymer of 1:1 Physical mixture of **UPBI-Py** and **OPVM-OH** in THF.

The narrow difference in mass of the two components involved in the supramolecular complex formation made their molecular weight characterization by GPC not reliable. In fact, a 1:1 molar mixture of **UPBI-Py** and **OPVM-OH** was prepared by mixing the powdered solid samples together. A solution of this sample was then prepared for GPC analysis in THF and injected into the GPC column. A part of the solid mixture was dissolved in THF and subjected to photopolymerization under conditions identical to that described earlier. This sample named as phymix polymer was also analysed for its molecular weight by injecting into the GPC column. Figure 5.4b compares the GPC chromatograms of the 1:1 physical mixture of **UPBI-Py + OPVM-OH** and phymix polymer sample. The GPC chromatograms appeared in between that of **UPBI-Py** and **OPVM-OH**. Even the 1:1 **UPBI-Py + OPVM-OH** did not appear as two separate peaks or as a peak with a shoulder demonstrating that the mass difference between **UPBI-Py** and **OPVM-OH** was not large enough for the GPC to differentiate among them. However, it should also be mentioned here that besides the lack of sensitivity of our GPC instrument to differentiate between the two low molecular weight samples, GPC would

not be a good choice for characterizing self-assembly in very dilute samples. Self-assembly being a dynamic process, complexation is not favoured under very dilute conditions. Noticeable from the GPC data was the shift in the chromatogram of the supramolecular polymer to higher molecular weight compared to that of **OPVM-OH** clearly demonstrating that at least oligomers were formed.

The ^{1}H NMR spectra of the supramolecular polymer complex **[UPBI-Py poly(OPVM-OH)]$_{1.0}$** was recorded in $CDCl_3$ and compared with that of the complex as shown in Figure 5.5a,c (expanded region from 4.0 to 9.5 ppm). The proton NMR spectra showed the presence of unreacted methacrylate double bond in the polymer, but its intensity had reduced compared to the OPV aromatic protons. The extent of double bond

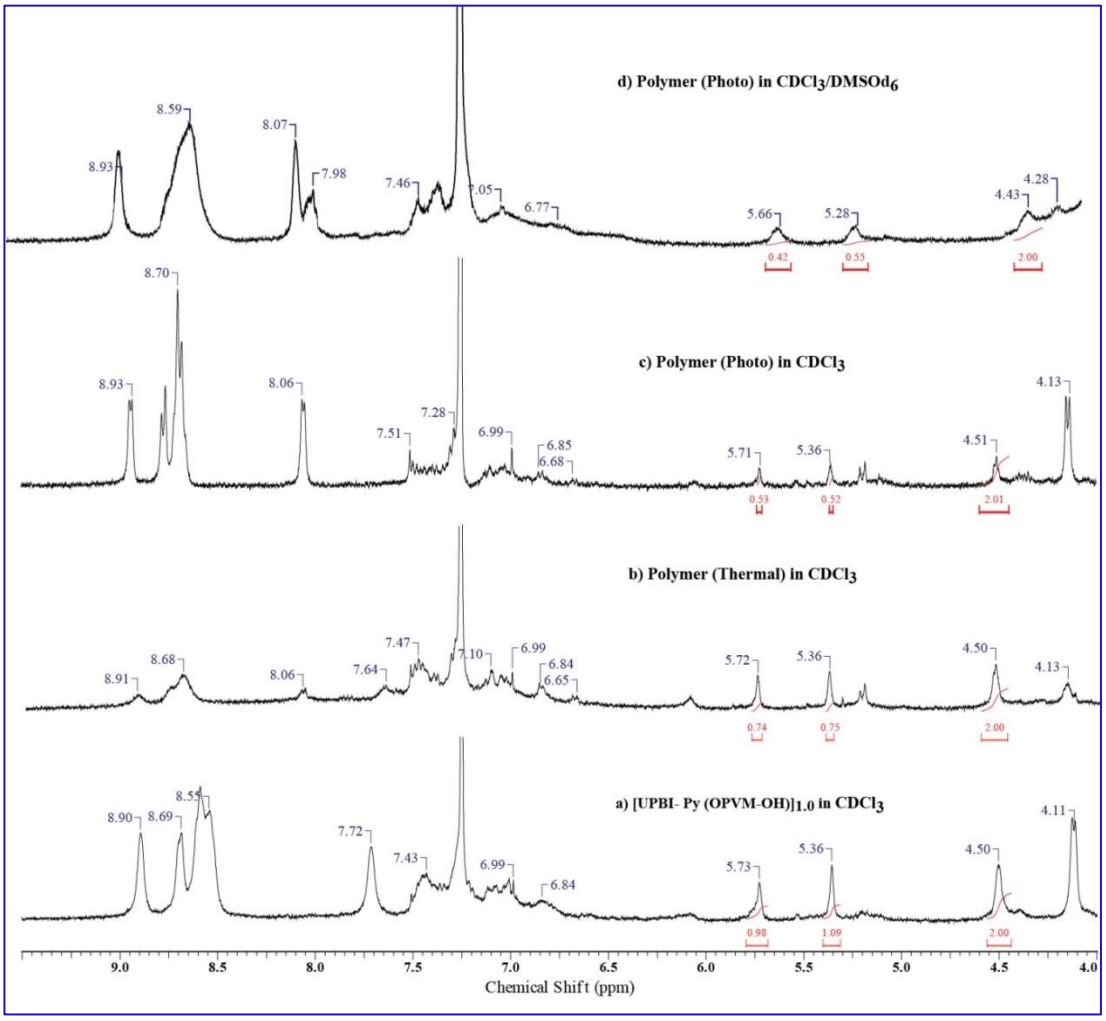

Figure 5.5: Comparison of the ^{1}H NMR spectra of **[UPBI-Py (OPVM-OH)]$_{1.0}$** with the supramolecular polymer **[UPBI-Py poly(OPVM-OH)]$_{1.0}$** prepared thermally as well as by photopolymerization recorded at 25 °C in $CDCl_3$ as well as in mixture of $CDCl_3$/DMSO-d_6.

conversion was estimated from the proton NMR integration values of the methacrylic peaks with respect to the peak at 4.5 ppm corresponding to two protons next to the amide linkage in **OPVM-OH**. The extent of polymerization was calculated to be around 48%. Free radical polymerization using BPO as the initiator and THF as solvent was also carried out to see if higher conversion could be achieved thermally. Figure 5.5b shows the proton NMR spectra of the supramolecular polymer complex synthesized thermally. The proton NMR spectra of the polymers covering the full chemical shift range are given in the figure 5.6. The extent of thermal polymerization was calculated to be ~30%. Another noticeable observation from the comparison of the proton NMR spectra of the complex and the polymer was the further downfield shift of the $H_{\beta\text{-Py}}$ of **UPBI-Py** from 7.72 to 8.06 ppm upon polymerization. This shift was observed for both the thermally polymerized sample as well as photopolymerized sample ruling out any photodegradation of the sample as the reason for this downfield shift by 0.34 ppm. Compared to the pristine **UPBI-Py**, the overall shift upon polymerization after complex formation was ~0.64 ppm, which was quite surprising considering the fact that the point of polymerization was on the OPV, which was spatially farther apart from **UPBI-Py**. Figure 5.5d also shows the proton NMR spectra of the polymer recorded in a mixture of solvents, namely, $CDCl_3$/DMSO-d_6. Addition of a few drops of DMSO-d_6 improved the solubility of the polymer considerably allowing higher concentration to be maintained. COSY experiments were conducted on the supramolecular polymer complex (in the solvent mixture $CDCl_3$/DMSO-d_6) to identify through space couplings within the sample. Figure 5.7 shows the COSY spectra highlighting the aromatic region of the **[UPBI-Py poly(OPVM-OH)]$_{1.0}$**. In addition to the cross coupling of the two peaks at 7.72 and 8.90 ppm corresponding to the $H_{\alpha\text{-Py}}$ and $H_{\beta\text{-Py}}$ protons of the pyridine ring of **UPBI-Py**, which was observed for the 1:1 complex, new off-diagonal peaks were observed connecting resonances from **UPBI-Py** and **OPVM-OH**. This is shown encircled in figure 5.7 indicating that the $H_{\beta\text{-Py}}$ protons of the pyridine ring of **UPBI-Py** at 8.02 ppm was spatially close to the aromatic protons of **OPVM-OH** at 7.30 ppm. This could explain the large downfield shift of 0.64 ppm observed for the $H_{\beta\text{-Py}}$ protons of the pyridine ring of **UPBI-Py** upon polymerization followed by complexation with **OPVM-OH**.

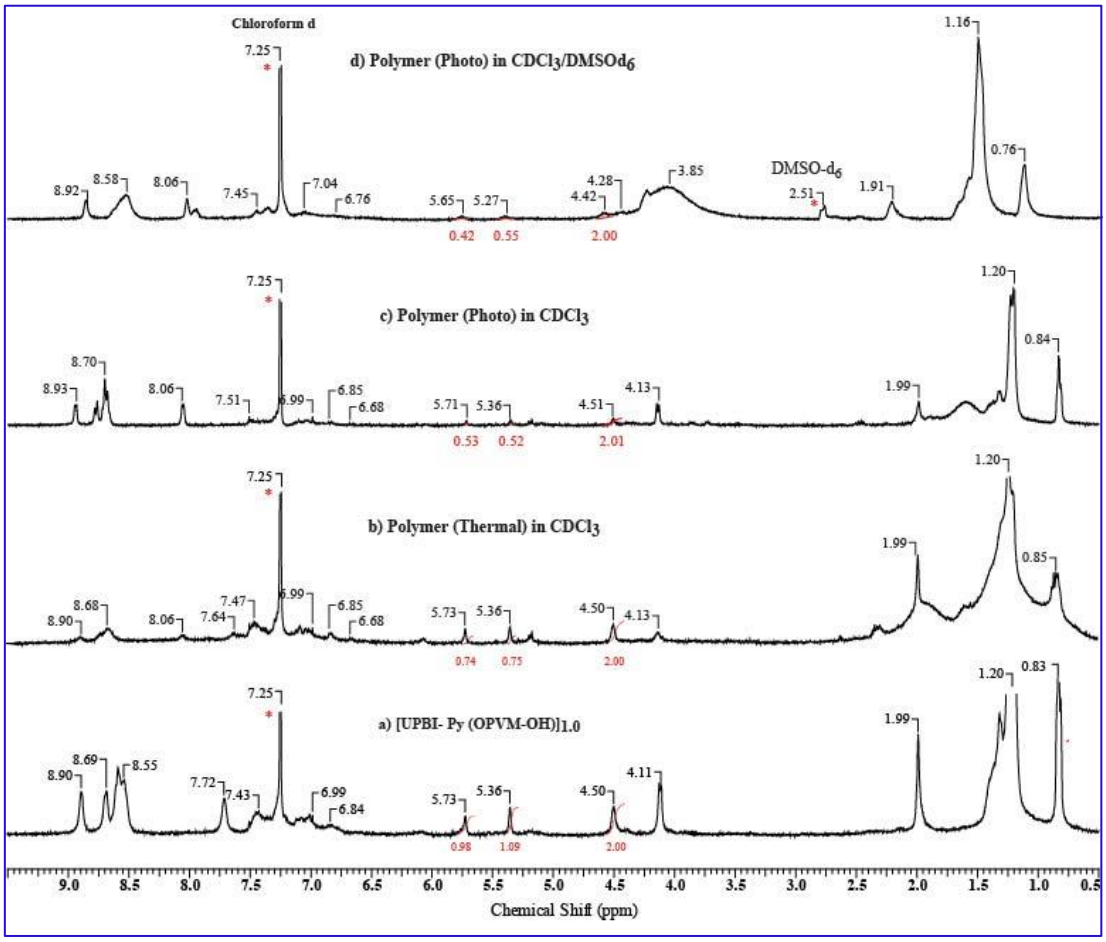

Figure 5.6: Comparison of the full range ^{1}H NMR spectra of **[UPBI-Py (OPVM-OH)]$_{1.0}$** with the supramolecular polymer complex **[UPBI-Py poly(OPVM-OH)]$_{1.0}$** prepared thermally as well as by photopolymerization recorded at 25 °C in $CDCl_3$ as well as in mixture of $CDCl_3$/DMSO-d_6.

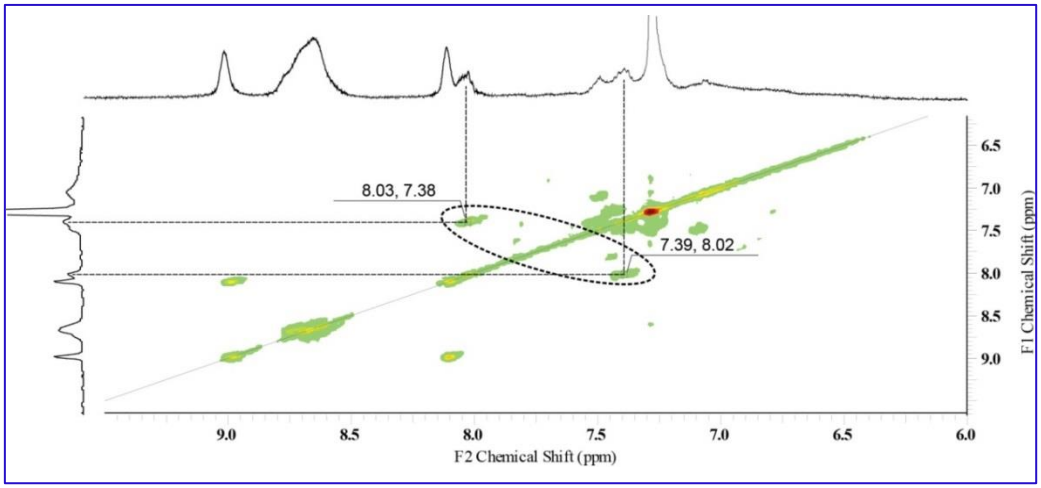

Figure 5.7: COSY spectra of **[UPBI-Py poly(OPVM-OH)]$_{1.0}$** showing selected NOE extract of the aromatic region (400 MHz, $CDCl_3$/DMSO-d_6, 298K). The peaks showing diagonal cross coupling is encircled.

5.4.3 Photophysical Characterization

Photophysical studies involving UV−visible absorption and fluorescence spectroscopy measurements were undertaken to get more insight into the nature of self-assembly of the donor−acceptor complex formed by **UPBI-Py** and **OPVM-OH**. DMF was used as the solvent for the photophysical studies since **OPVM-OH** had better solubility in DMF. Figure 5.8a shows the normalized absorption spectra of **UPBI-Py** and **OPVM-OH** taken in solution in DMF as well as drop cast as thin films from DMF. In solution, the absorption spectra of **OPVM-OH** was characterized by a broad spectra with peak at 375 nm, while **UPBI-Py** exhibited characteristic absorption of isolated perylenebisimide chromophore with peaks in the range 400−530 nm. The absorption spectrum in the solid state had more vibrational fine structures and the absorption maximum was blue-shifted from 375 in solution to ∼325 nm in film for **OPVM-OH** indicating H type aggregation.[29] In the case of films of **UPBI-Py**, the absorption was broad, and the peak intensities of the $A^{0\rightarrow0}$ and $A^{0\rightarrow1}$ changed compared with that of the solution spectrum. The ratio of the peak intensities of absorbance $A^{0\rightarrow0}/A^{0\rightarrow1}$ lower than 1.6 is generally taken as an indication for aggregation.[30−32] The value of this ratio in the film was 1.03, suggesting aggregation in the solid state. The peak maxima blue-shifted and a new red-shifted peak appeared at 547 nm, which were features attributed to rotationally shifted face-to-face aggregates.[32] The normalized absorption spectra of drop cast films (from DMF) of the 1:1 complex **[UPBI-Py (OPVM-OH)]$_{1.0}$** exhibited features corresponding to both the OPV and PBI chromophores. The normalized absorption spectra comparing the features of **OPVM-OH**, **UPBI-Py**, and **[UPBI-Py (OPVM-OH)]$_{1.0}$** are given in Figure 5.8b, while the absorption spectra plotted as a function of molar extinction coefficient (to highlight the contribution of each chromophore) is given in Figure 5.8c. No charge transfer band was observed in the absorption spectra of films of the DA complex indicating the absence of electronic communication between donor and acceptor moieties in the ground state.[33] The OPV absorption in the range 280 to 400 nm was more broadened due to the overlapping absorption of PBI also occurring in the same range. It was clear that both the OPV and PBI chromophores were aggregated in the 1:1 complex also since they were blue-shifted and exhibited features similar to that of the aggregated starting materials.

Figure 5.9 compares the emission spectra of **OPVM-OH**, **UPBI-Py**, **[UPBI-Py (OPVM-OH)]$_{1.0}$**, and **[UPBI-Py poly(OPVM-OH)]$_{1.0}$** upon excitation at both the OPV (368 nm in DMF solution and 375 nm in film) and PBI (∼555 nm) emission wavelengths as drop cast films from DMF. The figure also includes the emission spectra recorded in

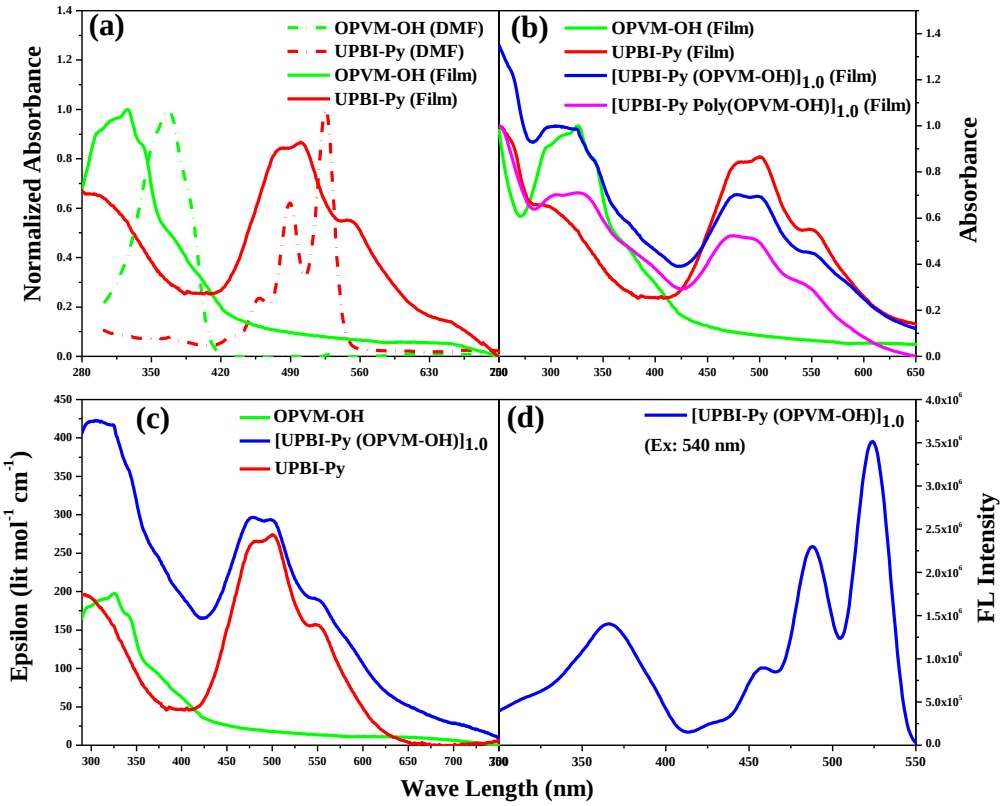

Figure 5.8: (a) Absorption spectrum of **OPVM-OH** and **UPBI-Py** in DMF solution and dropcasted (from DMF) film. (b) Comparison of absorption spectrum of drop cast film of **[UPBI-Py (OPVM-OH)]$_{1.0}$**, **[UPBI-Py Poly(OPVM-OH)]$_{1.0}$** along with that of **OPVM-OH** and **UPBI-Py** (c) Excitation Spectrum of 1:1 Complex **[UPBI-Py (OPVM-OH)]$_{1.0}$**.

DMF solution for all samples upon excitation at the OPV absorption maximum of 368 nm. **OPVM-OH** exhibited strong emission with maximum at 445 nm in DMF solution (Figure 5.9a). In the solid state upon excitation at 375 nm, the OPV monomer emission at 445 nm was suppressed and a broad redshifted aggregate emission was observed with peak at 500 nm. The blue-shifted absorption together with the red-shifted emission in film compared to that in solution has been shown to be due to existence of H type aggregates in film.[34] Upon excitation at the OPV wavelength ~375 nm, **UPBI-Py** exhibited intense emission (both DMF solution as well as film), which indicated that selective excitation of the OPV chromophore was not feasible. Two small peaks were observed at 410 and 430 nm along with typical emission of perylenebisimides with peak maxima at 534, 576, 626 nm in DMF (Figure 5.9b). However, in the solid state the PBI monomer emission at 534 nm was hugely suppressed, and a red-shifted intense broad emission was observed at 638 nm indicating aggregate formation. Upon excitation at 510 nm corresponding to PBI

absorption wavelength maximum, the emission peak shape remained the same showing aggregate emission at 638 nm, but the intensity was slightly higher.

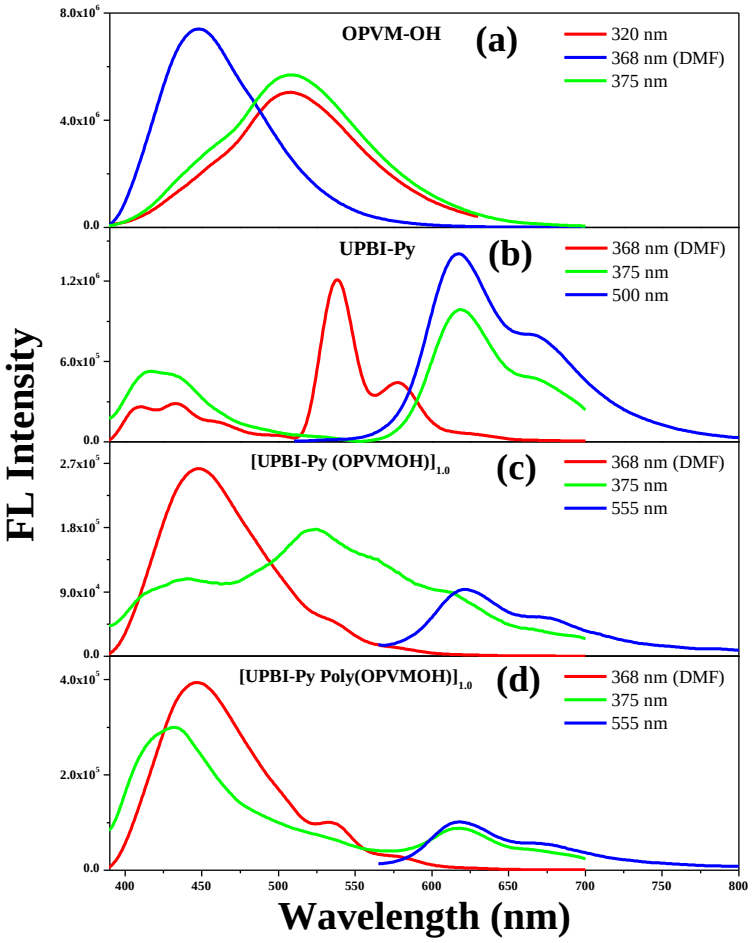

Figure 5.9: Fluorescence spectrum of (a) **OPVM-OH,** (b) **UPBI-Py**, (c) **[UPBI-Py (OPVM-OH)]$_{1.0}$** and (d) **[UPBI-Py Poly(OPVM-OH)]$_{1.0}$** upon excitation at different wavelengths in DMF solution and as drop cast films from DMF.

Figure 5.9c compares the emission from the 1:1 supramolecular donor−acceptor complex **[UPBI-Py (OPVM-OH)]$_{1.0}$** upon excitation around 370 nm both in DMF solution and as films. The emission from the film was considerably quenched compared to that in solution; therefore, the emission spectra collected in DMF had to be scaled down by a factor of 30 to plot them together. The emission from the D−A complex in DMF solution was very similar to that of the emission from molecularly dissolved **OPVM-OH** collected in DMF with maximum at 445 nm. However, a small shoulder was observed around 550 nm corresponding to emission from molecularly dissolved **UPBI-Py**. Although selective excitation of OPV was not possible and PBI chromophore also could be excited by excitation at 368 nm, a part of the PBI emission upon excitation at

368 nm could have contribution from energy transfer occurring from OPV to PBI also. This was supported by the observation of OPV absorption band in the excitation spectra of **[UPBI-Py (OPVM-OH)]$_{1.0}$** collected while monitoring the PBI emission at 540 nm (Figure 5.8d). Upon excitation at 375 nm, the emission from films of **[UPBI-Py (OPVM-OH)]$_{1.0}$** exhibited broad emission centered at 525 nm with shoulder at 430 and 620 nm. The emission of OPV at 525 nm was quenched 36 times in **[UPBI-Py (OPVM-OH)]$_{1.0}$** compared to that in the **OPVM-OH** alone. This was an indication of energy transfer from **OPVM-OH** to **UPBI-Py** in the film state in the 1:1 supramolecular complex. Unambiguous identification of the nature of origin of the peak around 420 nm was not easy since PBI as well as unaggregated OPV had emission in the same region. However, the shoulder at 630 nm could be attributed to the aggregate emission occurring from PBI units as could be confirmed from the emission spectra collected by exciting at 555 nm corresponding to PBI.

An attempt was made to obtain evidence for energy transfer from **OPVM-OH** to **UPBI-Py** in **[UPBI-Py (OPVM-OH)]$_{1.0}$** from the fluorescence emission lifetime decay studies. The sample films were excited using a nano LED source of 370 nm and monitored at the OPV emission of 450 nm as well PBI emission of 625 nm. Although the best fits were obtained to be biexponential, the most prominent species (α_1 = 0.99) in **OPVM-OH** film had a lifetime of 0.42 ns (table 5.1). This was much lower compared to the fluorescence emission decay value of 1.01 ns observed for **OPVM-OH** in solution (DMF).[35] The reduced lifetime for the emitting species confirmed quenching due to aggregation in the solid state. The 1:1 supramolecular donor−acceptor complex **[UPBIPy (OPVM-OH)]$_{1.0}$** was also excited at 370 nm and the decay observed both at the OPV

Table 5.1: Parameters (τ: decay time, α: pre-exponential factor, χ^2: chi-squared value) retrieved from the biexponential fit obtained by using nano LED 370 nm for excitation

Sample	Monitored at 450 nm		Monitored at 625 nm		χ^2
	$\tau_{OPV\,1}$ (ns) (α_1)	$\tau_{OPV\,2}$ (ns) (α_2)	$\tau_{PBI\,1}$ (ns (α_1)	$\tau_{PBI\,2}$ (ns) (α_2)	
OPVM-OH (DMF solution)	1.01 (0.64)	0.92 (0.36)			0.97
OPVM-OH (film)	0.42 (0.99)	5.41 (0.01)			1.41
UPBI-Py (film)	0.54 (0.97)	6.97 (0.03)	1.11 (0.98)	160.94 (0.02)	1.51; 1.22
[UPBI-Py (OPVM-OH)]1.0 (film)	0.48 (0.98)	6.25 (0.02)	1.11 (0.98)	164.88 (0.02)	1.37; 1.28

emission region of 450 nm and PBI emission region of 625 nm. At the OPV emission region of 450 nm, an emission lifetime decay of 0.48 ns (α_1 = 0.98) was observed, while at the PBI emission region of 625 nm, a decay of 1.11 ns (α_1 = 0.98) was observed. The increase in OPV emission lifetime decay values instead of the expected decrease in the donor−acceptor complex could be understood by studying the lifetime decay profile of **UPBI-Py** upon excitation at 370 nm. Upon exciting **UPBI-Py** at the OPV absorption wavelength of 370 nm, a decay time of 0.54 ns (α_1 = 0.97) was observed, which made establishment of existence of energy transfer from OPV chromophore to PBI impossible. The observed emission from PBI (at 625 nm) upon excitation at 370 nm also could not be unambiguously attributed to energy transfer process, because **UPBI-Py** alone exhibited emission at 625 nm with a lifetime decay of 1.11 ns (α_1 = 0.98) for the 370 nm excitation. However, the increased extent (36 times) of the OPV fluorescence quenching at 525 nm in **[UPBI-Py (OPVM-OH)]$_{1.0}$** compared to that in the **OPVM-OH** alone gave indirect evidence for the existence of energy transfer channels between OPV and PBI in the 1:1 supramolecular donor− acceptor complex. The supramolecular polymeric complex **[UPBI-Py poly(OPVM-OH)]$_{1.0}$**, which was obtained by photopolymerization of the **[UPBI-Py (OPVM-OH)]$_{1.0}$** complex, was also subjected to photophysical characterization. Figure 5.8b shows the absorption spectra of thin film sample of the polymer along with that of the 1:1 complex. Figure 5.9d shows, the emission in DMF solution (excitation: 368 nm; scaled down by a factor of 15) was very similar to that of **[UPBI-Py (OPVM-OH)]$_{1.0}$** with OPV emission peak at 445 nm having a shoulder peak at 550 nm corresponding to emission from molecularly dissolved perylenebisimide. The emission spectrum of thin film samples of the polymer was different from that of thin films of the 1:1 supramolecular complex. The monomeric OPV emission was observed with an almost complete suppression of the OPV aggregate emission beyond 500 nm in the polymer film. The emission was characterized by two peaks in its emission spectra, one at 429 nm with a shoulder at 417 nm and another peak at 618 nm corresponding to aggregated PBI emission. Although PBI also exhibited emission around 420 nm, based on the higher intensity of emission with respect to the PBI aggregate emission at 618 nm the peaks at 429 nm could be attributed to nonaggregated OPV emission. The OPV monomeric emission at 429 nm was very similar to that of **OPVM-OH** in dilute solution with peak at 430 nm. The emission spectra of the insoluble homopolymer **poly(OPVM-OH)** (produced by the photopolymerization of **OPVM-OH**) was recorded as solid powder sample and compared with that of the supramolecular polymer complex. Figure

5.10a compares the emission from thin film sample of **[UPBI-Py poly(OPVM-OH)]$_{1.0}$**, along with that of the emission from powder sample of **poly(OPVM-OH)**. The homopolymer **poly(OPVM-OH)** was characterized by two peaks in the emission spectra– one at 503 nm identical with that of thin film of its monomer **OPVM-OH** and another new red-shifted peak at 570 nm. The new red-shifted peak could have its origin in excimer luminescence originating from polymer interchain excitations.[35, 36] It is interesting to analyse the emission characteristics of the supramolecular donor− acceptor polymer in the context of the behaviour of the donor homopolymer. Although the starting donor−acceptor supramolecular complex exhibited red-shifted aggregate emission of OPV, this aggregate was disrupted upon polymerization. It was evident that the donor−acceptor small molecule assembly upon polymerization of the donor units exhibited a drastic change in emission characteristics of the donor, reflecting the change in organization of the donor units brought about by covalent linkage of their methacrylamide backbone. In order to rule out the role of the solvent (DMF) used for preparing the sample films influencing their self-organization, the 1:1 supramolecular donor−acceptor complex and its polymer films were prepared from another solvent−ortho dichlorobenzene (ODCB)–a solvent from which devices were prepared for bulk mobility estimate (described later). Figure 5.10b compares the emission at 375 nm from the sample films of 1:1 supramolecular donor−acceptor complex and its polymer prepared from both DMF and ODCB. The emission characteristics were similar in both sets of films suggesting that the changes observed in the emission spectra of the polymer was not

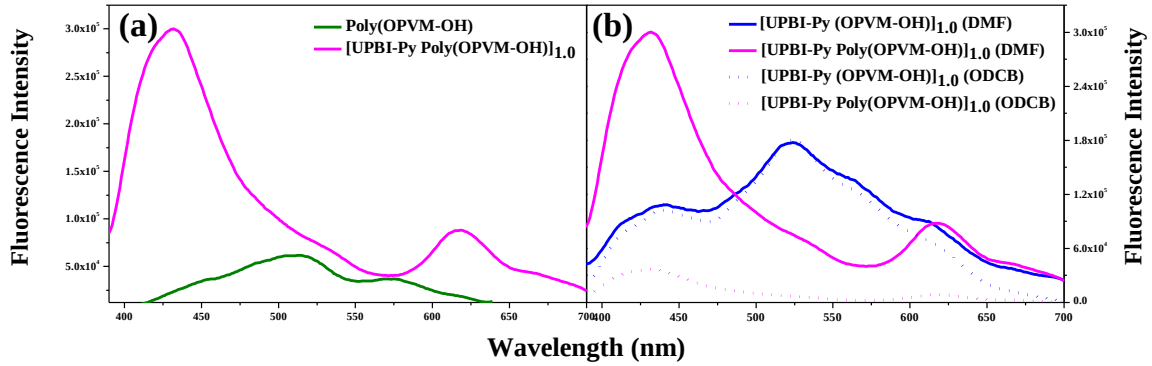

Figure 5.10: (a) Fluorescence spectrum of **[UPBI-Py (OPVM-OH)]1.0** and **Poly(OPVM-OH)** and (b) **[UPBI-Py (OPVM-OH)]1.0** and **Poly(OPVM-OH)** in DMF and ODCB.

brought about by solvent effect, but it had its origin in the changes in organization of the donor occurring due to polymerization. Thus, the photophysical studies involving emission from thin film samples established the donor−acceptor assembly in the 1:1 supramolecular complex as well as provided evidence for subtle changes occurring in their self-assembly upon covalent linkage of the methacrylamide units into a polymeric backbone in the donor moieties.

5.4.4 Bulk Structure Analysis

Figure 5.11a shows the normalized WXRD patterns for **UPBI-Py**, **OPVM-OH**, and the 1:1 complex **[UPBI-Py (OPVM-OH)]$_{1.0}$** measured at room temperature (25 °C) in the range 2θ = 2.5−35°. **OPVM-OH** did not exhibit any peak below 2θ = 3°, which was independently confirmed by small-angle X-ray scattering (SAXS) analysis (given in Figure 5.12a). Compared to **UPBIPy**, **OPVM-OH** was more crystalline with several sharp peaks covering the entire 2θ range from 2.5 to 35°. Attempts to index **UPBI-Py** were not successful; however, most of the peaks in the pattern of **OPVM- OH** could be successfully indexed and fitted to a monoclinic crystal lattice with cell parameters a = 29.843(24), b = 3.613(3), c = 25.709(23), and β = 122.74(5)0. The reflection at 2θ = 24.62° (d = 3.61 Å), indicated by arrow in Figure 5.11a, which was indexed as the (010) peak corresponded to the π−π interaction of closely stacked aromatic units, which is the typical π−π stacking distance reported for OPV units in the literature.[37, 38] The energy minimized conformation and length scale of both the **OPVM-OH** and **UPBI-Py** molecules were obtained with the help of DFT (B3LYP/6-31G (d.p.)) calculation, which are shown in Figure 5.12b. **OPVM-OH** had the methacrylamide moiety out of plane of the three OPV rings and the length of the molecule in the plane from the $-CH_2$ to O−H was ∼19 Å. However, the indexed cell lengths in the ac plane were much bigger than the molecular length as derived from computational studies indicating a more complex structure possibly a centred one. The 1:1 complex **[UPBI-Py (OPVM-OH)]$_{1.0}$** had peak pattern that was different from that of the **OPVM-OH** (although peaks corresponding to **UPBI-Py** was more or less intact), especially in the region of 25−28° corresponding to stacking distances. **[UPBI-Py (OPVM-OH)]$_{1.0}$** could be indexed to a monoclinic cell without taking into consideration the peaks from **UPBI-Py**. The cell parameters for the 1:1 complex **[UPBI-Py (OPVM-OH)]$_{1.0}$** was a = 34.774(21), b = 4.537(3), c = 16.987(10), and β = 118.13(5)º. The π−π stacking distance increased to a d spacing 4.537 Å corresponding to 2θ = 19.572° (dotted line in Figure 5.11a) in **[UPBI-Py (OPVM-**

OH)]$_{1.0}$. The angle β, also changed from 122.74° in **OPVM-OH** to 118.13° in the 1:1 complex **[UPBI-Py (OPVM-OH)]$_{1.0}$** indicating changes in the packing pattern upon complex formation. In order to further confirm the complex formation, two more complexes with varying mole ratios of the two molecules **UPBI-Py** and **OPVM-OH** were synthesized. They were **[UPBI-Py$_{1.0}$ (OPVM-OH)$_{2.0}$]** and **[UPBI-Py$_{2.0}$ (OPVM-OH)$_{1.0}$]**. Figure 5.11b shows the stack plot of the normalized reflections of the three

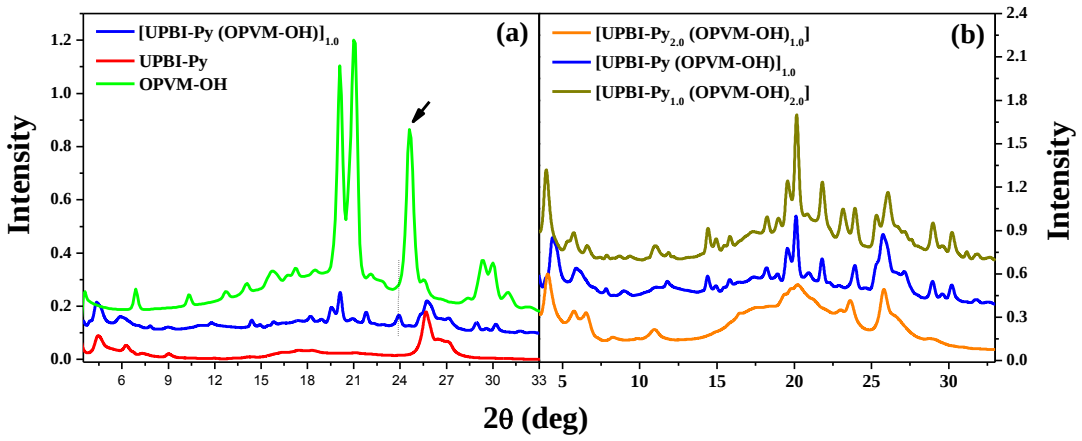

Figure 5.11: Wide angle X-ray diffraction pattern recorded at 25 °C (2θ from 2 to 35^0) for (a) **OPVM-OH, UPBI-Py,** and 1:1 complex **[UPBI-Py (OPVM-HO)]$_{1.0}$** (b) the three complexes **[UPBI-Py (OPVM-HO)]$_{1.0}$, [UPBI-Py$_{1.0}$ (OPVM-OH)$_{2.0}$]** and **[UPBI-Py$_{2.0}$ (OPVM-OH)$_{1.0}$]**.

complexes expanded in the range 2θ = 3.5−35°. It could be seen that all three complexes exhibited complex peak pattern compared to the parent molecules indicating multiple phases. **[UPBI-Py$_{2.0}$ (OPVM-OH)$_{1.0}$]**, which had higher molar ratio of **UPBI-Py** was less crystalline compared to the other complexes although the emergence of the crystalline peaks of the complex phase could be clearly observed. On the other hand, the **[UPBI-Py$_{1.0}$ (OPVM-OH)$_{2.0}$]** with higher molar ratio of **OPVM-OH** exhibited several sharp peaks that were not present in either **OPVM-OH** or **UPBI-Py**. An attempt was made to index these two complexes and the results in comparison with OPV and 1:1 complex are tabulated in table 5.2. Distinct changes in the cell parameters could be discerned as **OPVM-OH/UPBI-Py** ratio changed in the complex clearly demonstrating the interaction existing between the two parent molecules **UPBI-Py** and **OPVM-OH** resulting in formation of new complexes.

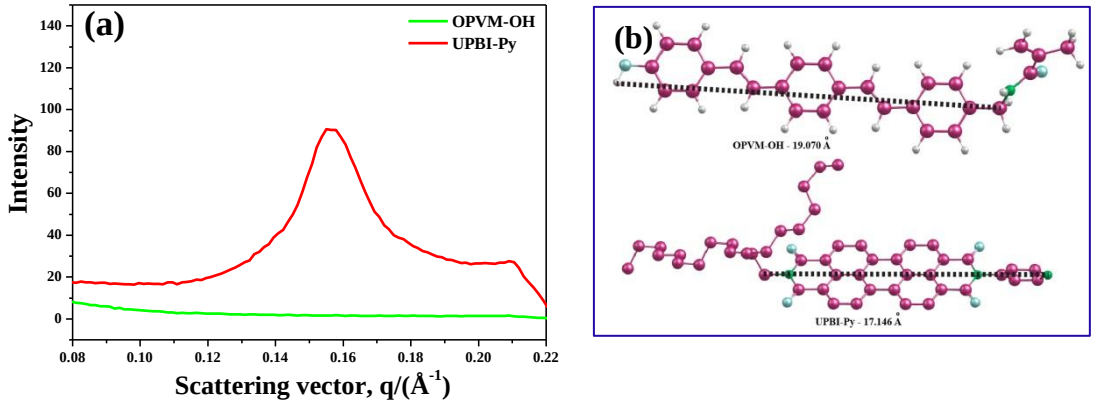

Figure 5.12: (a) SAXS data of **OPVM-OH** and **UPBI-Py** (b) DFT (B3LYP/6-31G (d.p.)) calculated energy minimized structures of **OPVM-OH** (top) and **UPBI-Py** (bottom)

Table 5.2: Summary of unit cell parameters of **OPVM-OH** and three D-A complexes

Sample Name	a (Å)	b (Å)	c (Å)	β	V
OPVM-OH	29.843(24)	3.613(3)	25.709(23)	122.74(5)	2331.71
[UPBI-Py$_{1.0}$ (OPVM-OH)$_{2.0}$]	31.675(19)	4.920(3)	17.326(20)	104.37(8)	2616.06
[UPBI-Py (OPVM-HO)]$_{1.0}$	34.774(21)	4.537(3)	16.97(10)	118.13(5)	2363.51
[UPBI-Py$_{2.0}$ (OPVM-OH)$_{1.0}$]	33.07(16)	4.387(4)	16.214(18)	98.68(19)	2325.59

The solid physical mixture of 1 mol each of **UPBI-Py** and **OPVM-OH** (prepared by mixing the powdered solid samples together), which was used earlier for the GPC experiments was studied for the WXRD reflections. Figure 5.13a compares the WXRD pattern of this mixture with that of **OPVM-OH** and **UPBI-Py**. Unlike the three complexes discussed previously, the solid physical mixture was a combination of reflections from both **UPBI-Py** and **OPVM-OH** and no shift was observed for the π–π stacking reflection ~2θ = 24° suggesting that complexation had not occurred in the physical mixture. Figure 5.13b compares the WXRD data of the supramolecular polymer **[UPBI-Py poly(OPVM-OH)]$_{1.0}$** with that of the 1:1 complex **[UPBI-Py (OPVM-OH)]$_{1.0}$**. An overall reduction in crystallinity was observed in the polymer compared to the 1:1 complex. This could be attributed to the presence of the flexible methacrylate polymer backbone. Table 5.3a-f gives the entire Bragg reflections and their corresponding 'd' spacings for the donor, acceptor, the supramolecular polymer, as well as the various complexes.

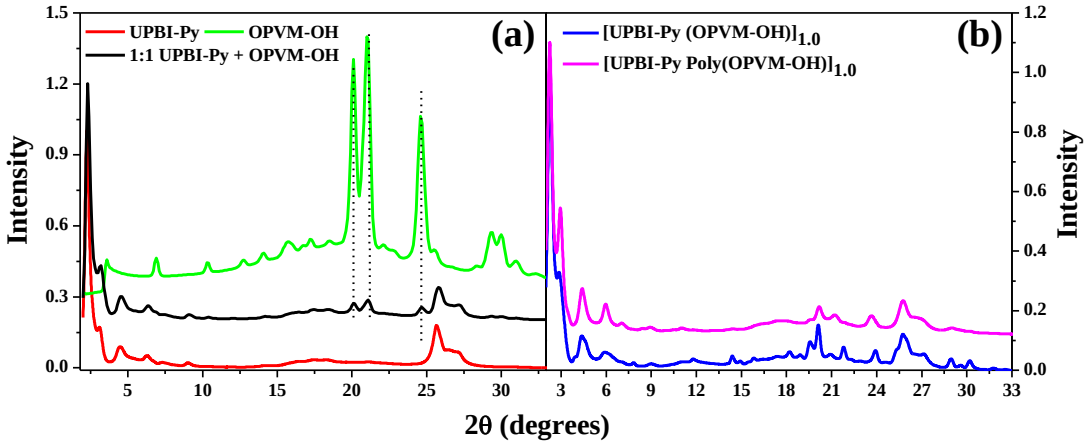

Figure 5.13: Wide angle X-ray diffraction pattern of (a) **OPVM-OH**, **UPBI-Py** and 1:1 (**OPVM-OH:UPBI-Py**) physical mixture; (b) **[UPBI-Py (OPVM-OH)]$_{1.0}$** and supramolecular polymer complex **[UPBI-Py Poly(OPVM-OH)]$_{1.0}$** recorded at 25 °C.

Table 5.3: Wide angle X-ray diffraction (WXRD) data of (a) **OPVM-OH**, (b) **UPBI-Py**, (c) **[UPBI-Py (OPVM-OH)]$_{1.0}$**, (d) **[UPBI-Py Poly(OPVM-OH)]$_{1.0}$**, (e) **[UPBI-Py$_{1.0}$ (OPVM-OH)$_{2.0}$]** and (f) **[UPBI-Py$_{2.0}$ (OPVM-OH)$_{1.0}$]**.

	(a) OPVM-OH			(b) UPBI-Py	
SL No	**2θ value (°)**	**d-spacing value (Å)**	**h k l values**	**2θ value (°)**	**d-spacing value (Å)**
1	3.64	24.24	1 0 -1	3.70	23.84
2	6.90	12.80	1 0 -2	4.59	19.21
3	10.34	8.55	2 0 -3	6.29	14.02
4	12.76	6.93	4 0 -3	7.41	11.92
5	14.14	6.26	4 0 0	9.01	9.80
6	15.79	5.61	5 0 -1	11.94	7.40
7	17.20	5.15	2 0 3	16.38	5.40
8	18.56	4.77	1 0 4	17.49	5.06
9	20.10	4.41	3 0 3	18.31	4.84
10	21.02	4.22	7 0 -4	25.75	3.45
11	24.62	3.61	0 1 0	27.13	3.28
12	29.39	3.04	5 1 -1	41.90	2.15
13	29.98	2.98	9 0 -1	--	--
14	30.97	2.88	1 0 7	--	--
15	40.67	2.22	4 1 -9	--	--
16	42.79	2.11	12 0 –11	--	--

(c) [UPBI-Py (OPVM-OH)]$_{1.0}$				(d) [UPBI-Py Poly(OPVM-OH)]$_{1.0}$	
SL No	**2θ value (°)**	**d-spacing value (Å)**	**h k l values**	**2θ value (°)**	**d-spacing value (Å)**
1	2.86	30.86	1 0 0	3.503	25.1989
2	5.89	14.96	0 0 1	4.328	20.4006
3	7.82	11.29	3 0 -1	5.956	14.8261
4	11.79	7.49	0 0 2	7.055	12.5198
5	14.39	6.14	5 0 0	8.841	9.9945
6	15.83	5.59	2 0 -3	10.018	8.8225
7	18.20	4.86	7 0 -1	10.783	8.1981
8	19.57	4.53	0 1 0	16.630	5.3264
9	20.11	4.41	4 0 2	18.004	4.9231
10	20.92	4.24	4 0 -4	20.440	4.3416
11	21.80	4.07	6 0 -4	23.717	3.7485
12	23.92	3.71	5 1 -2	25.887	3.4389
13	25.34	3.51	4 1 -3	27.093	3.2950
14	28.95	3.08	213	42.093	2.1449
15	29.58	3.02	11 0 -4	--	--
16	30.19	2.96	7 1 -4	--	--

(e) [UPBI-Py$_{1.0}$ (OPVM-OH)$_{2.0}$]				(f) [UPBI-Py$_{2.0}$ (OPVM-OH)$_{1.0}$]		
SL No	**2θ value (°)**	**d-spacing value (Å)**	**h k l values**	**2θ value (°)**	**d-spacing value (Å)**	**h k l values**
1	2.87	30.78	1 0 0	2.71	32.57	1 0 0
2	5.35	16.51	1 0 -1	5.76	15.34	1 0 -1
3	6.60	13.38	1 0 1	6.52	13.54	1 0 1
4	11.84	7.47	3 0 -2	8.27	10.69	2 0 1
5	14.42	6.13	5 0 0	10.95	8.07	1 0 -2
6	15.84	5.59	0 0 3	20.23	4.39	0 1 0
7	18.24	4.86	1 1 0	23.62	3.76	2 0 4
8	19.58	4.53	7 0 -1	41.56	2.17	0 2 1
9	20.16	4.40	3 1 -1	--	--	--
10	20.87	4.25	0 1 2	--	--	--
11	21.82	4.07	4 0 3	--	--	--
12	23.16	3.84	5 1 0	--	--	--
13	23.93	3.71	5 1 -2	--	--	--
14	25.33	3.51	9 0 -1	--	--	--
15	28.97	3.08	5 1 -4	--	--	--
16	30.21	2.95	5 1 3	--	--	--
17	31.17	2.87	4 0 -6	--	--	--

5.4.5 Thin Film Morphology

Thin film morphology of the complex and supramolecular polymer were analysed using transmission electron microscopy (TEM). The 1:1 OPV:PBI complex was drop cast (2 mg/mL DMF solution) onto the copper grid and subjected to selective staining using Osmium tetroxide (OsO_4).[39] Striated nanostructure in the length scale of <10 nm formed by the lamellar structure of the complex was observed covering large area of the grid as

shown in Figure 5.14a−d. The dark lines corresponded to OPV layers stained by OsO_4 while the bright lines corresponded to those of crystalline perylene units. The statistically averaged thickness of the dark and bright region measured from the TEM image using the instrument software was ~18 Å. The starting materials **OPVM-OH** and **UPBI-Py** did not exhibit any characteristic morphology under identical conditions. Figure 5.14i−l and 5.14m−p shows the TEM images of drop cast samples of **UPBI-Py** and **OPVM-OH** on TEM grids. Therefore, it was obvious that the donor (OPV) and acceptor (PBI) had formed well developed alternating parallel nanostructured lamellae as a result of the self-assembly. There are reports in literature on the large area self-assembly of small organic molecules where the self-assembly in solution was translated in thin films upon processing.[40, 41] Hydrogen bond directed supramolecular self-assembly between oligo(*p*-phenylenevinylene) containing ureidotriazine and perylenebisimide were shown to form lamellar structures as well as chiral stacks.[42−44] The thin film morphology of the polymer

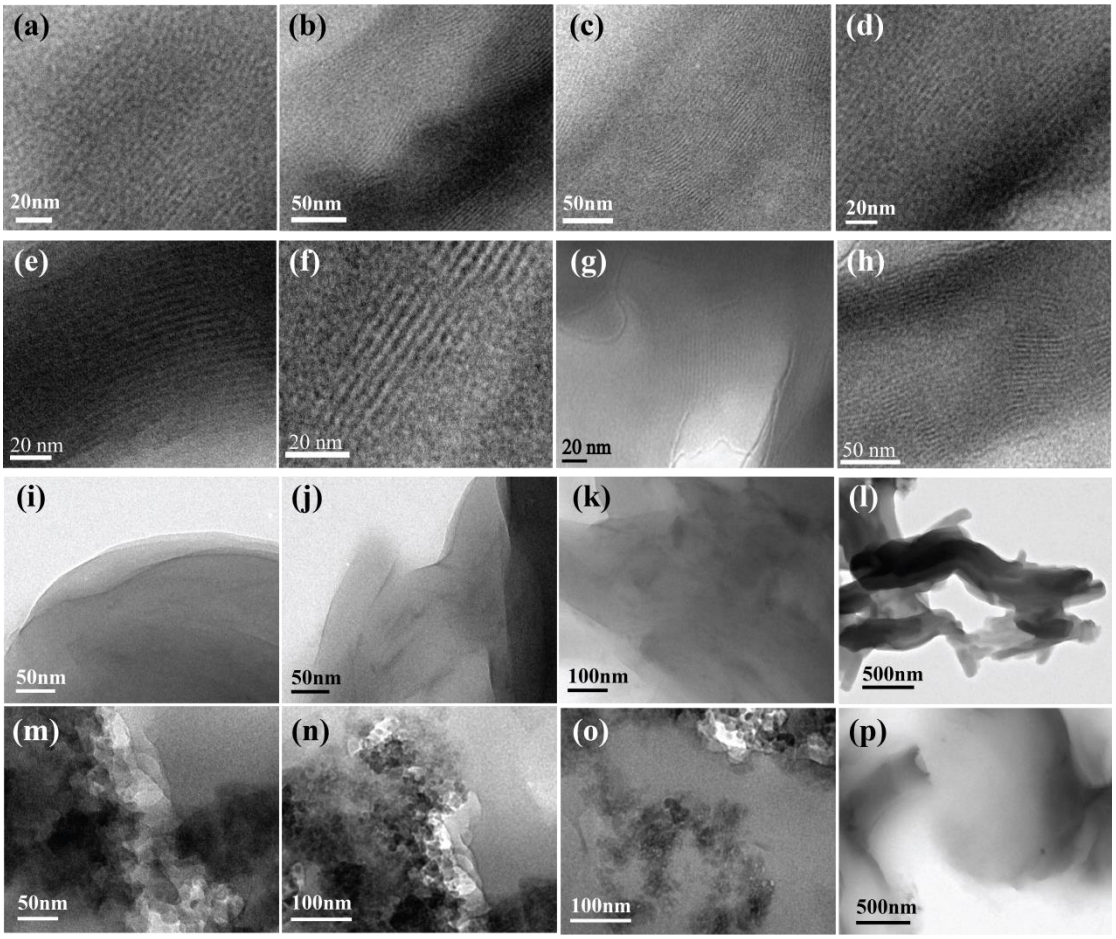

Figure 5.14: TEM images of (a-d) 1:1 complex **[UPBI-Py (OPVM-OH)]$_{1.0}$**; (e-h) supramolecular polymer complex **[UPBI-Py Poly(OPVM-OH)]$_{1.0}$**; (i-l) **UPBI-Py** and (m-p) **OPVM-OH**.

formed by thermal polymerization as well as photopolymerization was also analysed using TEM. Figure 5.14e−h shows the images for the supramolecular polymer which was stained using OsO_4. Beautiful lamellar striations were visible covering large area of the grid for the supramolecular polymer complex also. The average thickness of the bright and dark area determined using the instrument software was ~18 Å. The length scale of ~18 Å observed in the TEM images correlated very well with the molecular length of **UPBI-Py** and **OPVM-OH** obtained using DFT (B3LYP/6-31G (d.p.)) calculation (figure 5.12b).

5.4.6 Electron Mobility and Photoconductivity Studies

The charge carrier mobility in the small molecule **UPBI-Py**, the 1:1 D−A supramolecular complex **[UPBI-Py (OPVM-OH)]$_{1.0}$** and the D−A supramolecular polymer complex **[UPBI-Py poly-(OPVM-OH)]$_{1.0}$** was evaluated using space charge limited current (SCLC) measurements. The current voltage characteristics of the devices made were measured in dark as well as under illumination. Space charge regime in J(V) was observed in **[UPBI-Py (OPVM-OH)]$_{1.0}$** and **[UPBI-Py poly(OPVM-OH)]$_{1.0}$** for the devices tested and mobility was estimated from J(V) relationship measured under dark condition. Table 5.4 summarizes the device parameters, and figure 5.15 gives the photo current vs bias voltage curve of the samples. The pristine **UPBI-Py** exhibited SCLC with a bulk mobility estimate of ≈ 10

Table 5.4: Summary of device parameters

Electron only device with ITO/Active layer/Al			
Sample Name	**Maximum mobility $\mu_{e,max}$ (cm^2/Vs)**	**Average mobility $\mu_{e,avg}$ (cm^2/Vs)**	**Mean deviation**
UPBI-Py	2.08×10^{-4}	1.62×10^{-4}	$\pm 4\times 10^{-5}$
[UPBI-Py (OPVM-OH)]$_{1.0}$	8×10^{-3}	7×10^{-3}	$\pm 5\times 10^{-4}$
[UPBI-Py Poly(OPVM-OH)]$_{1.0}$	6.2×10^{-4}	5.11×10^{-4}	$\pm 9\times 10^{-5}$

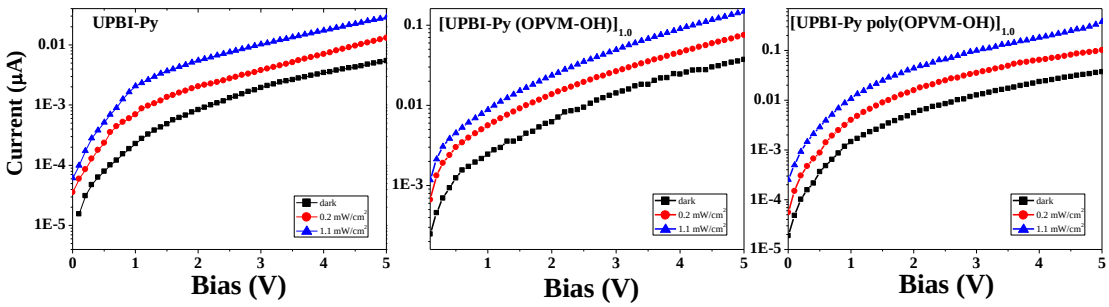

Figure 5.15: Photo Current Vs Bias voltage curve of **UPBI-Py**, 1:1 complex **[UPBI-Py (OPVM-OH)]$_{1.0}$** and supramolecular polymer complex **[UPBI-Py poly(OPVM-OH)]$_{1.0}$**

$^{-4}$ cm^2/Vs whereas the mobility estimate was an order higher for **[UPBI-Py (OPVM-OH)]$_{1.0}$** ~ 10^{-3} cm^2/Vs. The polymer complex **[UPBI-Py poly(OPVM-OH)]$_{1.0}$** exhibited mobility ≈10^{-4} cm^2/Vs. The intensity dependence of the photocurrent response of these samples also reveal interesting trends with a superlinear response in case of D−A complex and poly(D-A) complex. Figure 5.16 compares the photocurrent response of **UPBI-Py**, **[UPBI-Py (OPVM-OH)]$_{1.0}$**, and **[UPBIPy poly(OPVM-OH)]$_{1.0}$** and table 5.5 lists the maximum mobility $\mu_{e,max}$ (cm^2/Vs) under irradiation at two different light intensities. Higher photocurrent response was observed for **[UPBI-Py (OPVM-OH)]$_{1.0}$** and **[UPBI-Py poly(OPVM-OH)]$_{1.0}$** with high responsivity (≈1 μA/W) compared to the pristine acceptor **UPBI-Py** device. The higher photocurrent could be attributed to the facile photoinduced charge generation and separation factors prevailing in the D−A system. The network required for independent electron and hole transport however is constrained leading to sizable trapping and recombination losses, and can be the cause for the superlinear intensity dependence. Additionally, the presence of the insulating methacrylate polymer backbone in case of the supramolecular D−A polymer complex could also lower the mobility and photocurrent magnitude compared to the observed trends in case of the D−A complex. In short, the observed trend in the different systems provides a guide toward design of appropriate D−A building blocks for efficient optoelectronic properties.

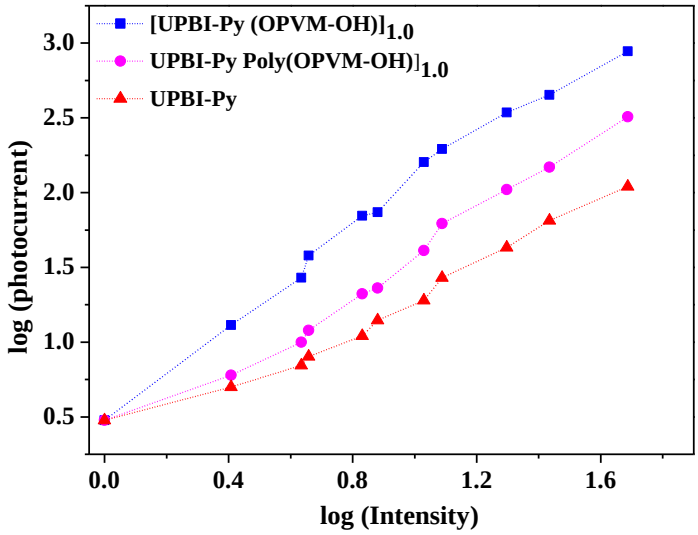

Figure 5.16: Photoconductive characterization upon irradiation with increasing power density at -2V bias (normalized photocurrent in pA and Intensity in mW/cm^2).

Table 5.5: Photoconductivity characterization in the dark and under white light irradiation of increasing intensity

Sample Name	Maximum mobility $\mu_{e,max}$ (cm^2/Vs) (in dark)	Maximum mobility $\mu_{e,max}$ (cm^2/Vs) (under irradiation; Intensity 0.2 mW/cm^2)	Maximum mobility $\mu_{e,max}$ (cm^2/Vs) (under irradiation; Intensity 1.1 mW/cm^2)	Responsivity (nA/W)
UPBI-Py	2.08×10^{-4}	4.53×10^{-4}	1.13×10^{-3}	10
[UPBI-Py (OPVM-OH)]$_{1.0}$	8×10^{-3}	2.4×10^{-2}	5.4×10^{-2}	1000
[UPBI-Py Poly(OPVM-OH)]$_{1.0}$	6.2×10^{-4}	1.7×10^{-4}	4.57×10^{-3}	100

5.5 Conclusion

In conclusion, we have shown that donor and acceptor small molecules based on complementarily functionalized oligo(*p*-phenylenevinylene) (**OPVM-OH**) and N-substituted perylenebisimide (**UPBI-Py**) for hydrogen bonding interactions could be organized into lamellar structures in the domain range 5 to 10 nm using the concept of supramolecular assembly. A 1:1 supramolecular complex of **OPVM-OH** and **UPBI-Py** was prepared, structurally characterized and further subjected to polymerization thermally as well as by photo irradiation resulting in supramolecular donor−acceptor complex polymer. The homopolymer of the donor alone without complexation with the acceptor **UPBI-Py** resulted in an insoluble polymer which could not be fully characterized. Complexation improved the solubility of the donor−acceptor polymer by several folds. The emission from thin drop cast films of the 1:1 donor−acceptor complex was considerably quenched compared to the donor alone or acceptor alone thin film samples. The emission spectra of thin film samples of the supramolecular polymer complex exhibited subtle organizational changes occurring in the donor (OPV) emission upon its polymerization. Compared to the red-shifted aggregate emission from OPV observed in **[UPBI-Py (OPVM-OH)]$_{1.0}$**, the supramolecular polymer **[UPBI-Py poly(OPVM-OH)]$_{1.0}$** exhibited monomeric OPV emission indicating that the self-assembly of OPV was disrupted upon polymerization due to the formation of methacrylamide linkage in the backbone. Solid state measurements such as FTIR and WXRD and thin film morphology using TEM were undertaken to understand the self-organization. WXRD studies showed that donor−acceptor complex formation between **UPBI-Py** and **OPVM-OH** resulted in distinct changes in the cell parameters of **OPVM-OH**. Polymerization of the donor within the supramolecular D−A complex resulted in a reduction in overall crystallinity in the

supramolecular complex polymer. Photo response measurements of the D−A supramolecular complex indicated a clear trend of higher conductance compared to pristine **UPBI-Py**. This is the first time that such superior lamellar organization of the donor and acceptor organic semiconducting molecules has been achieved without the aid of a templating polymer or block copolymer. The highlight of this approach was the improved processability afforded by the improved solubility of the D−A supramolecular complex compared to the donor or acceptor alone, while at the same time maintaining the crystalline organization also. This concept is extendable to the analogous complementarily functionalized donor−acceptor pairs (such as oligothiophene and perylene/naphthalenebisimides), which can be further polymerized in order to facilitate processability.

5.6 References

1. Aida, T.; Meijer, E. W.; Stupp, S. I. *Science* **2012**, *335*, 813-817.
2. Neuteboom, E. E.; Meskers, S. C. J.; Van Hal, P. A.; Van Duren, J. K. J.; Meijer, E. W.; Janssen, R. A. J.; Dupin, H.; Pourtois, G.; Cornil, J.; Lazzaroni, R.; Bre´das, J-L.; Beljonne. D. *J. Am. Chem. Soc.* **2003**, *125*, 5174-5176.
3. Jalani, K.; Kumar, M.; George, S. J. *Chem. Commun.* **2013**, *49*, 14968-14969.
4. Park, B.; Cho, S. E.; Kim, Y.; Lee, W. J.; You, N. –H.; In, I.; Reichmanis, E. *Adv. Mater.* **2013**, *25*, 6453-6458.
5. Aiyar, A. R.; Hong, Jung-Il.; Izumi, J.; Choi, D.; Kleinhenz, N.; Reichmanis, E. *ACS Appl. Mater. Interfaces* **2013**, *5*, 2368 –2377.
6. De Boer, B.; Stalmach, U.; van Hutten, P. F.; Melzer, C.; Krasnikov, V. K.; Hadziioannou, G. *Polymer* **2001**, *42*, 9097-9109.
7. Mativetsky, J. M.; Kastler, M.; Savage, R. C.; Gentilini, D.; Palma, M.; Pisula, W.; Müllen, K.; Samorí, P. *Adv. Funct. Mater.* **2009**, *19*, 2486–2494.
8. Zapala, J.; Knor, M.; Jaroch, T.; Maranda-Niedbala, A.; Kurach, E.; Kotwica, K.; Nowakowski, R.; Djurado, D.; Pecaut, J.; Zagorska, M.; Pron, A. *Langmuir **2013**, 29, 14503–14511*.
9. Ikkala, O.; ten Brinke, G. *Science* **2002**, *295*, 2407-2409.
10. Hanski, S.; Houbenov, N.; Ruokolainen, J.; Chondronicola, D.; Iatrou, H.; Hadjichristidis, N.; Ikkala, O. *Biomacromolecules* **2006**, *7*, 3379−3384.
11. Ruokolainen, J.; Mäkinen, R.; Torkkeli, M.; Mäkelä, T.; Serimaa, R.; ten Brinke, G.; Ikkala, O. *Science* **1998**, *280*, 557-560.
12. Ruokolainen, J.; ten Brinke, G.; Ikkala, O.; Torkkeli, M.; Serimaa, R.; Komanschek, E., *Phys. Rev. E* **1996**, *54*, 6646-6649.
13. Narayan, R.; Kumar, P.; Narayan, K. S.; Asha, S. K. *Adv. Funct. Mater.* **2013**, *23*, 2033–2043.
14. Rancatore, B. J.; Mauldin, C. E.; Fréchet, J. M. J.; Xu, T. *Macromolecules* **2012**, *45*, 8292−8299.
15. Rancatore, B. J.; Mauldin, C. E.; Tung, S. H.; Wang, C.; Hexemer, A.; Strzalka, J.; Fréchet, J. M.J.; Xu, T. *Acs Nano.* **2010**, *4*, 2721-2729.
16. Perepichka, I. I.; Lu, Q.; Badia, A.; Bazuin C.G. *Langmuir* **2013**, *29*, 4502-4519. 29, 4502-4519.
17. Hu, H.; Gopinadhan, M.; Osuji, C. O. *Soft Matter* **2014, *10***, 3867-3889.

18. Cummins, C.; Borah, D.; Rasappa, S.; Chaudhari, A.; Ghoshal, T.; O'Driscoll, B. M. D.; Carolan, P.; Petkov, N.; Holmes J. D.; Morris, M. A. *J. Mater. Chem. C* **2013**, *1*, 7941-7951.
19. Kao, J.; Thorkelsson, K.; Bai, P.; Rancatore, B. J.; Xu, T. *Chem. Soc. Rev.* **2013**, *42*, 2654-2678.
20. Thorkelsson, K.; Mastroianni, A. J.; Ercius, P.; Xu, T. *Nano Lett.* **2012**, *12*, 498−504.
21. Ruokolainen, J.; ten Brinke, G.; Ikkala, O. *Adv. Mater.* **1999**, *11*, 777-780.
22. van Zoelen, W.; van Ekenstein, G. A.; Polushkin, E.; Ikkala, O.; ten Brinke, G. *Soft Matter* **2005**, *1, 280–283.*
23. Ono, R. J.; Todd, A. D.; Hu, Z.; Vanden Bout, D. A.; Bielawski. C. W. *Macromol. Rapid Commun.* **2014**, *35*, 204−209.
24. Wang, J.; Higashihara, T. *Polym. Chem.*, **2013**, *4*, 5518-5526.
25. You, C-C.; Würthner, F. *J. Am. Chem. Soc.* **2003**, *125*, 9716-9725.
26. Lane, T. J.; Nakagawa, I.; Walter, J. L.; Kandathil, A. J. *Inorg. Chem* **1962**, *1*, 267-276.
27. Moussa, K.; Decker, C. *J Polym Sci Part A: Polym Chem*. **1993**, *31*, 2197-2203.
28. Rekha, N.; Asha, S. K. *J. Appl. Polym. Sci.* **2008**, *109*, 2781–2790.
29. Schenning, A. P. H. J.; Peeters, E; Meijer, E. W. *J. Am. Chem. Soc*. **2000**, *122*, 4489-4495.
30. Shao, C.; Grüne, M.; Stolte, M.; Würthner, F. *Chem. Eur. J.* **2012,** *18*, 13665-13677.
31. Emily R. Draper, E. R.; Walsh, J. J.; McDonald, T. O.; Zwijnenburg, M. A.; Cameron, P. J.; Cowan, A. J.; Adams. D. J. *J. Mater. Chem. C* **2014**, *2*, 5570-5575.
32. Chen, Z.; Stepanenko, V.; Dehm, V.; Prins, P.; Siebbeles, L. D. A.; Seibt, J.; Marquetand, P.; Engel, V.; Würthner, F. *Chem. Eur. J.* **2007**, *13*, 436 – 449.
33. Zhang, J.; Hoeben, F. J. M.; Pouderoijen, M. J.; Schenning, A. P.; Meijer, E. W.; De Schryver, F. C.; De Feyter, S. *Chem. Eur. J.* **2006**, *12*, 9046−9055.
34. van Hutten, P. F.; Brouwer, H-J.; Krasnikov, V. V.; Ouali, L.; Stalmach, U.; Hadziioannou, G. *Synthetic Met.* **1999**, *102*, 1443-1446.
35. Ramakrishna Matte, H. S. S.; Jain, A.; George, S. J. *RSC Adv.* **2012**, *2*, 6290−6294.
36. Samuel, I. D.W.; Rumbles, G.; Collison, C. *Phys. Rev. B* **1995**, *52*, RII 573-RII 576.
37. George, S. J.; Ajayaghosh, A. *Chem. Eur. J.* **2005**, *11*, 3217–3227.
38. Hutten, P. F. V.; Krasnikov, V. V.; Hadziioannou, G. *Acc. Chem. Res.* **1999**, *32*, 257-265.

39. Brochon, C.; Sary, N.; Mezzenga, R.; Ngov, C.; Richard, F.; May, M.; Hadziioannou, G. *J. Appl. Polym. Sci.* **2008**, *110*, 3664–3670.
40. De Luca, G.; Liscio, A.; Battagliarin, G.; Chen, L.; Scolaro, L. M; Müllen, K.; Samorì, P.; Palermo, V. *Chem. Commun.* **2013**, *49*, 4322-4324.
41. Ciesielski, A.; Szabelski, P.; Cadeddu, A.; Cook, T. R.; Stang, P. J.; Samorì, P. *J. Am. Chem. Soc.* **2013**, *135*, 6942–6950.
42. Schenning, A. P. H. J.; van Herrikhuyzen, J.; Jonkheijm, P.; Chen, Z.; Würthner, F.; Meijer, E. W. *J. Am. Chem. Soc*. **2002**, *124*, 10252-10253.
43. Würthner, F.; Chen, Z.; Hoeben, F. J. M.; Osswald, P.; You, C.-C.; Jonkheijm, P.; van Herrikhuyzen, J.; Schenning, A. P. H. J.; Schoot, P. P. A. M. v. d.; Meijer, E. W.; Beckers, E. H. A.; Meskers, S. C. J.; Janssen, R. A. J. *J. Am. Chem. Soc.* **2004**, *126*, 10611-10618.
44. Pascal, J.; Stutzmann, N.; Chen, Z.; de Leeuw, D. M.; Meijer, E. W.; Schenning, A. P. H. J.; Würthner, F. *J. Am. Chem. Soc.* **2006**, *128*, 9535-9540.

Chapter 6

Summary and Conclusions

Several optoelectronic applications demand the well-defined nanoscale assemblies of semiconducting materials. Well-defined nano structure of semiconducting materials can be achieved with the help of templated assembly with polymer support (e.g. poly(4-vinyl pyridine) (P4VP)). Ikkala and ten Brinke *et. al* studied many hierarchical architecture formation between small surfactant molecules and P4VP or its block copolymer with polystyrene–PS-b-P4VP. Some p-type and n-type semiconducting materials were incorporated to the polymer back bone of P4VP which showed promising results for the improvement in device performance. In this context, the thesis entitled "**Improving Charge Transport via Self-assembly in Semiconducting Donor/Acceptor Supramolecular Polymers**" describes the design and synthesis of n-type (perylene and naphthalenebisimide) and p-type materials (oligo (*p*-phenylenevinylene)) followed by formation of nano organization of these materials into polymer matrix via non covalent interaction like hydrogen bonding. These n-type and p-type materials retained their small molecular properties like crystallinity with the attractive processing advantages of polymers. These materials can find applications in various types of optoelectronic devices.

Initially in this work, two types of naphthalene molecules were synthesised namely naphthalenemonoimide (**NMI**) and naphthalenediimide (**NDI**) which were incorporated noncovalently into the back bone of polybenzimidazole (**PBImz**). **PBImz/NMI** supramolecular composites formed free standing film where as **PBImz/NDI** composites did not form free standing film. The noncovalent hydrogen bonding among **PBImz** and **NMI/NDI** was confirmed by FTIR and ^{1}H NMR spectroscopy. Strong π-π interaction was observed for **PBImz/NMI** composites which was evident from WXRD. The strong π-π stacking interaction occurring between the **NMI** core drove the self-assembly within the composite, which was stable in solution as well as solid state. Uniform nano-spherical morphology was observed for **PBImz/NMI** and **PBImz/NDI** composites under transmission electron microscope. Both composites exhibited semiconducting properties. To the best of our knowledge this is the first demonstration of using commercially important **PBImz** polymer to from composite with organic semiconducting molecule. The semiconducting properties of these composites can be tuned and improved further by changing the semiconducting materials over a wide range. However, the low value of charge carrier mobility ($\sim 10^{-7}$ cm^2/Vs) promoted the search for new polymer backbone capable of supporting better charge carrier mobility with respect to the pristine state.

In the second chapter, symmetric ditopic hydrogen bondable rylenebisimides (perylenebisimide (**PBI-PDP**) and naphthalenebisimide(**NBI-PDP**)) were developed with

free aromatic –OH group at both termini. A supramolecular crosslinked polymer network was developed by mixing the rylenebisimide with Poly(4-vinyl pyridine) (P4VP) making use of noncovalent interaction like hydrogen bonding and π-π interaction etc. Complex formation was confirmed by FT-IR spectroscopy. Single crystals of **PBI-PDP** could be grown with space group of $P2_1$. Thermotropic liquid crystalline behavior was observed in naphthalenebisimide derivative (**NBI-PDP**), while both **PBI-PDP** and **NBI-PDP** exhibited lyotropic liquid crystalline behaviour in tetrahydrofuran (THF). The liquid crystalline behaviour was characterized using combination of differential scanning calorimeter (DSC), polarized light microscopy (PLM) and X-ray diffraction (XRD) studies. Both supramolecular polymer crosslinked networks peserved their mesomorphic behaviour in THF. Layered morphology was observed in rylenebisimide-P4VP complexes as observed under TEM. A stretching of the rylenebisimide molecules was observed after complex formation with P4VP backbone which was evidenced from WXRD studies. This improvement in organization resulted in high electron mobility in **P4VP-PBI** complex (μ_e = 1.03 x 10^{-3} cm^2/Vs) compared to its pristine state (μ_e ~ 1.0 x 10^{-5} cm^2/Vs). Thus liquid crystalline rylenebisimide based supramolecular crosslinked polymer network with layered structure was successfully fabricated.

Third chapter introduced supramolecular polymer complex with donor and acceptor material into P4VP backbone with improvement in charge carrier mobility. It described the synthesis of acceptor molecule, based on unsymmetrical perylenebisimide with pentadecyl unit having free –OH group and 2-ethylhexyl alkyl chain at either termini (**UPBI-PDP**). A donor molecule, Oligo(*p*-phenylene vinylene) with hydroxyl (-OH) group and cyanide (-CN) group at either termini (**OPVCN-OH**) was also developed. Supra-molecular self-assembled nano organization of **UPBI-PDP**, **OPVCN-OH** in to the polymer matrix of P4VP was obtained with the help of noncovalent interaction like H-bonding and π-π interaction. FT-IR and ^1H NMR spectroscopy were used for confirmation of complex formation. Small angle X-ray scattering (SAXS) and wide angle X-ray diffraction (WXRD) were used to understand the solid state supramolecular organization. Thin film morphology of all donor-acceptor complexes with P4VP was clearly visualized with the help of transmission electron microscopy (TEM), which showed nice lamellar arrangement in the range < 10 nm. Absorption and fluorescence spectroscopy studies showed the effect of self-assembly on energy transfer between donor and acceptor molecule complexed with P4VP. Effect of self-organization of donor acceptor assembly on bulk mobility was measured via SCLC method and highest hole mobility (μ_h) was obtained in the order of 10^{-2} cm^2/Vs.

In the final working chapter, the insulating polymer chain P4VP was removed and a donor-acceptor nanostructured supramolecular assemblies were formed between oligo(*p*-phenylenevinylene) (**OPVM-OH**) complementarily functionalized with hydroxyl unit at one termini and polymerizable methacrylamide unit at other termini and an unsymmetric perylenebisimide functionalized with pyridine at one termini (**UPBI-Py**) via hydrogen-bonding interaction. The resulting supramolecular complex **[UPBI-Py (OPVM-OH)]$_{1.0}$** was subjected to polymerization in presence of suitable photoinitiator. FTIR spectroscopy was used for the confirmation of complex formation. The polymerization of the supramolecular D-A complex was confirmed from the disappearance of methacrylate double bond in FT-IR as well as ^{1}H NMR spectroscopy. The bulk structure and morphology of the supramolecular polymer complex **[UPBI-Py Poly(OPVM-OH)]$_{1.0}$** was studied using small angle X-ray scattering (SAXS) and wide angle X-ray diffraction (WXRD), which revealed the highly crystalline nature of the polymer as well as the appearance of a new reflection corresponding to π-π stacking of the rigid aromatic core at a 'd' spacing of 3.76 Å. The 1:1 small molecular complex as well as polymer complex showed uniform lamellar structures in the domain range < 5 nm under transmission electron microscope (TEM). The electron mobility as well as photocurrent response of the acceptor part was investigated to understand the effect of self-assembly in charge transport behavior for **[UPBI-Py (OPVM-OH)]$_{1.0}$**, **[UPBI-Py Poly(OPVM-OH)]$_{1.0}$** and pristine **UPBI-Py**. The space charge limited current (SCLC) bulk mobility estimated for donor-acceptor supramolecular complex **[UPBI-Py (OPVM-OH)]$_{1.0}$** was one order higher in magnitude with respect to the pristine **UPBI-Py**. Thus, a simple and facile method was developed to obtain nanostructured n-type and p-type semiconductor materials based on perylenebisimide and oligo(*p*-phenylenevinylene) with improved photocurrent response without the aid of templated self-assembly.

To conclude, this thesis work mainly focused on the development of special arrangement of the active n-type and p-type semiconducting materials in nanoscale to improve the charge carrier mobility in actual devices. A facile and easy route was developed to get nanostructured semiconductor assemblies with the help of noncovalent approach. The structure-property relationship was studied in depth with the help of several advanced techniques. All the supramolecular complexes developed in this work were examined for device performance, which showed an overall increase in charge carrier mobility with respect to their pristine small molecular state.

Publications in International Journals

1. B. Saibal, A. Z. Ashar, R. Nandini Devi, K. S. Narayan, S. K. Asha. Nanostructured Donor-Acceptor Self Assembly with Improved Photoconductivity. *ACS Appl. Mater. Interfaces* **2014**, *6*, 19434−19448.

2. Nagesh B. Kolhe, Shekhar Shinde, **B. Saibal**, S. K. Asha. Novel Approaches in the Design of Donor-Acceptor Oligomeric and Polymeric Materials for Photovoltaic Applications: D/A Blend versus Self-assembly of D/A by Covalent or Non-Covalent Interaction. *Org. Photonics Photovolt.* **2015**, *3*, 71–100

3. B. Saibal, S. Chithiravel, S. K. Asha. P4VP and Oligo(phenylenevinylene)-perylenebisimide Mixed Donor-Acceptor Supramolecular Comb Polymer Complexes with Improved Charge Carrier Mobility. *J. Polym. Sci. Part A: Polym. Chem.* **2016**, *54*, 2403–2412.

4. B. Saibal, Rekha Narayan, S. Chithiravel, S. K. Asha. Liquid Crystalline Supramolecular Crosslinked Polymer Complexes of Ditopic Rylenebisimides and P4VP (Manuscript submitted).

5. B. Saibal, Nagesh B. Kolhe, S. Chithiravel, S. K. Asha. Poly(benzimidazole)/ Naphthalene-imide Semiconducting Composite by Complementary Hydrogen Bonding (Manuscript under preparation).

6. Asha Syamakumari, Rekha. N, Shekhar. S, **Saibal. B**. Comb-Coil Supramolecular Crosslinked Polymer. Patent Publication number WO2013128475 A1, also published as DE112013001258T5, US20150111982, WO2013128475 A4.

Symposia Attended/Poster Presentation

1. Saibal Bhaumik and S.K. Asha. "Nanostructure formation of Donor-Acceptor Comb Polymer via Self Assembly." **National Science Day**, CSIR-NCL, Pune, **2013.**

2. Saibal Bhaumik and S. K. Asha. "Nano Structure Formation of Donor-Acceptor Comb Polymer via Directed Self Assembly." **MACRO+FAPS 2013 - International Conference on Frontiers of Polymers and Advanced Materials**, Indian Institute of Science, Bangalore, **2013**.

3. Saibal Bhaumik and S. K. Asha. "Nano Structure Formation of Donor-Acceptor Comb Polymer via Directed Self Assembly." **2nd TAPSUN conference on Advances in Futuristic Solar Energy Materials and Technologies**, CSIR-CLRI, Chennai, **2013**.

4. Saibal Bhaumik, A. Z. Ashar, R. Nandini Devi, K. S. Narayan, and S. K. Asha."Self-Assembly Directed Nanostructured Donor-Acceptor Comb Polymer with Improved Photoconductivity." **8th Asian Photochemistry Conference**, CSIR-NIIST, Thrivananthapuram, Kerala, **2014**.

5. Saibal Bhaumik, S. Chithiravel, K. Krishnamoorthy and S. K. Asha. "Nanostructure formation of Donor-Acceptor, P4VP Complex *via* Template Hydrogen Bonding." **Macro 2015 – International Symposium on Science and Technology**, Indian Association for the Cultivation of Science, West Bengal, Kolkata , **2015**.

6. Saibal Bhaumik and S.K. Asha. "Self-Assembly Directed Nanostructured Donor-Acceptor Comb Polymer with Improved Photoconductivity." **National Science Day**, CSIR-NCL, Pune, **2015**.

7. B. Saibal, S. K. Asha. "Nanostructure formation of Donor-Acceptor, P4VP Complex *via* Template Hydrogen Bonding." **International Conference on Nanoscience and Technology**, IISER Pune, **2016**.